A NUMERICAL INVESTIGATION OF AN OROGENIC MESOSCALE CONVECTIVE SYSTEM

by GREGORY J. TRIPOLI

Atmospheric Science
PAPER NO.
401

DEPARTMENT OF ATMOSPHERIC SCIENCE
COLORADO STATE UNIVERSITY
FORT COLLINS, COLORADO

A NUMERICAL INVESTIGATION OF AN OROGENIC MESOSCALE CONVECTIVE SYSTEM

by

Gregory J. Tripoli

Research supported by the

National Science Foundation
under Grants ATM-8312077 and ATM-8512480

Department of Atmospheric Science
Colorado State University
Fort Collins, Colorado

Atmospheric Science Paper No. 401

ABSTRACT OF DISSERTATION

A NUMERICAL INVESTIGATION OF AN
OROGENIC MESOSCALE CONVECTIVE SYSTEM

The interaction of topographically induced thermally and mechanically driven diurnal flow regimes in the lee of the Rockies is shown to lead to the growth of a mesoscale convection system (MCS). The results are based on a series of two-dimensional and three-dimensional non-hydrostatic numerical simulations of an intensively studied convective event based on data gathered in the 1977 SPACE (South Park Area Cumulus Experiment)/HIPLEX (High Plains Experiment).

The results have been used to define six stages in the MCS genesis. The first stage, described adequately by Cotton et al. (1983), is typified by the growth of the mountain boundary layer during the morning. The second type begins as a deep convection forms in the early afternoon over the high mountain peaks. The third stage begins with the formation of an eastward propagating convective squall line system of meso-β proportions in the lee wave/slope flow convergence zone 60 km east of the Continental Divide. The fourth stage occurs as the meso-β system moves eastward into a supression zone east of the foothills and weakens. The fifth stage begins with explosive growth of the meso-β system east of the supression zone. The final and sixth stage occurs after nightfall and is typified by the decoupling of convection from the surface and the lateral spread of meso-β scale vertical motion into dispersed regions of meso-β scale convection.

The results demonstrate that precipitating convection is of basic importance to deepening the mountain/plains solenoid from 5 km depth for a dry circulation to tropopause depth. The persistent deep cellular

circulation induces an atmospheric wind response on the scale of the Rossby Radius of Deformation (a meso-α-scale).

The system core also contains a meso-β scale transient circulation comprised of an internal gravity wave train. The result is the temporal oscillation of vertical motion within the core. Since convective elements (meso-γ circulation) are contained primarily within the core, their intensity varies as the core meso-β scale vertical motion oscillates. The core always exists at the western edge of the plains temperature inversion (which caps the boundary layer) until after dark. This effectively localizes the convection by preventing its horizontal spread by the emitted gravity wave motion. As a result the meso-α response can grow and the meso-β core becomes long-lived.

The meso-β core and meso-α scale atmospheric responses move eastward with the mean tropospheric wind. Traveling internal waves emitted from the core travel at near 30 m s-1 and are inefficient in initiating convection by themselves. Most of their energy travels upward into the stratophere during the sunlight hours.

After sunset radiative effects are found to trap the meso-β scale internal waves emitted by the core and force strong vertical motion at considerable lateral distances from the core. It is suggested that this may be leading to transition to popcorn convection in many observed mesoscale convective systems after sunset.

Gregory J. Tripoli
Dept. of Atmospheric Science
Colorado State University
Fort Collins, Colorado 80523
Summer, 1986

ACKNOWLEDGEMENTS

I would first like to express my thanks to my wife Bonnie Tripoli who endured years of uncertainty and frustration while extending her considerable support so that we could achieve this goal. I also extend my deepest appreciation to Dr. William Cotton, my thesis advisor, for his suggestions, encouragement and support throughout this research. I also wish to thank Dr. Duane Stevens, who served as one of my committee members for much of the time and provided valuable comments and insights into the problem. I am grateful to my remaining committee members, Dr. Richard Johnson, Dr. Wayne Schubert, and Dr. Jon Peterka for their helpful comments on the research and on the text.

I extend special thanks to Mr. Craig Tremback for many helpful suggestions and critisisms and for a great deal of model development support. I also am grateful to Mr. Ray McAnelly, who organized and supplied me with much of the data on which this study was based. I also thank Mr. Ming-sen Lin for many helpful discussions which helped in my interpretations. Thanks also to Mr. Michael Fortune who took time to read the manuscript and extend his helpful suggestions.

I would like to acknowledge the technical support of Mrs. Brenda Thompson and Miss Nancy Duprey who helped type, organize, and edit the manuscript. I also thank Lucy McCall for drafting the figures.

Finally, I extend my appreciation to all other members of the Cotton clan, whom helped through their suggestions and discussions over the course of the research.

This work was supported by the National Science Foundation under grant ATM-8312077 and ATM-8512480. All computations were performed on the CRAY 1 machines of National Center for Atmospheric Research (NCAR), which is funded by the National Science Foundation.

TABLE OF CONTENTS

1. Introduction

Summertime convective rainfall in the midwestern United States occurs primarily at night, despite higher daytime conditional instability. The compilation over twenty years of data by Kincer (1916) demonstrated that more than half of all summertime precipitation occurs at night from eastern Colorado to western Kentucky. More recent climatological studies by Crow (1969) and Wallace (1975) confirm the early observations and demonstrate that the most frequent time of summertime rainfall gradually progresses from the late afternoon over the western high plains to the late evening over western Kansas and to the early morning in eastern Kansas (see Fig. 1.1).

Early attempts by Hann (1926) and Hewson (1937) were made to relate the nocturnal rains to the effects of longwave radiational cooling. Several years later. Bleeker and Andre (1951) proposed that convergence associated with the slope circulation leads to the development of nocturnal great plains thunderstorms 'in situ'. Then Means (1944, 1952) demonstrated that climatologically, nocturnal warm air advection occurs in the region 1.5 - 3 km AGL over the midwest. He suggested that the advection has a destabilizing effect leading to the occurance of nocturnal rains. Based on Wagner (1939), Means suggested the diurnal oscillation of winds in this region occurrs as a result of solenoidal circulations induced by the greater diurnal temperature ranges in the southwest, heating over high terrain to the west and the effects of the ocean to the south. An acceptable explanation for the existence of the

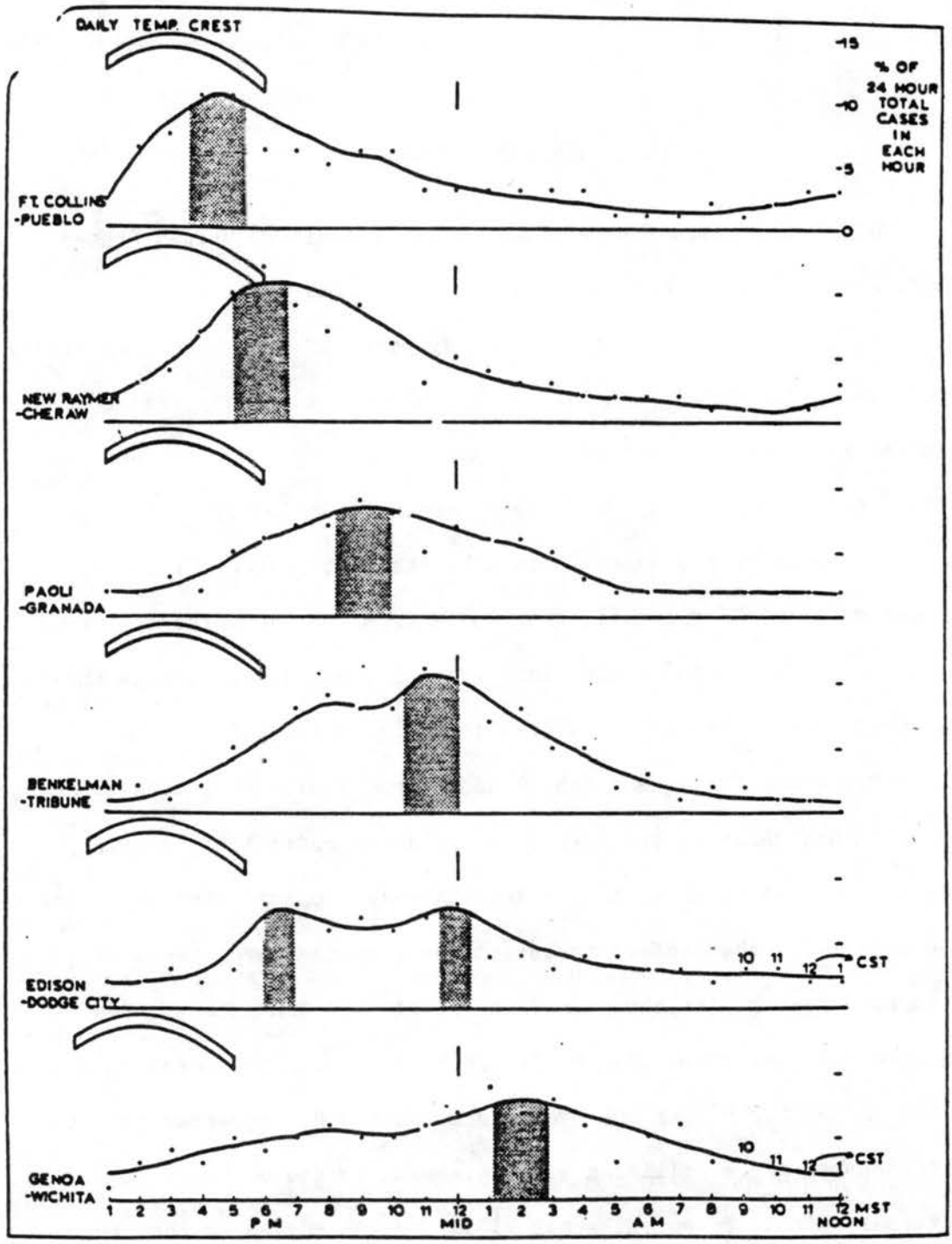

Figure 1.1. Timing of major convective activity for 10 year summary of hourly precipitation equal to or greater than .10 inch for six groups of stations with longitudinal separation of 55-62 km. (From Crow, 1967).

low level nocturnal jet was finally put forth by Blackadar (1957) and advanced by Wexler (1961). Bonner and Paegle (1970), McNider and Pielke (1981) and others. phenomena was found to be the result of an inertial oscillation about a mean geostrophic southerly flow occuring as the upper boundary layer adjusts to the decline of daytime thermally driven upslope flow.

Although the importance of the jet in supplying warm moist air to the nocturnal storms was clear, the dynamics and mechanisms of storm formation were not. The climatological studies indicated the nocturnal maxima moves increasingly later into the evening as one moves eastward from the Rockies, indicating a regular eastward progression of a region of precipitation. In a single case study of one such event. Bonner (1963) observed the associated convection to form far to the west over the Rockies during the afternoon and move into the region of the low level southerly jet during the night. He suggested that the convection was organized on the mesoscale in a squall line like structure. Moreover, he presented convincing evidence that this organization took place over or near the Rockies, prior to linking with the southerly jet. He concluded that the role of the southerly jet was to support existing mesoscale convective systems (MCSs) into the evening as daytime conditional instability wanes.

Studies of Colorado convection by Wetzel (1973), Karr and Wooten (1976), Phillip (1979), Maddox (1981) and Cotton et al. (1983) have all confirmed Bonner's far sighted hypothesis that daytime Rocky mountain convection often does propagate eastward into Kansas during the evening where it meets the low level support of the warm moist southerly jet during the night. Based on satellite observations, Maddox (1981) found

Midwest nocturnal storms to be most often associated with a particular circular shaped Meso-α (see Orlanski, 1975) scale convective disturbance which he termed mesoscale convective complex (MCC). Figure 1.2 depicts the trajectories of satellite observed MCCs for several years during July and August compiled by Maddox. Generally, the MCCs seem to originate preferentially over the high plains and eastern slopes of the Rockies.

It is apparent that to understand the phenomena of nocturnal thunderstorms in the Midwest, a clear understanding of the genesis of the MCCs which produce the rains must be sought. Uccelini and Johnson (1979), Maddox (1981), and others have sought to link the development of such systems to localized forcing from synoptic scale weather phenomena such as jet streaks or short waves. Although the support of such weather systems is often concurrent with MCC development, the diurnal nature and preferred region of genesis of these systems indicate that local forcing ultimately triggers the convection under the umbrella of synoptic scale support in the observed breeding grounds. Since local wind systems can initially organize convection on at least the meso-β scale (Pielke, 1974: Booker, 1963; Dirks et al., 1967; Dirks, 1969; Banta, 1982), they may play a dominant role in the initial growth phase of the MCS as well.

Most such local wind systems arise from solenoidal circulations produced from differential solar heating. In the preferred regions of MCC genesis there are several local wind systems which may develop. The most regular of these is the thermally driven mountain plains slope circulation. Convergence at or near mountain top associated with this circulation has been shown by Banta (1982). Braham and Draginis (1960),

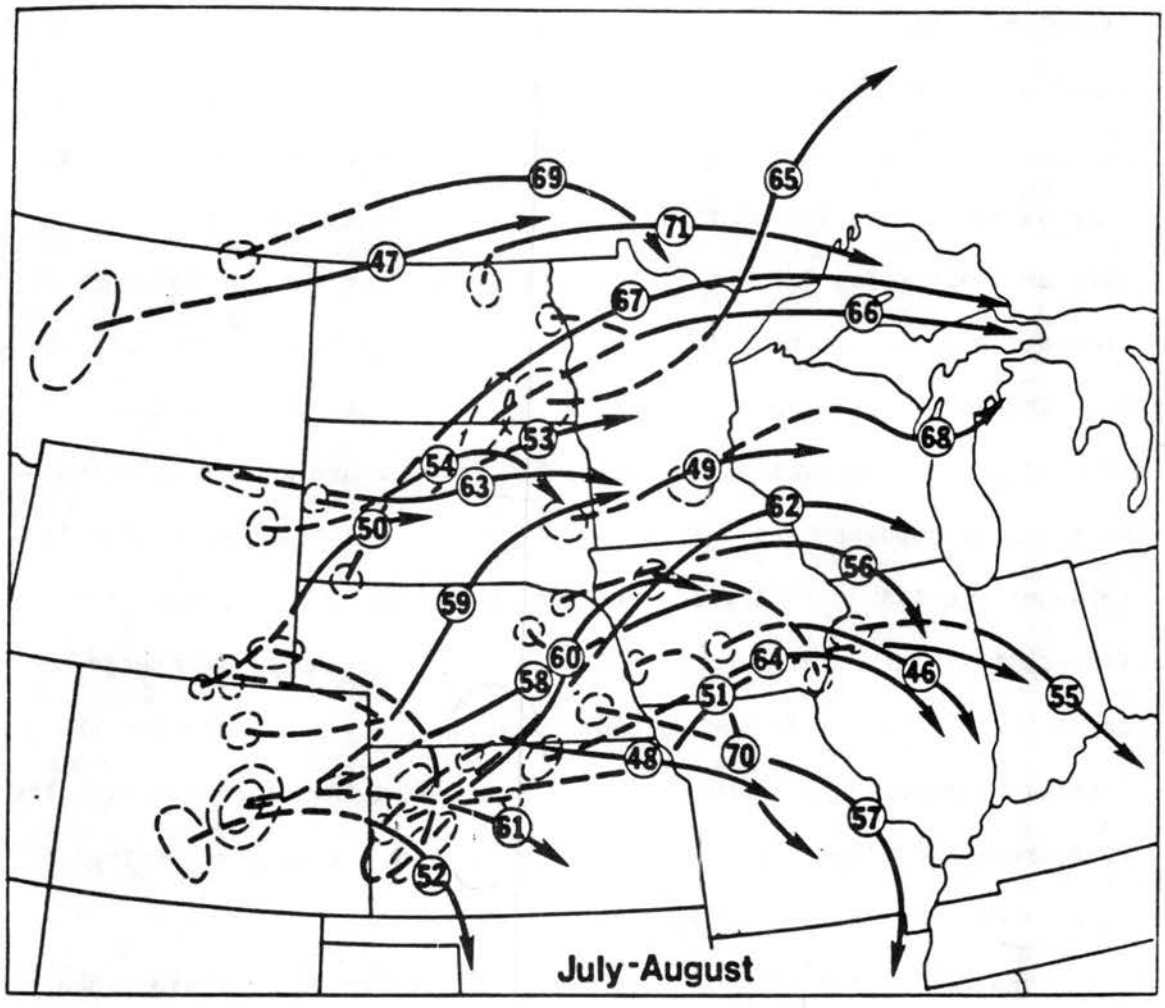

Figure 1.2. Tracks of 1978 and 1979 Mesoscale Convective Complexes during July-August. (From Maddox, 1981).

Orville (1968), Dirks (1969) and others, to be capable of initiating moist convection. Another class of diurnal circulation which could be important to regular MCS genesis are those arising from differential heating across the 'dry line' of the Central and Eastern Plains (e.g. Burgess and Davies Jones, 1979; McCarthy and Koch, 1982). On a less regular basis solenoidal circulations arising from surface moisture discontinuities have been implicated (see Sun and Ogura, 1979) in organizing convection on the mesoscale. Other local topographically induced local wind systems including low level convergences associated with varing topographical slope (Dirks, 1969), nocturnal downslope flow (Bleeker and Andre, 1951), or mountain lee waves (Dirks et al., 1967; Booker, 1963) may also lead to the eventual formation of mesoscale convective systems. In the case of mountain lee waves, although the forcing is more or less constant with respect to the diurnal cycle, the most preferred time of triggering would be when conditional instability is greatest in the late afternoon.

Considering the regular forcing of convection on the meso-β scale by local circulations, the question then arises: Given proper atmospheric conditions, can and does the mesoscale forced convection become self-sustaining through some mesoscale organization? If so, then it must be defined: What are the proper conditions? Emanuel (1983) refers to such organization as a 'flywheel' effect, where the persistent action of an ensemble of convective elements is able to store energy on a larger scale which in turn supports the convection through varying atmospheric conditions. The tendency for unstable growth of such an organized system of convective elements has been labeled Convective Instability of the Second Kind (CISK) by Charney and Eliassen (1963).

The mesoscale feedback to convection may be through surface friction induced convergence (frictional CISK) or by convergence induced by wave dynamics (wave CISK). One consistent shortcoming of the CISK hypothesis has been the lack of scale selection and slow growth rates (Emanuel, 1983). Perhaps the organization of meso-β scale convection by local wind systems overcomes these problems.

The underlying theme of this dissertation is the study of these questions. The approach will be to numerically model an observed situation where apparent triggering of convection by the thermally driven slope circulation of the Rockies took place and led to nocturnal Midwest thunderstorms. Sensitivity of the model dynamics to various physical processes will then be studied to reveal important mechanisms leading to the apparent organization of convection. The hypothesized daily development of Rocky Mountain convection resulting in the formation of an eastward propagating MCS which eventually feeds from the slope induced nocturnal jet will hereafter be referred to as the Rocky Mountain Convection Cycle (RMCC).

2. BACKGROUND

This dissertation will be an investigation of the mechanism by which convective activity translates from the mountain genesis regions in Colorado eastward onto the Great Plains during the night. Because orographically induced vertical motion initiates and modulates the convection, this study will necessarily address the subject of orographically induced flow fields. In addition, subsequent mechanisms of convection organization and propagation must be investigated. In this section, the current state of knowledge of these topics will be discussed.

2.1 Local Orographic Wind Systems

It was Defant (1951) who said: "...local temperature and wind conditions occur in the vicinity of large mountain ranges that are often so strong in their effect that, locally, they modify or even obscure the general weather conditions". This is most certainly the case on the eastern slopes of the central Rockies where a variety of orographally generated local wind systems operate and influence the climate throughout the year. The mountain barrier affects the local winds in two ways. First, elevated solar heating produces a diurnal thermally direct solenoidal circulation system called slope flows. This circulation has been studied over the past half century by Wagner (1931), Ekhart (1940), Defant (1951), Orville (1964), Dirks (1969), Banta (1982) just to name a few. The primary result is the production

of a upslope wind flow during the day while the terrain is heated and a downslope flow during the night as the terrain cools.

Numerous secondary effects also occur. The variation of slope between the Rocky mountain front range and the plains to the east was found by Dirks (1969) to result in a two celled slope circulation. Numerous levels of mountain valley and side wall wind systems, of which the general barrier is comprised, create interactions among themselves. For instance. Banta (1982) showed how a local slope wind over South Park, Colorado occurring early in the morning is later overwhelmed by a larger scale upvalley flow. He also showed how upslope flow begins beneath the dissipating nocturnal downslope flow such that there is a time when they coexist.

The slope flow system of the Rocky Mountains is large enough that coriolis force is important. As a result, the daytime eastern slope circulation produces a southeasterly flow along the Great Plains. The interaction of slope flow with surface friction and large scale pressure gradient is responsible for the creation of the nocturnal southerly jet (Means, 1952: Blackadar, 1957; McNider and Pielke, 1981). The effects of slope flow go beyond merely accelerating the local wind. Because the circulation system creates vertical motion, a conditionally unstable environment may produce unstable moist convection cells. Theories and observations of this will be presented later.

The second class of local winds produced by orography are those resulting from the mechanical interaction of the mountain barrier with the ambient wind flow. Airflow within a stably stratified atmosphere intercepting a mountain ridge will be forcibly lifted and will result in the creation of a number of wave types. What happens depends on the

stability, the wind profile, and the dimensions of the ridge. Let us define the Rossby number:

$$Ro = U/fL \tag{2.1}$$

where U is the mean wind, f is the coriolis parameter and L is the ridge half width. For Ro $\leq$ 1, coriolis force must be considered in studying the waves produced. The largest scales to be considered fall into a region where Ro may be as small as order 1 and coriolis can be important. The effect of coriolis will be simply to distort the horizontal flow pattern. Because potential vorticity is conserved within the airflow, vertical stretching will produce anticyclonic relative vorticity windward and cyclonic relative vorticity to the lee (Smith, 1979). This flow distortion tends to dampen quickly with height.

When Ro $\geq$ 1 ageostrophic gravitational oscillations caused by the vertical airflow displacement become of dominant importance. On scales less than 1 km (meso-γ from Orlanski, 1975), gravity waves diminish in importance as the timescale for flow to pass over the ridge becomes less than the period of a gravitational oscillation (Smith, 1979). Flows on these scales are below those of interest to this study.

The effect of mechanical lifting on the windward side of the mountain can be effective in releasing potential instability and forming convection. In general, Wetzel (1973) found heavy thunderstorm days on the eastern plains to be associated with a southeasterly ambient flow. Wetzel concluded that the most important effect of this flow was the transport of moisture into the region from the Gulf of Mexico. However, there is evidence that in some cases, an easterly component to the low level flow may be important in releasing potential instability through forced uplifting. The Big Thompson flood of 1976 described by Caracena

et al. (1978) is one such example. There seems to be no evidence given by Wetzel (1973) or Toth and Johnson (1985) that forced uplifting has any thing to do with the propagation problem addressed by this thesis. Therefore, this study will be concerned primarily with the mechanical effects of mountain generated gravity waves.

The internal gravity waves forced by a mesoscale mountain ridge can be subdivided into vertically propagating and vertically trapped lee waves (Durran, 1982; Smith, 1979). The two modes of wave propagation naturally arise from linear perturbation analysis of two-dimensional, steady, anelastic, inviscid flow over a ridge (see Scorer, 1949: Queny et al., 1960; Smith, 1979). If the atmosphere is of constant stratification and shear, then vertically propagating waves occur. Such waves are typified by a tilt into the flow and an increase in amplitude with height. When an atmospheric layer with rapidly changing stability or shear is found, mountain wave energy may be refracted back downward producing trapped lee waves. If such conditions occur, then trapped lee waves can produce a stationary vertical motion pattern for hundreds of kilometers downwind of a mountain barrier.

The vertical motion associated with the lee wave pattern can produce lee wave clouds (Durran, 1981). The vertical motion patterns have also been related to the modulation of convection in the lee of a mountain ridge by Booker (1963): Hosler et al. (1963), and Dirks et al. (1967). Dirks et al. studied the possibility of lee wave patterns to the lee of the Rockies during the summer months and found that typical stabilities and wind speeds would excite a lee wave length of 200-1100 km which corresponds favorably to an apparent convective activity wave length of 500-600 km viewed in satellite photographs. The recent work

of Durran (1981) has demonstrated that the effect of latent heating within the lee wave pattern is to damp the wave, and this was not considered in the Dirks' analysis.

2.2 The Triggering and Modulation of Convection by Orographic Local Winds

It was originally postulated that convection preferentially occurred over mountain peaks because of unstable thermals rising from the elevated heating (Silverman, 1960). Braham and Draginis (1960) were the first to fully recognize the importance of slope winds in initiating convection. They showed from observations that a nearly continuous convective chimney occurs slightly downwind of the mountain peak which spawns numerous convective clouds. Observations showed that air within the chimney is forced considerably above its neutral level. This forcing was attributed to the affects of the slope flow below.

The use of numerical modeling to study slope flows began in the early 1960's. The first attempt to simulate slope flow by Thyer and Buettner (1962) met with numerical problems which prevented a lengthy simulation. The first realistic two-dimensional simulation of slope flow was by Orville (1964). That simulation reproduced many of the features observed by Braham and Draginis (1959) and led the way to subsequent dry studies by Thyer (1966) and Fosberg (1967). The initiation of moist convection was first simulated numerically by Orville (1965) in a calm atmosphere and Orville (1968) with a mean wind. His results demonstrated numerically that the slope flow results in the convective chimney which spawns cumuli. When an ambient wind is considered, the slope convective chimney is displaced downwind and clouds are initiated on the lee side of the mountain ridge.

The effects of mountains on initiating convection was again addressed by Henz (1974) who found new convection to occur over selected climatological "hot spots" characterized by a particular favorable slope geometry or soil type. Subsequently, during the early 1970's, Colorado State University began conducting the South Park Area Cumulus Experiment (SPACE), to observe the formation and dynamics of mountain convection. The study culminated in the comprehensive 1977 experiment which employed doppler radar, portable automated mesonetwork (PAM), real-time ground weather stations, boundary layer profilers (BLP), aircraft, acoustic sounders, radiosonde, etc. From case studies of observed days, a number of interesting phenomena were found. Convection typically began over the steepest peeks in midmorning but progressed downwind (eastward) by noon. Hahn (1980) and Banta (1982) found that on both dry and moist days, a convergence line parallel to the ridge line was set up which propagated eastward throughout the day. The flow to the west of the line was well mixed vertically bringing westerly flow down to the surface. To the east of the line, the slope flow regime dominated the easterly flow at low levels. The line moved eastward by the momentum transported down from aloft (Banta, 1982). This same convergence line was observed on moist days to be responsible for convection during the early afternoon in the high mountains (Cotton et al., 1982; Motellabi, 1982). Cotton et al. found that individual cells moved relative to the convergence line, but new cell growth was always along the line. This was apparently a case of forced propagation of the convective system through convergence forcing induced by the thermal orographic circulation.

Both Cotton et al. and Motellabi observed that there came a time in the afternoon, usually around 1400 MDT, when the convection along the line grew large enough, that all the convection along the mountain seemed to simultaneously begin to trek eastward and out onto the plains. Motellabi observed the cloud structure to change from one featuring the updraft upshear to a line structure with the updraft downshear. This led to the speculation that perhaps a cold pool was created which eventually led to auto-propagation by density current. There seems to be no further study of what happens to the convergence line later on.

2.3 Convection on the High Plains

One of the first studies of the radar climatology of High Plains convection was by Hodges (1959). By studying hail occurences, he found that convection was most likely to occur in the absence of synoptic scale forcing. He did find the frequent occurence of a lee side trough associated with elevated heating on the plains which was often responsible for the movement of humid maritime air into the region from the southeast. Later studies by Schleusener et al. (1963), Marwitz et al. (1965) and Schleusener and Auer (1964) revealed 1) echoes generally traveled from the west with more intense storms more from the northwest, 2) echoes generally formed over rough terrain, 3) initial formation was around 1400 MST.

A more general study of the climatology of Great Plains moist covection cycle was made using satellite imagery by Dirks et al. (1967). They observed a climatological weakening of convective activity just to the lee of the front range and a subsequent intensification near the Colorado- Kansas border in the evening. They suggested that this modulation could be attributed to effects of mountain lee waves.

Later, Dirks (1969) used a two-dimensional numerical model to simulate the dry mountain-valley circulation of eastern Colorado. The results indicted the existence of a two-celled thermal circulation capable of enhancing or initiating convection some 50 km east of the front range foothills. No explanation was rendered for the observed eastward movement of convective activity, however, beyond the enhanced development due to the thermal circulation.

The comprehensive studies of summertime northeast Colorado thunderstorm systems by Wetzel (1973) and Karr and Wooten (1976) compiled nearly 2000 NHRE (National Hailstorm Research Experiment) soundings and two years of radar data from Limon, Colorado to determine mean convective storm paths and normal atmospheric conditions when thunderstorms are found to occur. Wetzel's mean echo paths (Fig. 2.1) further demonstrate the climatological diurnal eastward progression of convective activity from the east slopes of the Rockies at 1400 MDT to the Colorado-Kansas border by 2000 MDT.

Satellite observations were employed by Phillip (1979) to again observe the Rocky Mountain diurnal convection cycle. Her observations of High Plains convection during the summer of 1977 again showed a diurnal eastward progression of convection from the Rocky mountains onto the plains. It was found that development and movement of convective activity from the mountains to the plains occurred on 12% of the 1976 summer days and 17 % of the 1977 summer days. These systems were traced to account for as much as 90 % of the monthly precipitation (in some months) over western Kansas. In general, convection began in the southwestern and central Colorado mountains between 0700 and 1000 MDT. After 1500 MDT, new convection tended to be observed further east. It

was found that the regions of growing activity moved, rather than individual cells.

A composite satellite study of the Rocky Mountain - Great Plains convection cycle by Klitch et al. (1985) extended Phillip's analysis.. Their composite of convection during the summer of 1982 again showed the development of convection over the high mountain peaks around 1100 MDT, initial movement onto the plains around 1400-1500 MDT and movement into the eastern quarter of Colorado by 1700 MDT. They show the strongest activity to occur along the Palmer Lake divide, which is an east-west oriented ridge located in east central Colorado. Unlike Wetzel (1973), they do not find a similiar maxima along the Cheyenne ridge (also an east-west oriented ridge but along the northeastern Colorado boarder) during the 1982 months of July and August. It was also demonstrated that the cycle persists whether the day is characterized by severe storms or by smaller showery storms.

Erbes (1978), in a study of mountain convection over South Park, Colorado, concluded that the most important role played by mountain convection is its influence in modulating convective activity over the plains. It was postulated that mountain convection leads to forced subsidence over the plains, supressing convective activity. Satellite observations of Phillip (1979) seem to support these conclusions. In that study, she showed that as convection developed over the mountains, any existing activity over the plains appeared to weaken. Later in the day, the convective activity moves out onto the plains and the mountain convection weakens. The above evidence suggests that perhaps there is a meso-α wave like structure to the convection.

Recently, Toth and Johnson (1985) used the PROFS (prototype observational forecasting system) network of northeastern Colorado to take a climatological look at the diurnal surface flow cycles. Their observations depict a climatological wind shift associated with convergent flow, moving off the mountain barrier into the Platte valley around 1700 MDT. This pattern seems to correspond to the pattern of Platte Valley convection depicted by Wetzel (see Fig. 2.1). The PROFS data demonstrated that the 1700 windshift line occurs both on dry and moist days. Wetzel (1973) noted that the convection along the east-west ridges, often formed a convective line of meso-β proportions as it moved into Kansas by 2100 MST.

A detailed case study of a nocturnal MCC forming over western Kansas on August 4, 1977, was reported by Cotton et al. (1983). Wetzel et al. (1983) and Phillip (1979). The associated convection was again traced back to earlier mountain convection. The authors found the convection progressed in three stages. The first stage, occuring between 1000 and 1220 MDT, was characterized by small cumuli over the higher mountain peaks growing progressively deeper. Between 1220 and 1430 MDT the convection moved into the second stage characterized by deep mountain convection progressing to the edge of the plains. Upon reaching the plains, the third stage occurred, characterized by the formation of a north-south squall line which moved rapidly eastward. The formation and eastward progression of this squall line was likened to a convectively reinforced gravity wave similiar to the wave CISK theory of squall line propagation described by Raymond (1975, 1976). In the second part of that study, Wetzel et al. (1983) demonstrated that the eastward propagating line of convection played a key role in the

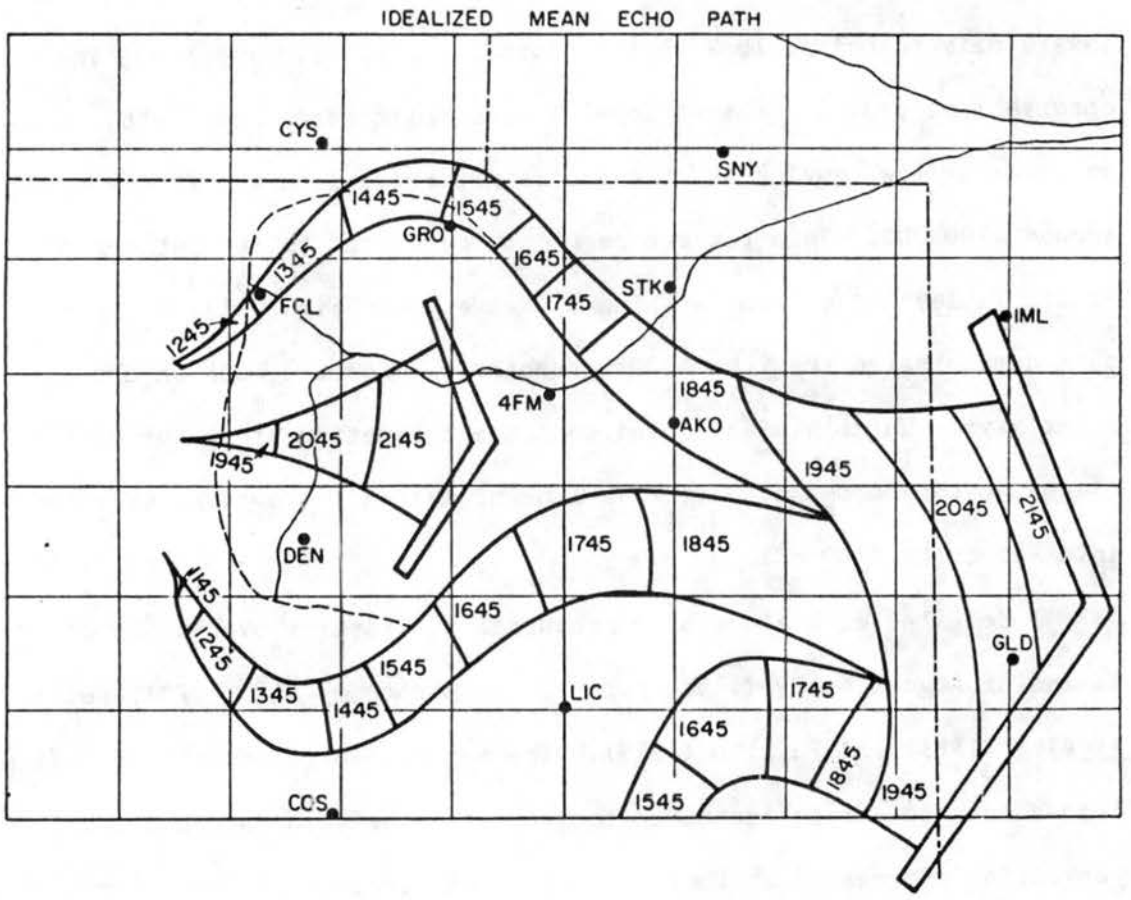

Figure 2.1. Idealized mean echo paths based on motion of areas of maximum echo frequency. Hourly position of maximum is given in MDT. (From Wetzel, 1973).

formation of a MCC over Kansas. It was pointed out that the 4 August, 1977 was the second of eight consecutive days when MCCs formed on the High Plains as nocturnal storms.

2.4 Theories of Convection Movement

The eastward movement of convection from the mountains to the Central Great Plains may occur by simple advection, forced propagation induced by external influences, or auto-propagation induced by the convection itself. The early experiments of Orville (1968) numerically simulated the development of small cumulus over a mountain peak which subsequently translated downwind by advection. This movement mechanism cannot explain the movement of Rocky mountain convection into central Kansas, however, because the lifetime of the system far exceeds that of a single cloud. Instead, the convection must communicate its energy eastward or its forcing must move eastward in order to obtain the observed propagation of the entire convective pattern.

Forced propagation of convective systems occurs when convection is parasitic on external mesoscale forcing such that the convection must follow the forcing. An example of forced propagation is the movement of convection associated with a sea breeze front. Pielke (1974) successfully simulated the movement of the sea breeze induced vertical motion fields over the Florida peninsula using a dry primitive equation model. Since the movement of the vertical motion closely matched that of observed patterns of cumulus activity, it is evident that the dynamics of the sea breeze front, to a large extent, determine the movement of the convective activity. Similiar boundary layer convergences are also produced by the ridge-valley solenoidal circulation (Banta, 1982; Orville, 1968, etc.) which may propagate

(Cotton et al. 1983, Toth and Johnson, 1985) and feed moist convection along the way.

Auto-propagation of mesoscale convection occurs primarily through the effects of self-generated gravity waves. The influence of convection on internal gravity waves and vise versa has been a subject of considerable research over the past half century (Haurwitz, 1947: Brunk, 1949; Tepper, 1950; Gossard and Munk, 1953; Williams, 1953; Eom, 1975; Uccellini, 1975; Lindzen and Tung, 1976; etc). Gravity waves are produced when heat is added to an air parcel within a stably stratified environment in the form of a vertical displacement. This produces an oscillitory motion which propagates radially away from the disturbance as waves. The waves transport the added energy away from the disturbance without net fluid displacement if the atmosphere is invicid, of uniform stratification and has no wind shear. Otherwise, the wave energy can be attenuated and converted to atmospheric kinetic or potential energy or vise versa.

The vertical motion created by the propagating gravity wave is of particular interest to those studying convection because of its impact in a conditionally unstable environment. The most obvious effect is its capability of outright initiation of an unstable updraft by radially propagating short wavelength gravity waves. Such wave activity typically propagates rapidly upward and is only capable of such initiation in the immediate vicinity of the responsible convective activity. The outward growth of convective regions by this process has been called "ensemble CISK" by Emanuel (1983). The discrete propagation of convective cells might fall into this catagory.

Under certain atmospheric conditions, it is possible for certain internal gravity waves to be trapped within layers changing stability and wind shear. For instance low level cooling by precipitation melting and evaporation can form an ensemble of trapped internal waves called a density current which can force convection through surface convergence (Byers and Brahm, 1949; Tepper, 1950, 1952, 1955; Williams, 1953; Fujita, 1963; Daly and Pracht, 1968; Charba, 1974; Purdom, 1976; Purdom and Marcus, 1982; Droegemeier and Wilhelmson, 1984; etc.). Although the period of oscillation of these shallow waves is short, their existence in an ensemble creates lifting over time scales of sufficient length to initiate convection.

Vertical changes in ambient stability and wind shear may vertically trap deep inertial gravity waves excited by convection as well. Called wave ducting (Lindzen and Tung, 1976), such trapping allows transmission of wave-induced vertical motion patterns along considerable distances from the parent convection (Uccellini, 1975; Eom, 1975; Miller and Sanders, 1980). For deep internal waves of this sort to be effective in initiating convection, they would have to have long horizontal wavelengths with periods on the order of a deep convective element lifetime.

If the period of convective growth and vertical profile of convective heating constructively reinforce a mode or modes of internal gravity wave formed, the gravity wave may grow from the convection it supports, even with considerable upward wave propagation allowed. This is the argument for wave-CISK created by Hayashi (1970) and advanced by Lindzen (1974), Raymond (1975, 1976), Davies (1979), Xu and Clark (1984) and others. A shortcoming of this approach, however, was that predicted

growth rates tended to be unrealistically small, there is almost a total lack of scale selection, and the wave form was too closely tied to a rather arbitrary vertical heating profile (Emanuel, 1983).

Some success has been found using the linear approach by introducing more "physical" cloud models. In particular, Davies (1979) followed by Raymond (1983) and Xu and Clark (1984) used a time-lagged cloud model. This resulted in a far greater degree of scale selection. In the case of Xu and Clark (1984), assumed cloud lifetimes of one-half hour, produced a significant wave growth on mesoscales of several hundred kilometers. Predicted phase speeds were consistent with some observations, as well.

If vertical variations of stability and wind shear are allowed for the wave-CISK problem, trapping can allow more efficient growth of otherwise weaker large scale wave-CISK modes. Such instability, called baroclinic wave-Cisk by Emanuel (1982), seemed more likely in view of the problems with pure wave CISK hypothesis. It will be shown later that a close study of baroclinic wave-CISK by Nehrkorn (1985) demonstrated that it poorly represented observed squall lines.

Another form of convection auto-propagation is caused by rotation induced pressure forcing of the updraft. In strongly sheared environments, tilting of horizontal vorticity into the updraft plane leads to cyclonically and anticyclonically rotating updrafts. Inertial effects force pressure lowering aloft laterally away from the updraft core. The associated pressure forcing has been shown by Klemp and Rotunno (1983), and Weisman and Klemp (1984; 1982), Tripoli and Cotton (1986), and others to force the updraft to split. When the vertical shear forms a curved hodograph, the vortex on the convex side of the

hodograph will be supressed while that on the concave side will be supported by the projection of horizontal helicity into the vertical (Lilly, 1983, Tripoli and Cotton, 1986). Since this form of propagation applies only to a single updraft cell, it has only limited applicability to the problem studied here. The occurence of right moving supercells over Colorado are not uncommon (Schleusener and Auer, 1964) during May and June. On weakly sheared summer days, which are of interest to this study, however,they are relatively rare and are certainly unimportant climatologically to the propagation studied in this paper.

Besides explicit propagation, there are other ways convective activity might be stimulated east of the mountains by the diurnal local wind systems. Some possibilities include a more complex slope circulation which forces convection to the east such as Dirks (1969) proposed. Wetzel (1973) suggested that moisture injected into midlevels by mountain convection moved over the plains during the afternoon destabilizing the atmosphere sufficiently to stimulate convection. Indeed Orville (1968) simulated such an effect numerically when moist bubbles created by the slope flow drifted downwind stimulating convective activity.

2.5 Mesoscale Convective Systems

When convective elements become organized, cause a constructive feedback on the mesoscale and thus become self-supporting, the entire circulation is labled a mesoscale convective system (MCS). This should not be confused with a simple mesoscale cluster of convection which may be driven by purely dry mesoscale convergence. Generally, growth of a MCS occurs because of energy supplied by convective heating.

The atmospheric response to convective heating can be divided into transient and balanced responses (Emanuel, 1983). Most typicaly, the transient response will take the form of an internal inertial gravity wave oscillation. These waves will transport energy horizontally and vertically away from the heat source. The atmospheric medium trough through which the wave travels is not affected permanently unless a non-linear interaction of the wave with the flow occurs.

It can be shown (Emanuel, 1983), that for linear invicsid flows, the gravity wave response is restructured to scales less than the Rossby Radius of Deformation. For a rotating fluid, Frank (1983) defines the Rossby radius of deformation as

$$L_R = \frac{c_g}{(f+\xi)^{1/2}(\frac{2V}{R} + \delta)^{1/2}} \qquad (2.2)$$

where f is the coriolis parameter ξ is the relative vorticity, V is the tangental flow with a vortex or radius R and C_g is the the internal gravity wave horizontal phase speed which can be approximated by

$$c_g = \frac{NH}{2\pi} \quad .$$

Here, H is the atmospheric scale height and N is the Brunt-Vaisalla frequency. Because the internal gravity wave response propagates upward, its influence is restricted to regions close to the heat source. The exception might be in the case where the gravity oscillation is vertically trapped (Emanuel, 1983). In that case a transient response to convective heating may extend for large horizontal distances from the source.

On scales beyond the Rossby radius, the atmosphere responds to heating in a balanced fashion. Most typically, the response is a gradient wind balanced system. The resulting flow and thermodynamic perturbation which grows relatively slow, but which is rather long lived. Emanuel (1983) show the time scale of the balanced response to be on the order of a pendulum day.

When considering the formation of a MCS, it is of central importance to show an atmospheric response or chain of responses which help to support further convection. Convection itself can be excited or supported in several ways. First, forced upward vertical motion might lift conditionally unstable air to its level of free convection, directly initiating a cloud element. Second, a region of general upward motion could act to support the growth of stronger convection as demonstrated by Tripoli and Cotton (1980). Third, upward vertical motion can act to thermodynamically destabilize the environment, indirectly supporting convection (Cotton et al., 1976). In both the second and third case, the environmental support is indirect in the sense that the large scale support does not itself initiate convective elements. For initiation, local turbulence or small scale gravity oscillations induced by existing convection act to initiate convection.

In each of the above cases, convection is supported by positive vertical motion. In particular, sub-cloud-base vertical motion will provide the needed support. The question must then be addressed: How can either a balanced or transient atmosphere response to convective heating act to support further convection?

The original CISK (Conditional Instability of the Second Kind) hypothesis, advanced by Charney and Elliasen (1963), is based on what

Raymond (1983) terms frictional CISK and pertains most strongly to balanced convective systems of scales beyond the Rossby radius of deformation. These systems, such as tropical storms, form cores of low pressure (in response to upper level latent heating) in approximate geostrophic balance at most levels. As these systems become intense, latent heat energy released by explicit vertical motion , becomes increasingly trapped (Schubert et al., 1980) as the Rossby radius shrinks. This causes the core to warm and pressure to decrease. Although in approximate gradient balance, vertical motion is forced through the effects of boundary layer Ekman pumping. The storm scale vertical motion in turn supports convective elements or storm scale vertical motion which in turn intensifies the circulation.

In the case of a transient response, gradient balance is not attained and significant fields of vertical motion are formed. If the wave response leads to growth, the convection or convection ensemble, then a wave-CISK (Lindzen, 1974) is operating. On scales less than the Rossby radius of deformation, disturbances of this type will consist primarily of ensembles of inertial gravity waves. In all wave-CISK models to date, linear theory has been used to predict modes of unstable growth and corresponding phase speeds. The greatest success against observation with the linear model approach has been obtained from some selected cloud scale systems (Raymond, 1975) and meso-α systems by Xu and Clark (1984). Because the linear approach often poorly selects a mesoscale growth, Xu and Clark (1984) successfully simulated such growth only after the "cloud model" was sufficiently "tweaked" with a time lagging. Their success seems to be limited to gravity-type disturbances such as observed by Uccelini and Johnson (1979) and Eom (1975).

Recently Nehrkorn (1985) critically compared predictions of a sophisticated linear baroclinic wave CISK model to observed behavior of squall type MCSs of severe and non-severe prefrontal types observed by Bluestein and Jain (1984) and Wyss and Emanuel (1984). It was determined that when the wave CISK model is tuned to reproduce observed squall structure, predicted phase speeds were too high by a factor of 2.5-3. Growth rates also were too small, possessing e-folding times of 20 hours or more. He concluded that his assumptions of constant shear, constant stability, and no momentum transport were minor problems. It was shown that the assumption of time lagging of downdrafts in clouds would improve the results only slightly. He speculated that the most potentially damaging assumptions were those of linearity.

A "density current" (Moncrieff and Miller, 1976), is typically formed by the combined effects of evaporation-induced cooling, melting-induced cooling, and the reflecting surface of the ground. It can be represented as a packet of long lived ducted waves which propagate along the surface forming what might be termed a pressure jump (Tepper, 1950) or pressure wave (Williams, 1953). Many, who have studied squall lines have predicted squall line movement with a simple density current model (Moncrieff and Miller, 1976; Tepper, 1952, etc.) while others attribute observed propagation to observed density current propagation (Purdom, 1976; Motellabi, 1982; etc.). Whether or not density current forcing is contained in traditional linear wave-CISK models is a point of controversy. It should be apparent that some of the most fundamental aspects are not. Density current forcing tends to occur in a rather shallow layer near the surface. The projection on deep internal gravity modes will be small and in itself have little ability to organize

convection. In reality density current forcing works by creating intense short vertical wavelength modes (from the action of the deep modes) which in turn initiate deep convection which projects strongly back onto the deep modes. Thus density current forcing is fundamentally a non-linear process which is represently very poorly in linear formulations.

Growth of convective systems through feedback by a density current is a transient atmospheric response to convection which might rightfully be called a CISK process. In this case the "flywheel" is the surface density pool which is a packet of trapped gravity waves, although trapped in a upside down sense. Very simple analytical models (e.g., Moncrieff and Miller, 1976) properly incorporating these effects have shown startling success in predicting squall line movement for some cases.

Recently, several investigators (Brown, 1979; Johnson, 1982; etc) have attempted to qualitatively explain some aspects of the mesoscale organization by considering the effects of longwave radiation and the melting layer in the stratiform anvil region. Obvservations have shown slow mesoscale ascent above the melting layer and decent below. Moreover, the divergence of flow near the melting level has been linked to the existence of an inflow jet at mid-levels. Some numerical investigations of this process by Brown (1979) and Chen (1986) lend support to the theory. This mechanism, however, fails to adequately explain the growth of the system from modest origins or its propagation.

A fourth type of CISK described by Emanuel (1983) is "ensemble" CISK. This is simply the growth of a region of convection by local excitation of elements in the immediate vicinity of ongoing convection.

Strictly speaking, this may not be a true MCS because there is no organization on the mesoscale which is supporting the convection.

Overall, previous attempts at a linear formulation of wave-CISK do in fact predict unstable growth, but, exhibit a poor relationship to many observed mesoscale convective systems. Some density current models of MCS movement have also had reasonable success in predicting movement in limited applications. MCSs have undoubtedly been simulated successfully in non-linear cloud and mesoscale models (e.g. Kreitzberg and Perkey, 1977; Fritsch and Chappel, 1979; Tripoli and Cotton, 1986; Weisman and Klemp, 1984; etc.). These studies, however, have not focused on the subject of a mesoscale wave response. The next step should be to begin to bridge the gap between non-linear formulations and simple understandable wave theory for the purpose of understanding the development and maintenance of mesoscale convective systems.

3. THE CASE STUDY

Beginning in 1973, Kelvin Danielsen and Dr. Lewis Grant of Colorado State University (CSU) began operating summertime field programs in South Park Colorado for the purpose of studing mountain thunderstorms. South Park is a relatively flat elevated basin (2.7 - 3.0 km MSL) conveniently situated in a known major thunderstorm genesis region (Henz, 1974). The early South Park programs of 1973, 1974 and 1975 were successful in observing thunderstorm formation with conventional radar, a surface mesonet, an instrumented aircraft and sailplane and photogrammetry.

The year 1977 was a down year for the National Hailstorm Research Experiment (operated by the National Center for Atmospheric Research, NCAR and the National Oceanic and Atmospheric Reasearch Administration, NOAA, in Northeast Colorado) and thus the observing equipment for that experiment became available. At the same time, the High Plains Experiment (HIPLEX) run by the Bureau of Reclamation was in operation directly to the east of South Park in Kansas. As a result, the South Park program was broadened (now called the South Park Area Cumulus Experiment SPACE (see Danielson and Cotton, 1977) to encompass, in addition to the previous measurements, triple doppler radar, the NCAR Portable Automated Mesonetwork (PAM), boundary layer profilers (BLPs), multiple aircraft and a sailplane, and radiosonde.

Spurred by interest in High Plains weather modification, SPACE was coordinated with HIPLEX to follow the progress of the observed mountain

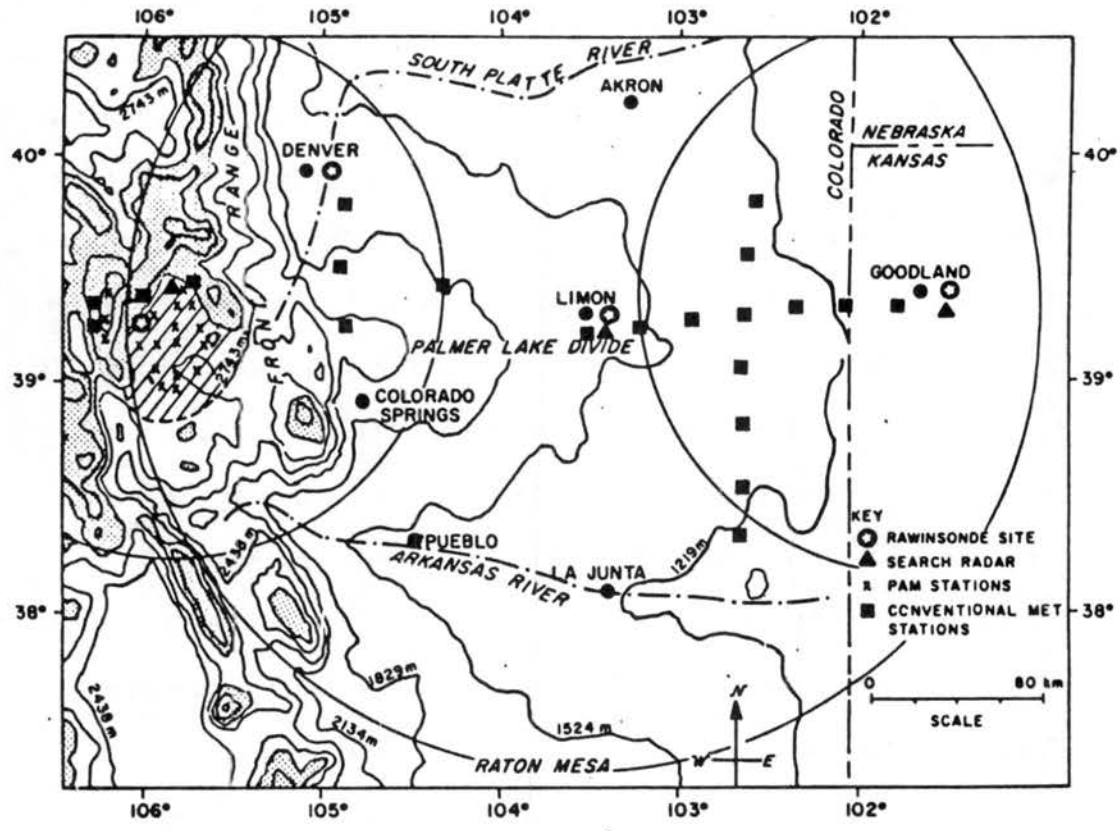

Figure 3.1. Map of extended SPACE/HIPLEX experimental area, with averaged terrain contours every 304.8 m (1000 ft) and terrain above 3048 m (10,000 ft) darkly shaded. The hatched region northwest of colorado springs represents the elevated basin [between 2743 m (9000 ft) and 3048 m (10,000 ft)] designated as South Park, Colorado. The large circles represent radar effective coverage areas. The CPS-4 radar (not included) is located 7 km southeast of the CP-3 radar. (From Cotton et al., 1983).

thunderstorms as they moved eastward (see Figure 3.1). Since the NCAR PAM was put in place in South park, CSU mesonet stations were moved east between the front range and the Kansas HIPLEX area. Additional high frequency radiosonde were taken over Limon, Colorado in coordination with the HIPLEX radiosonde at Goodland, Kansas. The combined coverage of the conventional radars of CSU at South Park, the National Weather Service at Limon, Colorado and HIPLEX at Goodland, Kansas provided continuous coverage of convection from the mountain genesis region to western Kansas. Radar coverage was supplemented with visible and infrared satellite coverage. On several occasions, such as 4 August, 1977, 3 minute "rapid scan" imagery was taken. SPACE/HIPLEX 1977 was to be the most comprehensive field study of Rocky Mountain generated convection and its downstream evolution ever undertaken.

During the course of SPACE, it became obvious that the mountain generated thunderstorms were directly connected with the major nocturnal convection in in the Midwest. The eight days between 3 and 10 August, 1977, was a particularly interesting time, for during that period eight separate Midwest MCCs were observed to form out of earlier mountain and High-Plains convection (Wetzel et al., 1983). One of these, the 4 to 5 August, 1977 MCC, spent the majority of its formative stage over the SPACE/HIPLEX observation network and was the subject of a comprehensive case study reported by Cotton et al. (1983) and Wetzel et al. (1983). Some major aspects of this case will be sumarized here, but for a more complete analysis, the reader is referred to the above references.

The synoptic situation in and around Colorado on 4 August, 1977 was relatively undisturbed. The 50 kPa flow (Figure 3.2) featured a longwave trough centered over the Hudson Bay with an elongated

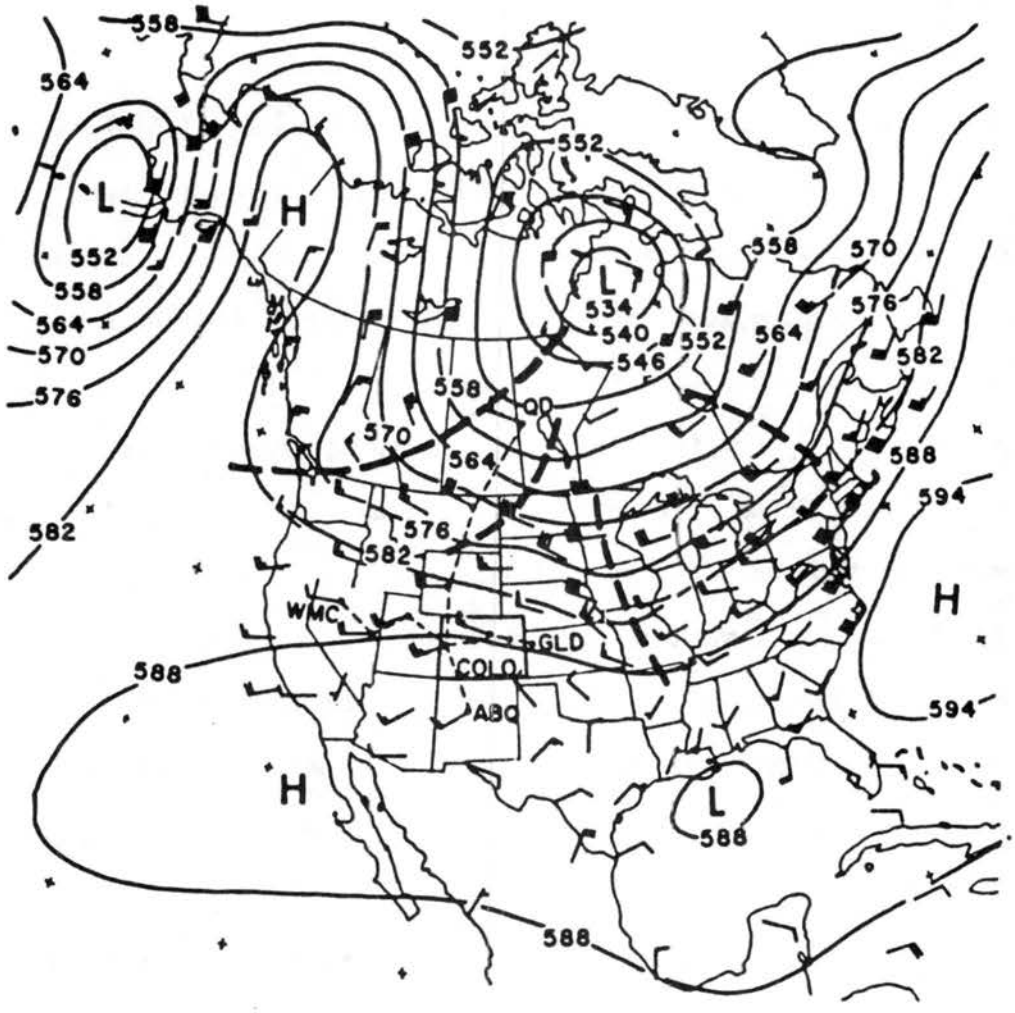

Figure 3.2. Continental-scale 50-kPa height analysis for 0600 MDT (GMT-6 h) 4 August 1977. Heavy dashed lines denote short-wave troughs. Height contours are labelled in decameters. Wind pennants, full barbs, and half barbs denote 25, 5 and 2.5 m/s, respectively. The dotted lines WMC-GLD and QD-ABQ show the cross section locations used in Figs. 6 and 7, respectively. (From Cotton et al., 1983).

subtropical high to the south producing a nearly zonal flow from western Colorado to the central Mississippi valley. Cotton et al. (1983) note that this more zonal pattern formed over several days prior to August 4 and persisted for sometime after. A meridional crossection analyzed by Cotton et al. (1983) is displayed in Figure 3.3. Note, in that Figure, the dual upper level baroclinic zone above Grand Junction, Colorado and the associated subtropical jet. It is likely that there are some thermal wind inconsistencies in this analysis, but nevertheless, the existence of the subtropical jet to the north of Grand Junction is apparent placing South Park in the subtropical air. Over the latitude of Grand Junction the zonal flow is reaching 23 m s^{-1} at 25 kPa.

At the surface a weak east-west oriented cool front was stalled on the Colorado - Wyoming border to the north. Not visible with this depiction, is the existence of a strong surface moisture gradient from southeastern to northeastern Colorado. At 1400 MST, Cotton et al. (1983) show surface mixing ratios decreasing from 12 g/kg in Pueblo to 9 g/kg in Denver. At mid-levels, CWMC found abundant moisture being advected across the Continental Divide from the west throughout the day. Associated with the moisture, there was evidence of weak PVA (positive vorticity advection) at mid-levels behind a region of weak anticyclonic flow evident in Figure 3.2.

The 0700 MST soundings at 6 stations across the observation network are displayed in Figure 3.4. In all cases east of the Continential Divide, the atmosphere is potentially conditionally unstable following afternoon heating. Very high midlevel moisture moving into the area from the west at 50 - 70 kPa is evident. In summary, on 4 August, 1977 the SPACE/HYPLEX region was under the influence of some weak PVA which

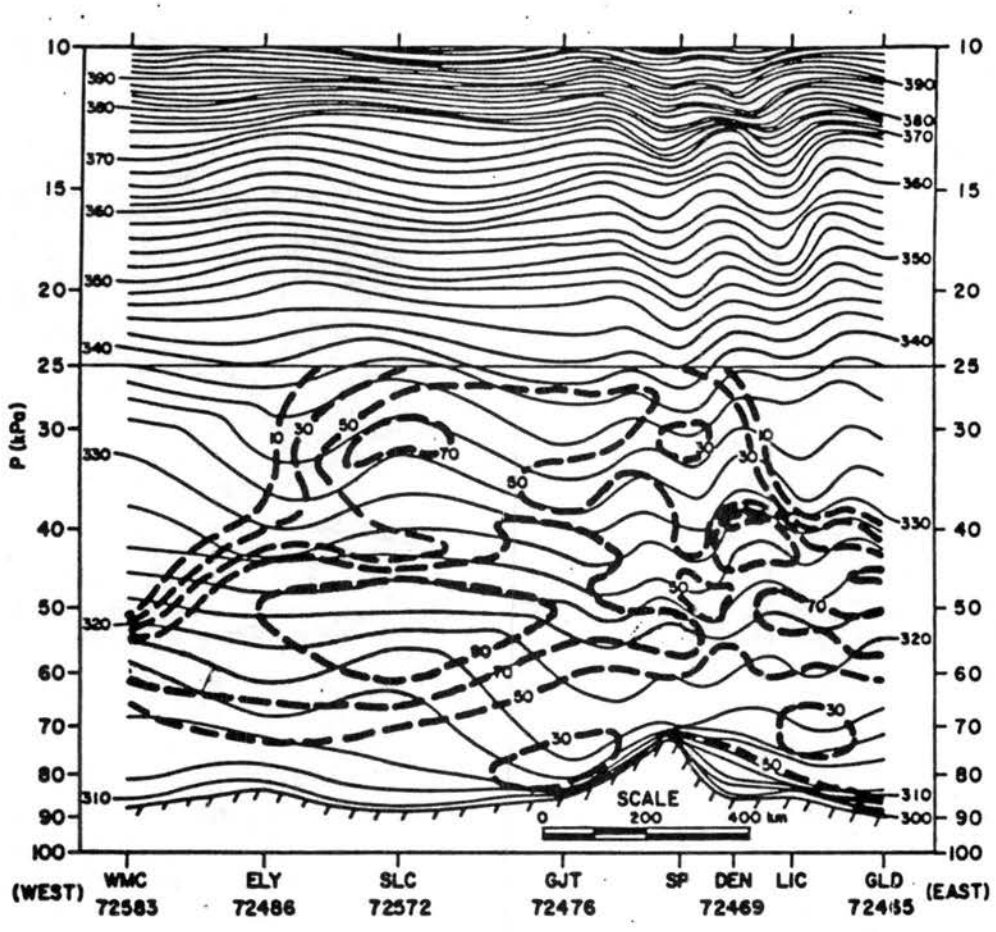

Figure 3.3a. East/west cross section near 40°N (along dotted line in Fig. 3) for 0600 MDT 4 August 1977. WMO stations (identified by international number in figure) include Winnemucca (WMC) and Ely (ELY), Nevada, Salt Lake City (SLC), Utah, Grand Junction (GJT) and Denver (DEN), Colorado, and Goodland (GLD), Kansas. Non-WMO stations are the base site in South Park (SP) and Limon (LIC), Colorado (see Fig. 1 for locations). Shown are isentropes (K, solid lines) and relative humidity (%, dashed). Areas of relative humidity greater than 70% are stippled. (From Cotton et al., 1983).

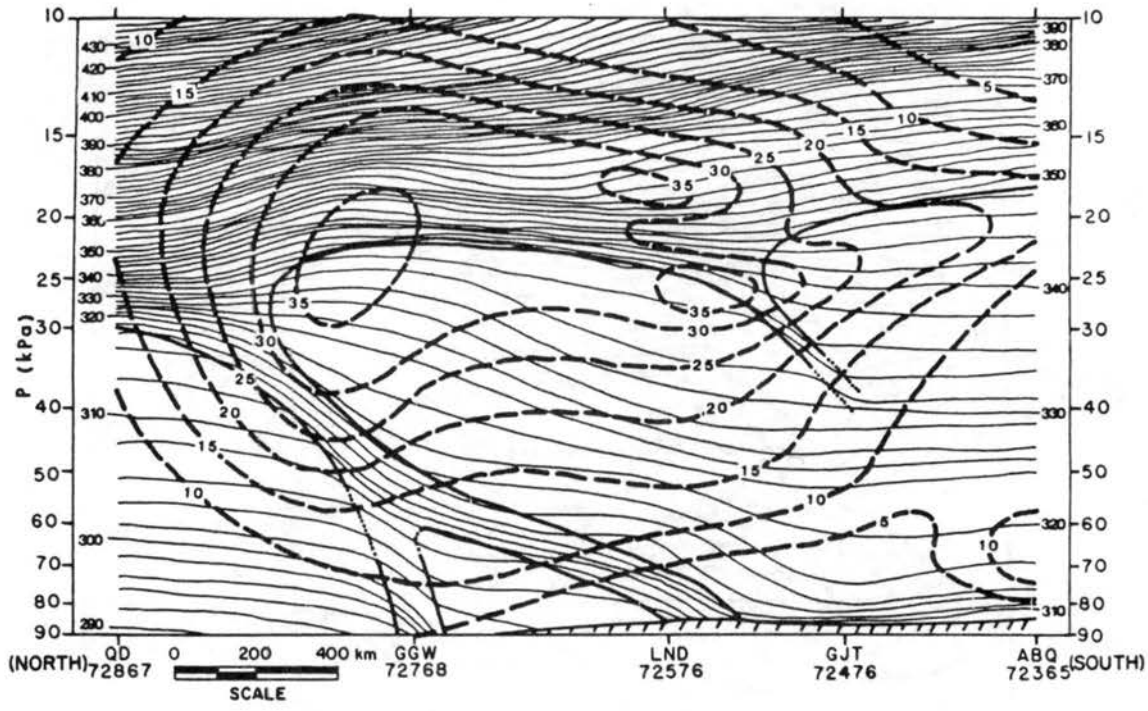

Figure 3.3b. North/south cross section near 107°W for 0600 MDT 4 August 1977. WMO stations (identified by international number in figure) include the Pas (QD), Manitoba, Glasgow (GGW), Montana, Lander (LAN), Wyoming, Grand Junction (GJT), Colorado, and Albuquerque (ABQ), New Mexico. Shown are isentropes (K, solid lines) and isotachs (m s^{-1}, dashed). (From Cotton et al., 1983).

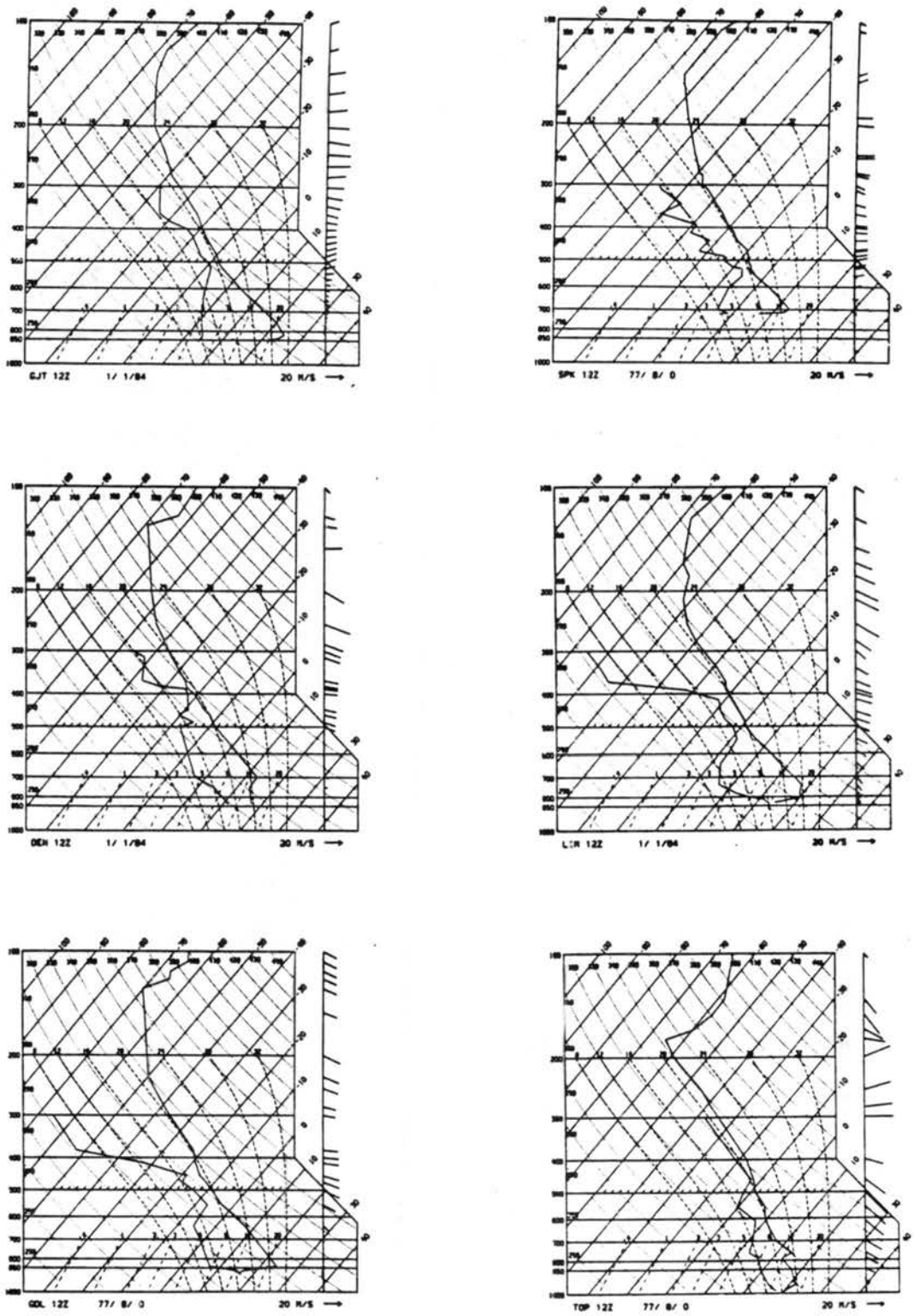

Figure 3.4. Skew-T log-p diagram of 1200Z GMT sounding observations taken at 6 stations across region of interest near latitude 39°N. Temperature and dew point profiles are displayed. Wind vectors are displayed to right of each diagram.

Cotton et al. (1983) suggest helped destabilize the sounding. The flow was nearly zonal aloft and governed by diurnal slope flows near the surface. The air mass was subtropical in nature with a moderate jet of 20-25 m s^{-1} near 25 kPa.

As reported by Cotton et al. (1983), the development of convection occurred in three stages. The first stage was characterized by the growth of the boundary layer over South Park. At sunrise, small-scale slope flows within the nocturnal inversion rapidly developed followed by a larger scale moist cool valley wind 2 hours later. By 0900 MST, small shallow cumulus appeared over the mountain peaks. By 1000 MST, deep convection began over the mountain peaks and moved into South Park by 1100 MST. Cotton et al. (1983) report that it was at this time that conditional instability reached into South Park.

The second stage of convection was characterized by the apparent organization of convective elements into a coherent squall line and its movement onto the High Plains. This stage took place between 1120 and 1330 MST. During this period, increasingly intense mountain thunderstorms formed over especially favorable regions or "hot spots". As 1330 MST approached, a north-south line of strong thunderstorms began to assemble on the edge of the High Plains. Associated with the storms were westerly surface gust fronts. A radar summary for stage 2, compiled by Cotton et al. (1983), is displayed in Figure 3.5.

Upon forming, the mesoscale squall line started moving eastward and the third stage of convection started. During the early afternoon, surface easterly slope flow was confined to the region south of the Palmer lake Divide and east of the Colorado border. Within the Platte valley, the surface flow was light and variable, primarily from the

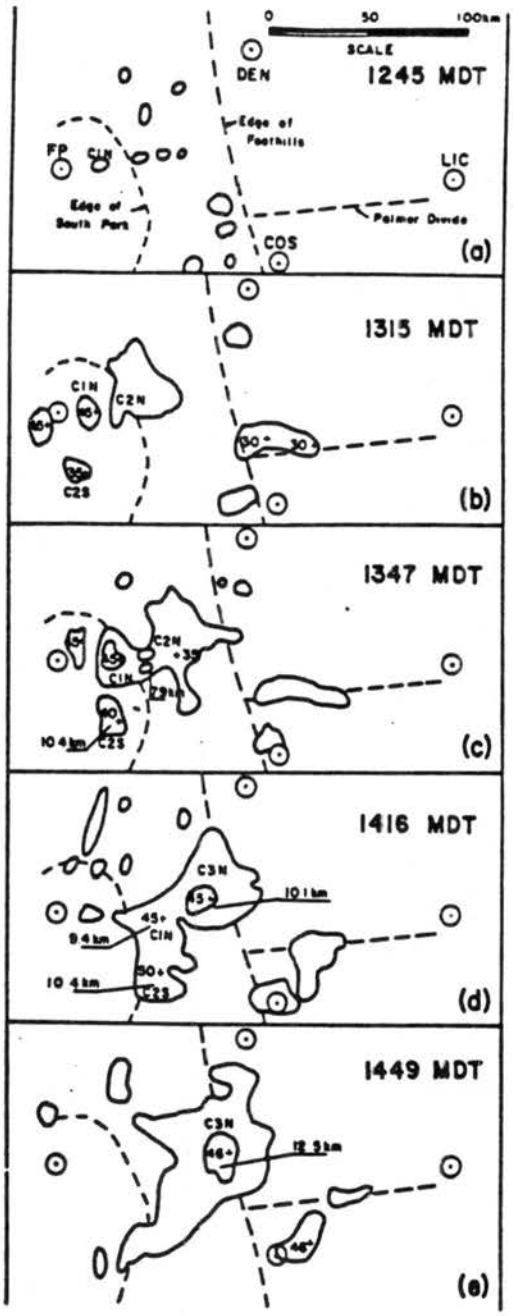

Figure 3.5. Composite radar summaries from the region between Fairplay (FP) and Limon (LIC). Outer contour is minimum detectable signal at Limon NWS radar. Inner reflectivity contours (40 dBZ), intensities of cell cores (dBZ), and echo tops (km MSL) are derived from composited Limon, CP-3, and CBS-4 radar data. Cells referred to in text are labeled. Dashed lines denoting South Park and foothill boundaries and Palmer Divide are qualitatively based on the more detailed topography in Fig. 1. Summary times are a) 1245 MDT, b) 1315 MDT, c) 1347 MDT, d) 1416 MDT, and e) 1449 MDT, 4 August 1977. (From Cotton et al., 1983).

north northeast. In addition surface moisture was considerably drier north of the Palmer Lake Divide in Eastern Colorado than it was to the south. The anomalous afternoon flow in northeast Colorado was a result of a weak but southward advancing cold front which seemingly stalled on the Palmer Lake Divide. This caused the surface air to be only marginally conditionally stable in northeast Colorado.

The initial convective line was mostly confined to the high ground near the Palmer Lake Divide. As the newly formed line moved eastward, showers began to break out to the north and finally move ahead of the southern portion of the line. The fact that the surface air was seemingly too dry to support the shower activity to the north, suggests that the inflow supporting their activity was transported from outside the region. The fact that the surface air to the north was cooled by the advancing cool front supports the idea that the air input for the northern convective activity was flowing from the south. In fact, the afternoon slope flows typically have a southerly wind component which would lead to this result. The fact that the showers weakened to the north and were non-existent on the normally favorable Cheyenne ridge (on the northern Colorado border) supports this hypotheses. As a result, for the purposes of this case study, the southern surface air properties will be considered more typical of the environment supportive of the convective line than those to the north. It is the working hypothesis that the effect of the cold front was not of primary importance to the organization of the meso-β squall line.

Echo tops within the meso-β squall line were observed as high as 15.5 km MSL. The eastward propagation, at a speed of about 10-14 m s^{-1}, brought the squall line to the Colorado-Kansas border by 2000 MST. The

convection within the line achieved TRW++ status (very heavy rain) early as it first formed and was relatively small in size. Then as it moved away from the foothills the showers weakened. Later as the line progressed east of the Limon, Colorado area, the intensity increased strongly and some TRW++ showers again appeared.

Figure 3.6 depicts the progress of the line throughout the afternoon and early evening. Note the tendency for the line to favor the Palmer Lake Divide and Raton mesa as the system passed through eastern Colorado. At the same time, No convection was present along the drier Cheyenne ridge. As the system progressed to the Colorado-Kansas border, where moisture was greater, the line became nearly continuous.

Subsequently, as the system passed into Kansas and encountered greater moisture, it expanded horizontally (see Wetzel et al. (1983)). It eventually merged with several other meso-β convective systems which formed ahead in central Kansas. This merger process is depicted in Figure 3.7. The result of the merger was the formation of a continuous circular anvil observed from satellite, which satisfied Maddox's criteria for a mesoscale convective complex (MCC). The satellite depiction of these later stages is displayed in Figure 3.8 (from Wetzel et al. (1983)).

Several questions arise from this analysis. The important questions for this study are: 1) Why, after growing for several hours in the immediate lee of the Continential Divide did the cells take on the form of a coherent squall line and move eastward? 2) By what physical mechanism did the meso-β squall line move eastward? 3) Of what importance were the "hot spots"? 4) Was the line moving with a mesoscale forced convergence or was the convection creating its own

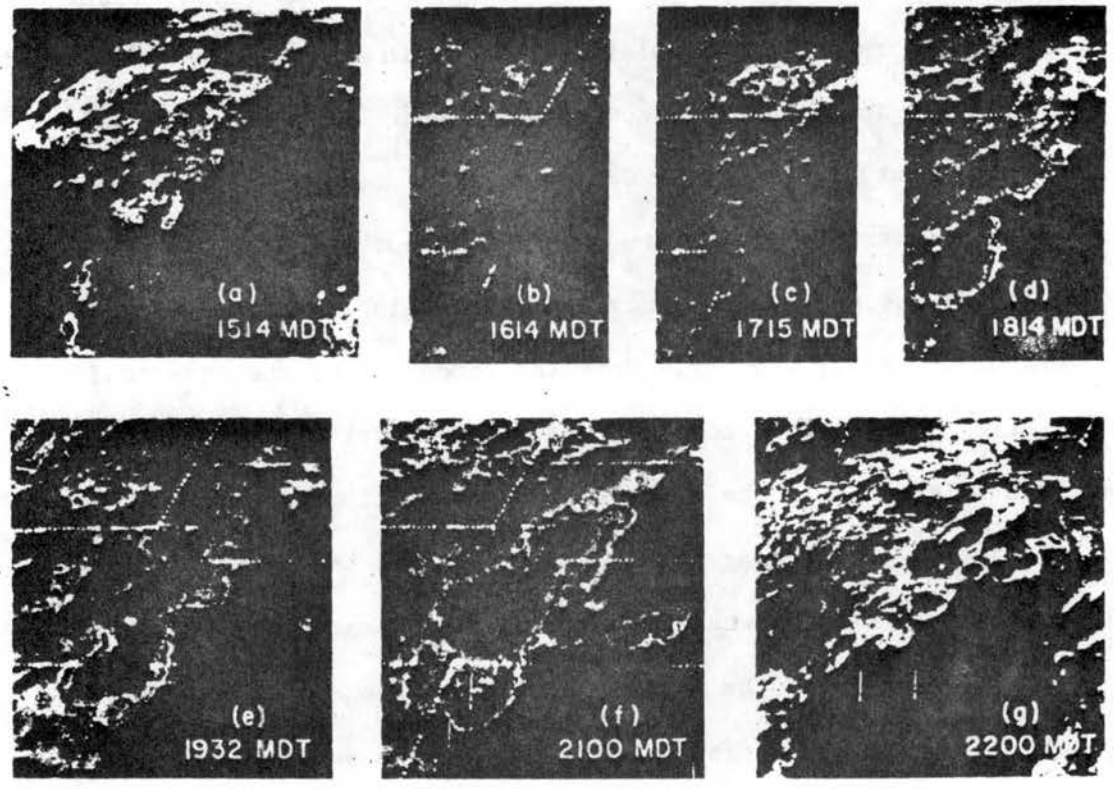

Figure 3.6. IR satellite images, centered near eastern Colorado, on 4 August 1977, for MDT times a) 1514, b) 1614, c) 1715, d) 1814, e) 1932, f) 2100, and g) 2200. The first and last images, at 1/2 the scale of the others, provide more extensive views of the storm system's environment. Gray shades are as in Fig. 4. Temperatures colder than -63°C (lighter shades within interior black contours) indicate convection reaching or penetrating the tropopause, which based on the 1700 MDT Limon sounding was at 13.2 kPa (15.0 km). (From Cotton et al., 1983).

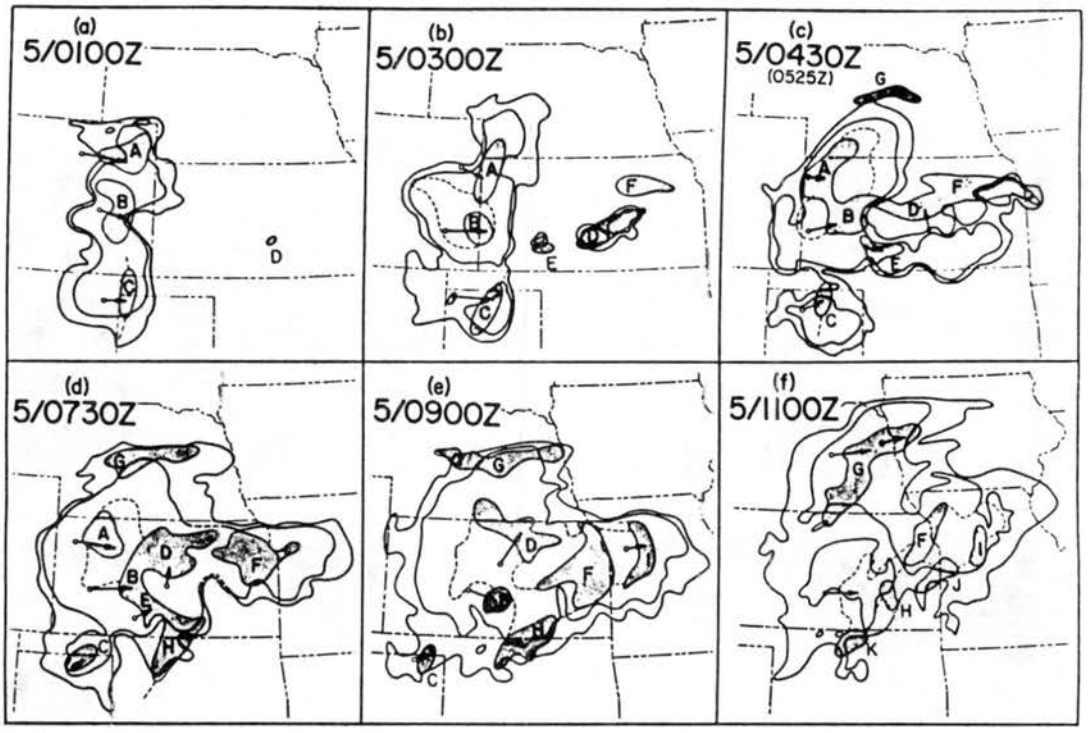

Figure 3.7 Schematic IR satellite and radar analysis at 2-h intervals, from 01 to 11 GMT 4 Aug 1977, for the western MCC #1. The anvil cloud shields are indicated by the -32 and -53°C IR contours (outer and inner solid lines, respectively), remapped from satellite images at the labelled times. Darkly shaded regions (identified by letters) denote significant radar-observed, meso-β-scale convective features at about 25 min after the indicated whole hour, with the vectors showing their previous 2-h movements. The dashed line segments extending from the meso-β convective features indicate flanking axes of weaker convection. In the more developed MCC stages, in (e) and (f), the light-shaded area within the dashed envelope indicates weaker, more uniform and widespread echo. (From McAnelly and Cotton, 1986).

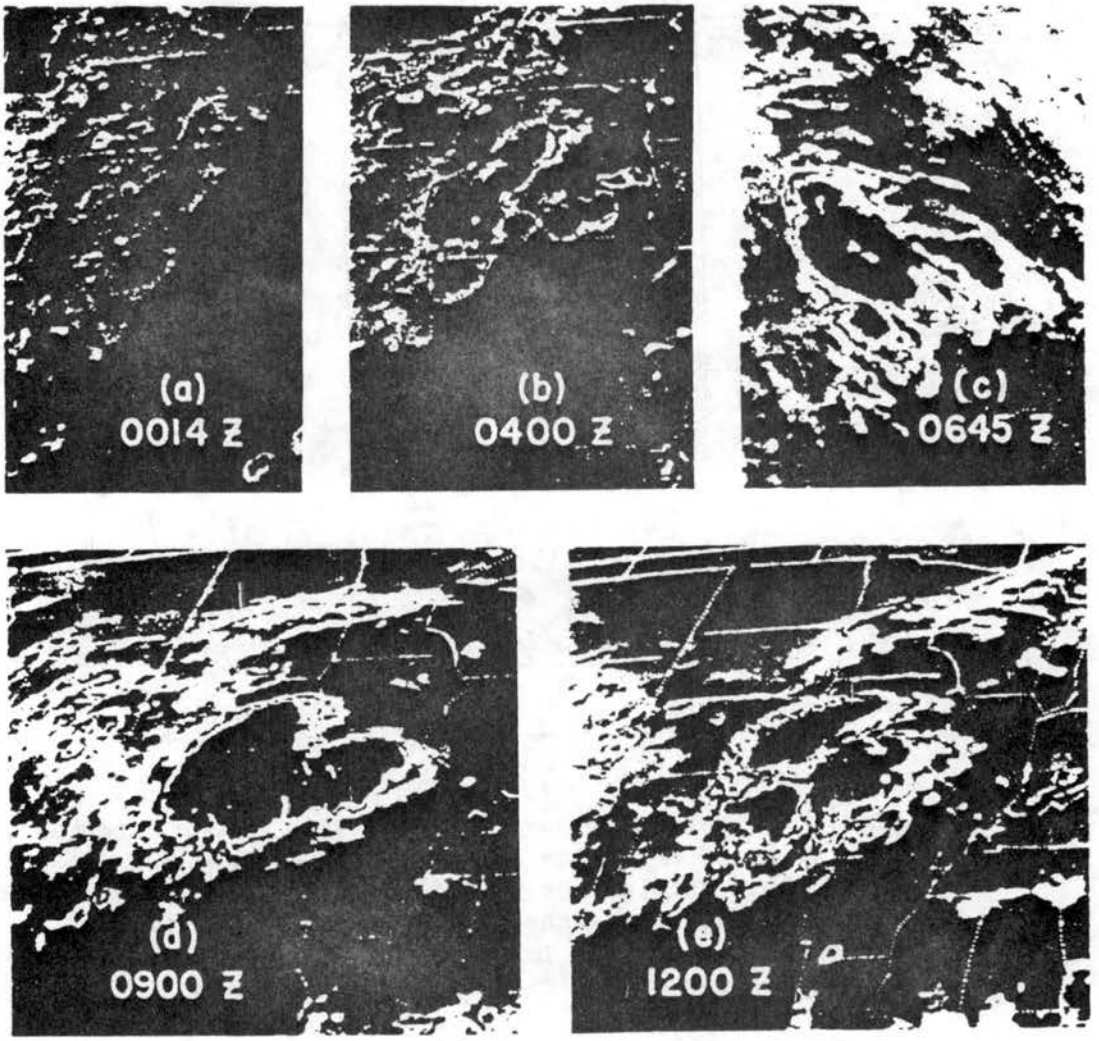

Figure 3.8. Enhanced IR image of the U.S. at 0300 MDT 4 August 1977, from the GOES satellite at 70° W longitude. The stepped gray shades of medium-gray, light-gray, dark-gray, and black are thresholds for areas with apparent blackbody temperatures colder than -32, -42, -53 and -59°C, respectively. Temperatures progressively colder than -63°C appear as a gradual black-to-white range. The cloudiness over Utah indicates the mid-level moisture source for convective development on 4 August over the Colorado mountains. The intense meso-α-scale convective complex (MCC) centered over eastern Kansas originated in the eastern Rockies and western plains the previous evening. (From Cotton et al., 1983).

convergence, i.e. was there CISK? 5) To what extent did the orogenic MCS influence the development of the Kansas MCS?

The following chapters will describe an attempt to model this observed senerio of MCC genesis with a sophisticated non-hydrostatic primitive equation model. The approach will be to retain only what is hypothesized are the essential aspects of the problem in topography, environment and physics. The results will then follow.

4. EXPERIMENTAL DESIGN

It is the purpose of this dissertation to investigate how deep moist convection interacts with the Rocky Mountains-Great Plains solenoidal circulation to produce the eastward propagating convective systems which are observed. The observations of 4 August, 1977, discussed in the previous chapter, inferred that deep moist convection formed by the mesoscale flow fields became organized in some way and propogated across the eastern plains as a mesoscale convective system.

In order to form a theory of the dynamics and thermodynamics governing these flows, a model, consistent with known theory, must be constructed which reproduces the process. Several approaches may be taken in this construction. If one is relatively sure what the dynamics of the process are, a very simple model of the process might be constructed to demonstrate a growth or propagation mechanism and test it against some facit of the observation. For instance, linear dynamic models have been used to study dynamics of numerous types of atmospheric waves with some success. Often, however, the models fail to reproduce the observed dynamics (Nehrkorn, 1985) and the process is not ultimately understood.

Another approach is to construct the most complex model possible, including as much physics as the computer can handle. This approach is very expensive, but if the model is successful, its complex dynamics can be studied explicitly revealing important physical mechanisms. Unfortunately, such models often lead to a study of purely "numerical

weather", or in other words, the dynamics they predict may be fortuitous. As a result, the modeler must rely on observations to verify as much of the simulated processes as possible.

In this dissertation, the second approach will be taken with some modification. A basic hypothesis of this study is that the orogenic mesoscale convective system is generated by local wind systems. Therefore, the approach will be to reduce the complexity some by excluding the effects of observed horizontal variations. Then if the simulations are successful in reproducing observed features of the convective cycle, this hypothesis also will be shown to be consistent.

In this chapter, the model used for this study will be very briefly described. A more complete description can be found in Appendix A. The model's credibility will then be discussed, including some rigorous testing of its performance in simple linear situations against analytical theory. In the remaining sections, its implementation for this study will be presented. First, it will be shown how a representive atmospheric structure was chosen. Then given that structure, a realistic diurnal surface heating and moistening cycle will be constructed which has the proper variation with surface elevation. Finally, the choice and philosophy of choosing a suitable domain which makes optimum use of computer resources will be described.

4.1 Model Description

In numerical studies of tropical and midlatitude MCSs it is customary to represent convection by use of a convective parameterization. Recently Rosenthal (1979) demonstrated that representive heating can be obtained with explicit latent heating based on parameterized latent heat release. As demonstrated by Molinari

(1985), however, these explicit parameterizations applied to coarse grids (which do not resolve the scales of actual towers) tend to delay heating for too long and when it turns on it is too strong. This problem has been addressed in the context of parameterized microphysics by Redelsperger and Sommeria (1986) who employed a "partly cloudy" type scheme to precipitation and microphysics.

In any case, to represent convection on a coarse grid, compromises must be made, the results of which are not always known. Therefore, for this study, a nonhydrostatic cloud model will be used which is capable of simulating individual cloud elements. If the resolution is fine, realistic clouds will be produced. If the resolution is coarse explicit heating can occur, although it may be delayed and will choose unrealistic scales of cloud circulation. Within the framework of coarse resolution a cumulus parameterization may be applied. A recent study by Tremback et al. (1984) demonstrated that there is no greater efficiency for using a hydrostatic assumption when grid scales are less than 10-20 km. The following is a condensed description of the numerical model employed for this study. A more detailed description of the model is given in Appendix A.

The model formulation used is a modified form of the CSU cloud/mesoscale model described by Tripoli and Cotton (1982) and Cotton et al. (1983) which is now part of the CSU Regional Atmospheric Modeling System (RAMS). The cloud/mesoscale model employs the quasi-boussinesq approximation described by Dutton and Fichtl (1969), for deep convection. Whereas the earlier formulation predicted density and diagnosed pressure, the current formulation, based on Klemp and Wilhelmson (1978), predicts exner function (π) and diagnoses density

variations. Recent testing of the previous formulation against linear theory revealed catastrophic shortcomings which necessitated the reformulation.

Time dependent partial differential equations are prescribed for the three velocity components, u, v, and w, the exner function (π), the ice-liquid water potential temperature (θ_{il}, see Tripoli and Cotton, 1981), the mixing ratio of total water and the mixing ratios of rain droplets, pristene ice crystals and graupel particles. Potential temperature, temperature, cloud droplet mixing ratio, water vapor mixing ratio, and pressure are diagnostic (diagnostic procedure described by Tripoli and Cotton, 1982).

There are physical parameterizations for microphysics (Cotton, et al., 1983), longwave and shortwave radiative tendencies on θ_{il} (Chen and Cotton, 1983), the surface layer fluxes of heat, vapor and momentum (Louis, 1979). Soil temperature and soil level moisture are predicted with an underlying soil model described by McCumber and Pielke (1981) and a surface energy balance model described by Tremback and Kessler (1985). Mixing is diagnosed using the eddy viscosity approach (Lilly, 1962) modified for enhanced mixing in unstable regions (see Appendix A).

These equations are solved on an energy conserving staggered grid described by Tripoli and Cotton (1982). A terrain following sigma-z vertical coordinate system is applied using the system developed by Gal-Chen and Sommerville (1975a,b).

The basic time differencing scheme is a time split 4th order leapfrog scheme, where acoustically active terms are integrated on a small combined forward/backward (horizontal) and Crank-Nickleson (vertical) time integration scheme. The mixing uses a combined forward

and Crank-Nickleson scheme proposed by Paegle et al. (1976). All physical parameterizations are integrated using a forward model. All advective terms are differenced using a 4th order scheme in the horizontal, while all other spacial differencing is second order.

The vertical boundary conditions are for vanishing mean vertical fluxes at the surface with diagnosed turbulent momentum (friction), heat and vapor fluxes. The top boundary condition is the normal mode gravity wave radiative technique developed by Klemp and Durran (1983). For lateral boundary conditions, gravity wave radiative conditions described by Klemp and Lilly (1978) and modified by Durran (1981) are employed together with a mesoscale compensation region outside the simulation domain (Tripoli and Cotton, 1982).

This study is concerned with the dynamics of cloud system propagation. As pointed out in Chapter 2, it is likely this will involve both advection and gravity wave dynamics. It is essential to verify that the model can properly simulate these phenomena before it is extended to the simulation of internal wave phenomena which cannot be easily verified with observations.

Recently, Durran (1981) demonstrated that a modified form of the Klemp and Wilhelmson (1978) cloud model did a credible job simulating the known analytical hydrostatic internal gravity wave response to a 1m mountain. A 1m mountain was used because the small ratio of mountain height to atmospheric scale height leads to an approximate linear response, which can be solved for analytically. The dry RAMS non-hydrostatic model is very similiar to that of Durran and so a similiar good verification is expected, if coded properly.

In order to verify the ability of RAMS to simulate simple gravity waves, the 1m mountain simulations performed by Durran (1981) for vertically propagating and resonant trapped lee waves were repeated. In each case the model performance was as accurate as or better than the results displayed by Durran (1981) and Klemp and Durran (1983).

Besides these simple tests against linear theory, complex simulations of observed thunderstorm systems (see Tripoli and Cotton, 1986; Knupp, 1985) and orographic cloud systems (Cotton et al., 1986) have further verified its ability to simulate observed dynamic and microphysical systems. Therefore prior experience with this model together with the above tests against linear theory indicate that the described RAMS dynamical and thermodynamical framework is suitable to simulate cloud and internal gravity wave phenomena.

4.2 Composite Sounding

A hypothesis of this dissertation is that given favorable conditions, local orogenic circulations can lead to the generation of a mesoscale convective system, even in the absence of explicit external forcing (such as cold fronts or dynamic lifting associated with secondary synoptic circulations). For this study, the 4 August, 1977 case study discussed observationally by Cotton et al. (1983) and Wetzel et al. (1983) was chosen because synoptic forcing "seemed" of secondary importance.

It is consistent with this hypothesis to simulate the Rocky Mountain Convection Cycle within an atmosphere representive of the gross features observed on the case study day and ignore the observed horizontal variability. The approach will be to construct a thermodynamic and wind profile which is based on the observations across

the region and which captures what is hypothesized to be the important structure leading to the genesis of a MCS.

Figure 3.4 displayed 6 observations across the region taken on August 4, 1977. Since these are morning soundings, there appears a surface nocturnal inversion in each case in addition to the remains of the deeper daytime boundary layer representive of the previous day. The wind structure in the lowest 3 km does not show much continuity across the network, since it is strongly modulated by local flows.

Cotton et al. (1983) show that on the morning of 4 August, 1977, there was moisture advection into the region from the west which reached the genesis area in time to be a factor in storm development. Because westerly winds dominated aloft, and because there was some significant changes occuring from advection aloft, it was decided to use the gross features of the thermodynamic and wind structure above 700 mb which were observed at Grand Junction.

Nearer to the surface, the atmosphere was much more moist on the High Plains than observed at Grand Junction and the winds were weak. Because of the changing elevation, the low level moisture region is especially difficult to capture in a composite sounding. The approach taken was to specify a deep stable layer below 850 mb in the composite sounding. This helps limit daytime temperatures to reasonable values across the region. Then, a 1 km deep layer of moist air of composite sounding value plus 3 g/kg was added locally above the surface as the model was initialized. Finally, the model integration began at sunset on the previous evening, and so the observed inversions could be created by simulating their formation. This leads to a realistic variation of

inversion depth across the region, dependent on effects of the surrounding topography.

The composite sounding finally used is displayed in Figure 4.1. In constructing this sounding, care was taken to remove all small vertical fluctuations as they are not likely to be typical of the whole region (the region is from the Utah/Colorado border eastward to central Kansas). Because the observed flow was light near the surface, the airflow decreases to calm below 800 mb. Since no consistent strong flow was observed below these levels, assuming weak flow helps eliminate some potential problems with the initialization procedure.

The composite sounding, as displayed, is extremely unstable for surface elevations below the 950 mb pressure level. It should be noted that most surface elevations across the domain range from 900-700 mb and none below the 960 mb level. Therefore the strongest instabilities will never be put into the model and those that do will be found to be 'capped' by an inversion forming from the developing wind systems. The sounding is designed as a guide for specifying the range of surface humidity and potential temperature with elevation. As will be shown, further adjustments are made after its direct interpolation onto the model grid.

4.3 Vertical Grid Structure

The vertical grid structure selected for this study is a compromise between economy of computer resources and ability to represent important vertically structured phenomena. In particular, the ability to simulate the atmospheric boundary layer concurrently with deep strong vertically structured gravity wave and convective phenomena is central to this topic.

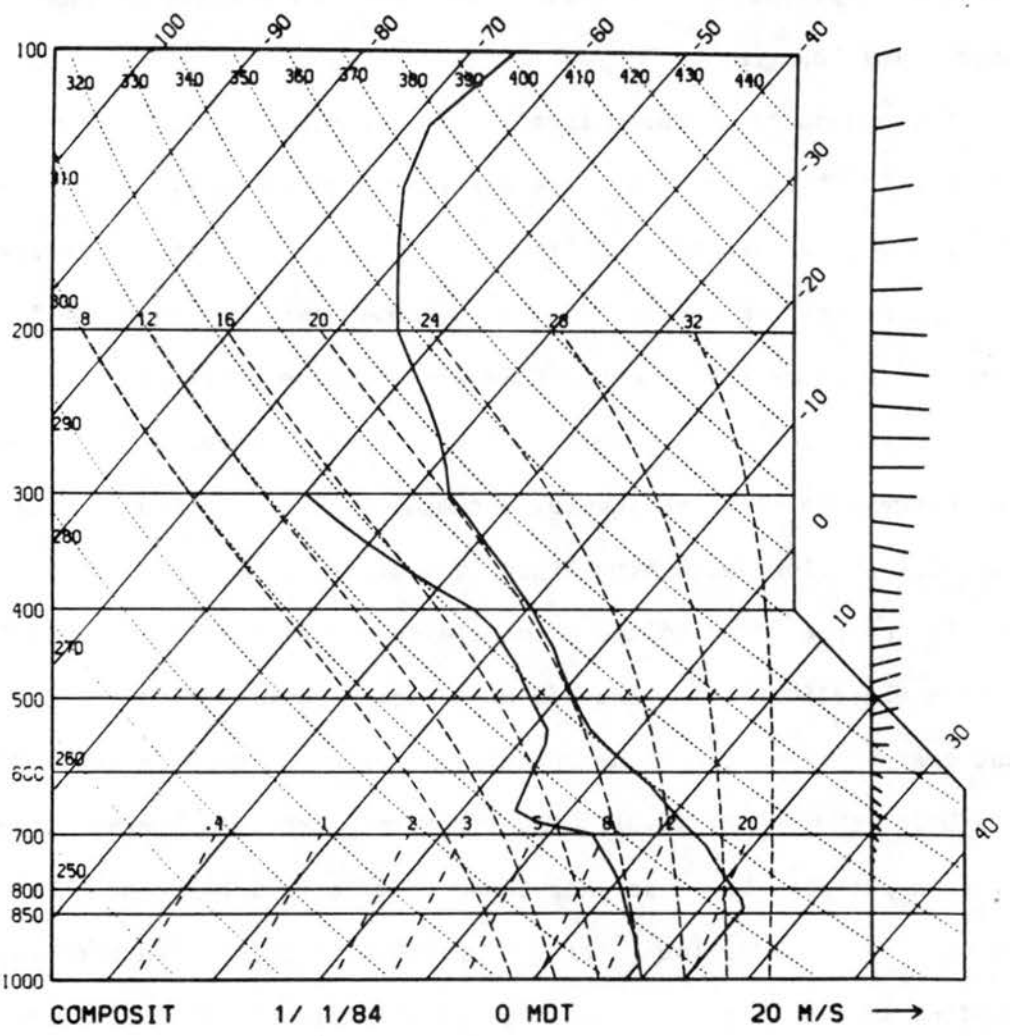

Figure 4.1. Skew-T log-p diagram of composite sounding. Temperature and dew point are displayed. Wind vectors are displayed.

The earlier numerical study of the RMCC (Rocky Mountain Convection Cycle) by Hughes (1979) suggested the lack of a good boundary layer simulation led to his inability to simulate the observed thermally driven upslope flow over Eastern Colorado. Banta (1982) demonstrated that the early stages of the high elevation slope flows forms within the decaying nocturnal inversion which is charactized by downslope flows. The depth of these slope flows has been observed to be less than a few hundred meters. In addition, the gust fronts associated with convective storms are observed to often be only a few hundred meters deep. In order to represent these structures, a very fine resolution is needed. Alowing a minimum of 4 grid points to marginally resolve a wave, a grid spacing of 100-200 m in the vertical would be desirable to represent these flows.

The simulation of internal gravity waves is also a central consideration. For small linear perturbations in a hydrostatic atmosphere of constant Brunt-Vaisalla frequency and shear, the vertical structure equation is:

$$w_{zz} + (k_s^2 - k^2)\, w = 0 \qquad (4.1)$$

where the Scorer parameter (k_s) is (neglecting unimportant density stratification terms):

$$k_s^2 = N^2/u_o^2 \qquad (4.2)$$

where N is the Brunt-Vaisalla frequency defined:

$$N^2 = g/\theta \; d\theta/dz \;, \qquad (4.3)$$

and k is the vertical wave number. The solution to Eq. 4.1 for a finite

vertical displacement produces a dominant vertical wavelength given by:

$$L_z = 2 \pi u_o/N \ . \qquad (4.4)$$

Here it is best to let u_o be the speed of the mean flow relative to the perturbation source. For the composite sounding (used to initialize the simulations and discussed later in this chapter), the tropospheric N is about 0.010 in the free atmosphere. If it is assumed that the perturbation is stationary relative to the earth, such as a mountain producing a mountain wave, the mean flow is near 10 m s^{-1}. Then L_z is about 6 km. In the lower stratosphere both N and u_o (relative to perhaps a thunderstorm disturbance) both increase and so a wavelength on this order is also plausable. In order to properly resolve a wavelength of this size, vertical spacing no larger than 1km is required. It would be preferrable to have spacing no larger than 500 m to have 10 grid points across the wave.

Since a convective circulation will, at times, penetrate several kilometers into the stratosphere (tropopause at about 10 km), the grid should reach at least 5-10 km above the tropause. A preferable vertical grid of 100 m resolution would require a resource-prohibitive 200 gridpoints to reach to 20 km. Based on overall resource considerations, it was determined that about 30 vertical gridlevels should be used. As a result, the following vertical grid structure given in Table 4.1 was arrived at.

Because the vertical scale length of turbulent phenomena is proportional to the distance above the surface, it is appropriate to have higher resolution near the surface. Unfortunately, the boundary layer resolution is still at best marginal. Very shallow slope flows

below 300m in depth will not be resolved. However much of their impact on the deep atmospheric vertical motion field will still be predicted. In essence, instead of explicitly simulating the surface wind direction, the mean wind change over a 200-400 m depth will be depicted. This can produce realistic vertical motions but will likely not predict local upslope moisture advection. Most likely, however these very shallow slope flows will not transport moisture substantial distances.

Table 4.1

Height	Pressure	Δz
0	1000	-
125	986	250
388	957	275
677	926	303
995	893	333
1344	858	366
1728	821	403
2152	782	443
2617	741	587
3128	698	536
3678	653	563
4268	608	618
4913	561	673
5625	513	750
6375	465	750
7125	421	750
7875	381	750
8625	344	750
9375	309	750
10125	277	750
10875	248	750
11625	222	750
12375	197	750
13125	175	750
13875	155	750
14625	138	750
15375	122	750
16125	107	750
16875	95	750
17250	89	-

The vertical resolution aloft is also marginal, but will be sufficient to capture much of the dynamics of a 4km vertical wave

length. The constant vertical resolution above 4 km will reduce numerical refraction of vertically propagating internal waves and vertical advection. This is an important consideration because numerically induced reflection/refraction can produce misleading physical results. The 750 m resolution used is identical to that used successfully by Tripoli and Cotton (1980) to simulate deep convection in the Florida environment.

4.4 Initialization Procedure

There are several initialization techniques which can be used. For this study, the time dependent variables will be initialized with a horizontally homogeneous interpolation of the composite sounding and given time to adjust before daily heating begins. Because slope flows often occur beneath a nocturnal inversion initially, it is desirable to incorporate these effects. It would be difficult to prescribe the inversion and appropriate dynamic balances associated with it initially. Instead, the model is initialized at 8pm MST on the evening prior to the day of interest. The model is then integrated through the night so that the nocturnal temperature inversion forms with a structure appropriate for the topography.

The soil model is initialized as an appropriate function of the initial low-level sounding temperature and moisture. In order to find what was appropriate, a simple one dimensional calculation of the diurnal cycle together with the soil model was integrated with several different soil types, soil depths, soil grids and initial temperatures in order to produce realistic diurnal temperature and moisture ranges. An appropriate soil temperature was found by setting the deep soil temperature to observed climatological values (corresponding to High

Plains climatology) and letting surface values equal the local initial temperature. This seems to be valid for the 2000 MST initial time. Appropriate diurnal ranges were obtained using a vertical soil grid and initial moisture profile derived from experimentation with a one-dimensional test version of the model. A soil type of 50% clay loam and 50 % sandy loam (see McCumber and Pielke, (1981) was used. Based on the composite sounding used and the vertical grid spacing of the simulation, these initial soil specifications led to the diurnal ranges for three different elevations shown in Figure 4.2.

Since the initial field contains flow over a mountain barrier, the flow field must be initialized dynamically. This was done by interpolating the base state momentum profile to grid levels for all grid heights above the elevation of the local topography. The total momentum in the vertical grid column is then integrated vertically and compared to the integrated base state momentum integrated total momentum. Any excesses or deficits in the local total momentum is then added locally over the lowest 10 grid points weighted by a linearly decreasing with height function. For flow perpendicular to a ridge, this produces a jet-like structure near the surface. This seems to be appropriate for a first guess of the flow structure. This assumed flow structure is calculated for both the horizontal wind components and added in gradually to the initial flow specified at rest over a period of 1/2 hour. Assuming zero vertical motion at the surface, vertical motion in balance with the assumed vertical momentum profile are also added in. The advantages of this technique are:

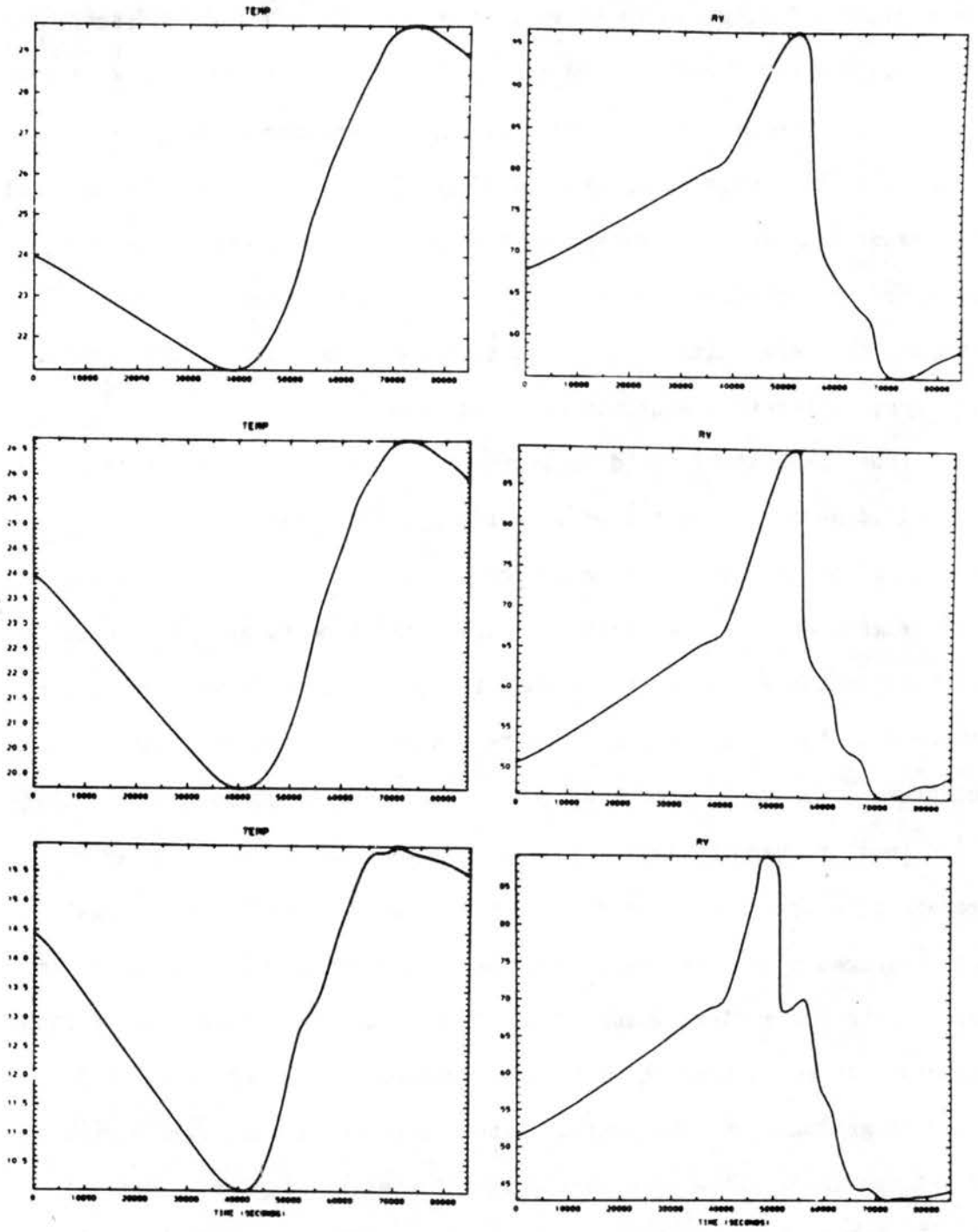

Figure 4.2. Diurnal temperature and vapor mixing ratio variation at 250 m MSL produced as a result of the surface energy budget for several elevations. Parts (a) and (b) are for surface at 960 mb, (c) and (d) are for surface at 850 mb and (e) and (f) are for surface at 700 mb. Vertical axis is temperature in celsius and vapor mixing ratio in 0.1 g kg^{-1}.

1. Vertically integrated horizontal momentum is conserved between grid columns which eliminates general pressure trending and does not excite vertical motion in the upper atmosphere.
2. The initial flow field aloft is absolutely horizontal which forces any waves to travel up from below rather than unrealistically being created *in situ*.
3. The initial field is added gradually, leaving time for adjustment and preventing the production of high frequency acoustic and gravity waves occuring from gross flow inbalance.

It was demonstrated by Klemp and Lilly (1980) that dynamic adjustment to flow over a witch of Agnesi shaped ridge will take a time of $35a/u_o$, (where a is the barrier halfwidth, and u_o is the mean wind) to reach 95% of the full adjustment value within the first vertical wavelength. The adjustment occurs from below, so that full adjustment will work upwards with time (Durran, 1981, Tremback *et al.*, 1984). Since, in this study, an equivalent barrier halfwidth of about 50 km is considered with a mean wind flow of about 10 ms^{-1}, adjustment times of about 2 days can be expected. This is beyond the time scale of the persistence of the mean observed flow and so such full adjustment should not be necessary. The integration will be initiated at 2000 LST on the day prior to that of interest. This will give about 16 hours for adjustment prior to the onset of convection. This adjustment time should be sufficient to provide a realistic mountain wave flow field aloft, although not necessarily exactly that which occurred. Because very little observed mean flow actually intersects the surface (only above 2.1 km MSL) vertically adjusted mountain wave energy is likely limited even in reality. Instead locally evolving diurnal flows will

likely dominate the internal wave energy, and these will not exist long enough to reach any kind of full adjustment. It is the purpose of this dissertation to simulate an evolving pattern of such topographically and convectively forced waves.

4.5 Topography and Horizontal Grids

For this study, convection over a region about 1000 km in the zonal direction (from the western Colorado border to central Kansas) and 400 km in the meridional direction (the distance across Colorado) is under consideration. The choice of a horizontal grid setup again represents a compromise between dimensionality, resolution, and computer resources available. Clearly it would be most desirable to simulate the developing ensemble of convective elements explicitly in three dimensions, but this is several orders of magnitude beyond the available computer power. In the past, the representation of convection within meso-α simulations has been accomplished largely through cumulus parameterization. Unfortunately, all cumulus parameterizations build in assumptions about the convection which can bias the final outcome.

In the absence of cumulus parameterization there are several approaches which can be taken. On one extreme, convection might be resolved in two dimensions explicitly with the 2D slab oriented east/west along the primary observation path. This will simulate explicit convective circulations, but will be confined to two dimensions. It is well known that there are differences in the down gradient turbulent energy cascade in two dimensions, convective elements act differently, and flows are prevented from flowing through convective lines. These serious considerations will force any results produced to be suspect.

Another approach, on the other extreme, would be to simulate the cycle in three dimensions with coarse meso-β resolution. The result will be more realistic three dimensionally, but individual convective elements, if they exist, will be forced to at least the 4-6 ΔX scale, which would be on the order of 50 - 75 km. Convection on this scale is also clearly unrealistic.

A middle-of-the road approach might be to use a less coarse resolution in the zonal direction and a very coarse vesolution in the meridional direction in the context of a quasi-3D framework. This would give a better representation of convection (although probably less than what is critical) than the coarse resolution, and still allow some three dimensional aspects of the flow.

It was decided that the middle-of-the-road option was the most undesirable because it did nothing well. The coarse resolution three dimensional approach has some merits, but does not attack the main organizational hypothesis well because convective elements are not depicted on the proper scales. Therefore, it was decided to approach this problem primarily two dimensionally and with high resolution (enough to resolve clouds). The 3D coarse resolution approach was not abandoned altogether, however. This approach will be used together with a two dimensional coarse resolution approach in order to demonstrate the three dimensional effects that occur. In addition, because a two dimensional coarse resolution approach is relatively inexpensive, it will be used as a test bed for hypotheses or less important sensitivity studies that do not warrant the considerable expense of a full blown high resolution 2D run.

Since a multi-resolution and multi-dimension approach will be used, the same variations in the topography used might be considered. The actual topography with a resolution of 30^{o} latitude and longitude is displayed in Figure 4.3. It is beyond the hypothesis of this study to consider the importance of each topographical feature. The hypothesis simply addresses the response of convection to the general nature of the Rocky Mountain barrier and the east-west ridges over the plains. Therefore, the complex topography depicted in Figure 4.3 will likely only confuse the ultimate interpetation of the result. In addition, less detailed topography will be necessary for coarse resolution studies than high resolution calculations. Hence there will be further uncertainty interpeting the results.

As a result, it was decided to only use what is hypothesized to be the important features of the topography. These features are the general slopes and barrier of the Rocky mountains and the east-west ridges extending onto the western Plains. It is obvious from Figure 4.3, that these east-west ridges are quite wave-like in the north-south direction. It is desirable to take advantage of this fact and assume a cyclic domain for the 3D grid in the meridional direction. This eliminates the effect of a north and south boundary condition, and reduces the size of a 3D simulation in the meridional direction to the distance from ridge top to ridge top. The disadvantage is that ambient meridional gradients of temperature, moisture or wind cannot be considered. This is acceptable, however, because the hypothesis is that large scale horizontal variations are unimportant.

Following these arguments, the actual topography depicted in Figure 4.3 was placed on a grid running from the Arkansas valley on the south

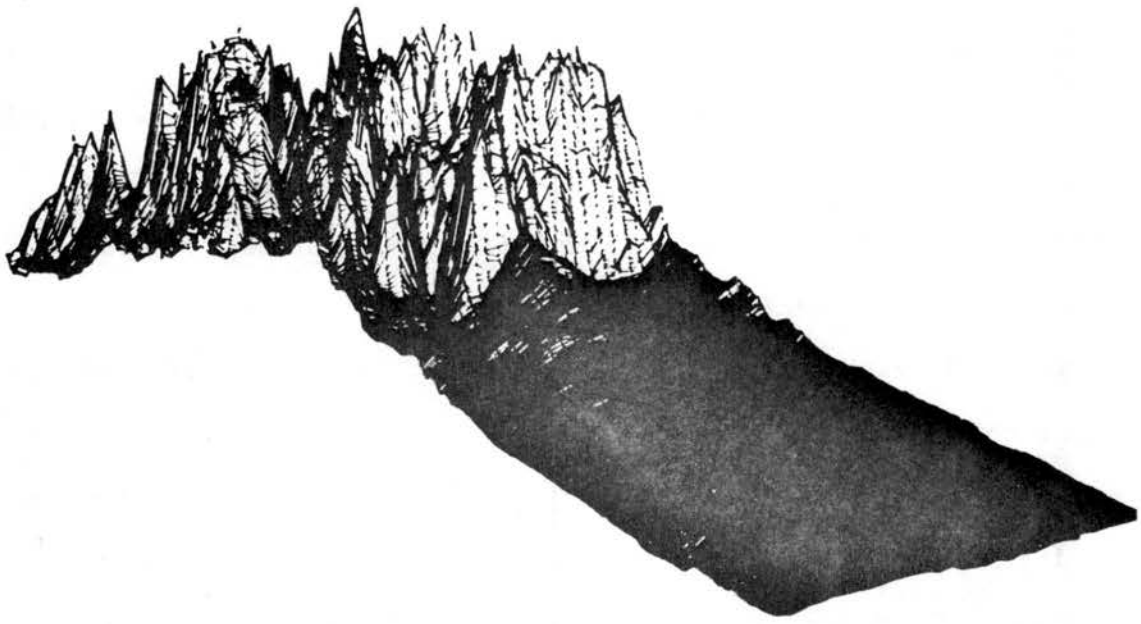

Figure 4.3. Topography surface sampled at 30° latitude and longitude intervals. Sampling area ranges from 37° N to 41° N latitude and 110° W to 98° W longitude.

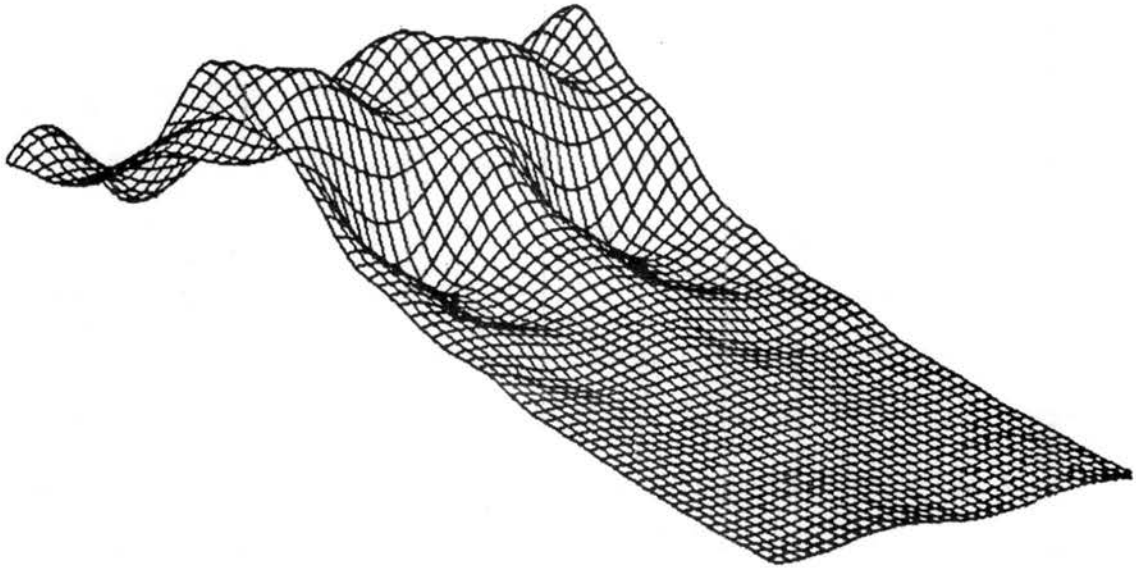

Figure 4.4. Same as Figure 4.3, except with band pass filter and cyclic adjustments explained in text. The cyclic region runs from 38° N latitude to 40° N latitude. The regions south and north of this band are repeated in a cyclic fashion from the region within.

to the South Platte Valley on the north so the study area is centrally located. After forming a mirror image of the topography to the east of the domain (to make the topography cyclic in the zonal direction, a 2D band pass fourier filter was then applied to the entire domain. Wave lengths of greater than 115 km in the zonal direction were retained and only 222 km in the meridional direction (wave number 1 and 0 to represent the east west ridges with a simple sine wave). The result is displayed in Figure 4.4.

This simplified topography contains all of the features which are hypothesized to be important, namely, the east-west ridges, the Rocky Mountain steeper barrier, and the steeper barrier slope between the east-west ridges. At the same time, the wavelengths retained will be resolvable by the coarse mesh as well as the fine mesh resolution experiments.

For the coarse mesh resolution, the grid spacing of $1/6^{o}$ longitude (14.4 km) and $1/8^{o}$ latitude (13.9) is used. For the 3D coarse grid this will give a grid of 72 in the zonal and 16 in the meridional direction. The 2D coarse will be 72 grid points in the zonal direction oriented along the Palmer Lake Divide which is the line along which the observation network was centered (see Cotton et al., 1982). For the 2D coarse grid, a resolution of $1/80^{o}$ longitude (1.08 km) was used. This resolution is marginal for convection, but it is the maximum that can be afforded.

4.6 Numerical Experiments

The simulation experiments to be performed are categorized into 2D fine mesh runs, 2D coarse mesh runs, and 3D coarse mesh runs. A control simulation, to which all others will be compared, is depicted for each

category. The fine mesh 2D simulation is selected to be a general overall control to which all categories are compared.

The approach of this presentation will be to first study closely the primary control experiment which will be labled "the control case". This simulation will incorporate all the physics mentioned earlier in this chapter. As indicated earlier, the experiment will run from 2000 MST 3 August, 1977 until the system either moves out of the domain or weakens. This time turns out to be 0200 MST, 5 August, 1977.

Next, several sensitivity tests will be run in the 2D fine mesh frame work and 2D coarse framework in order to investigate model sensitivities. These tests will include investigations into the roles of radiation, wind speed, precipitation, and overall latent heating in the fine mesh frame work. The three-dimensional framework will be used primarily as a tool to gain understanding of some of the three-dimensional aspects of the problem which were not included in the control. The 2D coarse framework will be used in this discussion only as a tool to bridge the gap between the control 2D fine mesh case and the 3D coarse mesh case. However, the 2D coarse mesh was employed extensively for testing purposes prior to the actual use of the considerably more expensive fine mesh.

5. THE CONTROL SIMULATION - EVOLUTION AND COMPARISON WITH OBSERVATIONS

5.1 Stage 1: Development of Early Morning Boundary Layer

The integration began at 2000 LST, using solar angles for 4 August and a latitude of 39 N. As expected, during the first night no condensate formed. Instead local surface flows have evolved as the ridge cooled. At this time, temperatures at the lowest prediction level (125m) have fallen from initial values by about 2.5 K in western Kansas, 3.75 K over the ridge top and 5.5 K on the easternmost High Plains where cool air has drained from the steeper slopes to the west. At the same time, upper soil temperatures have fallen by 10-15 K. Below 2.5 km MSL and in the region near 8 km MSL, temperatures generally dropped 1.25-2 K.

Because synoptic scale deep subsidence was not specified in the initial conditions, the drop in temperatures aloft (from longwave radiation divergence) is probably greater than observed. Since diabatic heating was neglected in the pressure tendency equation, the continued longwave cooling leads to proportionally greater air density that will be manifested as a surface pressure rise. In fact, this first eight hours of cooling led to a general 2.5mb pressure rise at the surface.

The predicted fields at 0400 MST (add 1 hour for MDT) are displayed in Figure 5.1. Meso-γ scale perturbations are filtered by applying a running 80 grid interval (86 km or 1 degree longitude) average to the simulated variations. This was done so that the meso-β response could

Figure 5.1. Predicted meso-β-scale fields at 0400 MST for control case. Variables are as labeled. The fields represent 80 grid point (86 km) running averages of actual predicted variables. The variables v', r_v, p' and θ' have their horizontal average removed. Contour intervals are 2 m s^{-1} (200 cm s^{-1}) for u and v', 5 cm s^{-1} for w, 1 g kg^{-1} (100 x 10^2 g kg^{-1}) for r_v, 0.2 mb (200 dynes cm^{-2}) for p', 0.5 K for θ', 2 K for θ_e and 0.5 g kg^{-1} for r_l and r_{ice}. Negative contours are dashed. θ_e is an ice conservative equivalent potential temperature described by Tripoli and Cotton (1981). The heavy dark contour surrounds regions of condensate. The surface topograhy is depicted by the black shading. The vertical axis is height in km above mean sea level (MSL) and the horizontal axis is west longitude. The vertical distance is exaggerated by a factor of 30.

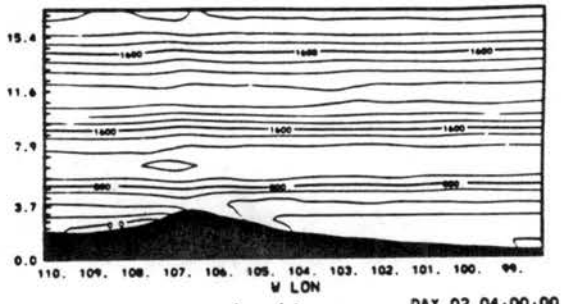

u (cm/s) DAY 02 04:00:00

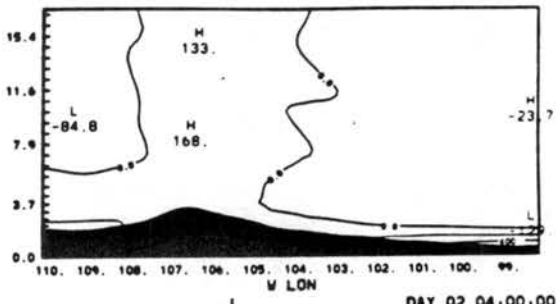

p' DAY 02 04:00:00

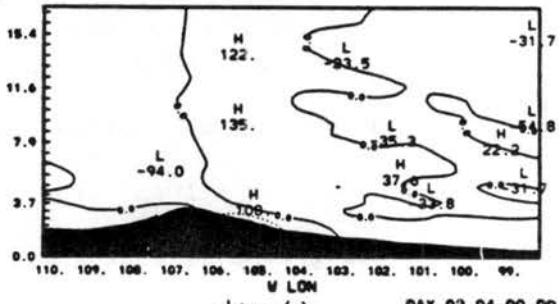

v' (cm/s) DAY 02 04:00:00

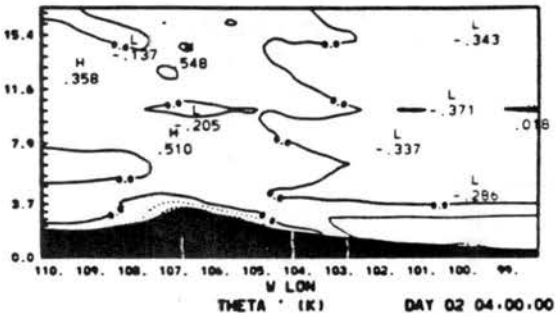

THETA ' (K) DAY 02 04:00:00

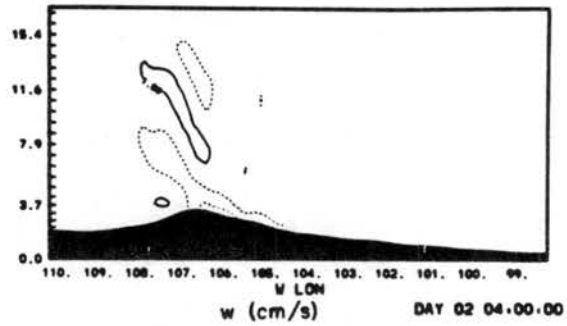

w (cm/s) DAY 02 04:00:00

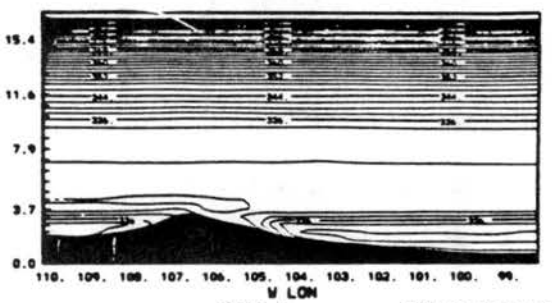

THETA E DAY 02 04:00:00

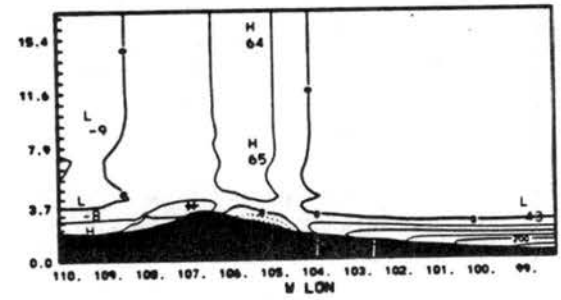

rv (g/g)

be viewed in the absence of very high frequency convective scale fluctuations which cannot be displayed adequately on this scale.

In order to depict local effects more clearly, Figure 5.1 displays only pressure and potential deviation from a horizontal average rather than the assigned base state. For averaging purposes, perturbations relative to the reference state are extended from their values at surface levels down to mean sea level. As a result, pressures at elevations below ridge top may be biased slightly by comparing their value to an average which includes some "reduced to sea level" pressures. Local horizontal averaging for the purpose of filtering, on the other hand, is only with respect to above topography values. When the averaging distance intersects a lateral or topographical boundary, the point closest to the boundary is assumed constant into the boundary.

The cool early morning surface temperatures led to the generation of local down slope flows. Examination of the grid point data (not shown), reveals that flows reach 1.6 m s^{-1} (over the first 250 m above the surface) in opposition to the meanflow upwind of the ridge and 7.6 m s^{-1} in the direction of the mean flow on the steepest leeside slopes at 0400 MST. The strong lee side downslope is supported by downward momentum transport from aloft. The downward motion associated with the transport is part of a deep mountain wave system with a vertical wave length of about 8 km. Over the very gently sloping terrain to the east, the slope flows become very weak and actually turned upslope in Central Kansas. This appeared to be due to a response to the formation of dynamically-induced low pressure to the lee of the mountains associated with wave drag effects.

Associated with the drainage flows is the appearance of low level meridional flow directed to the right of the down slope flow. Meridional flows are on the same order or exceed the drainage winds at 0400 MST. It is obvious that they oppose further acceleration of the drainage winds by tending toward a geostrophic balance with the zonal pressure gradient. As the baroclinically-induced pressure gradient weakens when surface heating begins, the meridional wind will play a role in accelerating the developing upslope flow. The meridional flow seems to have become relatively steady by this time (0400 MST) and so its effect upon the onset of upslope flow should be realistic. This would not have been simulated well had the simulation begun in the morning.

The sun rises about 0500 MST. By 0800 MST, soil temperatures rise to near their initial levels. The ridge top temperatures (see Figure 5.2) have warmed only to their 0400 MST levels, while valley and high plains temperatures are still 1-2 K cooler than the 0400 MST values. As a result, the combined impact of the developed meridional wind and the relatively warm upper slopes had already weakened the drainage flows on both the lee and windward side of the ridge. In fact, upslope flow is already occurring on the windward slopes where the downslope flow is opposed by the ambient wind. Because of the relatively coarse vertical grid resolution, the weakened downslope flow on the lee side can be interpreted as the development of very shallow upslope flow beneath a deeper persisting combined drainage and ambient flow as observed by Cotton et al. (1983). The unfortunate consequence of coarse vertical resolution is that any upslope transport within the strong gradients of the surface layer will not be resolved. This should not have a strong

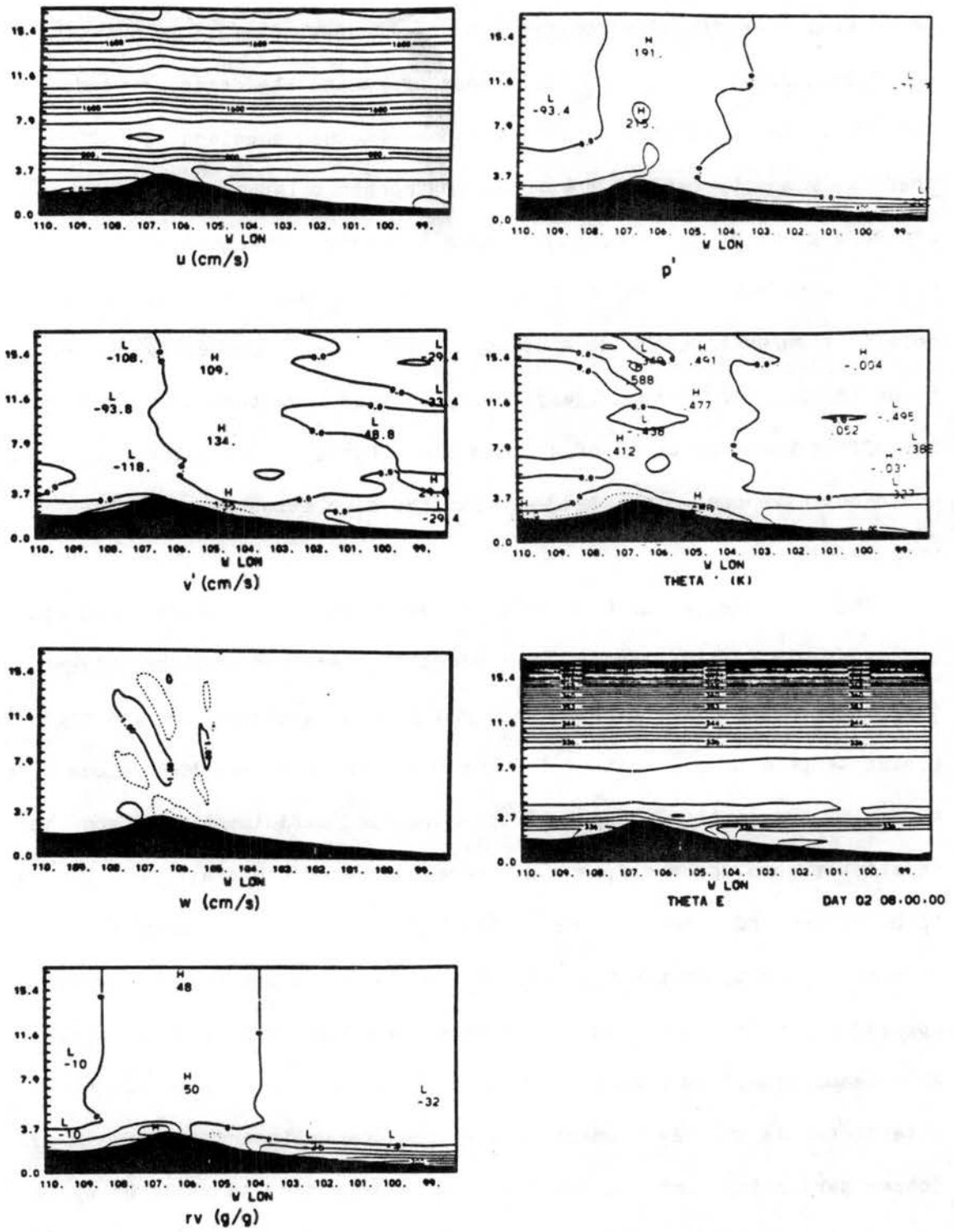

Figure 5.2. Same as Figure 5.1, except for 0800 MST.

affect on the large scale transports because this flow regime is very shallow and short lived so that transport over large horizontal scales is not likely.

The thermally-driven upslope flows continue development in conjuction with increasing soil temperature throughout the morning. It is not until 1130 MST that the first shallow convection forms. The observations of Cotton et al. (1983) demonstrate that, in reality, the first convective elements occurred as much as 1 hour earlier. The reason that convection occurred late in this simulation can be explained as follows.

The initial convection in this simulation (see Figure 5.3) was forced by the interaction of the large scale flow with the shallow valley breeze on the scale of the entire ridge. This is because all small scale peaks were removed in this idealized topography which eliminated "hot spots" (Henz, 1974). Cotton et al. (1983) attributed early convective elements to such small scale topographically forced circulations. During initial testing for this experiment, a simulation was run where short wave length topography was included (see Figure 5.4). In that case convective elements did form by 1030 MST over isolated peaks. The impact of these early convective elements on the evolution of the valley breeze, however, is not obvious.

From Figure 5.3, it can be inferred that the formation of a cloud over the ridge top is associated with the upslope advection of moisture from the west to cloud base. The windward upslope advection is enhanced by the development of thermal upslope flow in addition to orographic lifting by the ambient flow over the ridge. A comparison of west slope moisture to east slope moisture at 3 km MSL shows that considerably

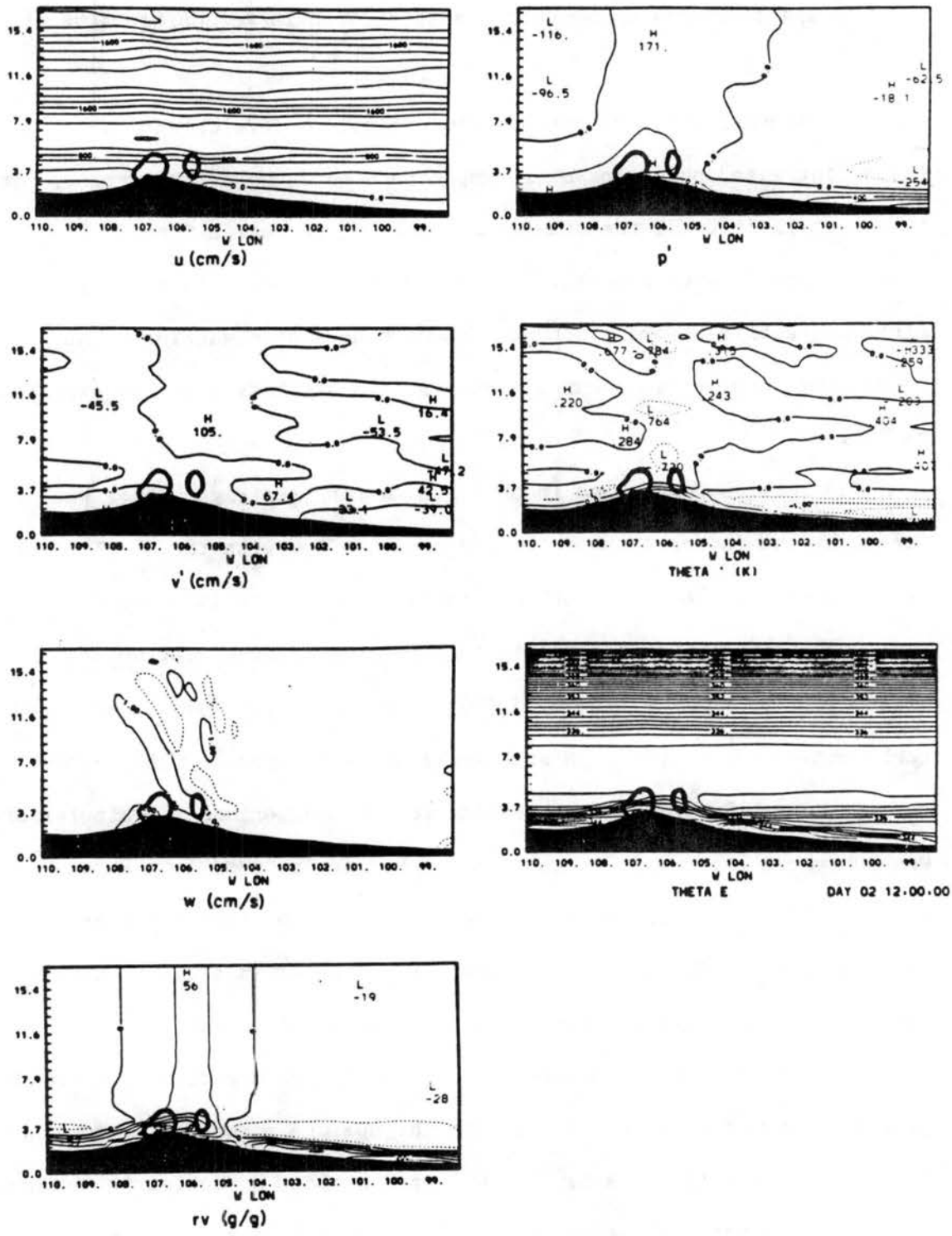

Figure 5.3. Same as Figure 5.1, except for 1200 MST.

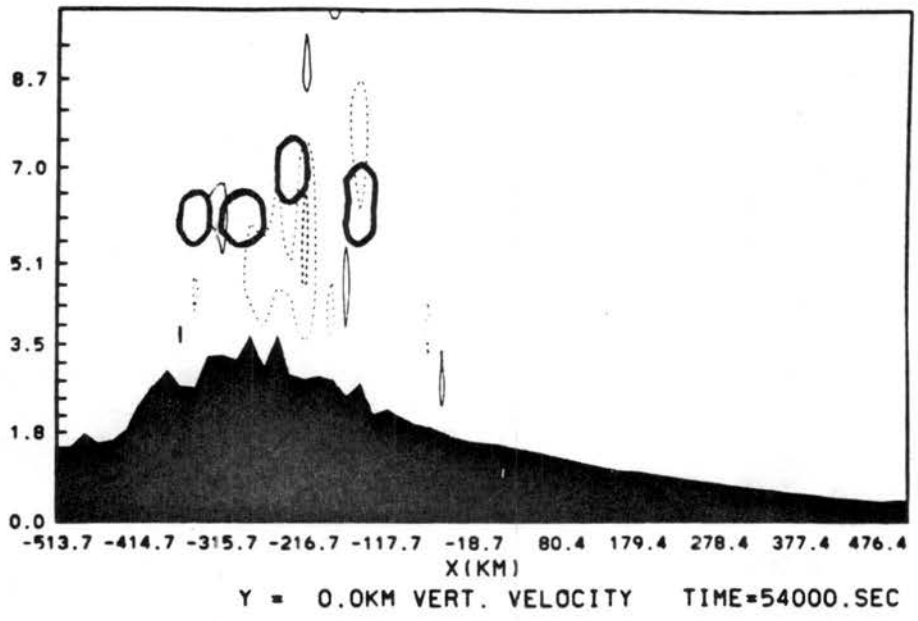

Figure 5.4. Same as Figure 5.1, except only w field, for a rough topography test case, and at 1100 MST (5400 seconds simulation time). Also the horizontal axis is labeled in kilometers from center and the vertical distance exaggeration is by a factor of 50.

higher moisture exists on the west slope. Observationally, such moistening has been found on occasion during a southwest monsoon which also leads to higher moisture on the west slopes.

The second region of cloud formation (see Figure 5.3) is associated with a reversal of the surface horizontal flow 60 km to the east of the ridge top. Note continuity of westerly flow from aloft down to low levels just to the lee of the ridge. It is significant that this westerly flow persisted at 5-6 m s^{-1} (which is 3-5 m s^{-1} stronger than the ambient flow) from the night time hours in this region. In fact, it seems that this region of uplift is an extension of the mountain wave pattern aloft which is evident in Figure 5.2. Along with the direction reversal is found an increase in water vapor mixing ratio associated with upward transport from lower elevations in conjunction with the east slope thermally-driven upslope. Although the mountain wave and thermally-driven slope flow interaction produces a stronger region of shallow convergence and resulting vertical motion to the east, the western ridge top convection dominates at first because of greater moisture advection from the west.

Some aspects of this simulated morning flow regime are supported by the observations. First of all, the low level wind profiles observed by Cotton et al. (1983) in the South Park region showed only very shallow easterly flow, usually only at the surface observation level. Cotton et al. (1983) report that a deep valley breeze never reached South Park (10-60 km east of ridge top) during the morning. Second, initial convection over the "hot spots" was characterized by weak isolated cells. The stronger line of convection which developed near 1300 MST,

organized just to the east of South Park (see Figure 3.5); the same place the strong convergence is being forced in this simulation.

5.2 Stage 2: Deep Convection Begins

The appearance of simulated deep precipitating convection did not take place until 1245 MST. The initial stages of the simulated cumulonimbui are displayed in Figures 5.5 through 5.7. As can be seen in Figure 5.5, both regions of initial cloud formation produce deep convection. The convection beginning near ridge top is initially dominant because of a greater supply of moisture transported up the western slopes, despite weaker surface convergence. The observations, on the other hand, showed deep precipitating convection occurring by 1200 MST. The observed precipitation radar echos grew most rapidly in the region of strong simulated convergence 60 km east of ridge top, but only with the participation of "hot spot" cells moving into the region. In the simulation, development of deep convection was within a relatively laminar slope flow in the absence of "hot spots". Thus triggering had to occur by the lifting of massive volumes of air by the mesoscale convergence. It is for this reason that the deep convection was somewhat delayed in the simulation.

The region of deep convection simulated over the ridge top was, in a sense observed. Since this is a feature forced, in part, by the "chimney" effect at ridge top, it is in some ways similiar to observed convection to the west of South Park at ridge top. As with the observed ridge top convection, the simulated convection progresses eastward across South Park, but at a somewhat later time. This convection weakens as it moves east of the ridge top, away from the supporting influence of the west slope flows. Because the simulated

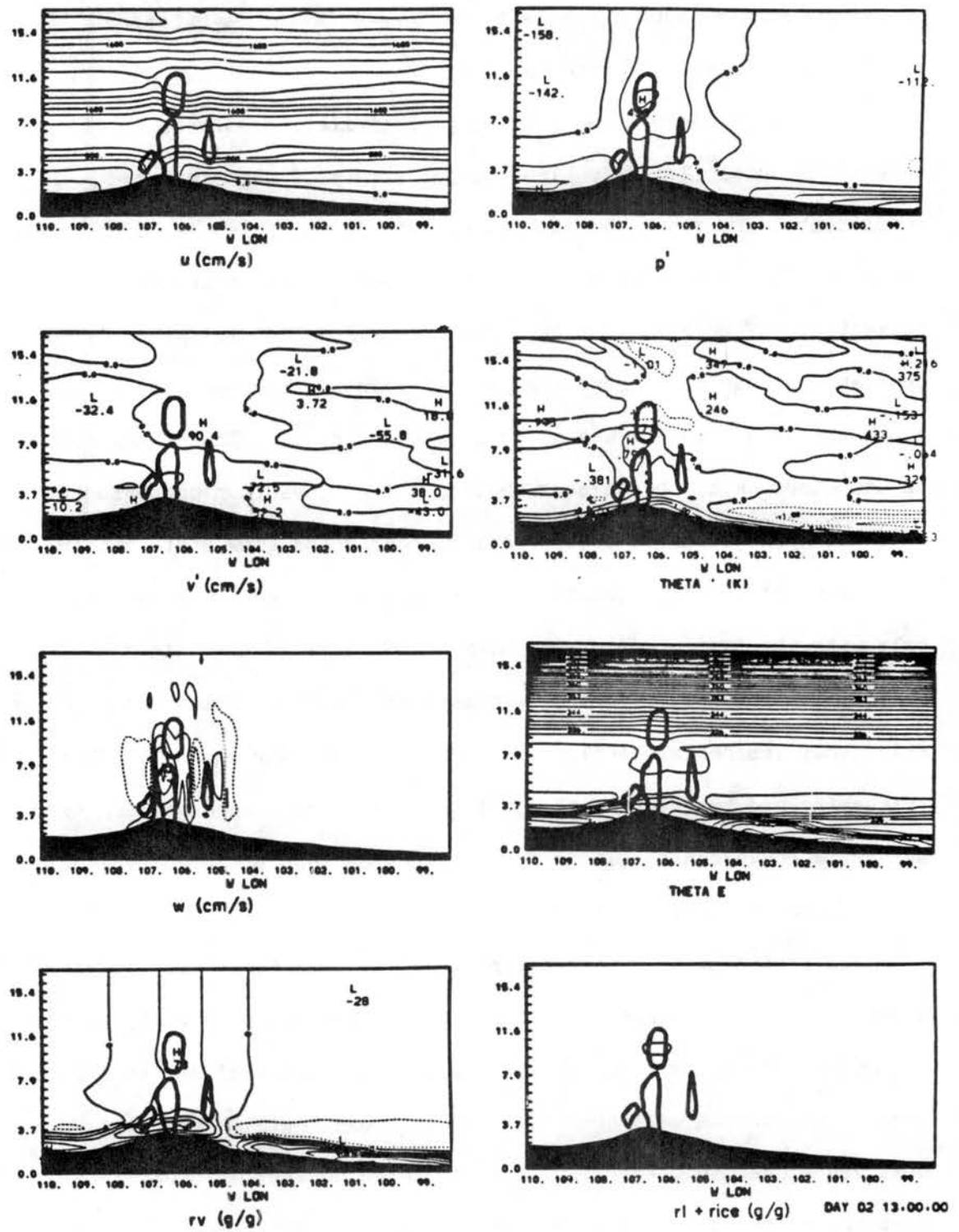

Figure 5.5. Same as Figure 5.1, except 1300 MST.

high mountain boundary layer inversion is weakened or broken, this convection encounters little resistence as it crosses the South Park region, and weakens very slowly.

The simulated movement is at about 10–12 m s^{-1} which is near the speed of the mean flow between the surface at about 3km and the flow at 12 km AGL (the upper reaches of the convection). The associated surface convergence pattern is preceded (to the east) by surface low pressure. The surface flow behind the convection is simulated to be 5–8 m s^{-1}, considerably slower than the eastward progression of the system.

For reasons already mentioned, the eastern convective area is weaker and as a result fails to influence its mesoscale forcing. As with the western system, it moves eastward at about 10–12 m s^{-1}. The low level convergence with which it was originally associated remains stationary, however. As the convection moves eastward, the plains boundary layer capping inversion is encountered and this region of convection dissipates by 1500 MST.

At 1400 MST (see Fig. 5.6) a region of shallow convective towers is simulated to form from the ridge top to 160 km to the west where the togopography slope lessens. This convection forms in response to the continued combined lifting and moisture advection of the mechanically driven and thermally driven upslope flows. At the same time, the original ridge top convection has moved eastward, approaching the region of strong surface support. Upon encountering the region of low level convergence and wave induced uplifting between 1400 and 1500 MST, existing convective elements grow to intense proportions, now strong enough to induce a mesoscale response.

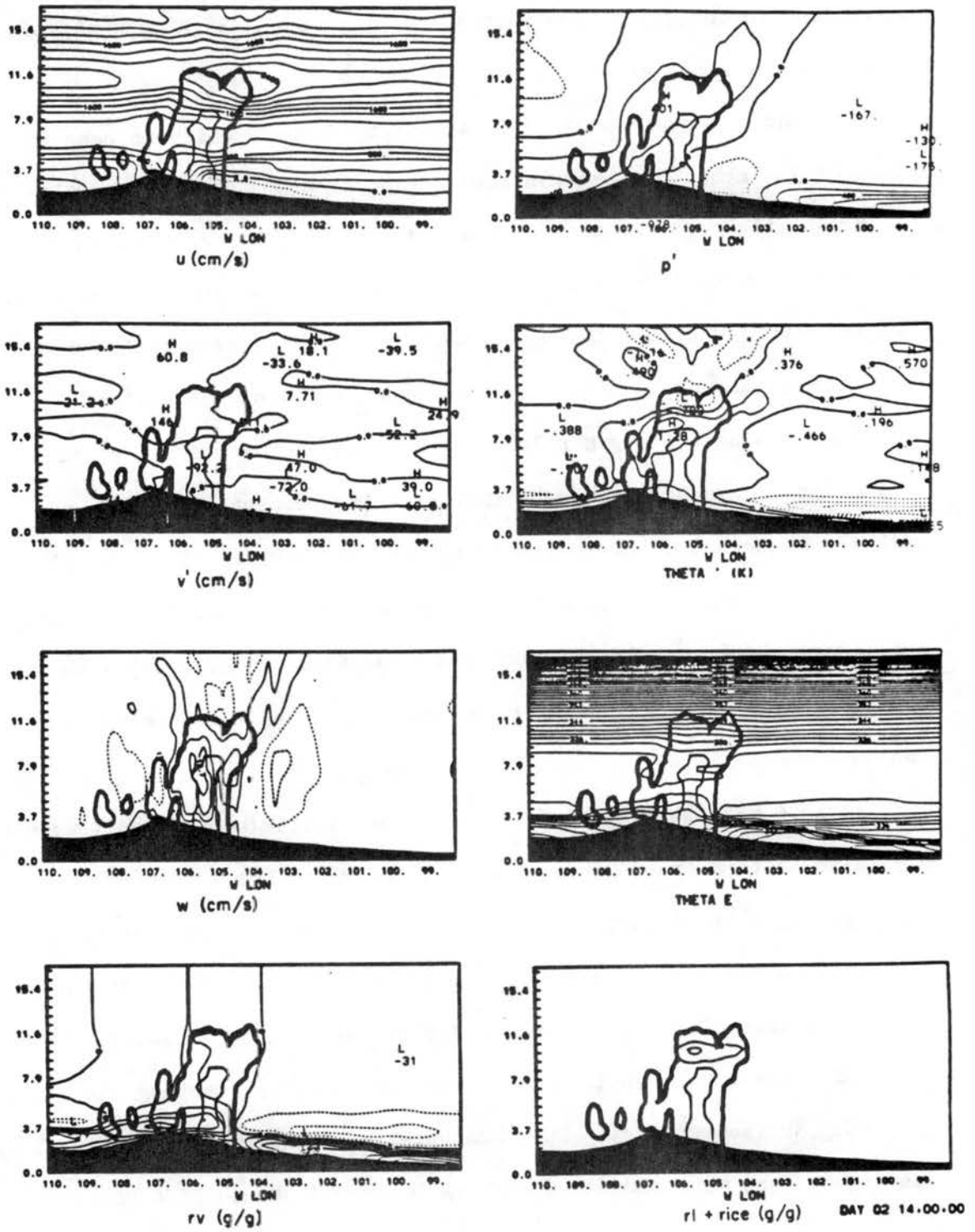

Figure 5.6. Same as Figure 5.1, except 1400 MST.

By 1500 MST (not shown) a second region of convection appears at the ridge crest. This convection is considerably less intense than the initial moist convection forming in that region. It seems that the influence of the initial ridge top regime, now 90 km to the east and strengthening, is helping suppress further western development.

By 1600 MST (Fig. 5.7) the west slope convection has lessened. Rainfall west of the Denver longitude (105 W) has subsided. Note, at this time, the effects of a strong inversion at about 1 km AGL over the eastern plains (most evident in θ_e field). This forms from cool upslope advection in the lowest 1 km AGL (see θ' field) and downslope warming above. As the strength of the slope flow increases, the inversion strengthens. The weakening easternmost rainshaft has almost completely dissipated. The developing region of convection previously between South Park and Denver (105.3 W) one hour earlier has moved about 40 km to the east in conjunction with the supporting boundary layer mesoscale convergence. The entire boundary layer flow field between this region of convection westward to ridge top has become westerly. At this point it is evident that stage 3 (Cotton et al. (1983), 1983), which is associated with the eastward progression of a mesoscale squall line, has begun within the simulation.

In summary, the organized mesoscale convection began with the formation of initial convective elements associated with mountain peak convegence. This convection persisted as it drifted eastward over the unstable mountain boundary layer where the surface inversion was broken by daytime mixing. When mesoscale supported low level surface convergence was encountered between South Park and the eastern plains, the convection strengthened. As the system continued to progress

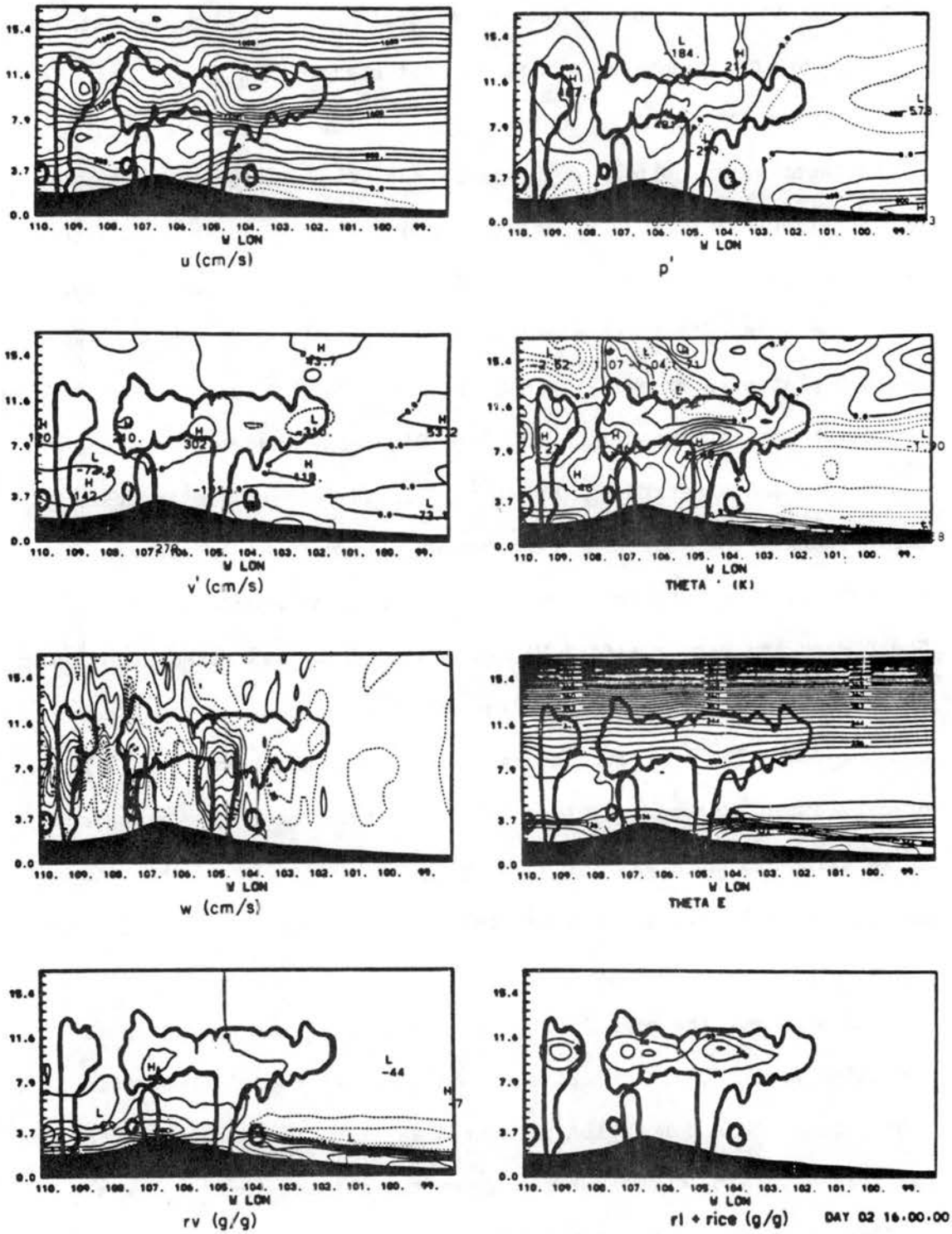

Figure 5.7. Same as Figure 5.1, except 1600 MST.

eastward, the low level convergence moved as well. Hence in the region 50-100 km east of South Park, a basic mesoscale organization took place in the simulation where the mountain generated convection became coupled with existing mesoscale convergence. After this point, the convection and the surface convergence became synergistic and moved eastward together. Unlike the first lee-side convection regime, the coupled system continuously washed out the strong plains boundary layer inversion producing a favorable growth regime for discretely propagating convective elements. This coupling, which occurred about 1500 MST in the simulation, was observed by Cotton et al. (1983) and represents the transition from stage 2 to stage 3.

The appearance of simulated stage 3 was about 1.5 hours late. This may be due to several shortcomings of the simulation to this point. It was pointed out that the lack of simulated "hot spots" delayed initial convection. The higher than observed west slope moisture together with a general lack of competing convection between ridge top and the region 60 km to the east may have placed undue emphasis on the initial ridge top convection. It should be recognized, however, that the organization around the mesoscale convergent flow 60 km lee of the ridge top was observed and hence was probably responsible for the intensification of convective activity leading the transition into stage 3.

5.3 Stage 3: Eastward Propagating Mesoscale Squall Line

The organization of the primary orogenic squall line began at 1500 MST. At this time, certain structural changes within the preexisting region of convection were found. Most evident was a strong increase in intensity and the beginning of a propagating synergistic relationship between convection and mesoscale surface convergence. Other mesoscale

signatures were noted as well and are discussed more fully later in this chapter.

The mesoscale structure at 1600 MST is displayed in Figure 5.7. At this time a strong graupel/rain shaft develops on the west side of the system. As it reaches the lowest 1 km AGL, low level cooling develops. By 1630 MST, seen in Figure 5.8, an intense surface high pressure dome developes with an excess pressure of about 0.6 mb over surroundings. The accompanying outflow undercuts the existing westerly flow to the west of the system. The easterly acceleration to the west of the system is also influenced by the development of low pressure (low of about -0.4 mb) to the west produced by convection induced subsidence warming aloft and continued high elevation surface heating. The result is a major weakening of the system, characterized by peak updraft speeds falling from 15 m s^{-1} at 1530 to 2 m s^{-1} at 1634.

The result of the surface divergence beneath the primary MCS is to reestablish the easterly flow regime on the east slope of the Rockies and again produce a surface convergence zone 60 km to the lee of ridge top. Here, a weak convective element is formed at 1800, this time lacking the support of a strong moisture supply from the east. The low level convergence associated with the primary convective system near 105 W is thus shifted to higher levels (above 2km AGL) as a result of the development of the surface divergent flow. The resulting vertical shear of u seems to positively reinforce this structure by supplying dry air to aid in the production of the downdraft and outflow.

It is known that the sudden increase in slope to the west makes this region around 105 W Longitude naturally divergent at the surface due to accelerating slope flows (Dirks, 1969). In addition, this is the

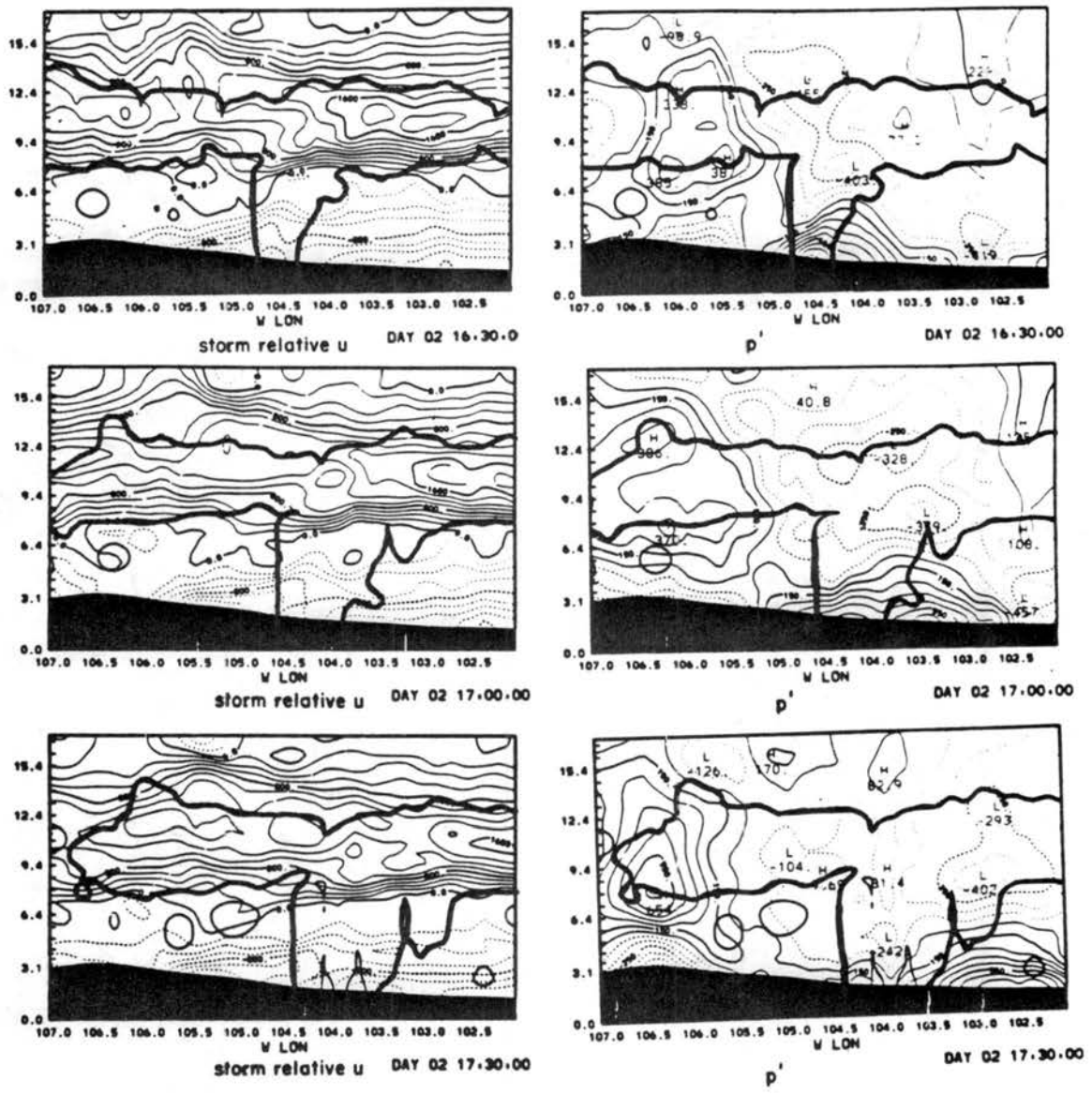

Figure 5.8. Predicted fields at 1630, 1700 and 1730 showing a closup of evolution near primary precipitation shaft. The fields represent a 20 grid point horizontal average (21.6 km) of actual predicted variables. Variables displayed are storm relative u (10 m s^{-1}), p', θ^{o} relative to plot are removed. Contour intervals are 2 m s^{-1} (200 cm s^{-1}) for u, 1 mb (100 dynes cm^{-2}) for p', 0.5 K for θ^{o} and 0.2 g kg^{-1} for condensate. The axis and condensate outline are as in Figure 5.1. The vertical coordinate is exaggerated by a factor of 20.

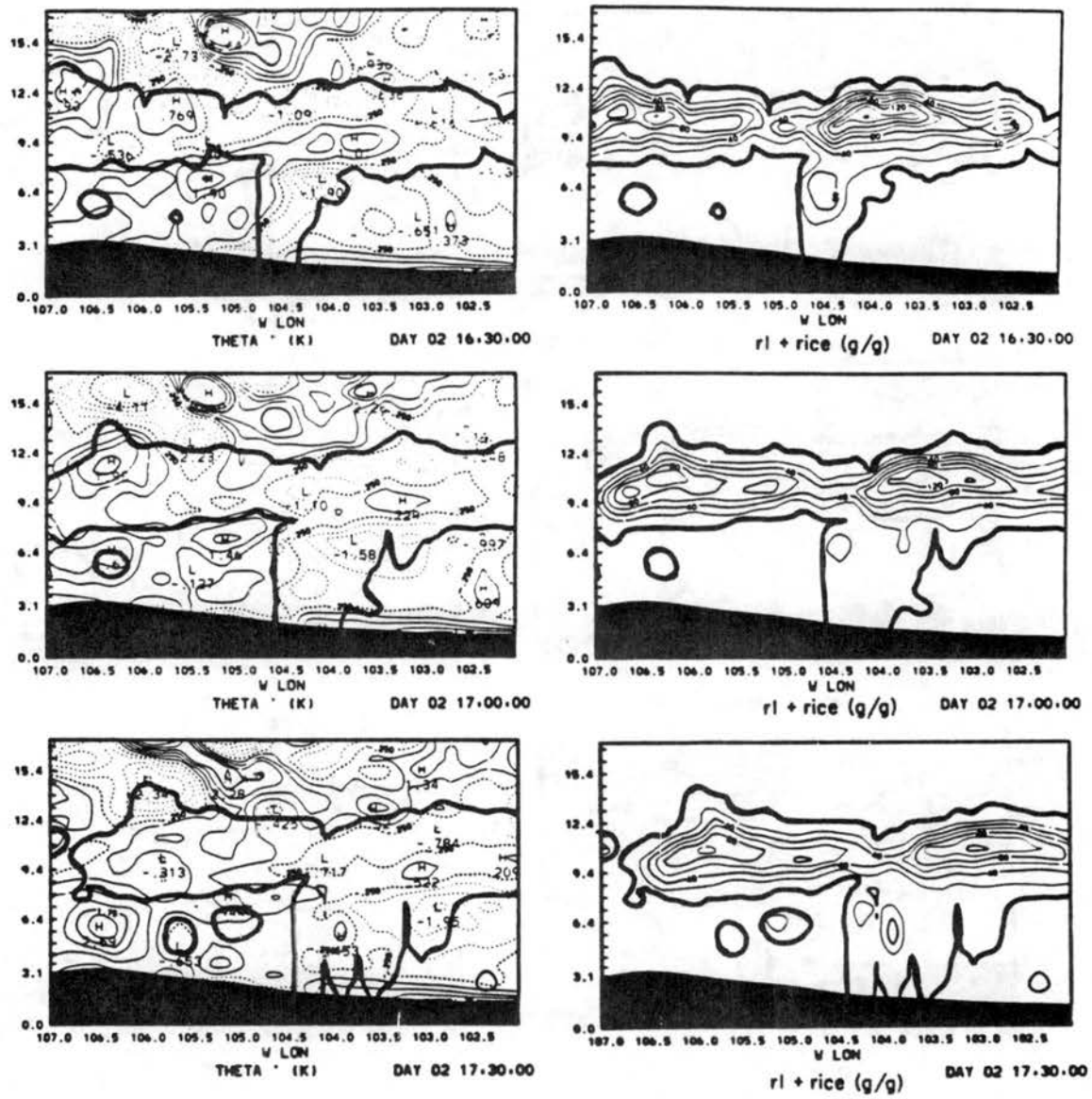

Figure 5.8. Continued.

region where Dirks et al. (1967) predicted that mountain lee wave subsidence might act to suppress convection. Examination of the 0400 MST w field, before the influence of deep convection and the effects of thermal upslope circulation, reveals that this is, in fact, a region of subsidence from mountain wave effects. It seems likely that the combined suppression by the mountain wave effect, the slope circulation and perhaps a natural oscillation in the convective system intensity, created an especially notable weakening of the mesoscale convective system (MCS) and associated convective elements as it passed through this region. The first evidence of the suppression was when especially strong mid-level entrainment occurred at the conclusion of the lifecycle of a particular convective element.

There also seems to be some evidence that the surface high beneath the system core was, to some extent, maintained by the effects of a region of large ice content aloft. Initially, at 1600 MST the mesohigh forms largely in response to the downdraft mentioned above. However by 1700 MST a broad region of surface high pressure has moved eastward at nearly the speed of the anvil level winds. Not coincidently, a maximum in upper level condensate (ice crystals) moves in concert with the surface high pressure zone. Along with these phenomena, the mid level air and upper anvil level air cools. The cooling can be directly attributed to radiational cooling above the anvil and the sublimation of ice below the anvil. All of these effects together produce the rapidly eastward moving surface high pressure signature.

As the high pressure pushes off to the east, and a smaller region of high pressure is maintained in the primary downdraft to the west of the main rainshaft, a relative low again forms on the eastern side of

the rainshaft by 1700 MST (Fig. 5.8). By 1730 MST, the relative low has reestablished in conjuction with a moderate convergent boundary layer flow regime. A particularly strong perturbation within the downdraft at 1715 MST (not shown) was initiated which forced a strong updraft within the convergent flow. By 1730 MST, peak vertical motion strengthens to 15 m s^{-1}.

The active updraft region, in all cases, lies on the western boundary of the plains inversion. It moves at a very constant speed of from 10–12 m s^{-1}. It is interesting that some pressure and temperature anomalies, such as that mentioned above, move faster with the flow above, while other phenomena, such as the surface gust front air, seem to move more slowly.

It seems evident that the observed system underwent a similiar weakening as it passed the apparent region of simulated suppression. Examination of radar echos of the system passing off the foothills and onto the plains, reveals at least 7 cells of intensity level 2 within the line at 1400 MST. This weakens to 1 cell of that intensity at 1500 MST and strengthening back to 5 cells of level 2 at 1600 MST. Recall that the observed system was about 1.5 hours ahead of the simulated system.

The rejuvinated simulated system at 1800 MST is depicted in Figure 5.9. The observed system at 1800 MST remains ahead of the simulated system. Assuming a propagation speed of 10 m s^{-1}, the system is about 1.5 hours ahead which is unchanged from the beginning of stage 3. In fact, if the time sequence of observed maximum echo is plotted from the results of Cotton et al. (1983), the observed system, like the simulated system, moves eastward at 10–12 m s^{-1}.

During the period between 1800 MST and 2200 MST the simulated convective system moves from the Limon, Colorado area eastward to the Colorado and Kansas border. Over the course of this progression, peak updrafts remain between 4-28 m s^{-1}, as the strength of individual convective elements and the mesoscale response vary.

Figures 5.9 through 5.11 depict the MCS evolution through this period. Note the strong temperature signature at upper levels which is most apparent at 2000 MST. Deep warming is found on the western side of the core and shallow warming extends from the core eastward into the anvil. Strongest warming (2k) is found near 8 km MSL in the region of the core. Analysis of mesoscale vertical motion reveals that the simulated MCS attains peak intensity at 2000 MST. The peak intensity at 2000 MST seems to occur when, for a brief moment, all of the mesoscale convergence is concentrated into the support of a single convective element. At this time, the mesoscale convergence was also especially intense.

Even stonger convective scale peak vertical motion, however, was attained in the mid-afternoon. This also is consistent with observations which show several of the most intense cells occurring near the same time of 1500 MST, when the mesoscale organization appeared smaller and weaker while fewer very intense cells formed later near dusk as the apparent mesoscale organization increased. Obviously, peak updrafts which occur earlier are in response to greater afternoon conditional instability.

A second precipitation shaft has formed over the foothills by 1900. This region of convection seems to form from two effects. First, it was mentioned above that during the suppression stage of the primary MCS,

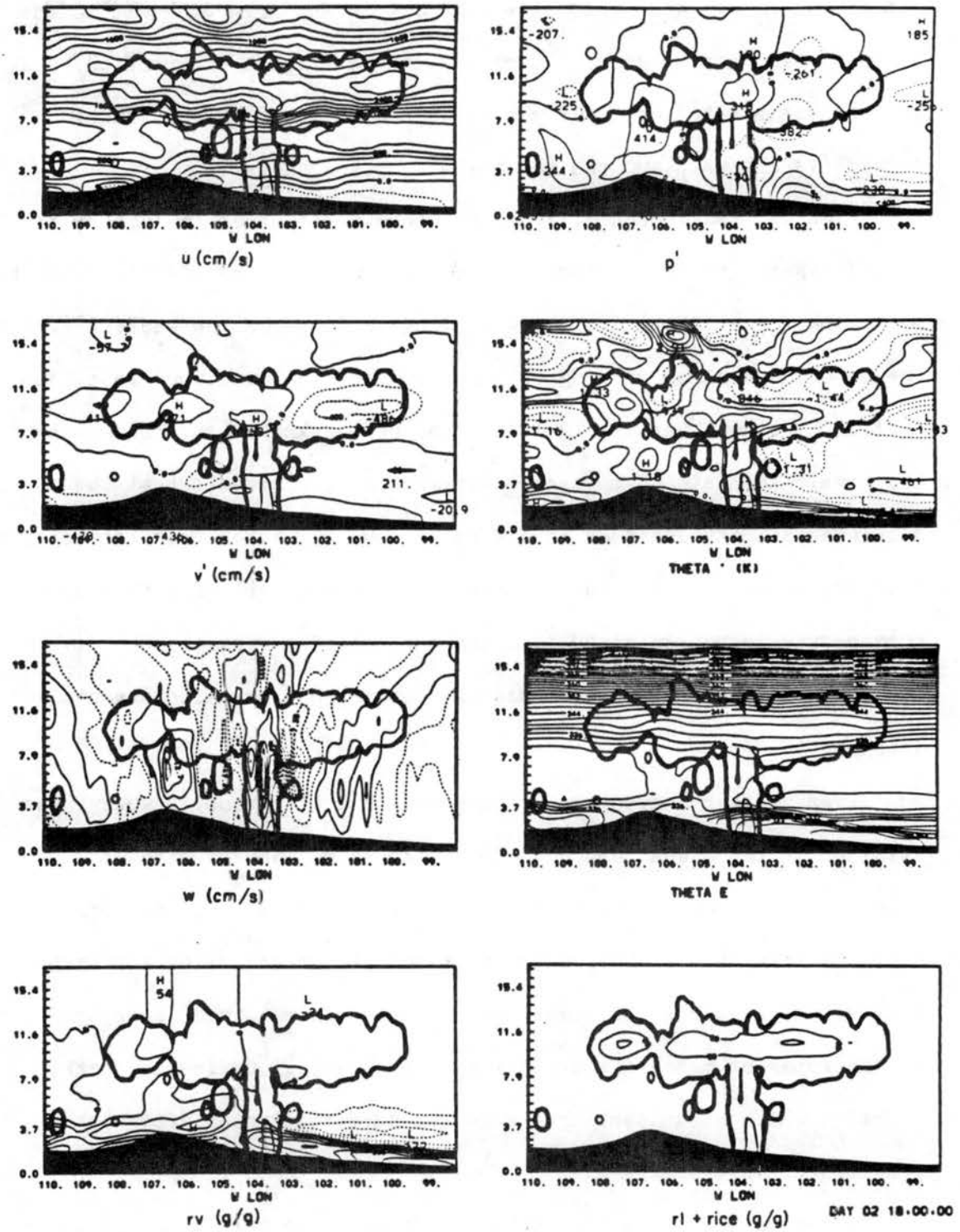

Figure 5.9. Same as Figure 5.1, except 1800 MST.

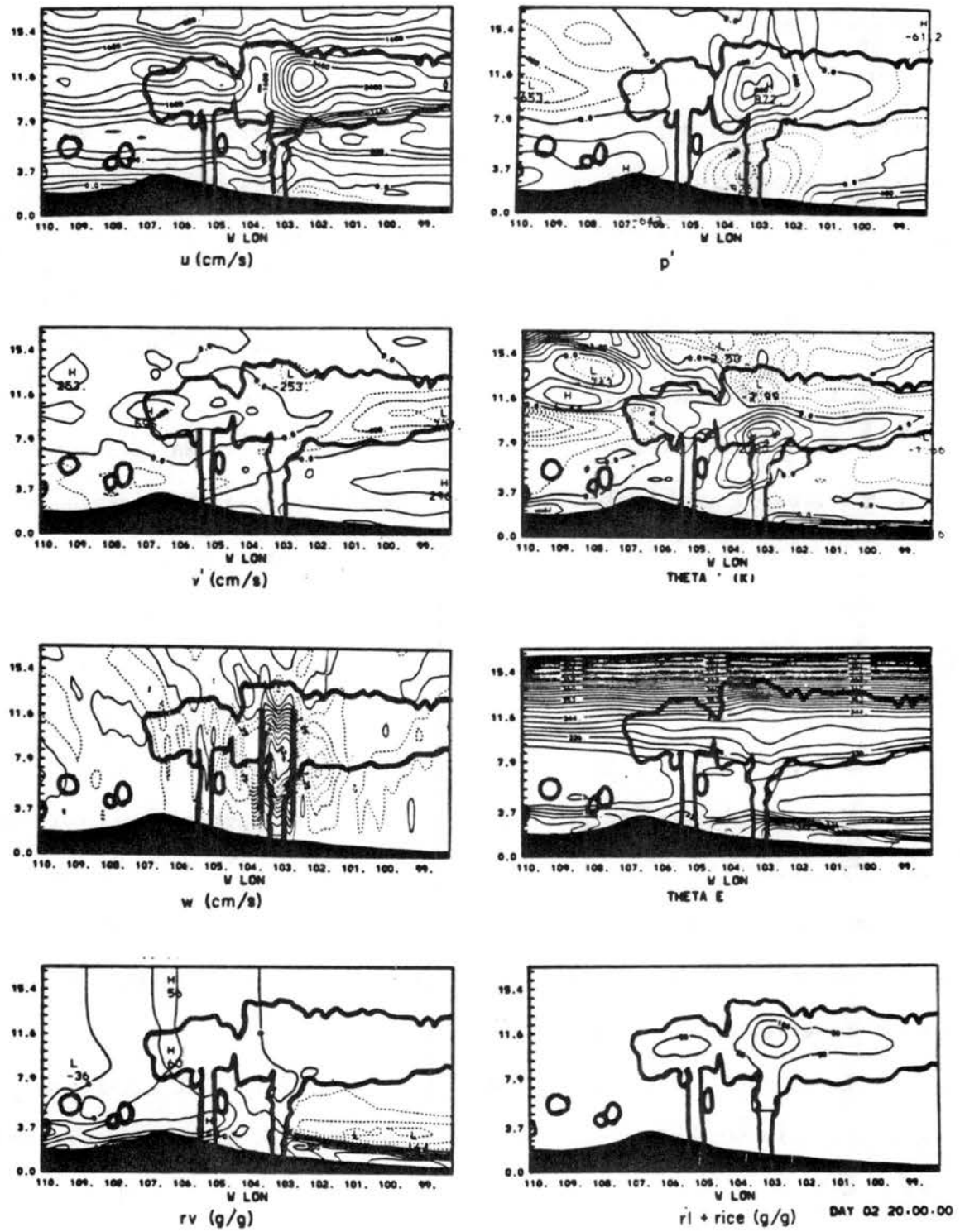

Figure 5.10. Same as Figure 5.1, except 2000 MST.

weak surface convergence was reestablished in that region bringing in some moisture from both the west and the east . Second, the sudden intensification of the primary MCS initiated the eastward and westward propagation of a deep internal gravity waves which triggered convection over the foothills.

The gravity wave oscillation was initiated as follows: The convection within the MCS core forced strong subsidence laterally as a result of pressure forces induced by the system core. It is hypothesized that convection within the MCS core intensified beyond its mesoscale support around 1800-1900 MST resulting in the entrainment of lower-valued θ_E air. This resulted in the weakening of the warm core, which lessened of lateral pressure forces. The result was a bouyant rebound of subsided air to the west and east of the main MCS core and the suppression of motion within the core.

To the east, the newly induced vertical motion remained above the inversion and failed to initiate convection. To the west, however, the rebound occurred over the natural zone of surface convergence, which had already accumulated a modest moisture supply from the west. The result was the mesoscale support of convection to the lee of South Park. Evidence of some echo activity along the foothills east of South Park is found observationally at 1600 MST as well.

The gravity oscillation of the buoyant core continued until the system dissipated. It seems that a wave train of deep gravity waves was emitted from the primary MCS which traveled laterally "like ripples emitted from the impact of a pebble in a pond". The vertical motion associated with the ripples could or could not initiate convective activity, depending on existing low level support. As the MCS core mean

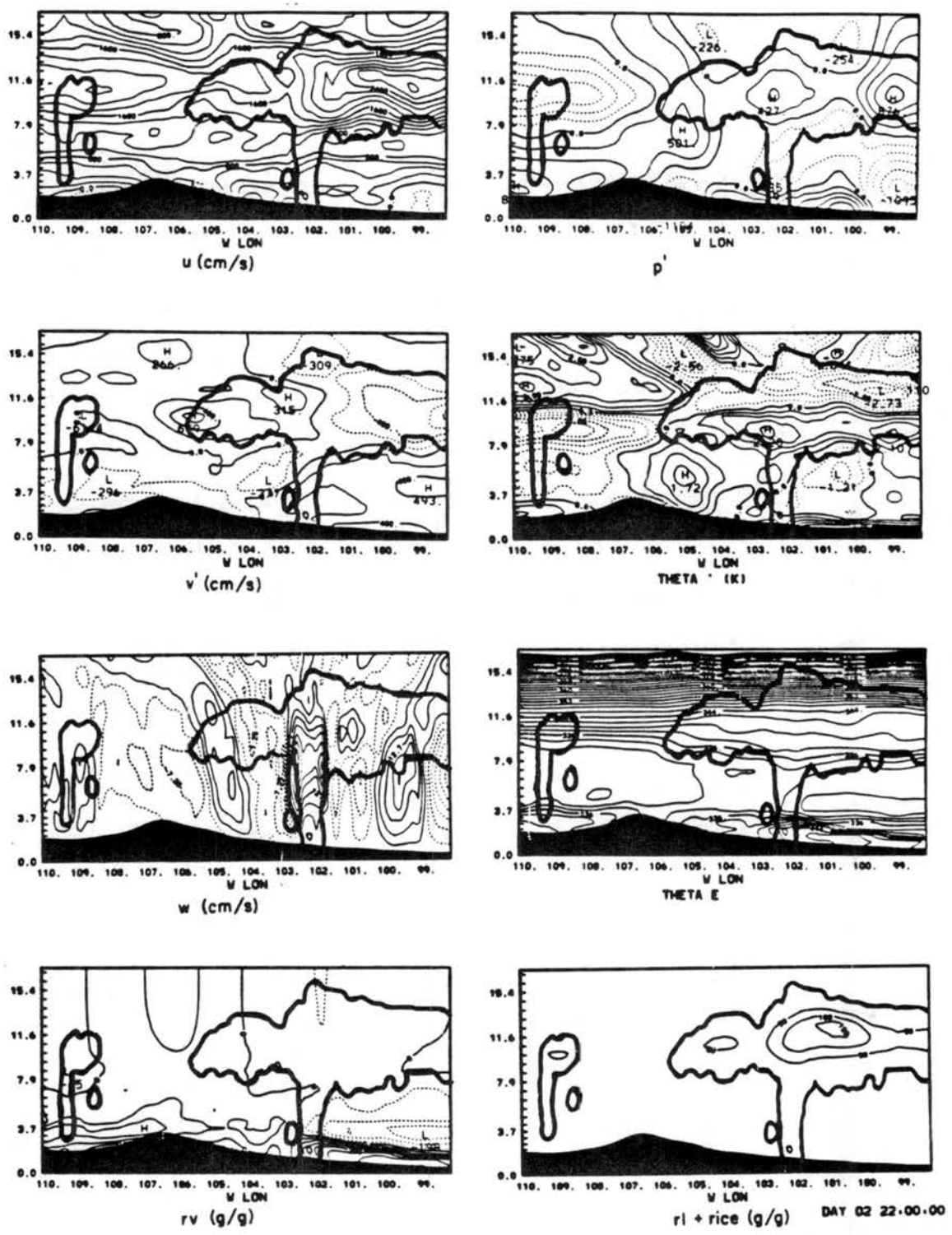

Figure 5.11. Same as Figure 5.1, except 2200 MST.

vertical motion undulated, the level of its convective activity oscillated as well. This oscillation of peak updraft with time is depicted in Figure 5.12. Note the increase in amplitude of the oscillation from 2000-2200 MST.

The oscillation of system intensity is also evident in the accumulated precipitation field given in Figure 5.13. Note the steady increase in precipitation (for control case) until the longitude of 105 W is reached. The suppression of precipitation is strongest at 104 W. Afterward precipitation recovers, but undergoes a strong oscillation moving eastward. A large component of this oscillation is on the 86 km scale which is just less than a 2 hour period for a system propagation of 10 m s^{-1}. Some oscillation on a 0.25^{o} longitude or 0.5 hour time scale is also apparent representing the lifetime of the meso-γ component. Note that east of 102 W longitude (the eastern Colorado border) the precipitation drops dramatically. This is a consequence of the system weakening as low level decreasing θ_e is injested into the system core.

Figure 5.11 clearly depicts the emitted internal gravity waves (w field), and shows the ongoing collapse of a core upward motion regime. Note the existence of upward motion as far east as central Kansas and as far west as Denver which lingers from the intense stage at 2000. A second intense stage around 2130 MST is collapsing at 2200 and regions of upward motion are beginning to separate and move apart.

The dominant horizontal wavelength is about 160-240 km. Using the 2000 MST positioning as a guide, the wave seems to move at 21 m s^{-1} to the west and 41 m s^{-1} toward the east. Since the mean wind speed is about 10 m s^{-1}, this corresponds to a 30 m s^{-1} relative phase speed.

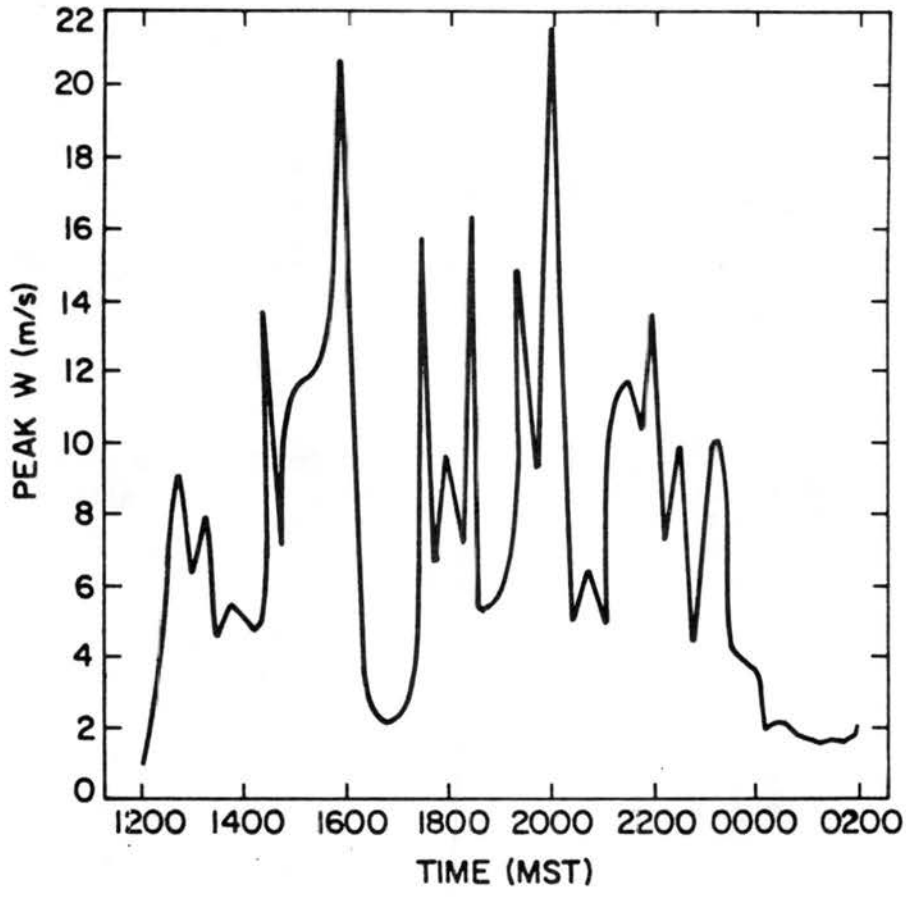

Figure 5.12. Peak vertical motion (associated with system core convection) versus time. Vertical motion is labeled in cm s^{-1}.

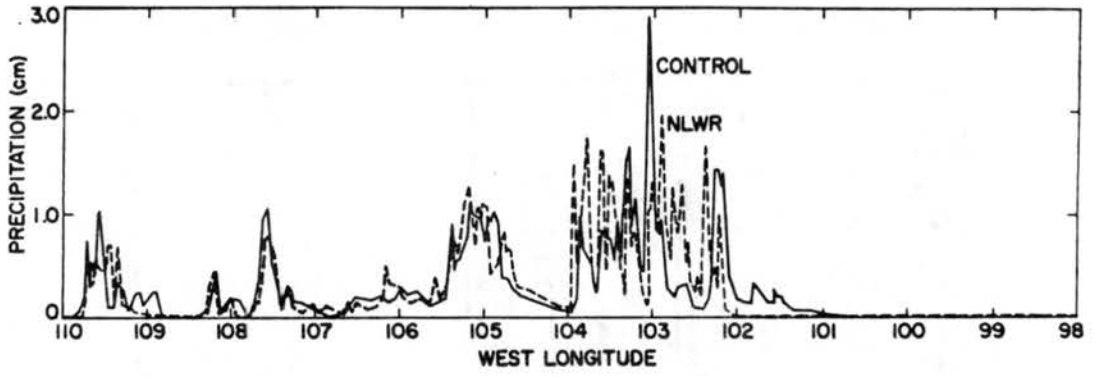

Figure 5.13. Accumulated precipitation in cm (vertical axis) versus horizontal location W longitude (horizontal axis). Curves for control case and NLWR case drawn.

Vertical propagation appears to be inhibited, perhaps from a wave ducting (Lindzen and Tung, 1976). The possibility of a ducting seems even more likely when the longterm maintenance of energy over a full wave cycle is maintained as it appears to be here. The upper wave Brunt-Vaisalla frequency is about 0.015 s^{-1} and the wave depth is about 12 km. This would give an internal wave phase speed of about 28 m s^{-1}, close to the observed movement.

It is also instructive to note the gravity wave structure. The eastward and westward travelling waves are strongest below anvil level. As the westward travelling wave exits the anvil (near 105 W at 2200 MST), the wave travels no farther to the west. This is qualitative evidence that the waves are somehow trapped below the anvil level. This enables their horizontal propagation over a considerable distance while maintaining much of the original amplitude. There will be further investigation of this phenomena later in this chapter.

The system core at 2000 seemed to draw from energy associated with the "daughter" system which formed over the foothills. As the western convection collapsed, foothills precipitation augmented developing surface high pressure which helped to intensify the region of the system core. At the same time, the MCS core encountered increasing moisture. The intensification caused significantly warmer temperatures at mid to upper levels in the vicinity of the system. This led to relatively low surface pressure. The result is an especially strong mesoscale response at 2000 MST.

In order to gain insight into the nature of the individual convective elements comprising the primary convective system, a close up look at the evolution of the main precipitation shaft is displayed in

Figure 5.14. The fields of w and Dw/Dt are displayed, where Dw/Dt is given by:

$$\frac{\partial w}{\partial t} = -\theta_o \frac{\partial \pi}{\partial x} + \left(\frac{\theta'}{\theta_o} + 1.61 r_v - r_T\right) \tag{5.1}$$

where all symbols are defined in appendix A. The value of $\partial w/\partial T$ is then the current Lagrangian acceleration of w by the hydrostatic imbalance. Note the convection is comprised of several elements. Together with w, the tendency of vertical motion is displayed.

All of the individual convective elements are contained within the general precipitation shaft. The precipitation shaft seems to move slightly faster than the individual elements. The non hydrostatic acceleration generally opposes the vertical motion elements. This indicates that they probably form rapidly and dissipate slowly. A dissipating element forces upward motion around itself leading to the formation of two daughter elements. This is a small scale version of the gravity oscillation discussed above for the mesoscale. If these elements are forced outside the main rainshaft region they dissipate. When two elements dissipate simultaneously, their lateral forcing combines to form an especially intense new element, usually close to the center of the system.

The initiation of daughter cells in this way has been studied theoretically by Lin and Smith (1986). The forcing originates as a reaction to the heating at mid to upper levels by the convection. New upward motion is initiated in the region where the parent cell forced maximum subsidence warming. As the parent cell wanes, the atmosphere rebounds in the warm regions, overshoots and initiates an unstable new updraft.

Figure 5.14. Predicted meso-γ fields at 1215-2200 MST. Variables displayed are w and Dw/Dt. Contour intervals are 2 m s^{-1} (200 cm s^{-2}) for w and 0.02 m s^{-2} (2 cm s^{-2}) for Dw/Dt. Negative contours are dashed. Cloud outline, axis and topography are represented as in Figure 5.1. Variable fields represent a 4 grid point (4.32 km) running average. The vertical coordinate is exaggerated by a factor of 4.

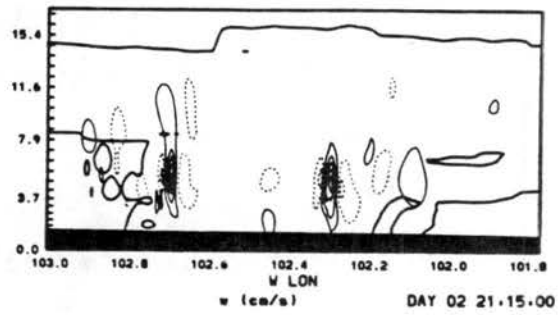
15.4
11.6
7.9
3.7
0.0
103.0 102.8 102.6 102.4 102.2 102.0 101.8
W LON
w (cm/s)
DAY 02 21:15:00

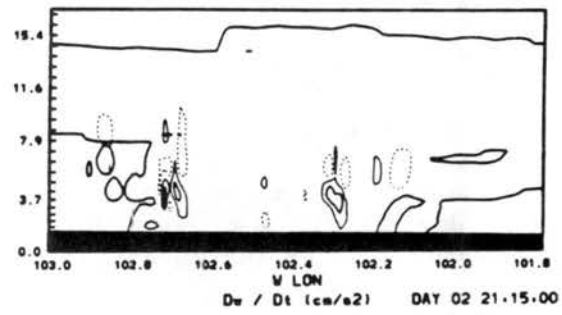
15.4
11.6
7.9
3.7
0.0
103.0 102.8 102.6 102.4 102.2 102.0 101.8
W LON
Dw / Dt (cm/s2)
DAY 02 21:15:00

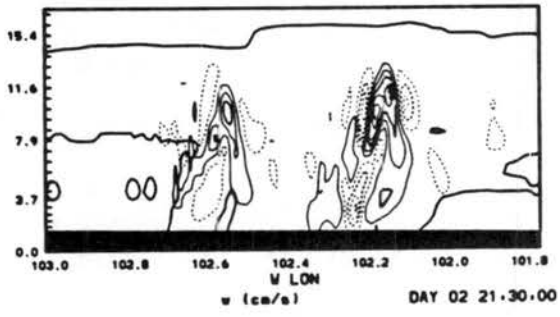
15.4
11.6
7.9
3.7
0.0
103.0 102.8 102.6 102.4 102.2 102.0 101.8
W LON
w (cm/s)
DAY 02 21:30:00

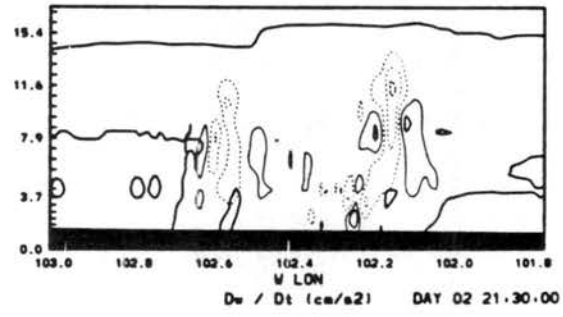
15.4
11.6
7.9
3.7
0.0
103.0 102.8 102.6 102.4 102.2 102.0 101.8
W LON
Dw / Dt (cm/s2)
DAY 02 21:30:00

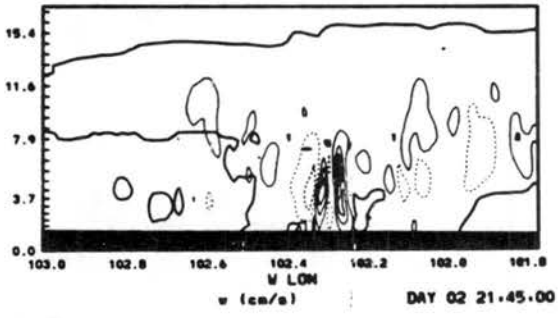
15.4
11.6
7.9
3.7
0.0
103.0 102.8 102.6 102.4 102.2 102.0 101.8
W LON
w (cm/s)
DAY 02 21:45:00

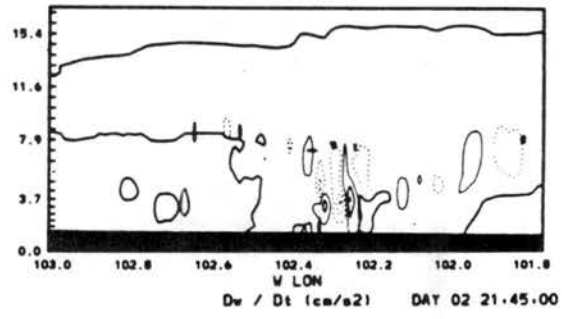
15.4
11.6
7.9
3.7
0.0
103.0 102.8 102.6 102.4 102.2 102.0 101.8
W LON
Dw / Dt (cm/s2)
DAY 02 21:45:00

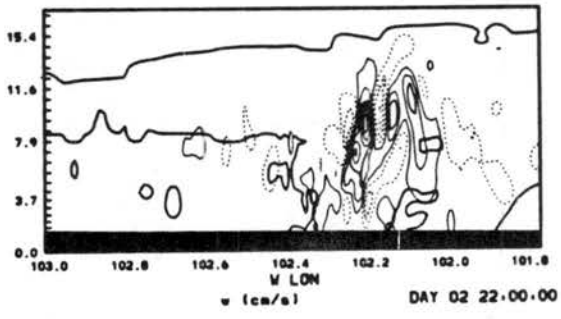
15.4
11.6
7.9
3.7
0.0
103.0 102.8 102.6 102.4 102.2 102.0 101.8
W LON
w (cm/s)
DAY 02 22:00:00

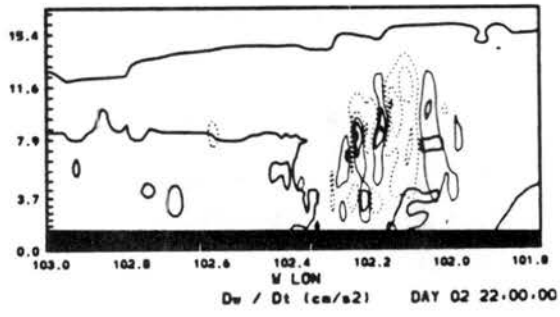
15.4
11.6
7.9
3.7
0.0
103.0 102.8 102.6 102.4 102.2 102.0 101.8
W LON
Dw / Dt (cm/s2)
DAY 02 22:00:00

The convective system reaches its overall peak mesoscale intensity at 2000 MST. At this time there is a coherent pressure, temperature, horizontal convergence and vertical velocity signature. Beyond this time, the mesoscale organization persists but the conditional instability wanes as nocturnal cooling sets in. This is countered to some extent, by the inception of greater and greater low level moisture and the retention of heat by the forward extending anvil to the east. As a result peak vertical motions only subside to 4-6 m s^{-1} between intense convective bursts until 2330 MST. At that time the bursts of intense convection subside and the base updraft wanes. The peak vertical motion history as a function time displayed in Figure 5.12 demonstrates this history.. The convective bursts are associated with the development of strong convective elements which constructively link up with the mesoscale vertical motion patterns. The lulls are associated with periods where convection is forced in less than optimum regions within the mesoscale forcing field.

The final stages of the system are displayed in Figures 5.15 through 5.16. The dissipating stages are typified by a basic change in the structure. As the surface cools, the thermal mesoscale support for the easterly slope flow wanes. Geostrophic adjustment to southerly flow built by the persistence of daytime and system forced upslope flow to the east begins to dominate the effects of pressure gradient resulting from the system mesoscale feedback. Since the surface cooling occurs from below, the effect is most prominent at the surface initially. The effect is that the mesoscale dynamics are no longer capable of lifting surface air to free convection at 0200 MST. The mesoscale "flywheel" persists, however, and the surface low pressure moves to 3-5 km AGL

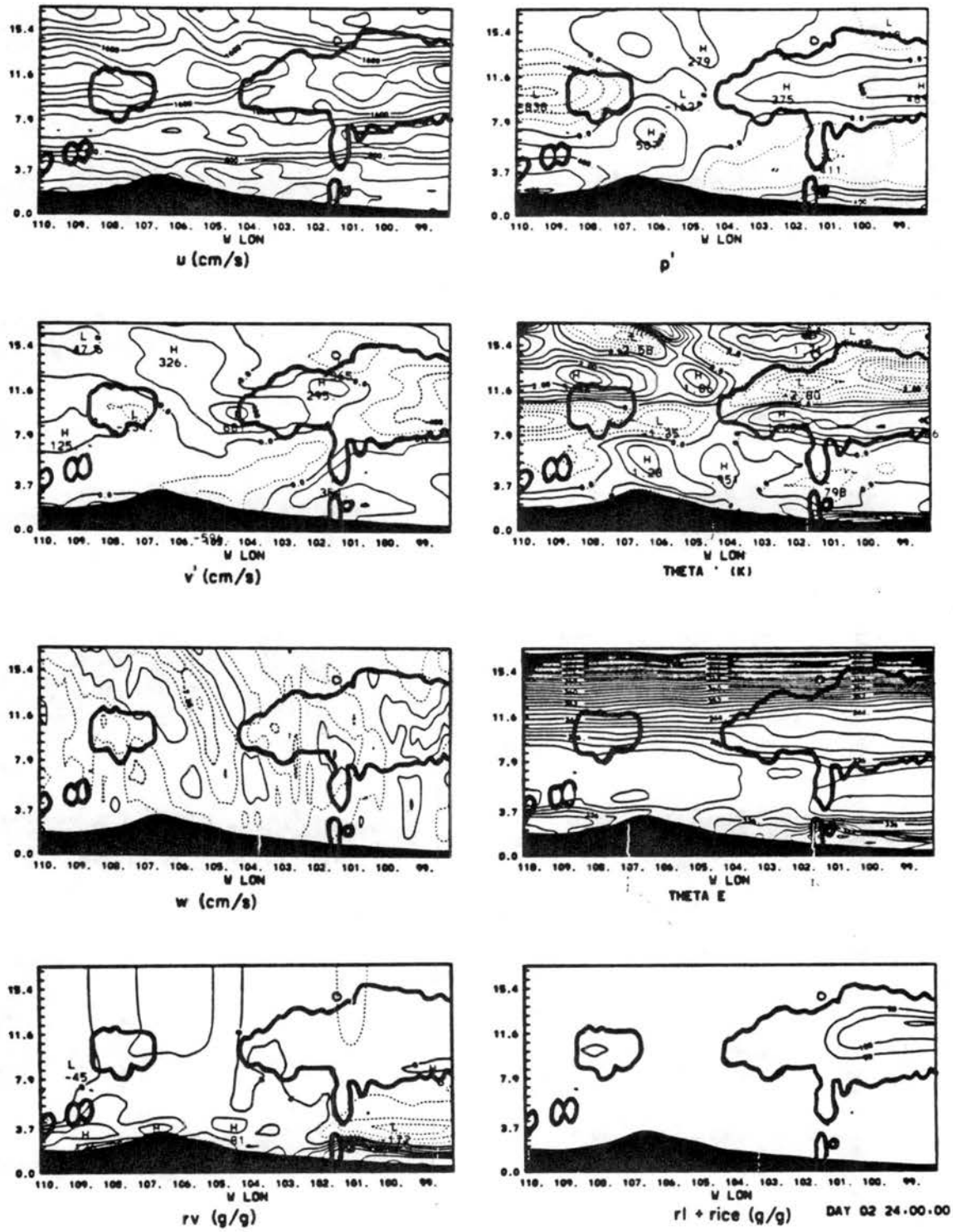

Figure 5.15. Same as Figure 5.1, except 2400 MST.

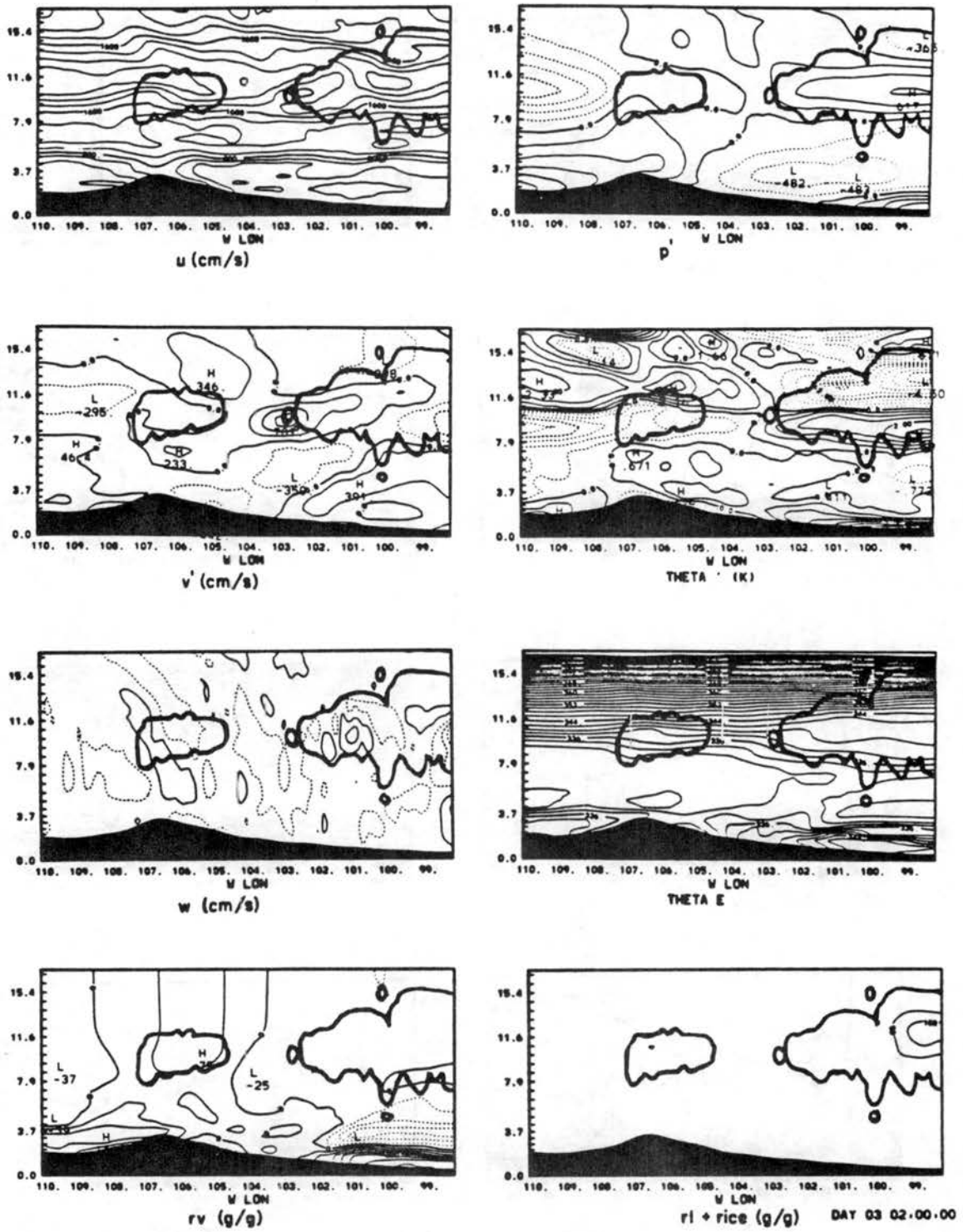

Figure 5.16. Same as Figure 5.1, except 0200 MST.

where the primary horizontal convergence now lies. In essence, this is similiar to the decoupling of the MCS from the surface observed by Cotton and others (personal communication) during the recent AIMCS and PRESTORM experiments in almost all cases as the system approaches the midnight hour.

The observed system grew larger at this time and finally reached MCC status (Maddox, 1981). The difference between observations and the simulations can readily be attributed to the following: the observed system was some 60-80 km east of the simulated location at the critical decoupling time. This was a location where the reference flow became especially invalid. In fact, a strong low level mean zonal pressure gradient was observed on the western boundary of the subtropical high. As a result a nocturnal southerly jet developed in response to geostrophic adjustment from the daytime circulation (Blackadar, 1957). As explained in chapter 1, the low level southerly jet transports large amounts of moisture to mid levels during the night. As the simulated system decoupled from the surface, it injested air strongly from the observed vertical levels of the low level jet. If this jet structure were simulated, it is likely that the simulated system would actually have reacted as observed, instead of dissipating. As it stands, it has been shown that the action of the mountain valley circulation in a basic horizontally homogeneous zonal flow, will, in itself deliver a suitable trigger to the region of the nocturnal southerly jet. The simulation of the interaction of this trigger with the jet is a topic for further study.

5.4 Streamflow Evolution and Trajectory Analysis

The MCS relative stream flow can reveal interesting features of the dynamic response which are not apparent from individual time frames of the propagating system. The meso-β storm-relative stream flow represents the parcel paths more accurately because the flow field is unchanging (except for intensity or discrete propagation).

The streamfunction is defined:

$$\rho_o (u - u_r) = - \frac{\partial \psi}{\partial z}$$
$$\rho_o w = \frac{\partial \psi}{\partial x} \qquad (5.2)$$

where ψ is the momentum streamfunction and u_r is the storm motion. The gradient of streamfunction is then a measure of total momentum. Now,

$$\nabla^2 \psi = - \frac{\partial (\rho_o u)}{\partial z} + \frac{\partial (\rho_o w)}{\partial x} = \zeta_y \qquad (5.3)$$

where ζ_y is the y component of relative vorticity. To display the streamfunction, Eq. 5.3 will be solved for ψ using the boundary conditions:

$d\psi/dx = 0$ (lateral boundaries)

$\psi = 0$ (surface)

$\psi = \psi 1$ (upper boundary)

where $\psi 1$ is integrated from the lower west corner clockwise using the relation:

$$\frac{\partial \psi}{\partial l} = V_n \qquad (5.4)$$

where V_n is the momentum normal to the boundary and l is the path length, positive in the clockwise direction. For momentum conservation, the u below topography is assumed to vanish.

The evolution of the stream function from 1200 MST until 0200 MST is given in Figure 5.17 for $u_r = 10$ m s^{-1}. Here, the storm relative flow evolution from formation to dissipation is depicted. At 1200 MST, there already is evidence of some deep tropospheric vertical motion in response to the slope circulation. Examination of flow at earlier times suggests that the deep vertical motion over the mountain peak is associated with the mountain wave flow. The upshear tilt, in this case, is smoothed by the meso-β 80 point averaging scale. The streamline linking relatively easterly flow below to westerly flow above in the region 100 km east of ridge top should be viewed with some degree of skepticism. The representation of the topography on the cartesian grid leads to some error in this analysis. There may be some significance to the upward branch indicating, perhaps the extent of the mountain wave flow. There is no evidence that the convection has attained such depths, even on the meso-γ scale.

By 1300 MST, it is evident that western region of convection has already altered the circulation pattern drastically. It seems that the eastern convection is in a region of subsidence, perhaps induced by its own collapse and evaporation. More likely, it is being suppressed by the more powerful convection moving off of ridge top. Similiar subsidence at a like distance to the west of the primary convection seems to confirm such a notion.

By 1400 MST, the upbranch of the circulation cell spans a broader region as the subsidence zone has moved laterally from the core. The total circulation of the plains solenoid, as it will hereafter be called, has increased to four stream line intervals.

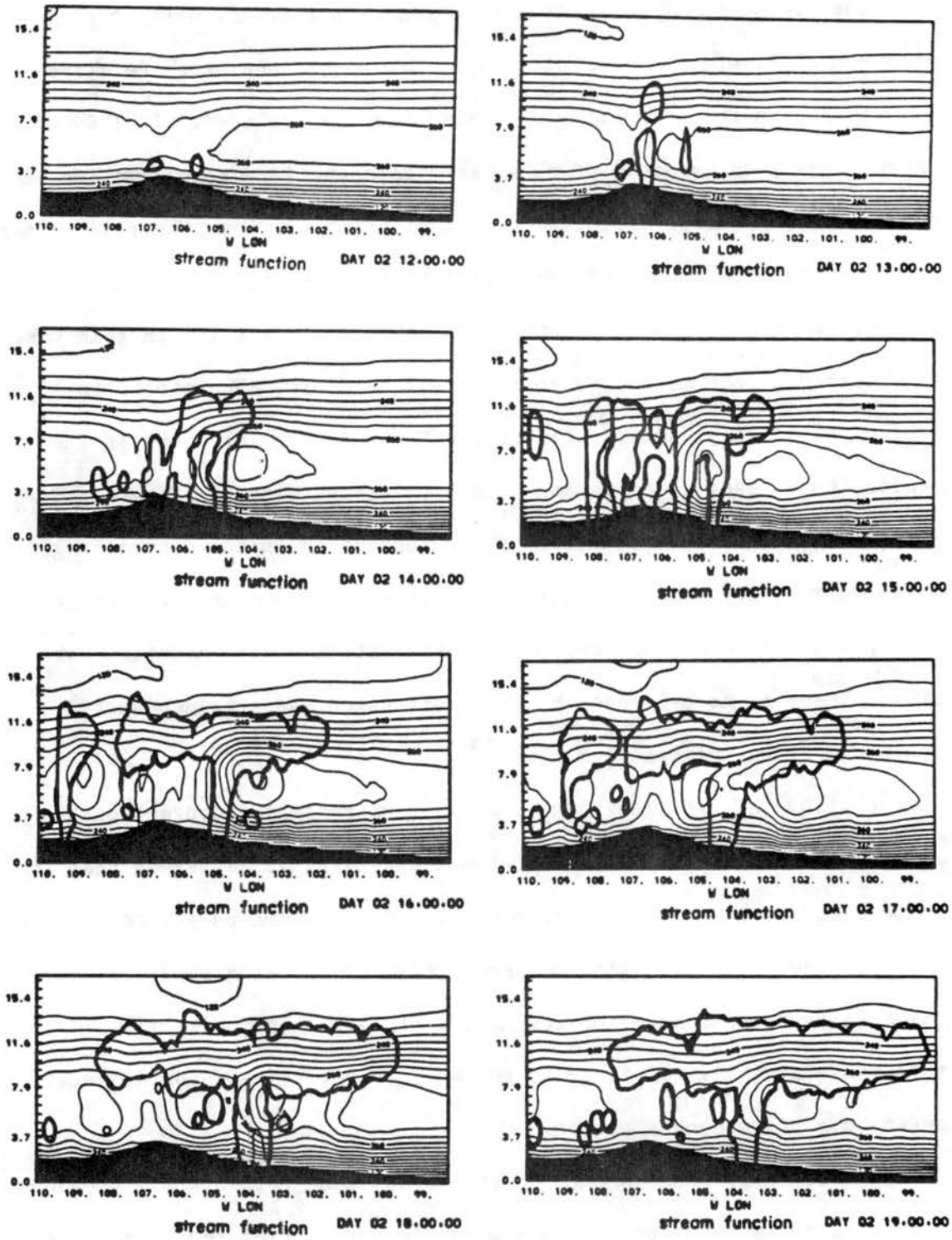

Figure 5.17. Streamline fields at times displayed (MST), based on 80 grid point (86 km) running averaged storm relative wind field. For the pruposes of this plot, storm movement is defined to be 10 m s^{-1}. Contour interval is 500 g cm s^{-1}. Cloud outline, vertical and horizontal axes, topograhy and exaggeration of vertical coordinate are as in Figure 5.1.

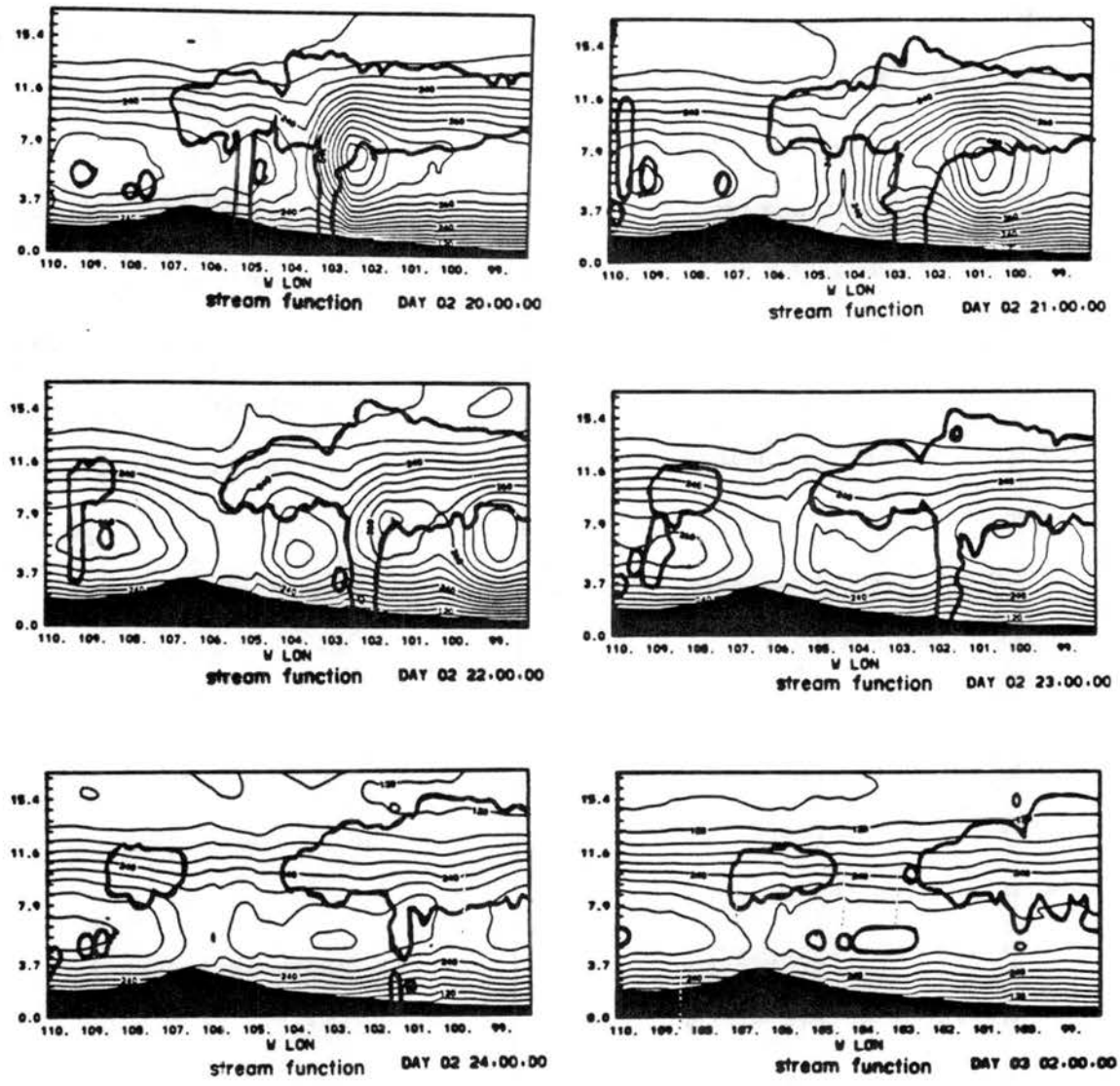

Figure 5.17 Continued

By 1500 MST the vertical branch has tightened considerably over the primary MCS rainshaft. A new zone of subsidence is now moving out from the center. It is evident that the west slope towers are associated with a weak up-branch of their own. Even at this time, a laterally propagating internal gravity wave train seems to be forming.

By 1600 MST, the MCS core up-branch of the circulation has intensified to 6 stream-line intervals. A distinct deep plains solenoid is apparent with the up-branch coincident with the system core. The circulation cell is reminiscent of the global scale, Hadley circulation except the pole to equator temperature gradient is replaced by a plains to mountain low level temperature gradient. As with the ITCZ (Inter-tropical Convergence Zone), the upward branch is associated with numerous convective elements which have little significant downdrafts. This type of circulation system has been labeled as "cellular" convection by Moncrieff (1981). The up-branch is moving eastward, apparently with the mean wind.

At 1700 MST, just after the time of maximum suppression, the up-branch splits and the system core is actually coincident with a weak down branch in the cellular circulation. By 1800 MST, the up-branch has reformed over the system core and the former down-branch is propagating laterally. The former split up-branch can still be seen, now centered near ridge top and in western Kansas (Colorado/Kansas border is 102 W Longitude). By 1900 MST, the up-branch has not strengthened, but the surrounding up-branches have weakened.

At 2000 MST, the system core has literally exploded! The up-branch streamflow has increased from 2-3 streamline intervals to 8. This is clearly the most significant mesoscale response up to this time. At

this time all other up-branches are obscured. However, a weak remnant of an upward branch is evident to the west of the western rainshaft. At this time, the western rainshaft is dynamically inactive.

The particularly strong circulation at this time seems to be due to several factors all coming together at once. First, the system is encountering rich plains moisture. Second, the gravity oscillation of the core is on the "up-swing." Third, nocturnal cooling combined with the collapsing western rainshaft is forcing a particularly strong westerly flow to the west. Fifth, on the convective scale, a single element was produced, further concentrating mesoscale response. Sixth, to be elaborated on later, the nucleation balance aloft is changing causing a "wave trapping," which is helping strengthen the gravity wave response. Beyond this time, surface cooling will gradually weaken the system.

At 2100 MST the pattern has again changed drastically. The central upward branch has split leading to an upward branch in eastern Kansas and one near Limon (104 W). The oscillation continues and at 2200 MST the central branch has again strengthened and is coincident with the system core. At the same time the other two upward branches can be seen to continue to propagate away laterally. The total circulation, however, seems to be waning.

By 2300 MST the core branch has weakened again and the circulation as a whole has begun to dissipate. A strong deep subsidence now seems to be occurring centered over the ridge top. This is having the effect of evaporating all of the cloudiness west of Limon. This deep subsidence appears to be linked to the development of the nocturnal slope flow. Its incredible depth, however, must be linked to the

combined influence of wave propagation from the system core. It seems that the nocturnal slope flow has provided the path of least resistance for the cloud mass flux. It is likely that geostrophic adjustment to the weakened convection is also playing a critical role in the development of this downslope flow.

By 2400 MST, the system core has weakened beyond recognition. Although the streamflow analysis is an enlightening look at the meso-motion field, parcel trajectories will move under the influence of the smallest scale motion considered. The meso-γ flow at the time of full system intensity at 2000 MST will now be viewed in order to gain insight into local air flows associated with the convection.

In order to obtain such trajectories, the local model flow fields saved on tape at 15 minute intervals are interpolated in time and a forward-backward trajectory model is applied to parcels initialized at selected positions. The start-up positions are obtained by selecting parcels across the updraft core and within the subsidence regions at 2000 MST. The trajectory model is then run both forwards (to see where the parcel goes) and backwards (to see where the parcel originates).

Admittedly, the time resolution on the history tape is much too crude to do an accurate analysis. However, because the convective motions are very intense and the surrounding motions less temporarily variant, it is hoped that this analysis can still provide some insight not obtained otherwise.

Selected updraft and downdraft trajectories are displayed in Figure 5.18. Like the streamline calculations, the storm movement of 10 m s^{-1} has been removed from the trajectories. It is interesting that the downdraft (or subsidence) forms to the west of the MCS core. The

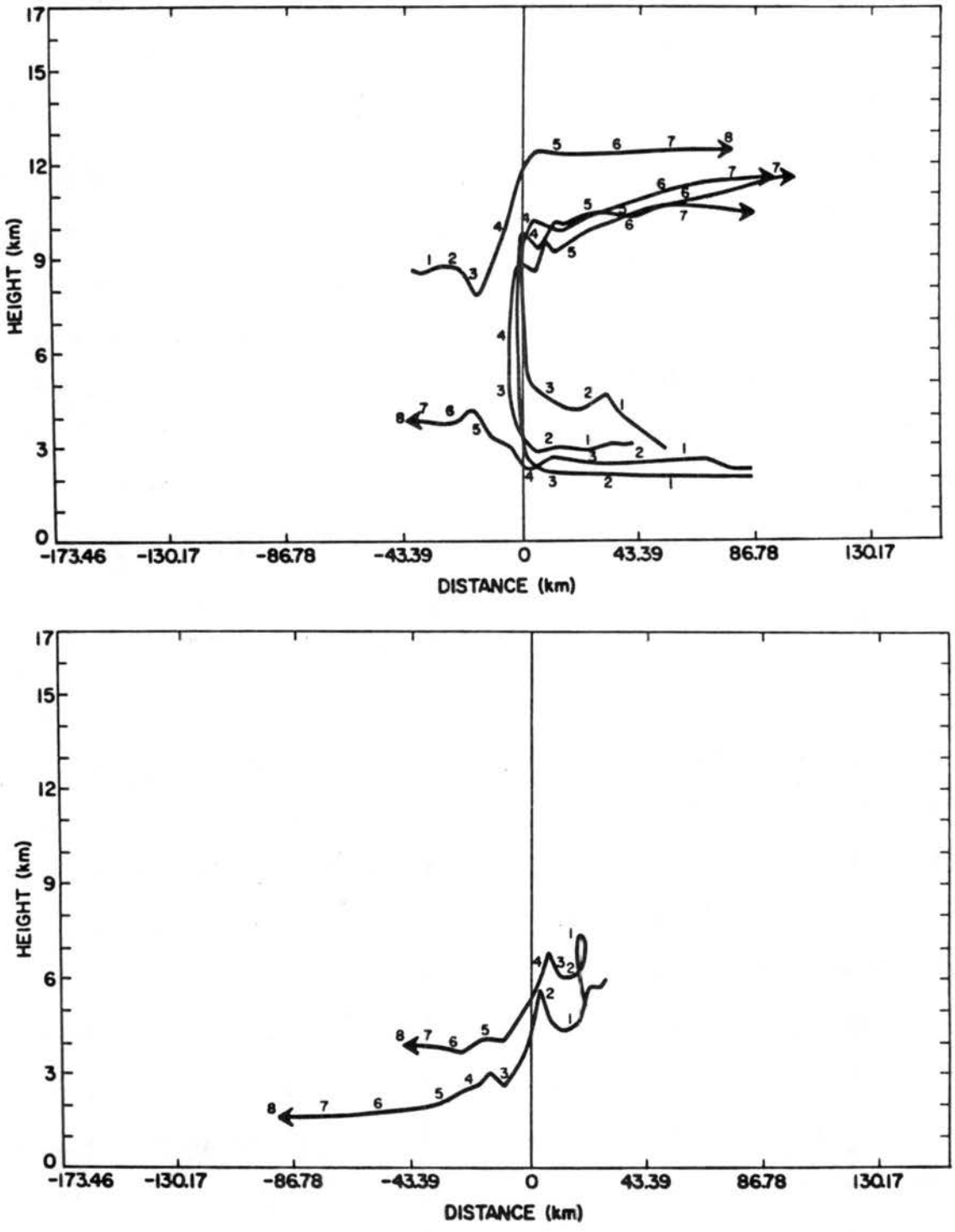

Figure 5.18. Parcel trajectory paths relative to the system core. The system core is represented by the vertical ine in the center of the plot. The horizontal axis is distance from the core center and the vertical axis is height above MSL in meter x 10. The numbered positions along the trajectories represent positions on consecutive 15 minute intervals. Position 4 is at time 2000 MST.

subsidence trajectories seem to be overtaken by the MCS from the front and "shot" out of the rear.

The updraft trajectories were much easier to find. There seem to be three types. The primary updraft trajectories approach from the east at low levels and exit back toward the east at upper levels. It can be seen that at least one of those trajectories was drawn upward prior to actually entering a convective updraft. The second type of updraft is similiar to Knupp's (1985) up-down downdraft component. It approaches from the east, begins to rise in the updraft and then subsides and is exhausted to the storm rear. Unlike Knupp's up-down downdraft component, this trajectory fails to subside to its original inflow level. This is because it is warmer than the air to the storm rear which originates at colder θ_e levels.

The third type of updraft is associated with strong jet-level flow which overtakes the storm and flows over the top. This is somewhat a 2D effect and would likely be lessened in 3D by flow around towers. It has the effect of moving anvil debris further out ahead of the storm than perhaps is realistic. A crude 3D simulation, presented in the next chapter, shows the 3D anvil to extend nearly as far.

Generally, the trajectory flow agrees with the streamflow pattern except for the following. The parcel trajectories indicate cross stream line (and even cross trajectory) flow at the base of the storm. This suggests a turbulent exchange of mass from the moisture-rich boundary layer to the up-branch of the streamflow and a reverse exchange for the downdraft and horizontally constant streamflow near the surface. This is not surprising and is certainly important in order to account for the high-valued θ_e of the up-branch and cool surface air to the west. It is

significant that the cool surface outflow is derived primarily from air parcels ahead of the system. This is contrary to some mid-latitude MCS models, but is consistent with this case where relative flow to the rear only occurs at high levels. Because the air behind the system has been modified by the convection and has been moistened at mid levels, it is especially difficult for it to support a downdraft. The low level structure resembles the tropical squall structure described by Moncrieff and Miller (1976), Gamache and Houze (1982) and others, in that both the updraft and downdraft air approach the system from the front. Unlike the tropical case, however, the system here moves with a mid-level steering wind rather than in excess of all winds. As a result, the anvil extends ahead of the system rather than behind in a tropical structure.

5.5 Spectral Evolution of the MCS

The results thus far suggest that the mesoscale slope circulation initiated an organized field of convective elements which produced a deep tropospheric mesoscale response. The synergistic relationship between convective elements and the mesoscale response led to a propogating mesoscale convective system which moved eastward away from its initial breeding ground. In this Section, the MCS evolution will be viewed in wave space in order to see quantitatively the relationship between meso-γ and meso-β variance.

For the purpose of this analysis, let any spacially varying quantity "A" be represented by the fourier transformation:

$$A = \int A_{l,m} e^{i2\pi \left(\frac{x_l}{L_x} + \frac{z_m}{L_z}\right)} + B_{l,m} e^{-i2\pi \left(\frac{x_l}{L_x} + \frac{z_m}{L_z}\right)} \qquad (5.6)$$

where L_z and L_x are the lengths of the domain in the z and x direction, l and m are the zonal and vertical wave numbers ranging from 0 to NX/2 and form 0 to NZ/2 where NX and NZ are the number of grid points in the x and z direction. The power in each wave number is then related to:

$$|A_{l,m}|^2 = A^2_{l,m} + B^2_{l,m} \quad . \tag{5.7}$$

By contouring $lm|A^2_{l,m}|$ on a l by m diagram, the spectral regions of important wave activity can be identified.

Figure 5.19 is such a diagram for the 1200 MST fields of velocity, pressure, θ and vapor. This represents the period just before significant convection began. Note the absence of significant variance in wavelengths shorter than 200 km in the horizontal (wave number 5). The exception is the w variance which has significant responses centered around 100 km horizontal wavelength and around 5-10 km vertical wavelength.

The preconvective atmosphere, possesses a partially developed solenoidal circulation imposed on a dynamic field containing a mountain wave response. The spectral diagrams indeed show primarily long wavelength variances. The development of a secondary relatively short wavelength peak in the w field is probably indicative of the beginnings of some mountain peak convection. The θ field response centered primarily on wave numbers 1 and 2 in the horizontal and wave numbers 3-5 in the vertical. This response can be attributed to the solar heating of the boundary layer which exhibits a shorter wavelength in the vertical and long wave length (that of the very smooth topography) in the horizontal. The vapor field has a somewhat longer vertical wavelength response. This is because the background vapor field varies

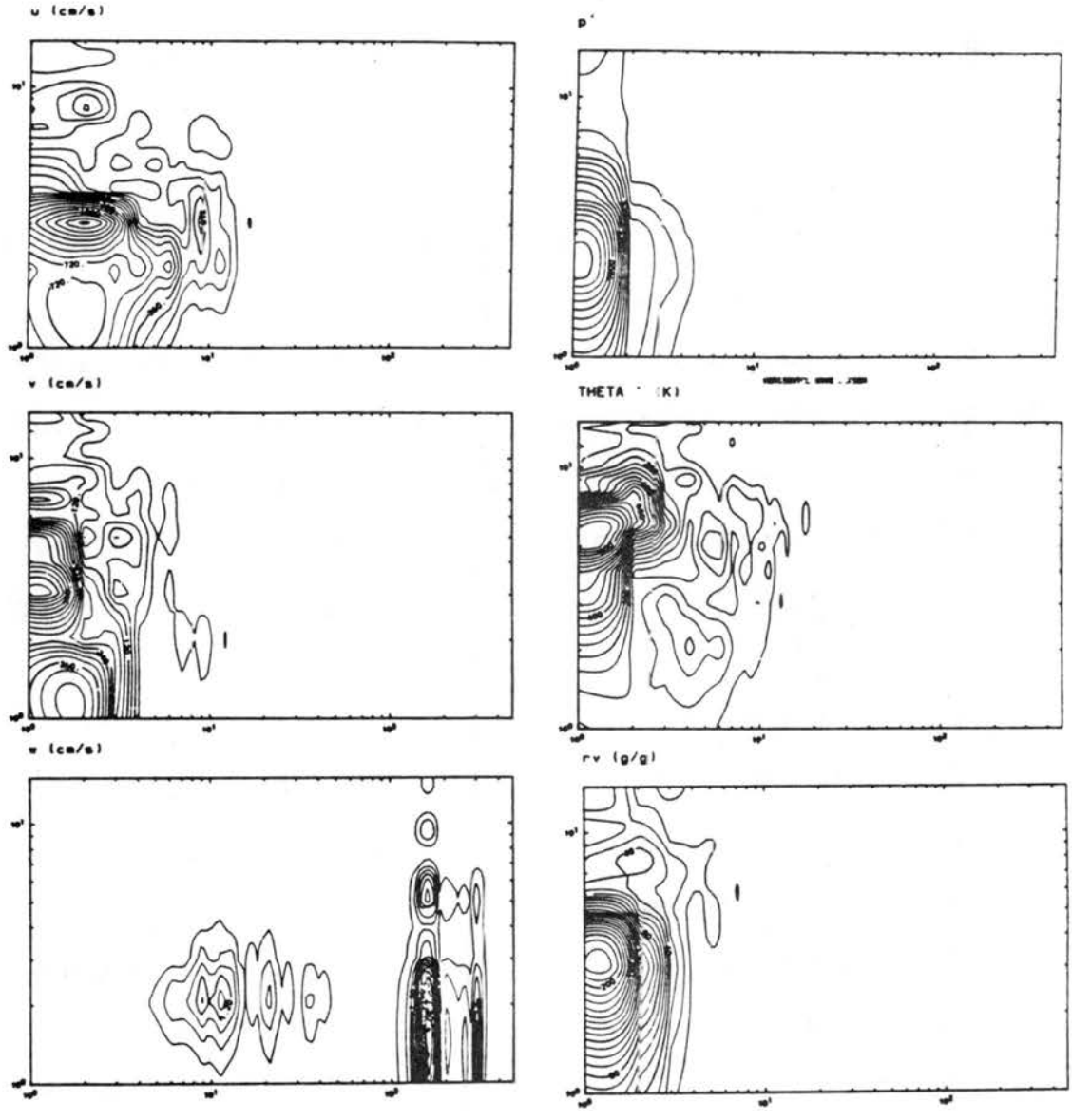

Figure 5.19. Power spectrum of variables fields at time 1200 MST. Contours are of $\ln|A_{l,m}|^2$. Horizontal axis is ln l and vertical axis is ln m. To obtain wavelength, take 1000 km/l for horizontal and 17 km/m for vertical. Contour intervals are 90 cm^2s^{-2} for u, 30 m s^2s^{-2} for v, 0.3 cm^2s^{-2} for w, 200 $dynes^2$ cm^{-4} for p' , 0.02 K^2 for θ' and 10^{-8} for r_v.

more strongly with topography than does θ field simply by the specifications of the initialization.

The u field response is centered around wave numbers 1-3 in the horizontal and represents primarily a solenoidal reaction to θ variance and the mountain wave response.

The v field only responds to the inertial oscillation associated with the ageostrophic acceleration of u. This is reflected in a long wavelength response which tends to look much like that of u. The favoring of longer horizontal wavelengths by v is related to its slow reaction time, causing it to be influenced only by the most persistent u motions.

The simulated spectral response at 2000 MST is depicted in Figure 5.20. This time is chosen to represent the period of most intense simulated mesoscale response. For each spectral plot, the peak variance has increased by over one order of magnitude over the 1200 MST plots. In the case of all fields, except w, considerably more energy resides on wave numbers 1 and 2 in both the horizontal and vertical. This, it seems, is a product of the simulated meso-α response to the convection. It may be significant that, given the predicted mean tropospheric Brunt-Vaisalla frequency of 0.008, the environmental Rossby radius of deformation given by:

$$R = \frac{c_g}{f} \tag{5.8}$$

is about 300 km for a 30 m s^{-1} gravity wave phase speed. This demonstrates that the dominant mesoscale growth is in the vicinity of the Rossby radius of deformation for a tropospheric wave.

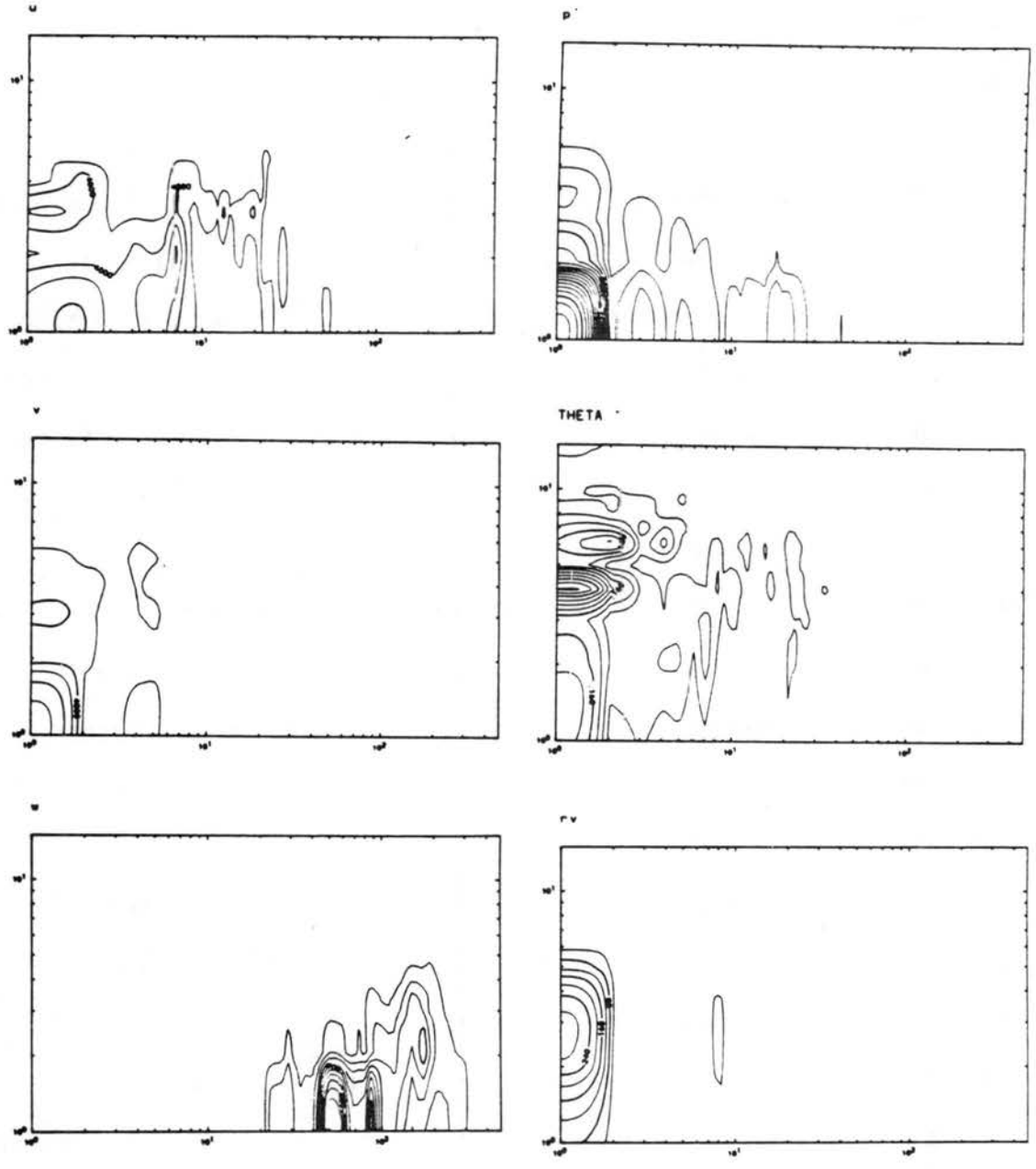

Figure 5.20. Same as Figure 5.19, except for 2000 MST and contour intervals. Contour interval for u and v are 2000 cm^2s^{-2}, for w is 100 cm^2s^{-2}, for p' is 2000 $dynes^2cm^{-4}$, for θ' is 0.04 K^2 and for r_v is 4 x 10^{-8}.

Unlike the other displayed variables, the growth of w variance has been greatest on the shorter wavelength scales of 10-20 km in the horizontal and wave numbers 1 and 2 in the vertical. This w response represents the convective scale motions of individual convective elements. A weak secondary w response is found at a 200 km horizontal wavelength and is associated with the mesoscale wave. This response also is centered at wave numbers 1 and 2 in the vertical. Because of the strong relative growth of the small scale component, this feature does not show up on the energy conservative plots of Figure 5.20, but can be seen on a simple amplitude plot. It should be noted, that although the mesoscale response is considerably weaker than the w convective scale response at 2000 MST, the mesoscale response has itself increased by over 3 orders of magnitude and shifted in emphasis from vertical wave number 2 to vertical wave number 1 and from horizontal wave number 9 (110km) to horizontal wave number 6 (167 km) since the simulated time of 1200 MST.

In conjunction with the growth of the meso-α system, there is a shift in emphasis of energy on longer horizontal wavelengths of wave numbers 1 and 2 (1000-500 km) from vertical wave number 3 and 4 (4-6 km) to vertical wave number 1 (17 km). This shift, most apparent in p', u, v, and θ', represents the growth of the shallow solenoidal circulation to depths of the troposphere. The change is, not surprisingly, most dramatic in the v field which is not responsive to short time scale convection. The vapor field (r_v) has the least shift because of the controlling influence of temperature on the saturation leve of the atmosphere.

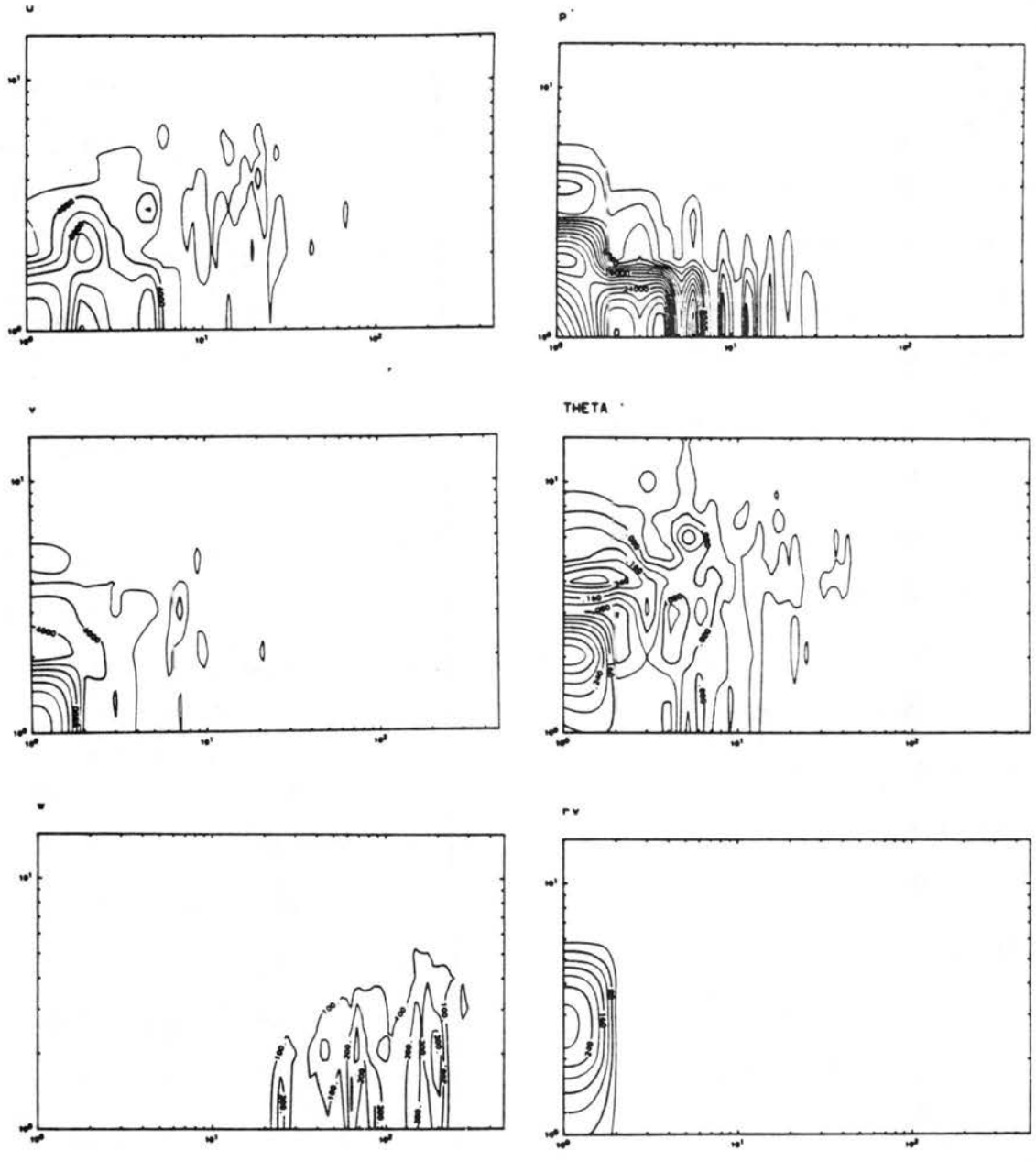

Figure 5.21. Same as Figure 5.20, except for 2200 MST.

By 2200 MST, (Fig. 5.21), there is another clear shift in emphasis to and horizontal wave numbers 5-7 on wavelengths 140-200 km. This is especially evident in the pressure and θ variance and weakly evident in the v variance. This shift is the result of the production of trapped internal gravity wave activity, occurring strongly after sunset. Because these gravity waves have only a minor inertial response, the shift is less clear in the v component. The weakening of the core has resulted in a dramatic weakening of the w variance on vertical wave number 1. This demonstrates the lessening of deep convective elements at this time.

The time evolution of meso-α variance (horizontal wave number 1-4, vertical wave number 1-2) contained in 250 km and larger wavelengths is displayed in Figure 5.22. The strong growth of variance is indicative of the strength of circulations on the meso-α-scale. As expected, v and w undergo the greatest increase in mesoscale strength. It is evident that peak mesoscale variance is obtained near 2000 MST.

The weakening of the w variance at 1630-1730 is a result of the system core encountering the suppression zone in the lee of the Rockies. It is evident also in the u, p and θ which show a lesser effect. The weakest growth is of the p' field meso-α variance, which roughly triples its 1200 value after 2000 MST. During the suppression at 1700, p' variance falls below its 1200 MST level.

The v variance shows a longer time scale of change than the others. Since the only source of v is from coriolis (surface friction), the v component represents the strength of the balanced response to heating. Note its growth until 2200 MST and its subsequent slow decay. It is significant that its peak variance on the meso-α lags that of w by about

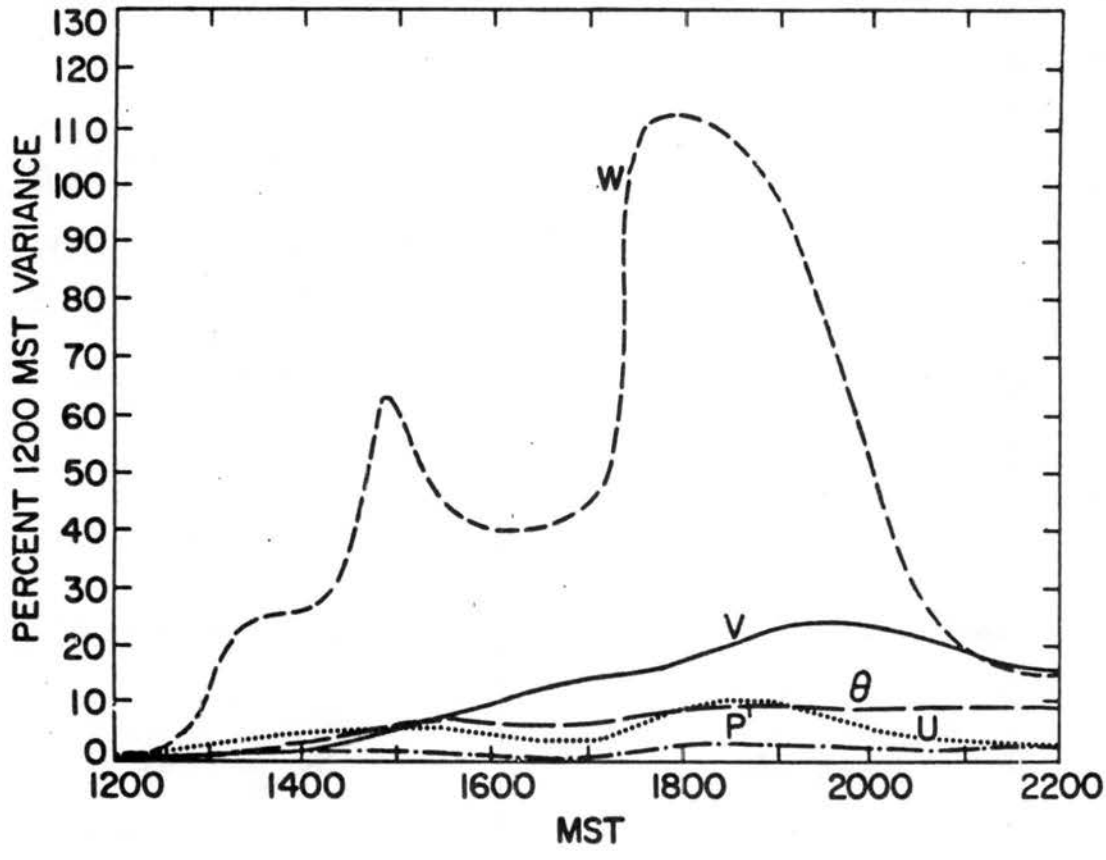

Figure 5.22. Meso-α-scale variance as a function of time. Sum of power in horizontal wave numbers 1-4 and vertical wave numbers 1-2 for variables displayed in Figure 5.19-5.21 (except r_v) as a function of time (horizontal axis in seconds). Power is normalized by power at 1200 (earliest time at plot and beginning of convective activity). Therefore vertical axis is power divided by power at 1200.

2 hours. This suggests that a balance was never obtained with the peak meso-β and meso-γ heating. It is interesting that after the peak meso-α response in v, the decrease in variance of u, w and θ level off. Perhaps the balanced circulation is helping to maintain the circulation after this point.

It is important to note that, although the system begins to weaken by 2200 MST, a high degree of organization is maintained into the night despite the strong weakening of peak updraft (Figure 5.15). This is indicative of the "flywheel" or balance system which builds slowly and weakens slowly.

5.6 Structural Analysis of Mature MCS

In Section 5.3, it was shown that the mesoscale organization reached its peak at the analysis time of 2000 MST. In the previous Section, it was shown that a significant increasingly important percentage of the variance in embedded within the meso-β processes as the MCS matures. Now, the mesoscale structure of the mature system is analyzed on the meso-β scale with regard to both meso-β motions and statistically inferred meso-γ forcing.

In the earlier mesoscale analysis, a running average filter was applied to the variable fields, with an averaging distance of 1 degree longitude or 80 gridpoints or 86 km. The resulting averaged fields represented primarily motions on scales of 100-1000 km, which is a meso-β response. Covariances with respect to this average will depict the contribution of convective scale processes. The averaging technique is chosen in lieu of a fourier band pass filter because of the solitary nature of the mesoscale response and its obvious effect of permanent modification of flow and stability in its wake.

5.6.1 Meso-β structure

The meso-β fields at 2000 MST, shown in Figure 5.10, display a remarkable degree of organization. The system core, coincident with the primary rainshaft at 103 W Longitude, is typified by intense mesoscale uplifting, reaching values in excess of 50 cm s^{-1} over horizontal scales of 80 km. Peak mesoscale upward motion occurs near 8 km or 350 mb pressure. This is a result of horizontally convergent flow over the entire layer below 8 km, even though flow reversal is only found in the lowest 2km AGL. The reversal from easterly flow preceeding the system to westerly flow behind the system at the surface was observed. As was pointed out earlier, the westerly low level flow behind the system is considerably slower than the system propagation. This eliminates the gust front as a likely mechanism forcing system propagation. Divergent flow characterizes the u component above the peak vertical velocity.

The upward branch of the circulation cell forms what appears to be in essence a "classic" MCS signature. A warm θ core has formed at 8 km MSL (350 mb) with relative cooling below (probably from precipitation melting and evaporation), and above (probably from overshooting updrafts and longwave radiational cloud top cooling). The vertically integrated effect of the core temperature regime produces a 0.8 mb high pressure center at 10 km MSL and a 0.9 mb low pressure center at 3.5 km MSL. The low level cooling is weak enough so that relative low mesoscale pressure exists at the surface. The pressure amplitude is somewhat less than observations of this case indicated. The differences are likely due to the existence of stronger cooling in the real atmosphere, possibly resulting from the intrusion of drier air from the west or microphysical considerations. Since the rain parameterization assumes a relatively

large mean droplet size of 0.027 cm, light drizzel type rain may evaporate too slowly, providing less cooling. The differences may also be a bit fictitious, and merely the result of pressure reduction to sea level in the observational analysis. The magnitude of the wind response, on the other hand, seems to be close to the surface observations.

Geostrophic adjustment to the divergent flow aloft and convergent flow below leads to anticyclonic shear aloft and cyclonic shear below. At low levels, the v-component has adjusted geostrophically to a southerly direction east of the system and a northerly direction west of the system. Because of the slow geostrophic adjustment time and because the system is moving faster than the low level flow, the formation of mesoscale northerly flow lags the system by 50-100 km. Maximum meridional flow aloft is separated by 600 km, or about twice the reference state Rossby radius of deformation.

Examination of the θ field shows a warm core system with the maximum temperature anomaly of 2-3 K at about 8 km MSL (approximately 350 mb) coincident with the mesoscale upward motion core. To the west, strong local subsidence extends much of the heating downward while to the east the effect is lessened because of the effects of precipitation advected ahead of the system. The warm core extends (within the lower anvil) to the east of the core. Examination of heating effects, presented later, show that this warming is forced locally by longwave warming and perhaps by some continued latent heat release by growing ice crystals.

Because the mesoscale response is less transient than the convective scale motions, it is these features that are likely to appear

in a composite of a MCS based on a large number of independent observations. Figure 5.23 displayed the MCC composite structure found by Maddox (1981). The similiarity to the simulated MCS structure in Fig. 5.10 is striking. The temperature anomaly aloft of 2-3 K is reproduced by the simulation at the composite height, the outflow and v shear pattern is reproduced, and the accompanying pressure pattern. The simulated low above the surface was not found by Maddox, however more recent composites by Lin (personal communication) reveal its existence. Moreover the scale of the flow is nearly the same in the simulation and the composite observation.

5.6.2 Moist static energy budget

The warm MCS core is maintained through the vertical transport of moist static energy and the diabatic effects of radiative transfer. This study offers the rare opportunity to calculate explicitly the heat transport by meso-β compared to meso-α motions in a numerical simulation. Previous studies have relied on either convective parameterization or explicit microphysics to depict heating on the mesoscale. In order to justify a convective parameterization, the assumption of a clear scale separation between resolvable and convective scale must be made.

Such an assumption infers that the convective heating is contained within the grid volume over which the parameterization is applied. Emanuel (1983) shows that convection induced subsidence occurs on scales less than the Rossby Radius, which is shown to be near 300 km for this case. Clearly this exceeds the grid resolution of many mesoscale models.

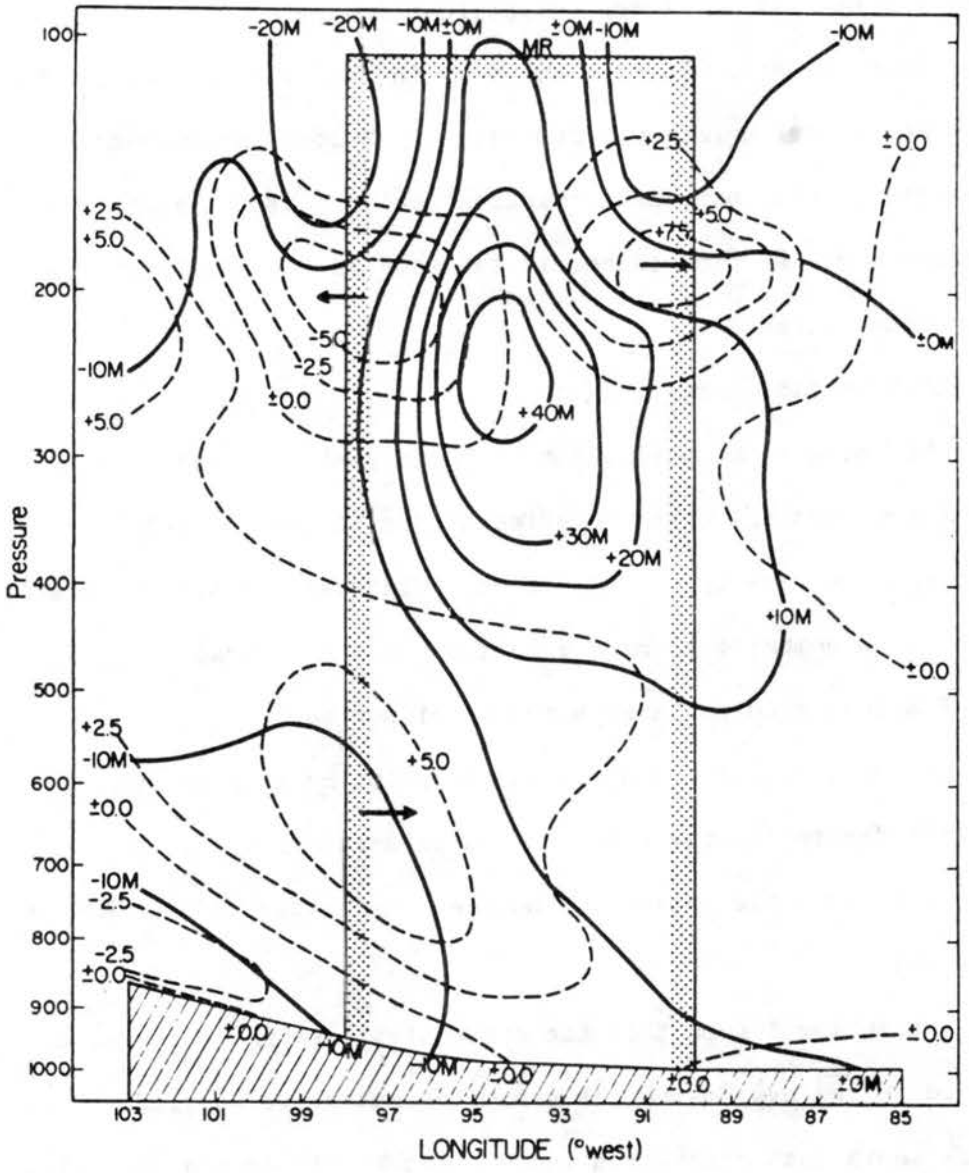

Figure 5.23a. West to east cross-section of mesoscale height (solid lines, in m) and u-component (dashed lines, in m s^{-1}) perturbations at the time of the MCC. (From Maddox, 1981).

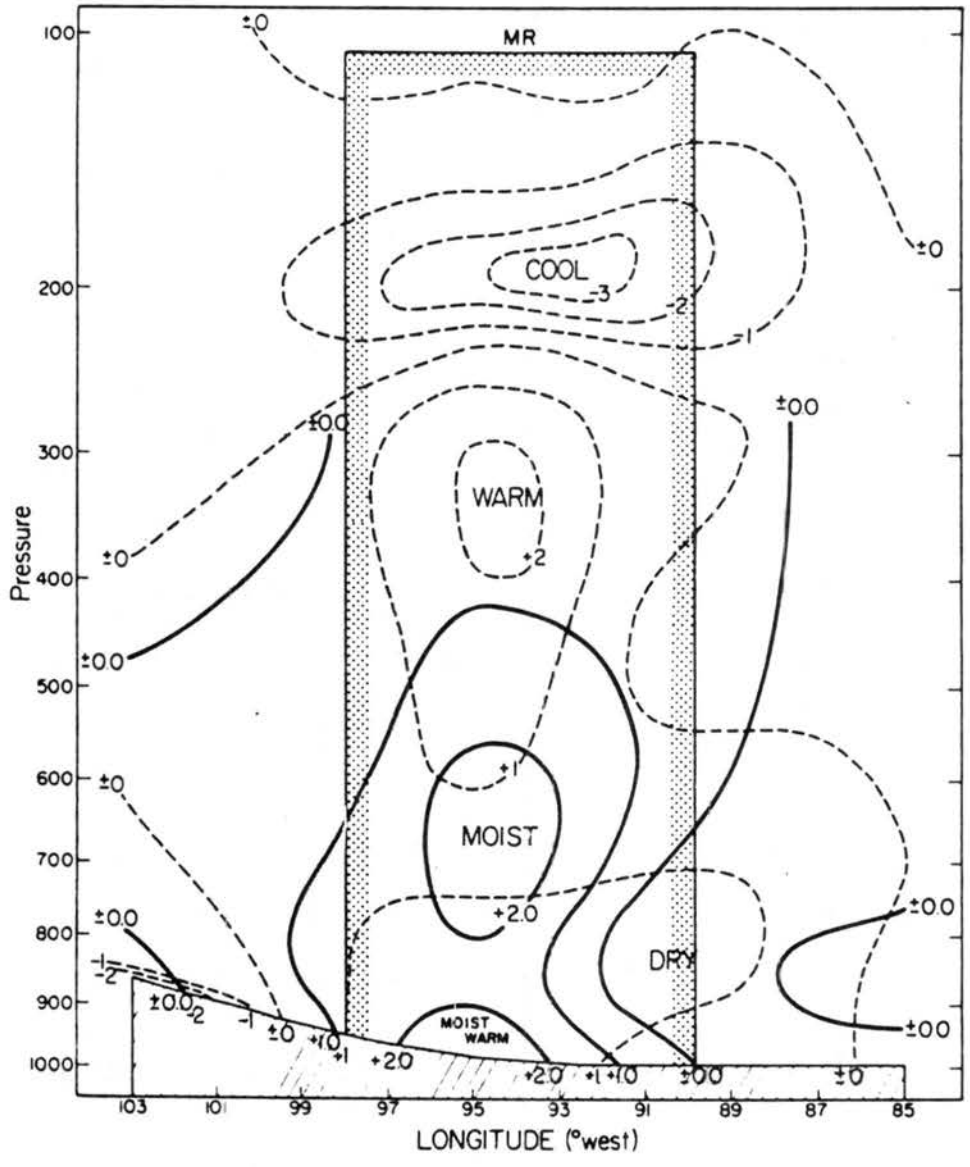

Figure 5.23b. West to east cross-section of mesoscale temperature (dashed lines in ^{o}C) and moisture (solid lines, in g/kg) perturbations at the time of the MCC. (From Maddox, 1981).

In this section, the scales and degree of convective heating within the control simulation will be explored. This will be accomplished by dividing the heating into a meso-β and meso-γ scales. In concert with the averaging scale of 80 km, used throughout this study, heating will be divided into that accomplished by the 80 km scale (meso-β) motions and that by the 2-80 km scale motions (meso-γ). This approach will display the heating rates that a parameterization for a 80 km grid scale should depict and test the validity of scale separation. The relative roles of radiative heating will also be viewed.

The moist static energy can be written:

$$h = \rho_o C_p T + \rho_o g z + \rho_o L_{iv} r_v \tag{5.9}$$

where $\rho_o C_p$ is the base state density, c_p is the specific heat at constant pressure, T is tha air temperature, g is the gravity acceleration, z is the height above the surface, L_{iv} is the latent heat of sublimation and r_v is the vapor mixing ratio. Because of the importance of the ice phase in this study, latent heat of sublimation more appropriately depicts latent energy than simply latent heat of condensation. The moist static energy may be expanded as:

$$h = \langle h \rangle + h'' = h_o + \langle h' \rangle + h'' \tag{5.10}$$

where the brackets are a meso-β averaging operator (80 grid points in this application), subscript "o" refers to the model domain average (meso-α scale), h' is the deviation of the meso-β average from h_o, and h'' is the deviation of a local h from $h_o + h'$. Then, it follows:

$$h = \rho_o c_p(\theta'' + \langle \theta' \rangle) + L_{iv}\, \rho_o(r_v'' + \langle r_v' \rangle) + h_o \quad . \tag{5.11}$$

The local tendency of moist static energy can then be expressed as:

$$\frac{\partial h}{\partial t} = -[w(h'' + \langle h' \rangle)]_z + Q_3 - wh_{o_z} + H \qquad (5.12)$$

where H represents horizontal transport terms and Q_3 represents the radiative tendency. Diffusion terms are dropped for convenience. Now average over a meso-β scale:

$$\frac{\partial \langle h \rangle}{\partial t} = -\langle w''h'' \rangle_z + (\langle w' \rangle \langle h' \rangle)_z + \langle Q_3 \rangle - \langle w \rangle h_{o_z} + \langle H \rangle$$

$$= -[\rho_o c_p \langle w''\theta'' \rangle + L_{iv}\, \rho_o \langle w'' r_v'' \rangle]$$

$$+\rho_o c_p \langle w \rangle \langle \theta' \rangle + L_{iv}\, \rho_o \langle w \rangle \langle r'_v \rangle]_z$$

$$+\langle w \rangle [\rho_o c_p \theta_o + L_{iv}\, \rho_o r_{v_o}]_z + \langle Q_3 \rangle + \langle H \rangle \quad . \qquad (5.13)$$

where the bracket refers to a meso-β 80 point average (80 points is 86 km or 1 degree longitude). The first two terms on the right hand side represent the transport of moist static energy by meso-β convection, the second two terms are the transport meso-β temperature and relative humidity perturbations by the meso-β motion field and the third two terms are the transport of reference state moist static energy by meso-β motions. Presumably, over a meso-α average, the average of the second two terms would represent the role of meso-β motions while the third two terms would likely vanish as $\langle w \rangle$ becomes very small. A comparison of the magnitudes of the flux quantities involved in the first four terms will then demonstrate the relative importance of the meso-γ and meso-β components to the vertical transport of moist static energy.

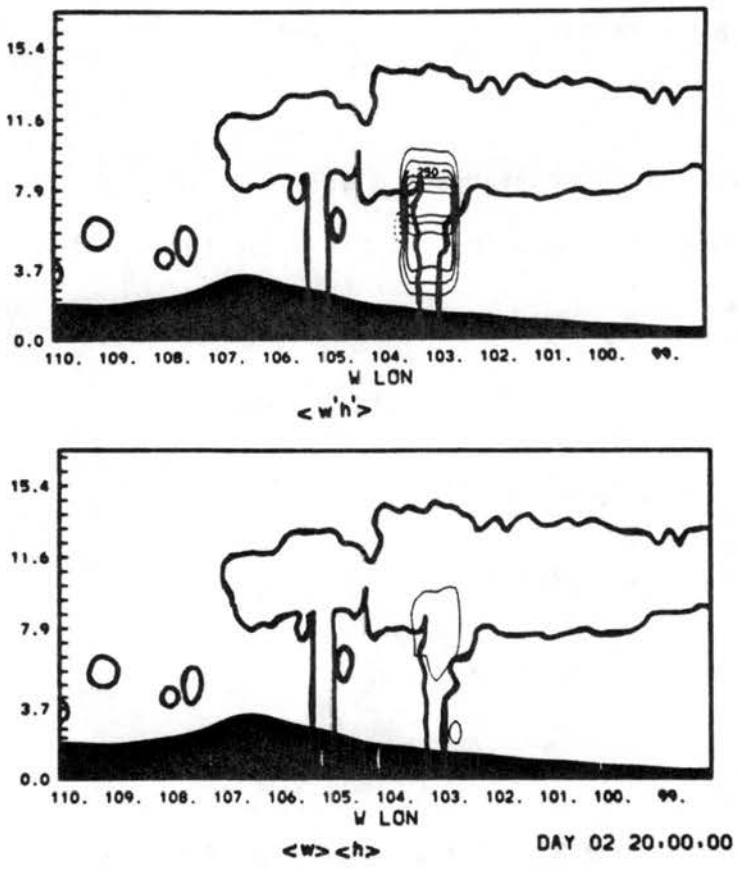

Figure 5.24. Fields of vertical heat flux of meso-γ and meso-β components at 2000 MST of control case. Contour intervals are 0.10 kg $cm^{-2}s^{-1}$. Vertical and horizontal axis, cloud outline and topography are as in Figure 5.1.

The meso-β transport cannot be directly translated into a true local heating rate because horizontal divergence will likely compensate for much of vertical convergence of heat. In addition, the interaction of the vertical motion with the horizontally averaged "base state" part of the potential temperature and vapor can actually lead to the opposite temperature tendency indicated by the perturbation transports. Because the meso-α (domain scale) average vertical motion is relatively small (streamlines indicate very little net net flow divergence), these effects will not lead to a large meso-α scale heating. The meso-β term is computed to demonstrate the variation of heating as a function of horizontal scale for the purposes of finding a simulated scale separation and justification for cumulus parameterization.

The meso-γ and meso-β fluxes of moist static energy at 2000 MST are displayed in Figure 5.24. It is most notable that all of the significant vertical transport is concentrated in a narrow region coincident with the system core. Despite the existence of an extensive anvil and a secondary rainshaft, there is no significant vertical transport outside the primary region. The comparison of the meso-γ and meso-β fluxes show that although the meso-γ fluxes clearly dominate, the meso-β contribution is at least on the same order and tends to be in the same direction.

The convergence of the vertical fluxes, related to the heating rate, is displayed in Figure 5.25. Heating rates up to 497 K day-1 are obtained as a net result of the convective motion field. The meso-β heating, on the other hand, is considerably less at this time, reaching peak magnitudes of less than 100 K day-1. Again, virtually all of the

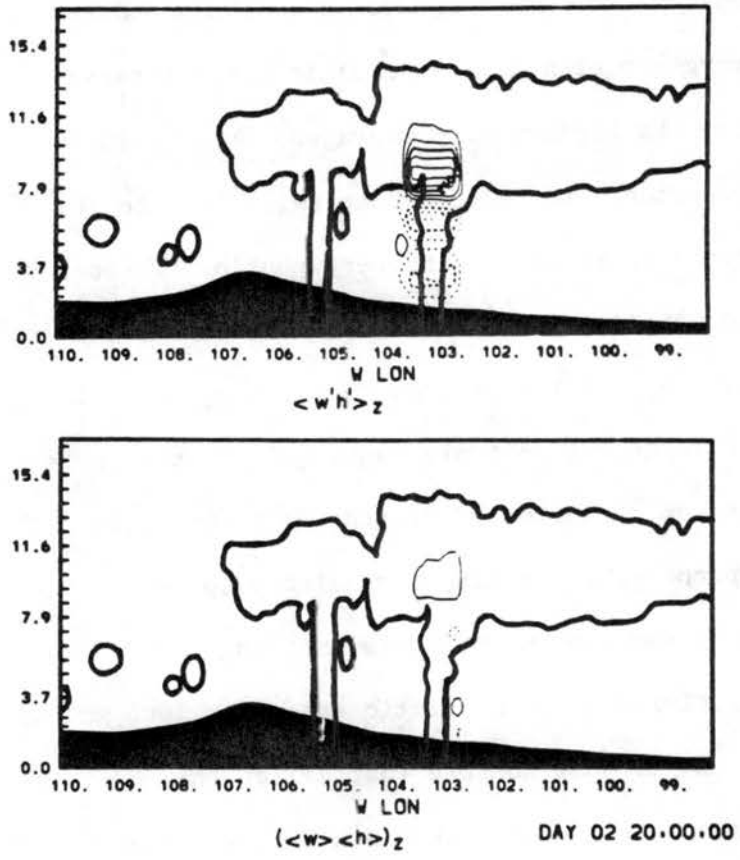

Figure 5.25. Same as 5.24, except convergence of the fluxes. The values are normalized by ρ_o cp 86400 to put in unites of temperature tendency per day. Contour intervals are 100 K day^{-1}.

heating is concentrated in the vicinity of the system core, at vertical levels just below the tropopause.

Since the 2000 MST analysis time is the time of peak intensity, it is desirable to find a more typical heating rate. This can be obtained by time averaging several of such computations over a period of varying system intensity. Figure 5.26 displays the vertical profiles of meso-β and meso-γ vertical heat transport for a horizontal average centered at the system core, and 80 gridpoints to the left and right of the core, and also for a horizontal mean of all contributions. These depictions represent an average of 5 model times spaced by 15 minutes and centered at the 2000 MST analysis time. It is obvious that the high meso-γ heating rate displayed in Figure 5.25 is anomalous and exceeds the hour mean by nearly a factor of 4. The meso-β heating, on the other hand, is less than but still within a factor of two of the meso-γ rate. This demonstrates that the meso-γ heating can fluctuate quite strongly over the period of an hour. Moreover, the mean meso-β heating rate is very close in magnitude to the mean meso-γ rate. These results draw a picture of a relatively steady meso-β heating rate with a superimposed strongly fluctuating meso-γ heating.

It is significant that there is no clear scale separation between the convective and mesoscale, ie almost 50% of the heating comes from motions on the scale of 80 km. The implications of this on the ability to parameterize such heating could be serious.

Although the magnitudes of heating seem to be similiar between the two arbitrary scales, the profile differs subtlety. In particular, the convective scale heating is concentrated at 8 km MSL while the meso-β heating is concentrated higher at near 10 km, where it exceeds the

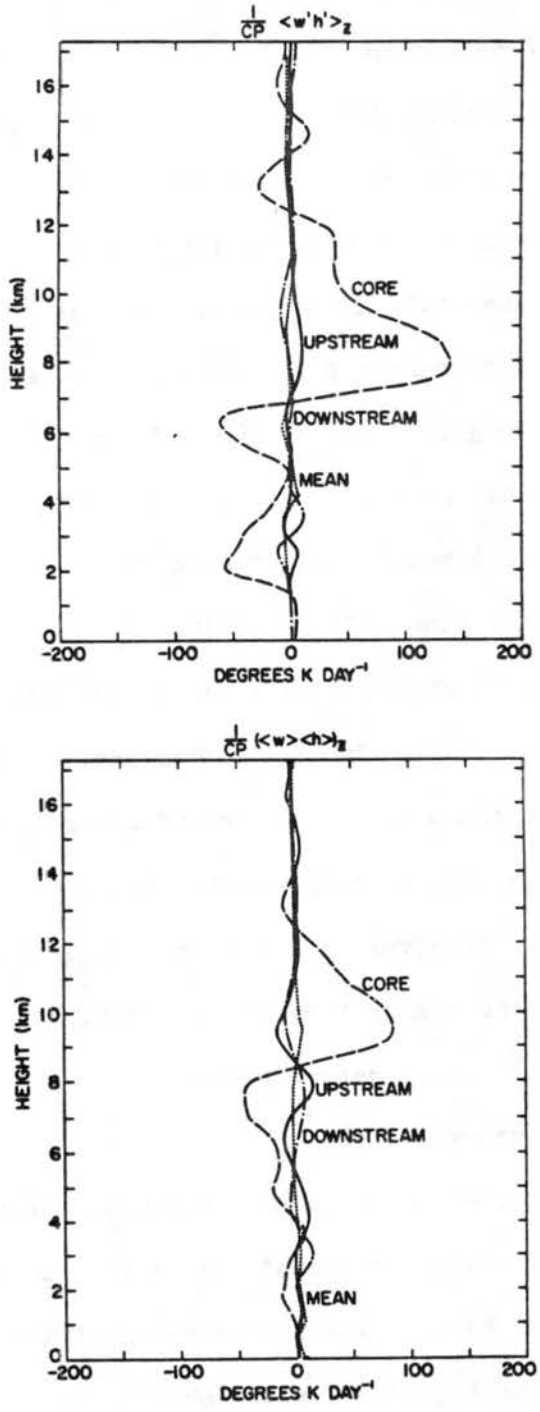

Figure 5.26. Vertical profile of meso-β and meso-γ heating (Figure 5.25) averaged over one hour and at four locations. The locations are (a) the system core, (b) 80 grid points left of the core, (c) 80 grid points right of the core, and (d) the horizontal mesn of all positions. Vertical axis is height (MSL) and horizontal axis is heating rate.

convective heating to a considerable degree. This feature seems to be consistent through the different analysis times, and there is a similiar feature in the momentum transport reported later.

The difference likely arises from a basic difference in the nature of the heating. It seems that at the top of the updraft, there is a tendency for the warm core to spread laterally as the vertical motion decelerates. This forces a greater portion of the temperature anomaly into the meso-β mean and emphasizes meso-β heating. Below, the updraft towers are narrow and the heating is primarily realized as a meso-γ process. The result is that the maximum meso-γ heating rate is considerably below the level of the peak updraft intensity.

As must be the case, the heating aloft is balanced by a loss at low levels. The rates are not area conservative in Figure 5.26 because the rates are normalized by inverse density so they can be expressed as a temperature tendency. It is interesting that the convective scale tends to deplete the moist static energy near the surface (the surface is at 1.5 km MSL) while meso-β motions seem to dry levels primarily above the boundary layer. The explanation can be seen by comparing the computed trajectories of motion to the mean streamline flow. The mean streamline flow indicates that most of the flow below 1km is actually passing under the system in the mean. However, trajectories reveal that much of the updraft motion actually comes from this layer. This means that convective scale motions cross the streamlines injecting the moist static energy into the system. The meso-β transport, on the other hand, occurs through the meso-β circulation which emphasizes the above inversion entrainment.

The advective heat transport is primarily within the updraft, although the warming is transmitted laterally and vertically by the propagation of gravity wave fluctuations. The impact of the heating can be found deep within the stratosphere, especially to the west of the system, in Figure 5.10. There is no reason to believe that the feedback, from the stratosphere, to the mesoscale dynamics is unimportant.

Figure 5.27 also depicts the regions of subsidence 80 km to the left and right of the system core and the average across the entire domain. It can be seen that even in the most active subsidence regions, the heating rates are but a fraction of the core tendencies for both the meso-β and meso-γ vertical transport terms. The meso-β tendencies clearly dominate this heating in this region, as might be expected. It is interesting that the transport tends to be of the opposite sign in these regions. This shows that the compensating motions are transporting the heat back downward.

The domain average heating reflects the transport in the system core. This confirms the notion that the great majority of heating is occurring in a rather small region. The combined heating rate is on the order of 10-20 K day-1 aloft. This is roughly of the same order as the radiational heating rate described below.

Of course, it must be emphasized that effect of the base state vertical gradients, not addressed here, will likely dominate the actual temperature change. The transports described here, are responsible for the net vertical transmission of latent heat from below to regions aloft. In doing so, some of the energy will be consumed in driving the mesoscale circulation. Much of the heating will ultimately become

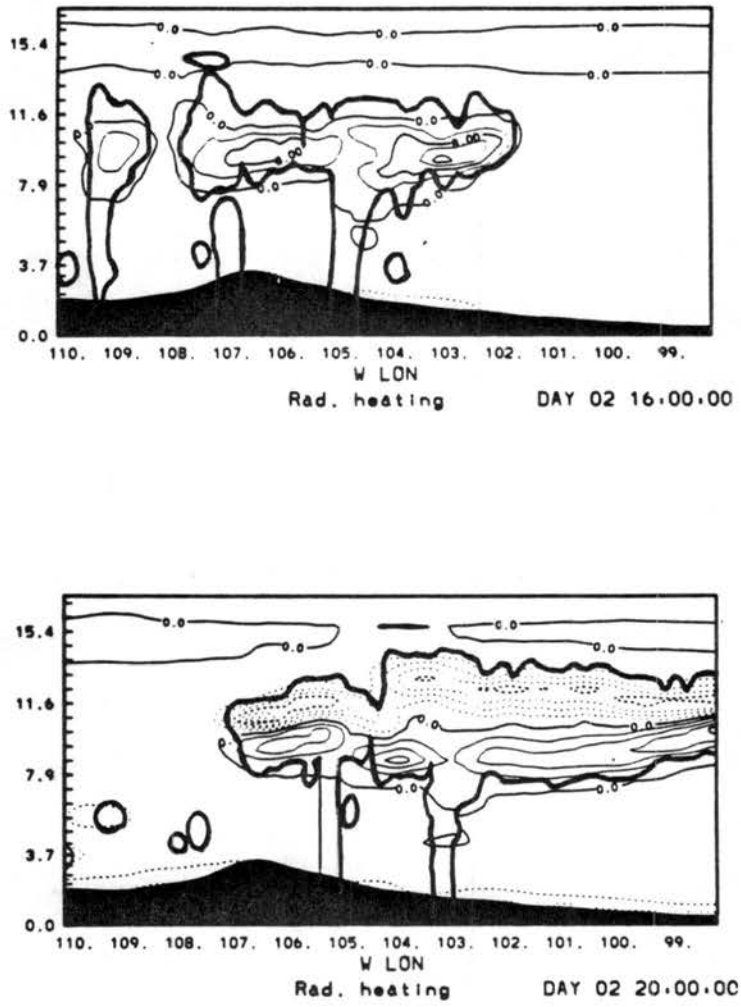

Figure 5.27. Same as 5.25, except radiation heating tendency at 1600 and 2000 MST. Contour intervals are 4 K day^{-1}. Negative contours are dashed.

internal gravity wave energy and be transmitted laterally and aloft through the stablely stratified atmosphere.

The radiation heating, Q_3, is also critical to the overall heat budget. Figure 5.27 depicts the magnitude of this term over the domain at 1600 and 2000 MST. Note that the radiative tendency is to warm the lower regions of the anvil during both the day and night. The upper layers of the anvil are cooled strongly (16 K day^{-1} at night and weakly (< 4 K day^{-1}) during the day. The difference arises from the shortwave absorbtion during sunlight hours. An important effect downwind of the system core is the destabilization of the anvil layer, which is especially strong as the sun sets. This can be seen in an analysis of the Brunt-Vaisalla frequency, displayed in Figure 5.28. Note the region of anomalously low stability within the anvil, likely resulting from the radiative effects. As the shortwave absorption subsides into the night, this effect will likely increase. The result of the destabilization of the anvil layer, is that an effective channel is formed whereby deep propagating internal gravity wave nodes, formed by the convective activity , can be effectively trapped below the anvil level allowing the activity in the convective core to spread laterally. The vertical motion analysis mentioned in the previous section quite clearly shows this effect. Viewing Figure 5.11 (w field), the gravity fluctuations to the east of the core are stacked vertically and cut off sharply above the anvil. To the west, as the fluctuations pass into the airflow without the radiatively induced wave channel effect, the waves tilt vertically upward toward the west and propagate to the model top.

The impact of radiation to the system core dynamics is not obvious from this analysis. As mentioned in Section 5.4, the oscillation of the

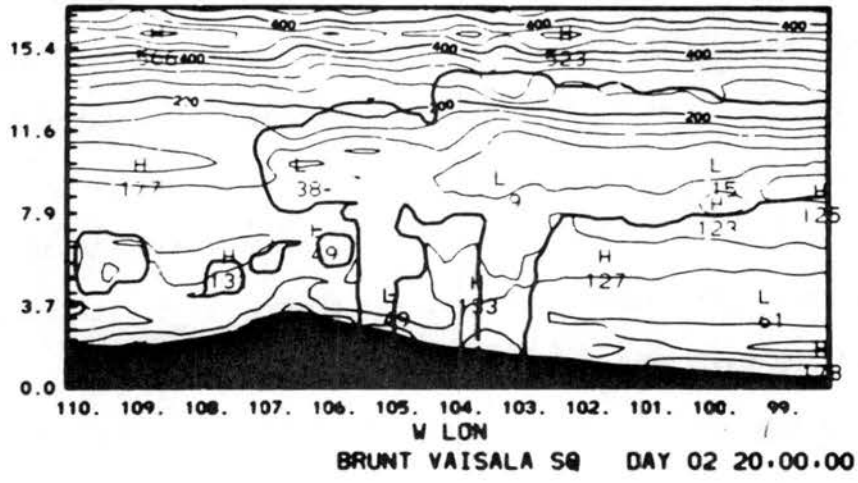

Figure 5.28. Brunt-Vasaillia frequency squared at 2000 MST. Contour interval is 50 s^{-2}. Vertical and horizontal axis, cloud outline and topography are as in Figure 5.1.

vertical motion at the system core coincides with intensity of the updrafts in the individual cumuli and the oscillation is part of the horizontally propagating gravity wave train. Whether the strength of the oscillation, and thus the intensity of the system will be affected through radiative effects by the attenuation of waves moving laterally from the core is unknown. Besides the wave channeling effects, destabilization of the anvil layer may act to increase system intensity by the effect of a cooling aloft. The increased anvil precipitation and possible net cooling may amplify the mean circulation through its reflection on the low level pressure field. The impact of radiation will be addressed in Chapter 7 by removing its effect and seeing how the system behaves as a result.

In summary, heating terms affecting the vertical redistributiuon of mean moist static energy were analyzed. It was found that the meso-beat and meso-γ components were of a similiar order but represented somewhat different processes. The radiative heating rates were substantially lower than the local vertical transport rates, but on the same order as the meso-α average of the transports. The anvil top heating by radiation and transport, roughly compensate each other. Finally, there is evidence that the effects of the radiative heating might also directly enhance the dyanmics of the mesoscale system.

5.6.3 Momentum budget

The processes responsible for the acceleration of air motion is now investigated. There are two subjects of interest, namely the acceleration of local mesoscale flow fields and the effect of the system dynamics on the zonal mean flow. Acceleration of zonal momentum occurs by pressure, coriolis and transport processes. Pressure forces, however

cannot produce acceleration of the mean flow. Because of the two-dimensional framework of this study, meridional acceleration will not be affected by a local meridional pressure gradient. However, a geostrophic base state meridional pressure gradient is implicit.

The accelerations by vertical momentum transport, pressure gradient and coriolis are displayed in Figure 5.29 and 5.30 for u and v respectively at the 2000 MST analysis time. Most evident is the dominant role played by the local pressure acceleration to zonal velocity. The meso-γ and meso-β accelerations are separated as in the previous Section for moist static energy. In addition, local transport of the mean shear flow is displayed. From this analysis, it is strongly evident that the acceleration of zonal momentum is dominated locally by pressure acceleration which reaches peak accelerations larger than transport and coriolis by nearly a factor of 4.

The acceleration by vertical transport meso-β and meso-γ scale acceleration terms are dominant in the region of the system core. Since, as was found with the heat budget, the 2000 MST peak intensity period is anomalously strong, the 1 hour mean vertical momentum transport acceleration profile is displayed in Figure 5.31. Note that peak accelerations remain near 0.2 $cm^2\ s^{-2}$. The maximum westerly acceleration is between 8 and 11 km MSL which is the lower half of the upper level westerly jet. Easterly acceleration is produced below. The vertical profiles of vertical zonal momentum flux, displayed in Figure 5.31, show that the accelerations are produced by a downward down gradient flux between 4 and 7 km MSL and an a upward up-gradient momentum flux between 7 and 11 km MSL. The behavior of these fluxes

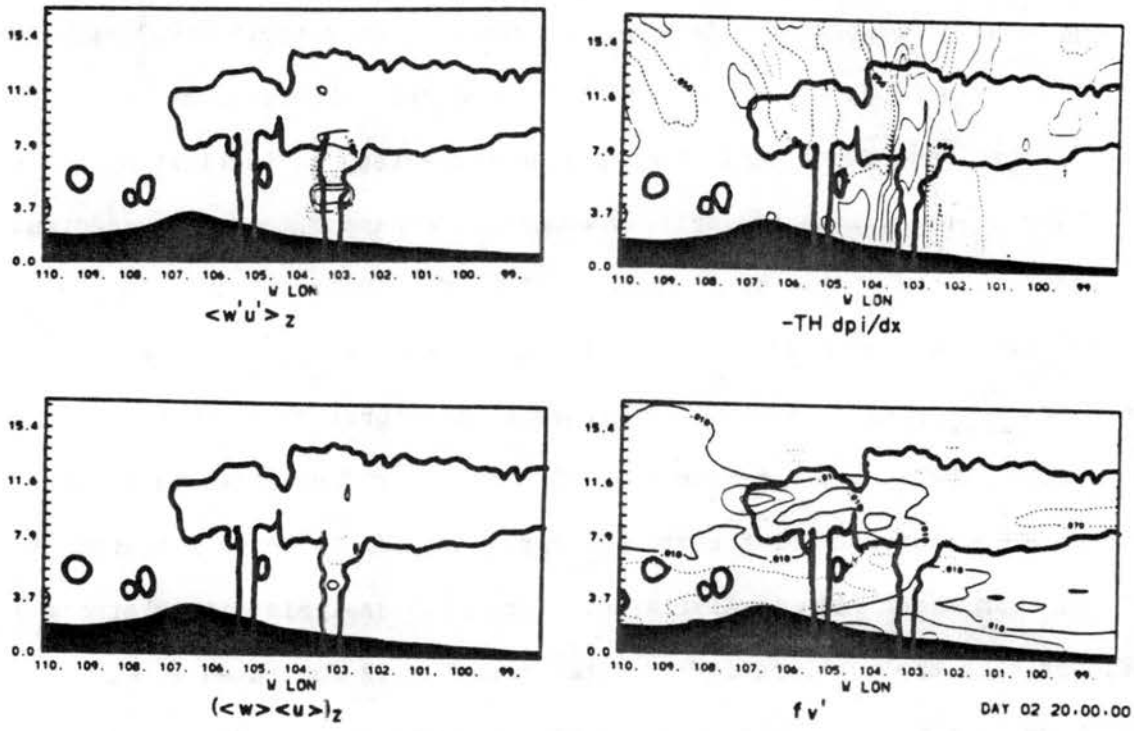

Figure 5.29. Terms in u equation for meso-β-scale accelerations as labeled for 200 MST of control case. Contour intervals are 0.2 cm s^{-2} for $\langle w'_2 u'' \rangle_z$ and $(\langle w' \rangle \langle u' \rangle)^2$, 0.02 cm s^{-2} for fv' and 0.1 cm s^{-2} for pressure gradient. Negative contours are dashed. Vertical and horizontal axes, cloud outline and topography are as in Figure 5.1

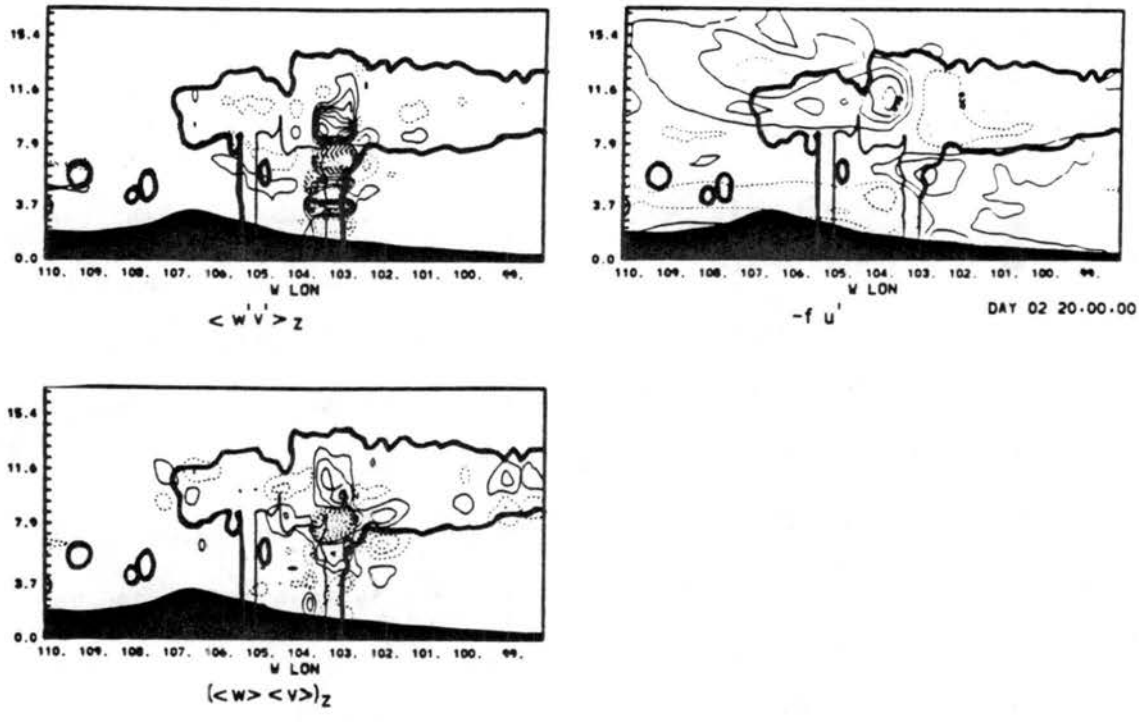

Figure 5.30. Same as Figure 5.29, except for v equation. Also, contours of $(\overline{w'v'})_z$ are at intervals of 0.02 cms^{-2}.

indicate that the flow is tilted upshear with height below 7 km and downshear with height above 7 km to 11 km MSL.

A comparison of the meso-β and meso-γ components reveal the transport is of comparable magnitude for both scales. As with the vertical heat transport, the meso-β component peak fluxes are shifted upward by approximately 1km. This again seems to indicate a shift in energy from small to larger horizontal wavelengths in the upper levels of the storm. This is, of course, a fundamentaly non-linear process.

The domain average vertical transport of zonal momentum, also displayed in Figure 5.31 shows a peak acceleration of only about 10-2 cm2s-2. This is clearly insufficient to have a serious impact on the domain scale momentum budget. It is likely that the net acceleration aloft comes from pressure forces. Although pressure cannot create net zonal momentum in a closed domain, it can increase net zonal momentum within this limited area domain with open boundaries. This is accomplished by the existence of a pressure gradient across the boundaries. Such a gradient arises through the resistence to free acceleration at the lateral boundaries imposed by the mesoscale compensation region. This is quite analogous to the feedback that would be expected from larger scales.

The affect of the coriolis acceleration, which is nothing more than an inertial oscillation of the ageostrophic wind, is to oppose the pressure-induced acceleration aloft and near the surface. On the scale of the MCS core, the pressure gradient clearly dominates and a geostrophic balance is not evident. Beyond 200-300 outside the convective core, the pressure gradient and coriolis forces reach comparable magnitudes and appear, at least in a gross sense, to be

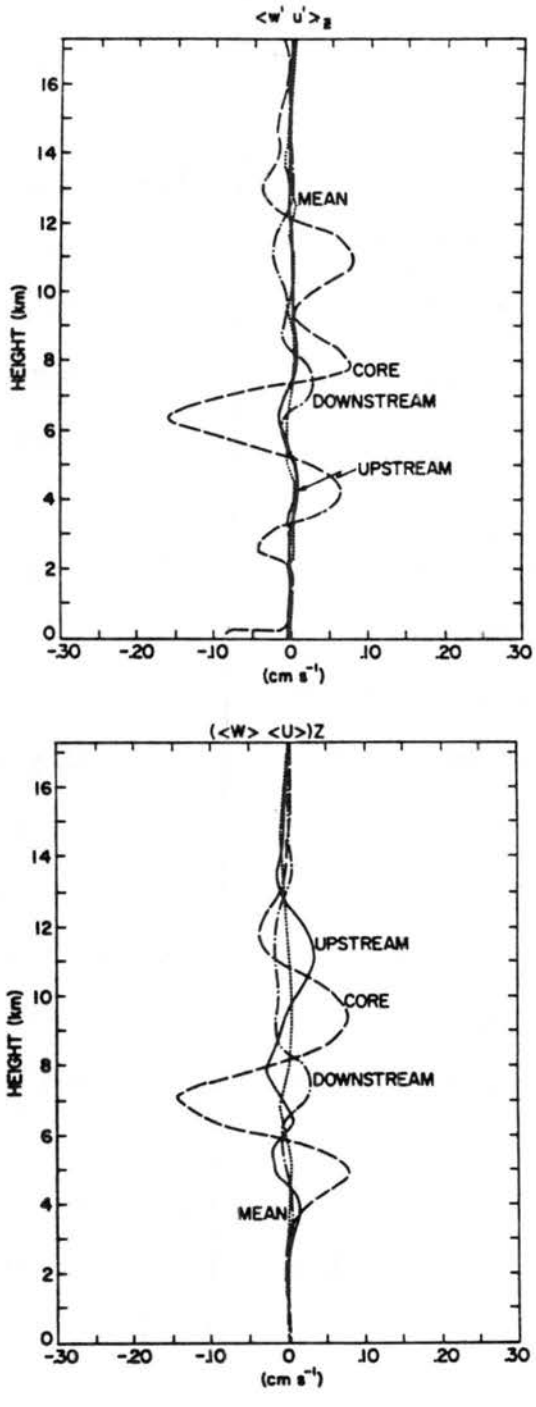

Figure 5.31. Same as Figure 5.26. except for vertical convergence of zonal momentum transport.

somewhat compensatory. This is consistent with the scale of the Rossby radius of deformation which is about 300 km for this case.

Terms affecting the acceleration of v are given in Figure 5.30. In this case, local pressure gradient acceleration is neglected and the coriolis acceleration clearly dominates the acceleration on the domain scale. Locally, vertical transport is important, however. The primary action of vertical transport seems to be the transport of relative southerly momentum from below into the upper storm levels. This implies a meso-β and meso-γ updraft sloped upward toward the north. A possible effect of the meridional transport might be to aid in zonal momentum transport through eventual geostrophic adjustment. In view of the weak magnitude, this is unlikely to be important.

Vertical motion is affected primarily by local accelerations produced by an imbalance between buoyant motions associated with a local density anomaly and the local vertical gradient of perturbation pressure. The magnitude of the mesoscale w acceleration by hydrostatic inbalance is given in Figure 5.32. It can be seen that the w acceleration is primarily at the base of the updraft while the deceleration is aloft within the updraft.

This is typical of the growing phase of the MCS. During a weakening phase, not shown, the tendency is for deceleration at all levels with upward w acceleration displaced laterally from the updraft where compensating subsidence was centered.

It is interesting to view the behavior of the non-hydrostatic acceleration on the meso-β where many modellers choose to assume such a balance. The simulated hydrostatic balance is always within about 2 orders of magnitude on the meso-β scale. As with smaller scales, the

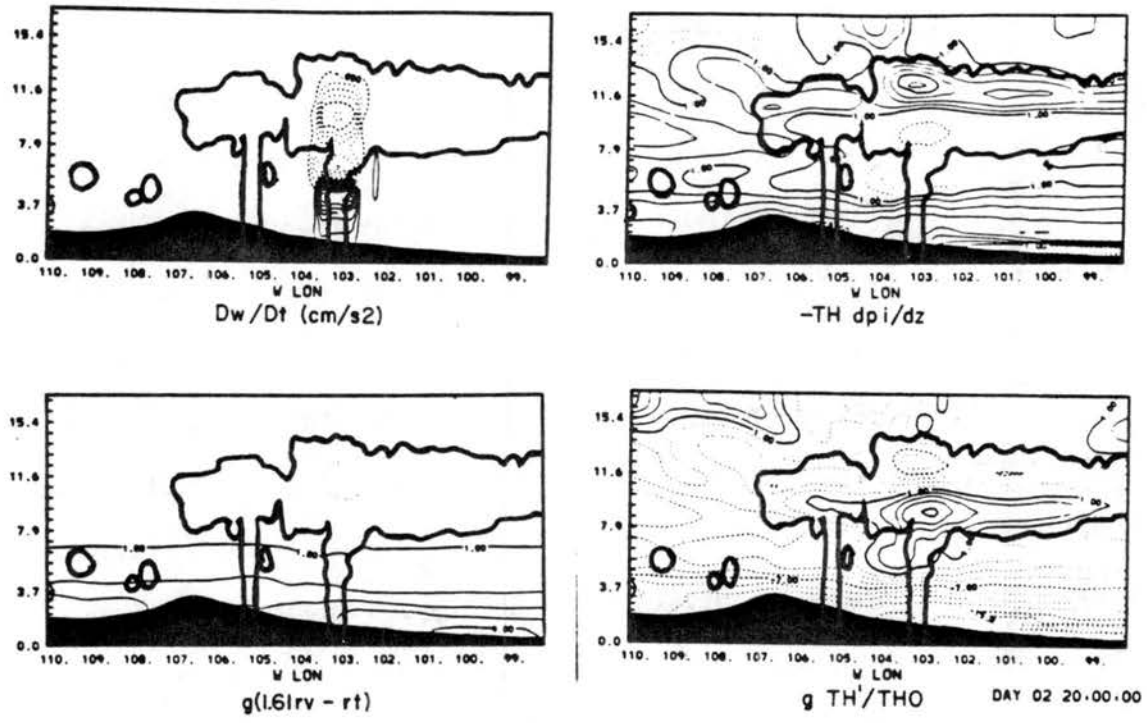

Figure 5.32. Same as Figure 5.29, except for Dw/Dt term in w equation and the three components which comprise it. Contour intervals are 0.1 cms^{-2} for Dw/Dt, and 2.0 cms^{-2} for all others. Negative contours are dashed.

nonhydrostatic acceleration is acting to brake the vertical acceleration of the meso-β vertical motion.

The question can be asked: Are any of the non-hydrostatic accelerations actually important? Perhaps a non-hydrostatic feature of this simulation is the buoyant oscillation of the trapped wave system. An important feature of these waves is the forced vertical oscillation of a parcel about its equilibrium level. It is important for the meso-β parcel to overshoot its equilibrium level in order to initiate a new up-branch on the circulation cell. Since the hydrostatic model assumes a balance of vertical forces, this cannot occur and so this oscillation can not occur. This is equivalent to the trapped mountain lee wave which does not exist in the hydrostatic framework but does in that of the non-hydrostatic.

5.6.4 Dynamical model of MCS

In many respects, the evolving circulation cell (Figure 5.17) resembles a solenoidal direct circulation, such as that associated with the initial valley breeze, but through a considerably deeper layer. The cell exhibits an explicit overturning through a depth of 9 km and horizontal scales in excess of 450 km (the domain size prohibits exact specification). Its circulation leads to a westerly jet aloft and a easterly jet at low levels. The amount of momentum transported by the solenoid is directly proportional to the stream line interval shown in Fig. 5.17. The flow directly above the circulation cell encompasses 13 streamlines (number of streamlines are directly proportional to momentum) compared to 7 on the western boundary. Approximate zonal momentum balance is achieved by three stream lines of forced subsidence to the west and 4 stream lines of forced subsidence to the east. Most

of the forced subsidence occurs within 200 km on either side of the mesoscale updraft.

It was shown in Sections 5.3 and 5.4, that the regions of alternating subsidence and mesoscale lifting appear to propagate as deep internal gravity waves possibly trapped and radiating from a pulsating convective core. Examination of the complete evolution of the stream flow reveals the transient nature to the mesoscale response. At 2000 MST the decaying upward branch of the local circulation forcing the western secondary rainshaft and residual subsidence to the west is still apparent. To some extent these effects are augmented by the two dimensionality. In 3D, the gravity waves might travel radially away from a center of action decreasing in amplitude with the inverse square law.

However, there is reason to believe the oscillation could be real. First, the strongly two-dimensional arrangement of the mountain barrier could and does produce a linear arrangement in the cloud organization. Second, the region of suppression directly east of the barrier seems to play a major role is setting off the oscillation, and it would likely be a coherent quasi-two-dimensional trigger in the real atmosphere. As shown in Section 5.3, there is some observational evidence to this effect.

This hypothesized role of the internal gravity wave is different from that envisaged in the classic propagating wave-CISK model of a mesoscale convective system discussed in Chapter 2. In that model, the convection travels with the wave and is continually forced by the waves convergence. Phase speeds, like that of the simulated internal wave, were obtained in wave-CISK studies by Nehrkorn (1985) and were shown to

be much too fast to explain squall line propagation. In these simulations, gravity waves are, in fact, generated, possess significant vertical motion and seem to initiate convection at a discrete distance from the parent convection which generates their oscillation. However it is not at all apparent that there is any tendency for the convection to move with the wave.

Instead, the convection is tied to the moisture supply on which it thrives and on its ability to draw on it. As can be seen in Figure 5.10, the region of the primary rainshaft has only one consistent trait for all time- and that trait is unyielding. The primary rainshaft lies on the western edge of the plains inversion. Propagating wave activity to the west encounters insufficient potential instability to form anything substantial while propagating wave activity to the east is too rapid and too weak to break the inversion protecting the surface moisture. The inversion thrives on the valley breeze system and is augmented by the persistent mesoscale response to the primary convective region on its western boundary.

It is evident that in order for the system to propagate, the plains inversion must be destroyed. It seems that two process act to do so. First, the upward motion of the mesoscale meso-β cellular circulation acts to support strong convective elements which act to mix away the inversion as they move into the region from the west. Second, the movement of moisture aloft in the anvil along with radiative cooling aloft, acts to cool the air above the inversion, neutralizing its effect. When all convective elements were nuetralized at 1700 MST, the inversion was broken apparently by the effect of precipitation induced mixing from above.

In some respects, the growth of mesoscale forcing exhibits similiarities to the advective wave-CISK model described by Raymond (1983). That model of convective instability is characterized by the advection of precipitation aloft ahead of the updraft which, by cooling, helps enchance surface convergence beneath the updraft. Although that process is not apparent on the convection scale it may be partly responsible for the growth of the mesoscale response. In was noted in Section 5.3 that the movement of precipitation aloft did seem to be reflected in the surface pressure to the east of the primary upward meso-β vertical motion, and helped enhance the inflow. Unlike the advective-CISK of Raymond, the surface high pressure ahead of the storm is induced by virga sublimation and radiational cooling aloft. This allows sensibly warm θ_E air to remain at the surface below the inversion thus maintaining the moisture supply.

5.7 Downwind Effects of Rockies on MCS Evolution

As the orogenic MCS progressed eastward to the region 100–150 km east of ridge top, a strong weakening of the system occurred. This feature supports earlier work which suggests that this is a region of suppression for eastward propagating mountain cumuli. Two explanations have appeared in the literature. First, as Dirks (1969) pointed out, the sudden change in the terrain slope forces surface divergence in this region. Second, the effect of the mountain wave also can force divergence in the same region (Dirks et al., 1967). There is evidence of both mechanisms in the simulation, but the slope flow effect seems most likely.

In order to confirm this hypothesis a course resolution simulation of this case study was performed with both the Palmer Ridge topography

(same as above) and the South Platte Valley topography. These simulations are discussed more fully in the next chapter. The valley topography possesses a much greater change in slope at the western extent of the high plains than does the Palmer Ridge slopes. In the similar Palmer Ridge case the system developed less realistically and far too late (after 1600 MST). However comparison with the valley topography case demonstrated that virtually no system developed at all. There was continuous downward motion of up to 10 cm s^{-1} on the scale of 20-30 km on the western extreme of the high plains which prevented development. It seems evident, that a primary effect of the Palmer Lake Divide is to weaken the suppression mechanism described by Dirks (1969) allowing eastward propogating orogenic mesoscale systems to survive. Obviously, when considering three dimensions, the ridge will form slope convergence of its own perhaps weakening further the suppression.

5.8 Summary

The results of this simulation indeed confirm that the diurnal evolution of local terrain flows, the Rocky Mountain slope flows in particular, do indeed lead to an eastward propagating mesoscale convective system with much the same structure as that found by Maddox (1980). From the above analysis it has been determined that in this 2D numerical study, the interaction of thermally driven slope flow with the mechanically driven mountain wave flow led to the development of a long lived MCS.

The control simulation has raised several questions, some of which will now be addressed in the next three Chapters. First, the consequences of the two dimensionality of this simulation will be investigated to the extent possible. Therefore, Chapter 6 will describe

a 3D coarse resolution simulation the MCS development and compare it to a coarse 2D simulation. Next, the effects of the diabatic heating by latent heat of various degrees, longwave cooling and low level evaporation and melting of precipitation will be investigated in Chapter 7. In Chapter 8, the dynamic effects of the ambient wind will be investigated.

6. SENSITIVITY TO NUMERICAL TECHNIQUE

Although a numerical model is a powerful tool for studying the dynamics of the atmosphere, caution must be taken to prevent misinterpretation of fictitious "numerical" weather for real observable phenomena. As with any numerical investigation, it was necessary in this study to make compromises in order that a solution be obtained within the constraints of current computer and modeling technology. Although innumerable assumptions and approximations were made, one stands out as possibly serious and potentially misleading. That assumption was the use of two dimensions to simulate the development of cumuli. In this Chapter, the consequences of using a 2D framework and those of some alternatives to two dimensions are investigated.

The results reported in the previous Chapter depict the simulated system as a circulation system which is a quasi-steady warm-core meso-β system that which acts to organize an environment conducive to deep convection. The convection, in turn, supplies the energy which drives the mesoscale circulation. Observations depict the meso-β system to be of a linear structure oriented parallel to the approximately two-dimensional mountain barrier which is hypothesized to be responsible for its organization. On the surface, the phenomena would seem to be quasi-two-dimensional.

Recent studies of several cloud and orogenic flow phenomena with apparent 2D structure have demonstrated important three-dimensional

dynamics imbedded within. In the case of orogenic flow fields, Clark (1981) demonstrated that the turbulence structure within breaking mountain waves is not captured adequately using a two dimensional representation. In the case of squall lines, Weisman (1985) demonstrated the importance of flow between individual convective towers, a fundamentally 3D structure, toward the maintenance of steady squall line convection. Moncrieff and Miller (1976) demonstrated a similiar importance of trajectories of downdraft air crossing the path of updraft air in the plane normal to a tropical squall line, to the maintenance of steady convective overturning. In the case of cellular convection, it is well known that convection in both linear and curved shear environments is strongly three dimensional. Studies, such as Cotton and Tripoli (1978) demonstrate significant differences in entrainment rates for small cumuli simulated in a 2D versus a 3D framework.

But there has been considerable successes using the 2D framework as well. For instance, the studies of orographic thermally driven slope flows in 2D by several authors including Dirks (1969), Gal-Chen and Somerville (1975a,b), Pielke and Marher (1977), Bader and McKee (1983), Banta (1981) and others have met with considerable success representing observed atmospheric flow fields. Mountain wave studies by Klemp and Lilly (1978), Durran (1981) and others have also been successful in simulating observed flows in the framework.

In the case of cumulus supported squall line studies, there have been successful 2D numerical studies by Hane (1972), Thorpe et al. (1982) and others. Weisman and Klemp (1984), using a three dimensional framework, demonstrated that certain vertical shear regimes are

supportive for truly 2D convection. Several analytical 2D squall line models have been proposed including the nonlinear models of Moncrieff and Green (1974), Moncrieff (1978), Thorpe et al. (1982), Moncrieff (1981) and the linear models of Raymond (1975, 1976, 1983), Xu and Clark (1984) and numerous others. Overall, there is evidence that at least some aspects of squall line systems and deep convection, in general, can adequately be represented in 2D while others can not.

Because this study deals with a supportive flow regieme spanning a scale of 1000 km, it was necessary to use a 2D framework to gain adequate resolution to resolve individual deep cumuli. The 3D alternative, traditionally used by other investigators of mesoscale cumulus systems, might be to use a coarse resolution and parameterize the convection. This approach has only been taken sucessfully for meso-α and larger systems and is fundamentally flawed for smaller systems as it has been formulated in the past. Part of the shortcoming lies in the fact that it is assumed in the parameterizations that the nature and timing of the convection is dictated by features of the large scale flowfield and thermodynamics. More important, the parameterization must specify exactly how the large scale affects the convection and vise versa. Since the feedback between scales is largely unknown, the foundation of the parameterization approach is weak indeed. Unfortunately, cumulus parameterization schemes are often used to study this very interaction. As a result, any conclusions drawn about the scale interaction between cumulus and the large scale which are based upon numerical experiments using a cumulus parameterization must be highly suspect.

The alternative 3D approach is to simulate with resolvable scale microphysics. In doing so, resolvable scale motions act to form clouds on resolvable scales. Because convection will tend to form on poorly resolved scales, a strong filter is normally included to force the motions on to scales which can be resolved (i.e. Ross and Orlanski, 1982; Rosenthal, 1979; etc.). It was shown in the previous Chapter that meso-β flow fields accounted for nearly 50% of the vertical moist static energy transport. In order for a cloud of similiar stature to be produced with a resolvable meso-β motion only, the meso-β motion will have to increase. This will obviously produce a somewhat altered dynamic response, perhaps more serious than the two-dimensionality itself. Nevertheless, some investigators such as Rosenthal (1979) and Orlanski and Ross (1984) claim considerable success in this way. Others, such as Molinari (1985), find significant differences in the development scenerio.

Clearly, it is impossible to verify the validity of this simulation by comparing it against a like simulation in 3D. Instead, the approach taken will be to simulate the Rocky Mountain Convective Cycle on a 2D coarse grid and then again on a 3D coarse grid using resolvable scale microphysics. A comparison of the 3D to 2D coarse mesh studies can then reveal significant 3D features of the Meso-β circulation. Comparison of the 2D coarse to 2D fine mesh will reveal what is lost with the coarse resolution and what is gained. This will aid in applying what is learned to the fine-mesh control case.

Finally, a non-equilibrium state-of-the-art cumulus parameterization scheme will be applied to the 2D coarse mesh scheme and compared to both the fine mesh solution and the coarse mesh solution in

the absence of parameterization using explicit microphysics. The results, if acceptable, both help verify the validity of the parameterization approach in a highly quantitative fashion and justify its use in the 3D framework. If unacceptable, the important question of "Why it didn't it work?" can be addressed. Moreover, invaluable insight can be gained into how a parameterization influences results.

Unfortunately, there is no adequate method to test the consequences of the assumed two-dimensionality of the cloud field on the mesoscale response. As a result of this and other assumptions, the conclusions of this study as any numerical study must be viewed as suggestive in view of the known shortcomings.

6.1 Comparison of 2D and 3D Coarse Mesh Simulations with the Control Case

Recently, several investigators have adopted a channel model structure for simulation of squall line phenomena in two-dimensions. In order to make the most efficient use of limited resources, the simulation domain along the direction of the squall line is taken large enough only to properly resolve 2-3 individual convective elements while the domain perpendicular to the squall line is considerably longer. The squall line is depicted realistically by the specification of cyclic boundary conditions which imply a repeating structure with the frequency of one along-line domain length. This configuration has the disadvantage that a line must remain perpendicular to the "channel" or break into channel width segments. Although not a truly "free" three dimensional depiction of a convection line, it does allow the freedom for ambient flow to pass around cells within a squall line, and this is thought to be the greatest shortcoming of the two-dimensional squall

line framework. The channel technique has been employed by Weisman and Klemp (1984), Ryan et al. (1986) and Nicholls (personal communication).

The affordable resolution will be 14 km or 1 degree longitude and 0.75 degrees latitude. The "channel" domain encompasses the cyclic topography shown in Chapter 4 of which the control experiment is simply a slice along the Palmer Lake Divide (referred to as "ridge topography" here). A possibly important aspect of the 3D framework is the variation in east-west topography slope between the mountain top and the valley. Therefore the 3D will be compared to 2D simulations along both the ridge and valley topography. The exact specifications of the coarse 2D and 3D grids are given in Chapter 4.

Because the "channel" simulation was performed early in the model testing stage, there is a minor difference between the channel experimental design and the equivalent 2D framework design. The difference is that the composite sounding used to initialize the "channel" experiment extends a -2 m s^{-1} meridional wind down to the surface. This leads to a more intense meridional ridge top flow initially as a result of momentum conservation. Because the meridional flow was found to be of minor importance as a dynamic term the consequence of this difference will be small.

In all three simulations the stage 1 evolution is qualitatively similar to that described in Chapter 5. This is not surprising in view of the spectral plots which show the majority of the variance is in wave lengths resolved by both scales. Figure 6.1 displays the perturbation temperature and vertical velocity field for each simulation near the time of first dectectable condensate, or about 1400 MST. As can be seen, in the case of ridge topography, initial convection forms over

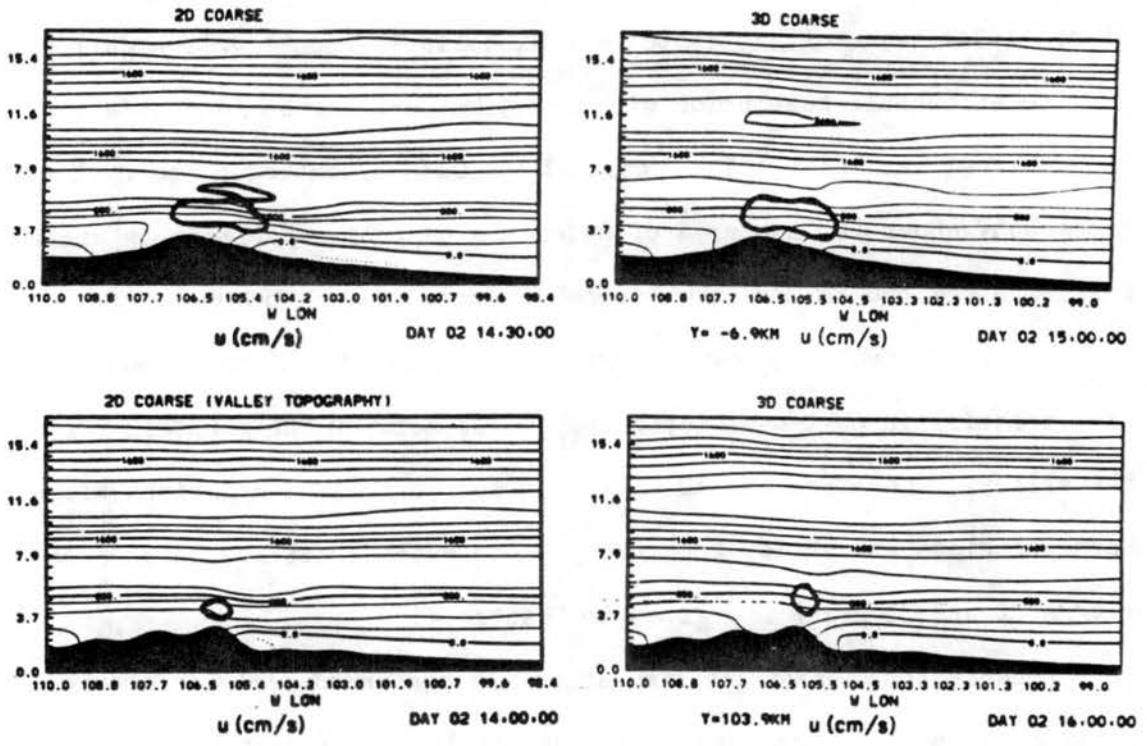

Figure 6.1. u field at time of first detectable condensate for valley and ridge topography using a coarse grid in both a 3D and 2D framework. Contour interval is 2 m s^{-1} (200 cm s^{-1}). Vertical and horizontal axes, condensate depiction and topography are all represented as in Figure 5.1.

both the mountain peak and 70 km east of the peak. The region 70 km east of the peak, as in the fine resolution case, is where the valley breeze meets the mechanically forced mountain wave flow.

The valley topography case, on the other hand, has initial convection only over the mountain peak. The ridge topography convection occurred about 1 hour earlier at the mountain peak than valley topography convection, probably because of the less steep western slope and reduction of chimney effect. The region 70 km to the lee also features surface flow reversal in the same manner as the ridge topography region, however, convective development is hampered by the existence of strong sinking motion above the boundary layer. This motion can be attributed to the thermally driven slope flow. It occurs in this region in the valley topography because of the more sudden change in slope. The phenomena is essentially the downward branch of the slope circulation which was predicted by Dirks (1969) who first suggested its importance in suppressing convection in precisely this region. Its existence as a slope flow phenomena is verified by its simulated evolution from rising motion at dawn. This is a particularly interesting result in view of the fact that the observed preferred early convective development on the Palmer Lake Divide and Cheyenne Ridge is most often attributed to the 3D effect of the east-west ridges in causing preferred convergence at ridge top. These results suggest that this could be of secondary importance at least at the time of initial development in the simulation.

The formation of deep convection is inhibited until after 1800 MST in the coarse mesh ridge simulation and along the east-west ridge in the 3D case. In the case of the valley coarse mesh 2D simulation and within

the valley in the 3D case, deep convection occurred later at about 2100 MST. This is displayed in fiqures 6.2 and 6.3. Although the system appears to move southward in the 3D channel experiment, its position appears similiarly in independent 2D slices of the 3D case. The exception is that the 2D ridge topography convection does not dissipate as the valley convection develops. This may merely be an artifact of the coarse 3D framework where the limited number of grid points in the meridionial direction can only support a single convective element and its subsidence.

The late beginnings of deep convection in all the coarse resolution experiments is a consequence of the lack of adequate resolution. The lifting of low level air to free convection levels by resolved scale motions is considerably slower and less efficient than when accomplished by convective scale motions. In the valley topography case, convection associated with the mountain wave convergence zone is supressed by the downward branch of the slope circulation and so only one cloud element is formed. The strong simililarity between the 3D simulation and the 2D simulation on this point supports this notion in lieu of one suggesting an important role of 3D effects.

Besides the initial deep convection being over 2 hours later than the control, at 2000 MST it is also almost 100 km west (or about 2.5 - 3 hours of travel time) of its simultaneous position in the fine mesh simulation. The initial deep convection is again coincident with the mountain wave convergence zone. Unlike the control run, the occurrence of deep convection is not directly linked to ridge top convection. The important factors leading to deep convection seem to be the advection of cloudy air over the mountain wave convergence zone and the gradual

Figure 6.2. Variable fields for 3D simulation at 2000 MST. Six east-west vertical sectors are presented along ridge axis and horizontal sections are presented at the lowest grid level (0.1 km) 5.6 km MSL and 10.9 km MSL. Contour interval is 2 m s^{-1} (200 cm s^{-1}) for u and v, 20 cm s^{-1} for w, 0.2 mb (200 dynes cm^{-2}) for p', 0.5 k for θ', and 0.5 g kg^{-1} for condensate in the zonal vertical cross sections. The variables represent 6 grid point (86 km) averages for vertical sections. Vertical and horizontal axes, topography and cloud outline are all as in Figure 5.1. Horizontal sections of p' have contour intervals of 0.2 mb (200 dynes cm^{-2}) at 0.1 km MSL and 0.1 mb at 5.6 km MSL and 10.9 km MSL. Vectors represent wind flow at each level. Heavy dark line is condensate outline. For horizontal plots, vertical axis is labeled in ^{o}latitude and horizontal axis in ^{o}longitude.

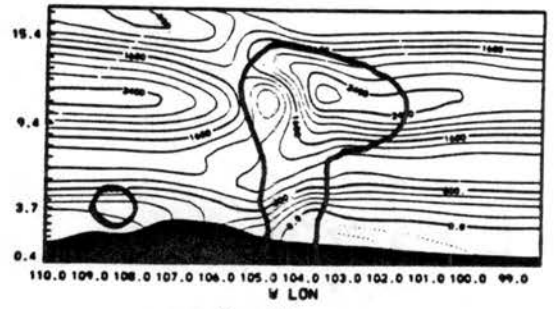

u (cm/s)

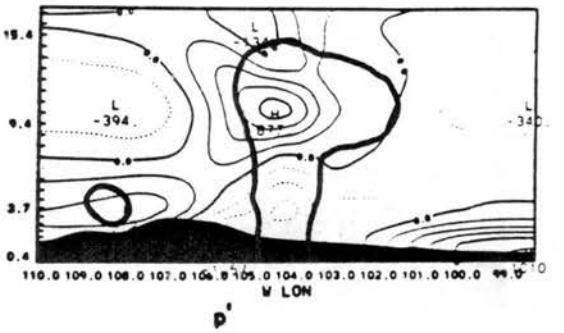

p'

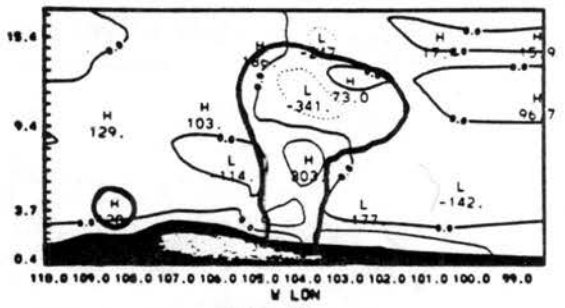

v' (cm/s)

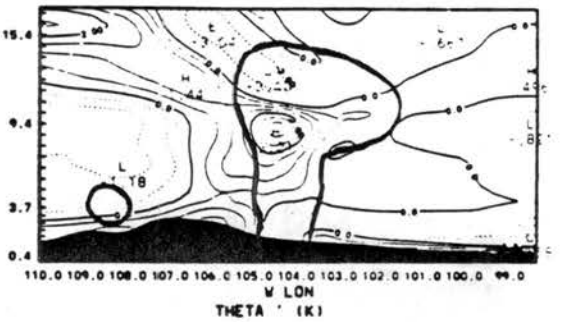

THETA ' (K)

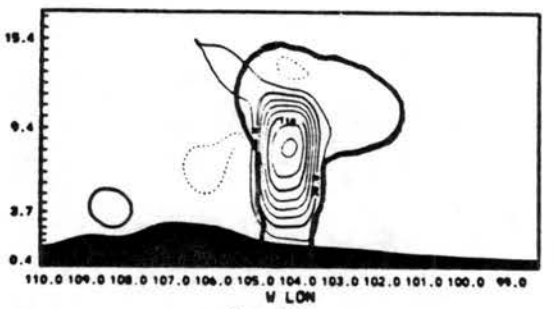

w (cm/s)

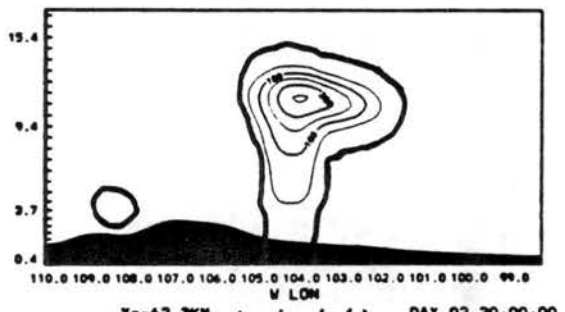

Y=-62.3KM rl + rice (g/g) DAY 02 20:00:00

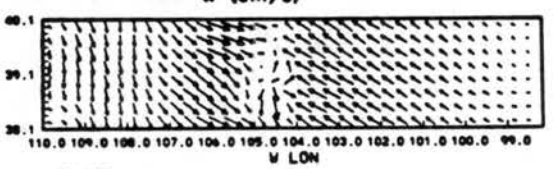

3 M/S

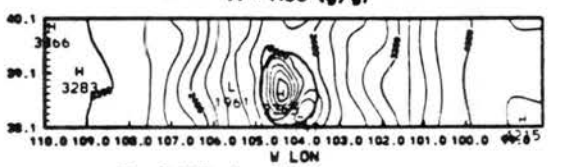

Z= 0.1KM p'

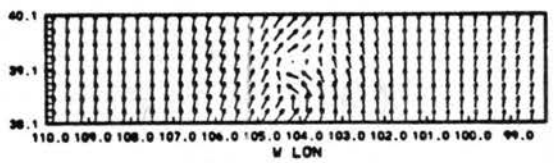

5 M/S

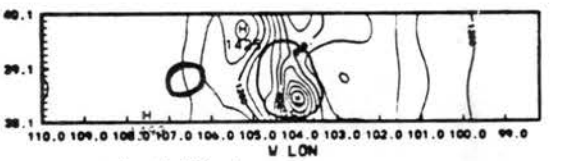

Z= 5.6KM p'

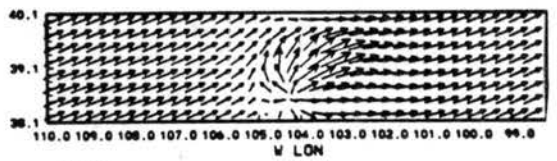

5 M/S

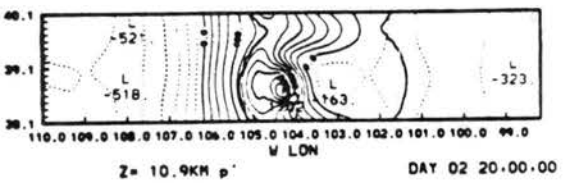

Z= 10.9KM p' DAY 02 20:00:00

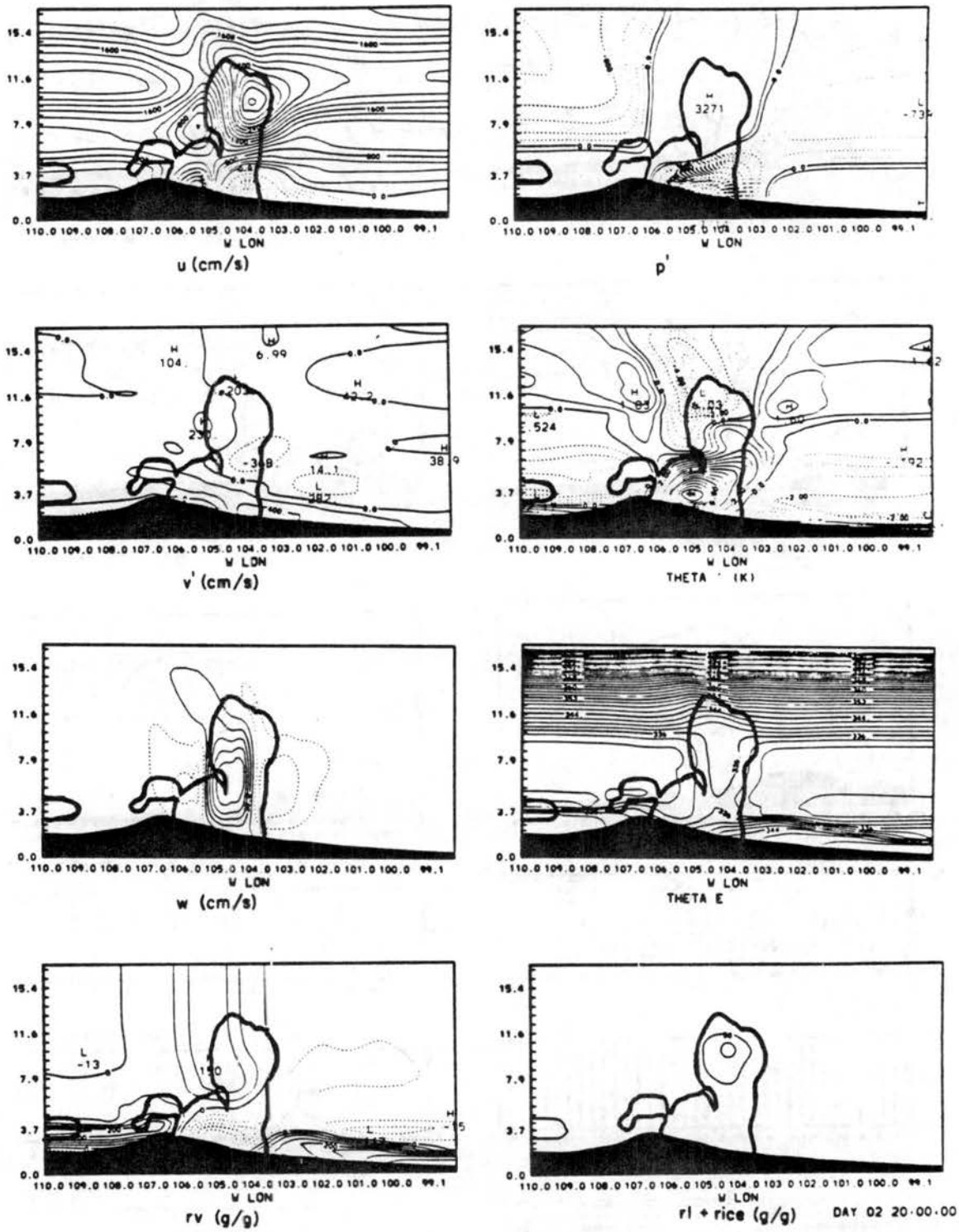

Figure 6.3. Same as Figure 5.1, except for 2D coarse ridge topography case, and at time 2000 MST. Also meso-β average is 6 grid point (86 km) average.

increase in surface convergence. The advection of cloudy air over the eastern slope has the effect of shading the region west of the convergence zone while the advection of moisture overhead increases the efficiency of advection. The result was a gradual increase in intensity of the surface convergence culminating in the growth to deep convection.

As the system deepened to the tropopause by 2000 MST, the movement is about 10 m s^{-1} toward the east as in the control fine mesh case and as found in the observations. The system also moves at 6 m s^{-1} toward the south. This movement is faster than the v component at any level. It is hypothesized that the meridional movement is a result of new growth into a region of more favorable support. This notion is consistent with the result that the 3D system seems to be in matching position with the 2D experiments run in the valley and on the ridge. Structurally, the 2D coarse and 3D coarse experiments are considerably different. Because individual cloud elements are not resolved properly, the system developes as a cloud on the minimum resolvable scale. The tendency to form 2 Δx elements was so great, that a strong 4th order filter described by Durran (1981) was necessary to control the simulation from entering a complete nonlinear instability breakdown in both the 2D and 3D simulations. As a result the circulation was forced to the scale of about 5-15 Δx. This means local convective heating, which occurs as subsidence normally, was forced up to 100 km laterally away from the updraft center.

In the 2D coarse resolution case, a large updraft core spanning nearly 60 km and reaching peak upward velocities of 3 m s^{-1} was formed. The mesoscale horizontal velocity response to support the updraft was enormous and unrealistic. By 2000 MST, see Figure 6.2, opposing surface

winds of over 30 m s^{-1} developed. The downslope winds lowered relative humidities to less than 1 g kg^{-1} in some boundary layer locations west of the core. Accompaning adiabatic boundary layer warming west of the core caused temperatures to rise by over 12 C. Upper level warming was less at 2-4 K. The heating rates (Figure 6.4), computed as in Chapter 5 for meso-β and meso-γ, show a dominant role played by meso-β. Surprisingly, the heating rates aloft are not unrealistically strong. However the level of maximum heating is lowered considerably, over the control case. In essence, a giant cumulonimbus of ridiculous intensity formed but only with the application of a very strong numerical filter necessary to keep the solution stable.

By 2200 MST, the ridge topography 2D coarse mesh MCS weakens. This seems to occur as the rainshaft decouples from the surface convergence. Unlike the control, the coarse mesh storm, despite its great intensity, failed to cause the surface windshift line to propagate. The reason is because the strong subsidence heating and drying to the west warmed the deep troposphere and lowered the surface pressure stabilizing the position of the convergence. As greater amounts of dry air were ingested into the giant updraft, its intensity waned. The flow aloft advected the precipitation field eastward and the adabatically warmed boundary layer rebounded both on the east and west flanks of the core. The result was an westward moving internal gravity wave west of the core and a weaker opposite regime to the east. This is a giant version of the single element scenerio in the control. To some extent a similiar fluctuation also occurred on the meso-β scale in the control. The breakdown of the 2D coarse circulation, however, was highly exaggerated over the control case. Because explicit convective circulations formed

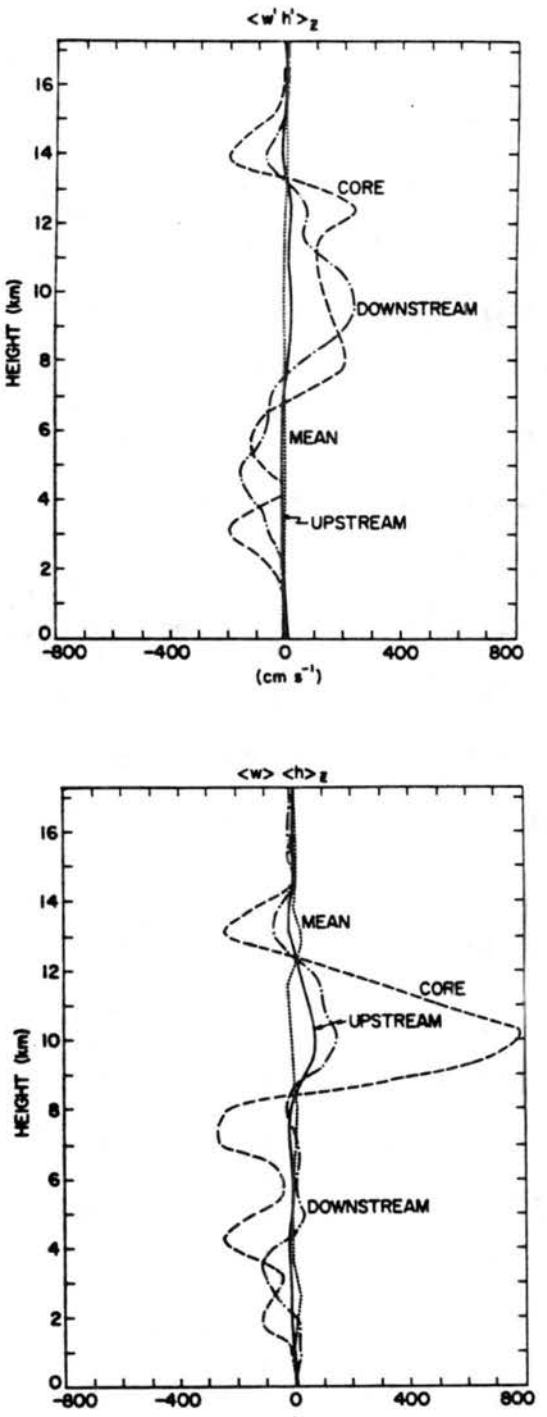

Figure 6.4. Same as Figure 5.26, except for the 3D experiment core at 2200 MST.

on the scale of 100-300 km, they contained considerably greater inertia than the control. As a result, they overshot equilibrium to a far greater degree and the collapse is much more severe.

The 2D coarse valley topography achieved its peak intensity between 2200-2300 MST. This was about the same time that the ridge case convection was strongly dissipating. The mature system at 2300 MST is displayed in Figure 6.5. Its lifecycle differed from the ridge case in both its late development and its lack of intensity. At its peak intensity, the 2D valley system reached only about half the peak updraft as did the ridge case. This is attributed to the late development and lesser CAPE at that time. In fact, the low-level horizontal convergence field of the valley system appears somewhat decoupled from the cooling surface. The later development over the valley was apparent in the observations, also at a weaker intensity than the convection over the ridge.

The unrealism of the convection size in 3D was somewhat moderated because of the ability of 3D to gather convergence with less mesoscale flow response. The mature 3D convection at 2300 MST, now over the valley, is depicted in Figure 6.6. As with the 2D case, it was necessary to apply a strong horizontal 4th order filter to keep the solution from non-linear instability in its effort to produce convection on truncation scales. Again, in 3D a single giant convective element is produced. The mean vertical motion is much greater than the 2D coarse case and reaches values of 7 m s^{-1}. On the meso-β average plots in Figure 6.6, mean vertical motion of over 1 m s^{-1} occurs on horizontal scales approaching 100 km. This produces highly unrealistic heating rates of 800 K day^{-1}. The heating profile is depicted in Figure 6.6.

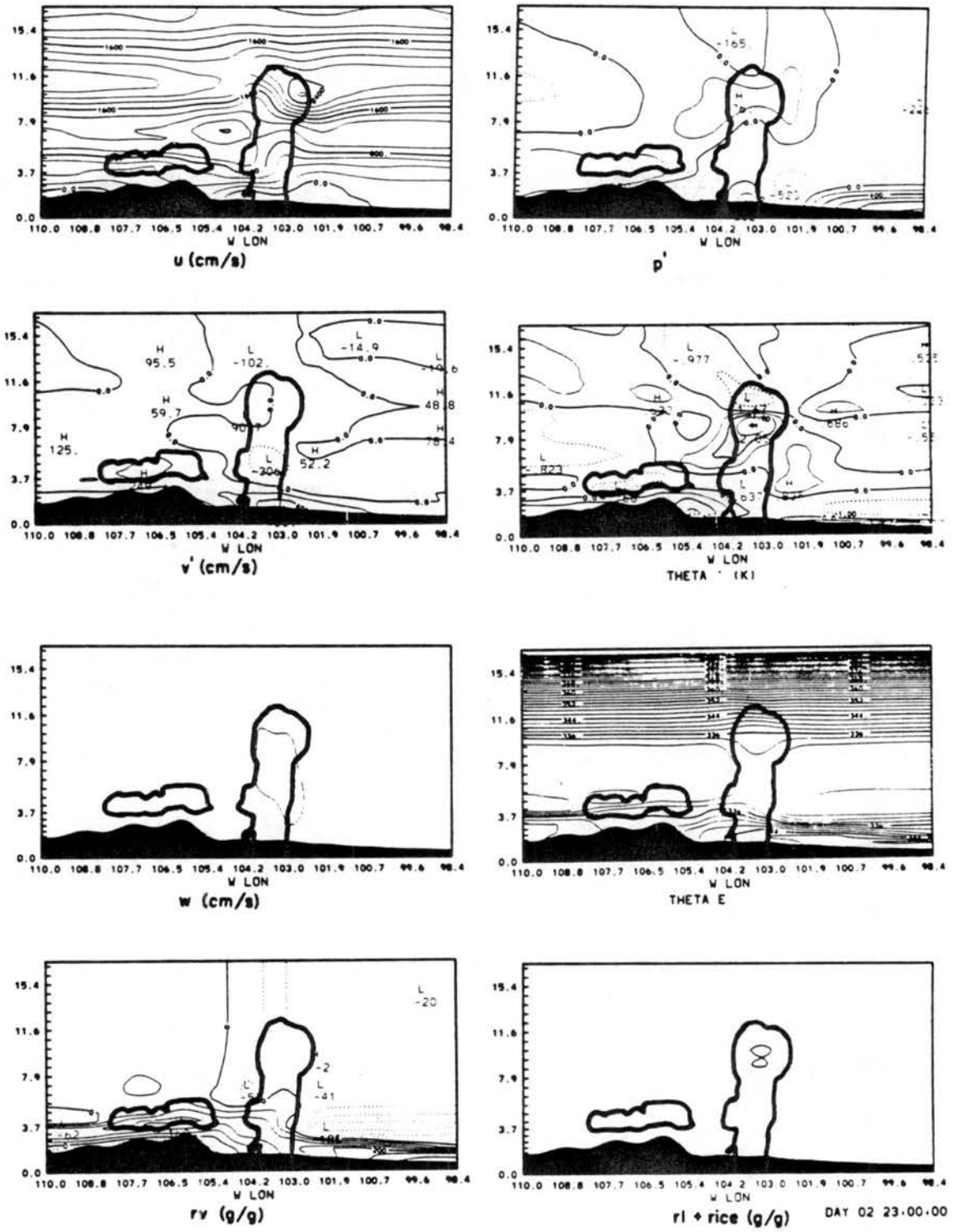

Figure 6.5. Same as Figure 6.3, except valley topography at 2300 MST.

The horizontal 3D wind response is less unrealistic in the x/z plane than in the 2D case. This is partially due to the added dimension of horizontal convergence. The low-level flow is a cyclonic inward spiraling flow with a tangential wind of 3.5 m s^{-1} at 90 km radius. This gives a relative vorticity 3.8 x 10^{-5} s^{-1}. A pressure low of .8 mb is attained at 4 km MSL. Precipitation cooling forces weak high pressure at the surface. The updraft is drawn most strongly from the downshear southeast quadrant where ambient air flows over a density current. High pressure aloft is of magnitude 0.9 mb. The flow aloft is anticyclonic about the high pressure core.

The storm has a mixture of supercell and MCS dynamics. It is like a supercell in the sense of its steady single cellular structure maintained by low pressure preserved by cyclonic rotation. Unlike a supercell, the rotation is derived from coriolis effect which is important because of the immense scale of this system. Whereas a supercell circulation will normally exist on a scale of 50-100 km, this simulated cell has a circulation scale in excess of 400 km.

The simulated 3D MCS moves east-southeast at 10-12 m s^{-1} which is near the mean wind speed of the troposphere. The strongest compensating subsidence is forced to the south (or north) of the system and cannot be seen in Figure 6.6. This is somewhat different than the 2D case where the subsidense was concentrated more to the front and rear of the system by necessity. Subsidense of at least the controls magnitude also occurs to the east and west of the 3D core and is apparent from the 3D perturbation θ structure.

Figure 6.6. Same as Figure 6.2, except vertical sections are at valley topography and at 2300 MST.

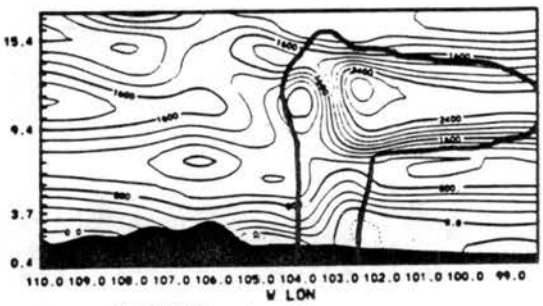

Y=103.9KM u (cm/s)

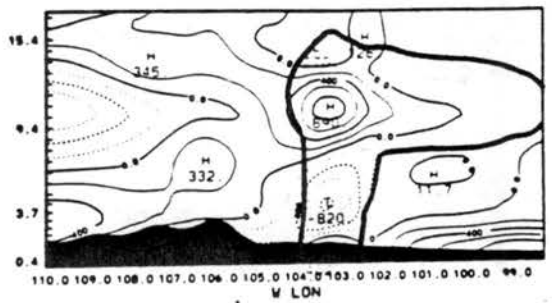

Y=103.9KM p'

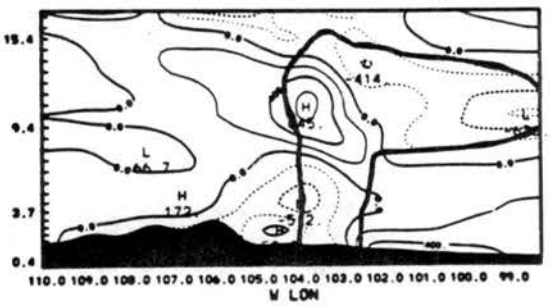

Y=103.9KM v' (cm/s)

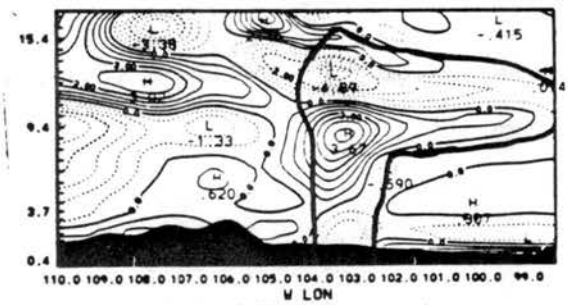

Y=103.9KM THETA ' (K)

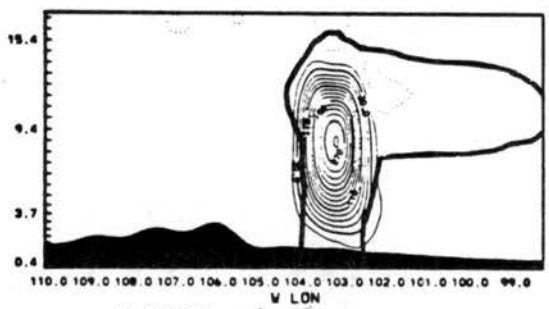

Y=103.9KM w (cm/s)

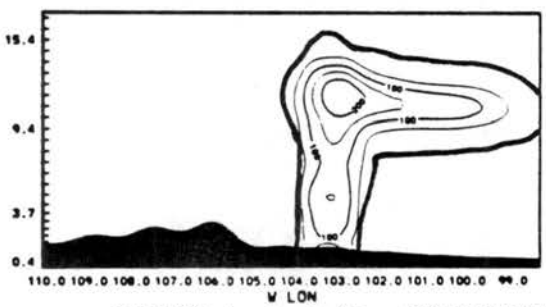

Y=103.9KM rl + rice (g/g) DAY 02 23:00:00

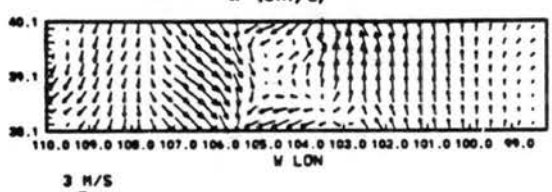

3 M/S

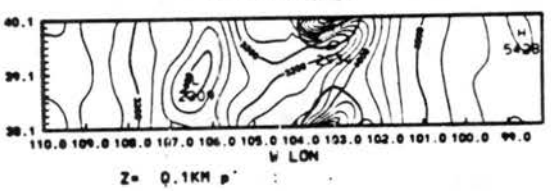

Z= 0.1KM p'

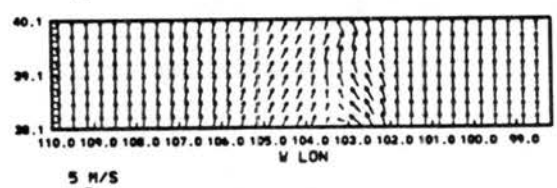

5 M/S

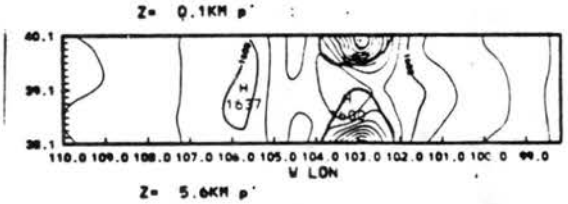

Z= 5.6KM p'

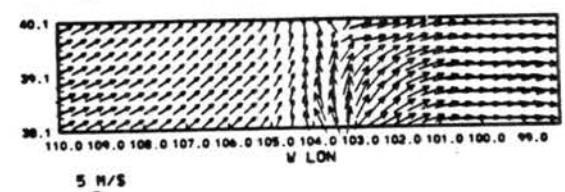

5 M/S

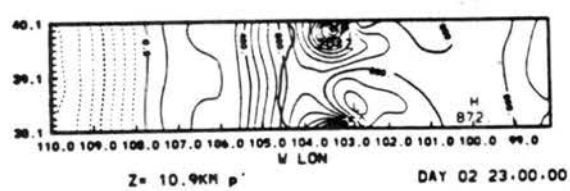

Z= 10.9KM p' DAY 02 23:00:00

The mature thermodynamic structure appears remarkably similiar to the control case. The temperature perturbation of 2-4 K at 8-9 km MSL is somewhat warmer than the control case, however. The anvil extends over 400 km downwind to the eastern domain boundary. Associated with the anvil is a warm anomaly at 8 km MSL associated with advected warm air from the core dynamics and longwave heating at the base of the anvil. As a result, a distinct minimum in Brunt-Vaisalla frequency has formed within the anvil at the tropopause level as in the control simulation.

Like the control case, a westward stratospheric propagating internal wave structure is evident west of the core at later times. Unlike the control, the ice content falls rapidly west of the system aloft. This also occurred in the coarse mesh 2D, and is evidently due to the inability to form weak convective anvil circulations with the coarse resolution.

Clearly, all of the coarse resolution simulations of convection with explicit microphysics lead to a less realistic result than the fine mesh 2D simulations. In fact, they bear little resemblence to the observations, beyond the speed of propagation. The three dimensional simulation fails to attain any linear structure as only a single cell is formed on the scale of the entire Palmer Ridge/Platte Valley topographical dimension. Because of the resolution, convection begins too slowly and attains unrealistic dynamics. The supercell like steadiness derived from rotation driven by convergence of coriolis, is unrealistic for a convective cell, but is plausable if viewed as a MCS. In fact a similar tendency is noted in the control and the observations to a much lesser extent.

Despite the shortcomings, these experiments suggest that at least the 3D effect of the mesoscale slope circulation is of secondary importance. This is demonstrated by the fact that the favoring of the Palmer Lake divide by early convection is due primarily to the greater discontinuity of the slope between the Rockies and High Plains in the valley topography than in the ridge topography. This produces an intense region of suppression over the valley and a less important region of suppression over the western High Plains in the ridge topography. This is in agreement with the results of Dirks (1969) who demonstrated a strong suppression for the valley topography case. Furthermore, because the 3D system moves much the same as both the 2D coarse and 2D fine mesh simulations, the simulated propagation mechanism is probably not suffering greatly from the 2 dimensionality.

It also should be pointed out that the extensive east side anvil is formed in the 3D experiment. This indicates that the unobserved eastward extent of the anvil is likely a microphysics problem rather than a 2D flow problem. There is no way to verify the realism of the structure, propagation or longevity of the fine mesh 2D elements based on this 3D test because of the far greater unrealism of the elements in these tests. It is important, however, that even with such grossly distorted convection, the coarse mesh simulations, both 3D and 2D, succeeded in simulating the phase speed of the system identical to the fine mesh. This suggests that the phase speed is not controlled by the dynamics of the individual convective elements, but rather by the collective heating or momentum transport of the ensemble of cloud elements.

6.2 Use of a Cumulus Parameterization with the 2D Coarse Mesh

The results of the previous section demonstrate that the use of explicit microphysics on a 14 km grid produces a less realistic mesoscale response. The alternative of representing the cumulus by a convective parameterization is now addressed. Convection development on the meso-β-scale is clearly a non-equilibrium process, where extensive convective instability builds up over a long time and is removed locally in a relatively short time. It is therefore appropriate and necessary to consider a non-equilibrium convective parameterization.

Unlike the equilibrium schemes used for meso-α and larger scale tropical simulations, the schemes developed by Fritsch and Chappel (1980) or Tremback (1986) introduce several arbitrary parameters which act to control when and how fast convection occurs. In both the above schemes, convection is triggered by vertical motion at cloud base defined as the lowest condensation level for the highest boundary layer θ_e air. Unlike equilibrium schemes, the convection then acts to stabilize the grid volume rather than maintaining equilibrium with the incoming energy supply.

As part of the 2D coarse resolution tests, the 2D coarse simulation case was repeated using the Tremback (1986) convective parameterization. This parameterization is a modified Fritsch and Chappel (1980) non equilibrium parameterization. Its application to the coarse resolution simulation is highly questionable because the 14 km resolution is too fine to validate many of the assumptions on which it is based.

The simulated evolution of convection using a cumulus parameterization is summarized in Figure 6.7. The vertical motion trigger was adjusted to force deep convection inititation near the

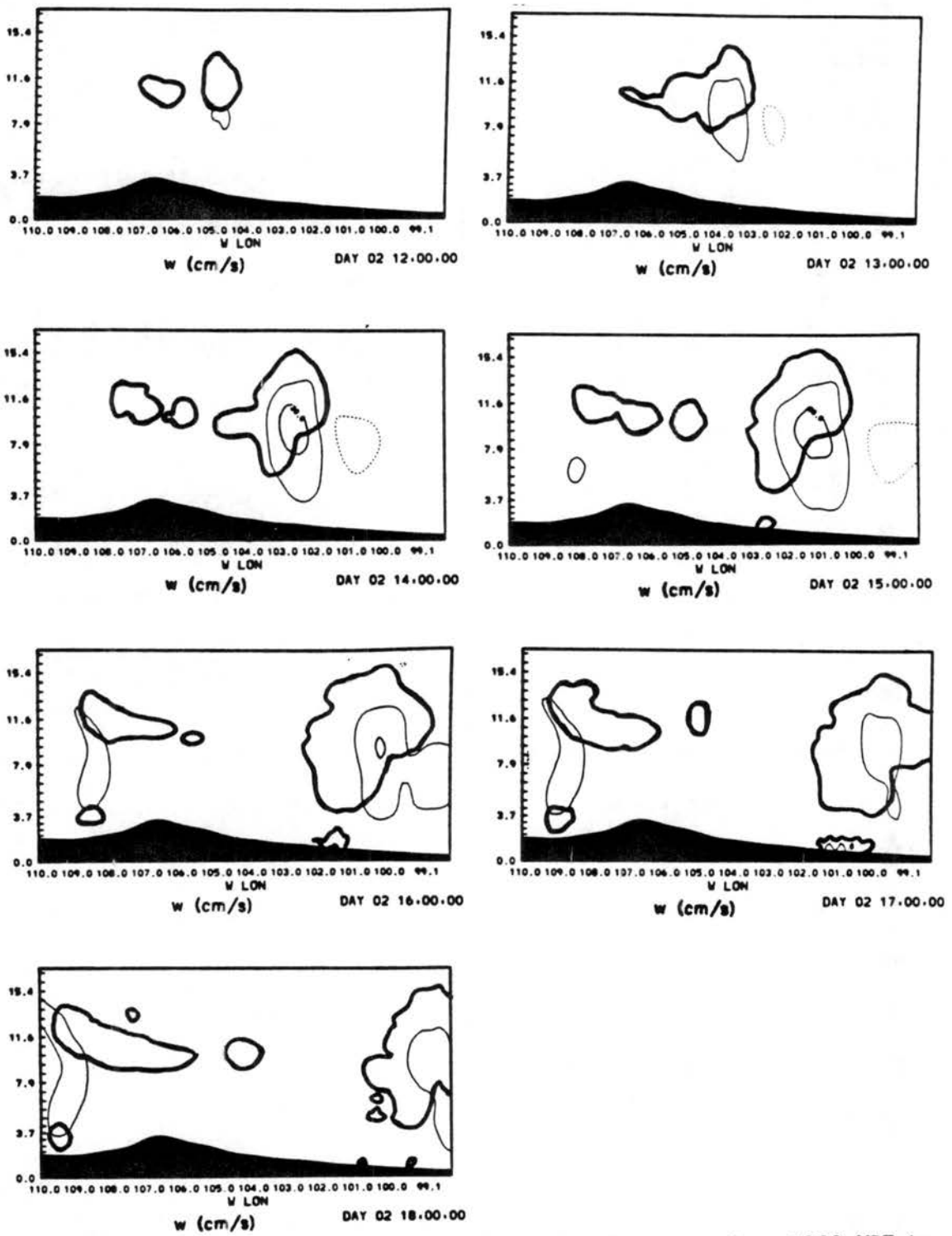

Figure 6.7. w field for cumulus parameterization case from 1200 MST to 1600 MST. Contour interval is 20 cm s^{-1}. Vertical axes and horizontal axes, cloud outline and topography are represented as in Figure 5.1. The w field represents 6 grid point (86 km) averages.

observed time of 1300 MST at the mountain wave convergence zone. This region is where peak vertical motion is produced by mesoscale circulations. The ensuing development is informative. After initiation, the convection intensified and finally began to propagate eastward at 25-30 m s^{-1}. Moreover, the system was not associated with a permanent wind shift at the surface. The speed exceeded the tropospheric flow at all levels. Close examination of the vertical motion and temperature field reveal a strong internal gravity wave structure. The result was a propagating MCS which moved into Kansas by 1600 MST and was out of the simulation domain by 1800 MST.

The simulated movement was obviously in strong disagreement with the observations which show a propagation speed corresponding to the mean tropospheric wind speed. The simulation was in good agreement with a previous wave-CISK study reported by Nehrkorn (1985). Moreover, the speed of movement is similiar to that of the trapped gravity waves found in the control simulation beneath the anvil. The evidence is that use of the convective parameterization led to the development of wave-CISK-like propagating convection.

The experiment was repeated using a coarser 28 km mesh. The result was more like the observations. The system moved more slowly at approximately 12 m s^{-1} to the east. Convection did not travel with the wave because the grid scale vertical motion failed to reach the arbitrary convection criteria.

These combined results demonstrate that the wave CISK mode exists in the non-linear model and preferentially developes as a result of the parameterization. It forms because the parameterization cannot distinguish between persistent vertical motion capable of initiating

deep convection and transient motion associated with gravity waves that are not capable of the same. In all instances of the control case, the fast moving wave either failed to initiate convection, or failed to support the convection as it developed. In the cases where the wave did initiate a convective cell, such as in the western rainshaft at 1900 MST in the control, it happened with the support of persistent surface convergence prior to the wave passage.

These results are important for two reasons. First they may very well indicate what is wrong with some wave CISK models. Second, they demonstrate the difficulty in applying a parameterization based on questionable assumptions to the dynamics of MCS's. Some wave-CISK investigators have mentioned in the past that a major problem with wave-CISK is its failure of scale selection. Xu and Clark (1984), Raymond (1983), Davies (1979) and others have proposed a phase lag between the updraft and downdraft to solve these problems.

These results not only support a need for phase-lagging, but also show a need for the convection itself to lag the forcing and for a convective element to properly interact with the environment.

There is little evidence of any gravity wave coupled deep convective elements in the control case. However, it is possible that the "trapped" anvil internal waves may have been partially maintained by energy derived from residual CAPE of the ice phase. This would be more likely since the anvil air is already at saturation and an immediate response to short term gravity wave lifting is more possible. In fact, the anvil waves may have been miniwave-CISK-like features.

In summary, it is found that the 2D fine mesh simulation most likely represents the organization and development of the convective

ensemble with reasonable accuracy. There is evidence that the use of coarse resolution 2D, or 3D with explicit convection, or coarse resolution with parameterized convection all have significant shortcomings exceeding those of the control simulation. The results in no way indicate that parameterization is not possible, although it is clear that even the gross characteristics of the resulting system may be dependent on details of the parameterization which are somewhat arbitrary. As a result, although shortcomings are recognized, it is concluded that the design of the control simulation is optimum for studying the topic of orogenic convection organization and MCS propagation.

It should be emphasized that despite the unrealism of the 2D and 3D coarse mesh experiments, the simulated convection still moved at the observed speed. This suggests that the speed is a function of the deep tropospheric wind and is not dependent on a wave-like propagation mechanism. This indication will be supported in the following two chapters which perform dynamic and thermodynamic sensitivity tests of the convection development.

Finally, the comparison of 2D and 3D simulations reveals that the reason that east-west ridges are so favorable to convection may not be due so much to the associated induced transverse slope circulations, but to the difference in slope change at the base of the foothills between the ridges and the valley. This slope change modulates the strength of the downward circulation branch, discussed first by Dirks (1969) which in turn more strongly suppresses convection over the valleys. Finally, the over prediction of the extent of the anvil is likely a microphysics problem because of its occurrence in the 3D case.

7. DIABATIC HEATING EFFECTS

In this chapter, the dependence of the simulated MCS growth, propagation and structure on latent and radiational heating will be investigated. In Chapter 5, it was suggested that diabatic heating might influence the MCS dynamics through several mechanisms. The most important is the release of latent heat within the storm core which can account for the simulated warming at 350 mb (or 8 km MSL), which is reflected as a low level pressure decrease. The low level pressure anomaly then excites a supportive meso-β or possibly meso-α dynamic response. It is hypothesized that the meso-β response then governs the system propagation and the mesoscale flow fields. There was evidence that the effects are even beyond the regime of the convection itself, affecting such seemingly detached phenomena as the nocturnal downslope development some 300 km away.

It was also suggested that diabatic effects of the storm modulate the degree to which the mesoscale response is effective by modifying the stability profile to form a "wave channel" which effectively "traps" emmitted internal gravity waves and allows them to propagate considerable distances laterally from the storm. This effect seems to occur largely from destabilization of the cloud top by the effects of longwave radiation.

There was also evidence that the ice-phase precipitation falling from the anvil ahead of the storm, in conjunction with the radiative effects aloft help intensify the meso-β circulation by cooling the air

column aloft ahead of the MCS core. This results in an increase in surface pressure without the cooling of the inflow air at the surface ahead of the storm. Then the increased pressure gradient into the storm core augments the storms intensification.

Contrary to studies by others, it was suggested that the surface cooling by evaporation and melting of heavy precipitation in the up-branch of the circulation cell was of minimal importance to system maintenance. Although the atmosphere behind the system was generally stabilized, the low level density current was simulated (and observed) to flow at far slower speeds than the system propagation.

More insight can be gained into these diabatic effects in this modeling environment by rerunning the control experiment with selective changes designed to reveal the roles of individual processes. The differences with the control simulation presumably will reflect the role played by the omitted process. In this Chapter, four such experiments will be reported. The first experiment will be to eliminate the effects of latent heat by not allowing condensate to form. This will reveal the role of the dry mesoscale slope circulation and will demonstrate the degree to which it was modified by the convection.

Next, the development of precipitation will be studied by rerunning the control without allowing precipitation particles to form. As a result, latent heat by liquid will still be released. However, the condensate will not move out of the parcel within the updraft and subsequent subsidence within the anvil will act to evaporate much of the water. Then over the course of a parcel trajectory, there will be little net latent heat release. This simulation will demonstrate the importance of precipitating convection to system maintenance.

The role of cloud induced longwave radiation divergence will be studied by rerunning the control simulation with the longwave radiation attenuation by condensate turned off. Hence, for the purposes of longwave radiation, the atmosphere will be assumed to be clear. This will reveal the role of longwave radiative processes to the growth and propagation of the system.

Finally the effect of boundary layer precipitation induced cooling, i.e., the gust front, on system propagation will be investigated. This will be accomplished by rerunning 2 hours of the mature storm phase without allowing evaporation or melting of graupel and rain. In order to preserve the effects of virga aloft, melting ice will be put into the cloud water category instead of the rain category. The extent to which the resulting simulation diverges from the control will demonstrate the importance of the gust front to system propagation.

These four sensitivity tests will be described in the remainder of this Chapter. Each test, except the gust front test, was initiated from the predicted fields at 1100 MST, which is just prior to the first formation of condensate. Each was run through the time of the mature phase of the control simulation. This was chosen to be 2200 MST. The gust front test was initiated at 1800 MST and run until the mature time of 2000 MST. This was a critical time in the development phase when the gust front should be of greatest consequence.

7.1 Simulation Without Latent Heating

The simulation was begun from the predicted control fields at 1100 MST. As the control convection deepened, differences between the two simulations became apparent. The 1500 MST prediction is given in Figure 7.1. Recall that this is the time in which the control simulation

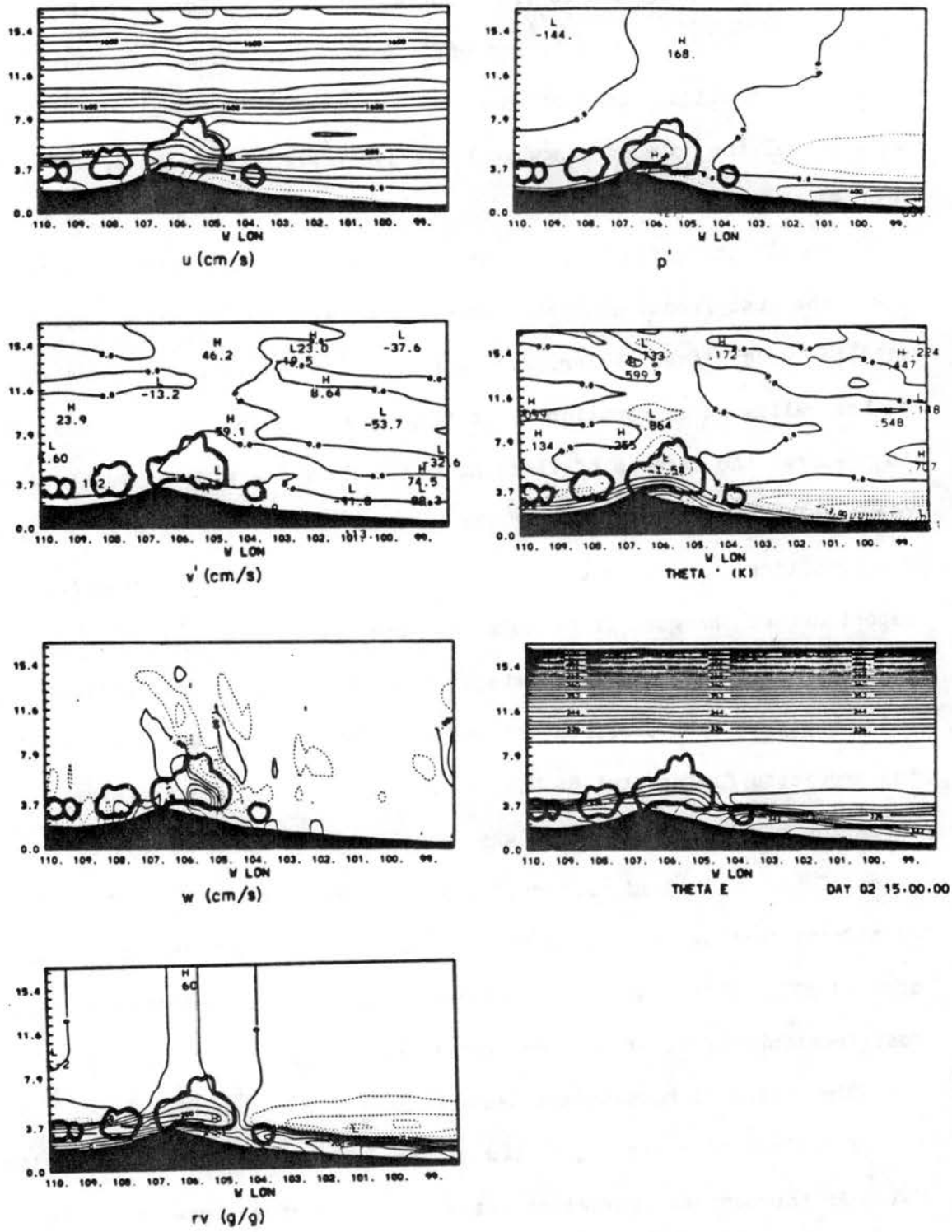

Figure 7.1. Same as Figure 5.1, except for no latent heat case and time of 1500 MST. Cloud outline is of saturated region.

(Figure 5.9) entered stage 3 characterized by deep propagating convection. Up until this time, ridgetop convection did not link up with the mesoscale surface convergence.

At this time, the surface u component switches sign near 106.5 W longitude for both the dry and control simulation. The w wind component shows a shallow vertical motion regime in the dry case, reaching only about 5 km MSL or 2.5 km AGL. Above this level, there is a upshear tilting w response associated with an augmented mountain wave effect. In contrast, the control simulation w field has deepened strongly to 12 km MSL.

The return zonal flow, in the dry case, seems to be forming between 4 and 7 km MSL, and has magnitudes of up to 4 ms^{-1} above the ambient flow at the 5 km MSL level. The zonal flow is increasing downwind of high pressure centered just downwind and about 2 km above ridge top. The high pressure extends toward the west; this makes the westerly acceleration favored over easterly acceleration. The control simulation, on the other hand, shows little u acceleration at low levels. Instead, the flow between 6 and 13 km MSL seems to be accelerating most strongly. It is apparent that the flow moving in excess of the system propagation speed of 10 ms^{-1} is effected most strongly. High pressure in the control simulation is centered near 10 km MSL, which is near the tropopause.

It is also found that the eastern upslope flow has deepened slightly in the control case over the dry case. In addition, the control slope flow has increased in strength over the dry case by 1-2 ms^{-1}. This is an increase of as much as 50% near the convection. The slope flow increase is interperted as a response to the convection.

In the dry case, the boundary layer is considerably warmer and more moist near ridge top in the case with no latent heat release. This can be attributed to the weaker vertical motion and lack of an ability to rapidly exhaust warmer temperatures through moist convective towers.

It is significant that at 1500 MST simulation time, the maximum surface convergence in both the dry and control case coincide verifying the notion that up to this point the convection has not altered the natural surface convergence pattern. It is evident, however, that the intensity of the convergence has been increased by the moist convection.

It is now of interest to view the time of 2000 MST, which is when the control simulation is at peak intensity. The fields predicted in the dry simulation are displayed in Figure 7.2 and can be compared with the control simulation depiction given in Figure 5.10. While the dry simulation has evolved very little from the 1500 MST time, the control simulation has been transformed into a powerful MCS. The most significant change in the dry simulation is the apparent development of an organized deep mountain wave response to the low-level circulation. There has been no significant change in the position of the surface convergence, however it has begun to slope upshear more strongly and has been vertically suppressed as a result of the deep gravity wave response.

High low-elevation moisture advected upstream has been advected within the return flow at 5km MSL and has moved east aloft as far as 103 W Longitude, (about one-half the distance from Limon to the Kansas border). Examination of the temperature response shows that the ridge top continues to be warm while the plains are relatively cool. Geostrophic adjustment to the dry slope flow has produced a cyclonic

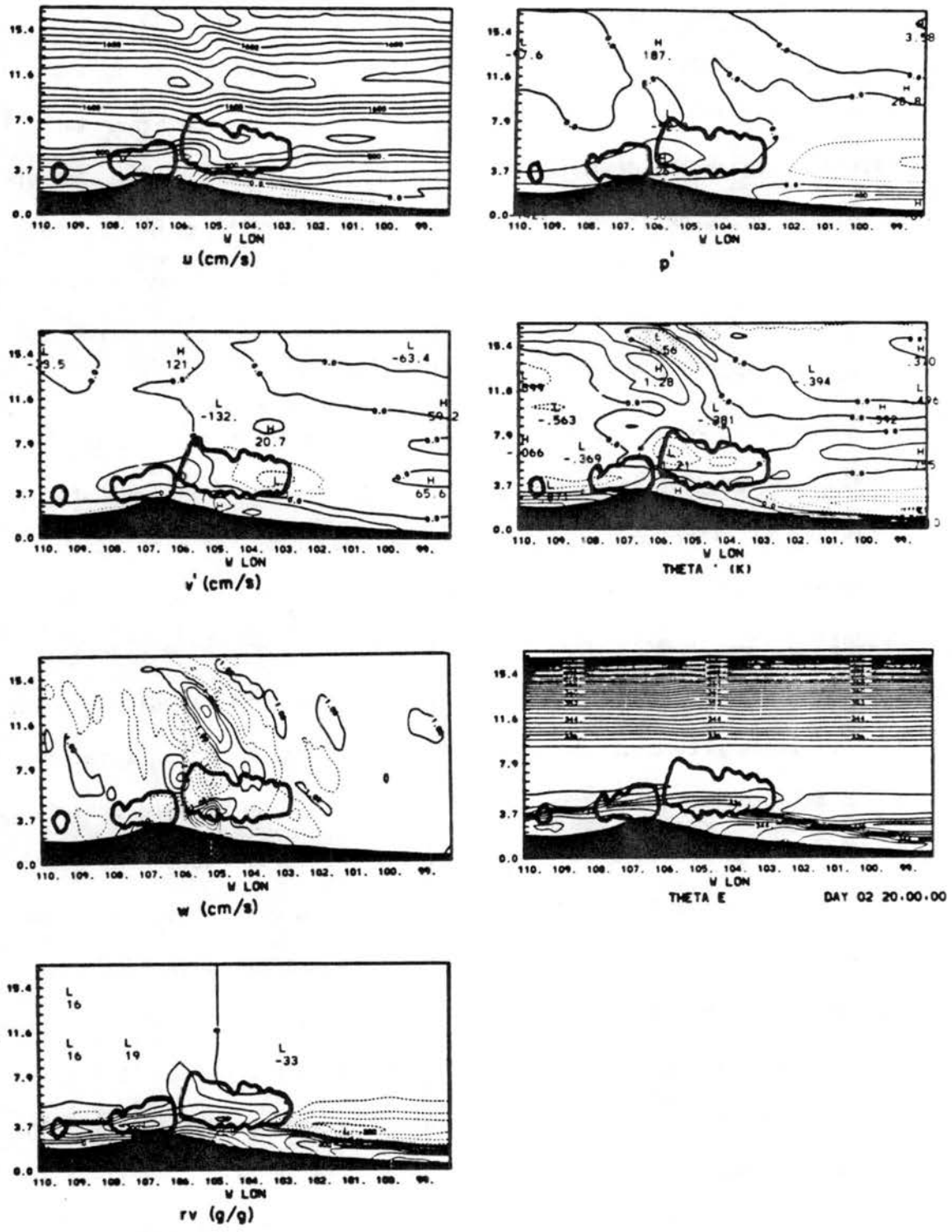

Figure 7.2. Same as in Figure 7.1, except at 2000 MST.

shear in low level v about the convergence zone at 105.5 W and anticyclonic shear about the high pressure at 5km MSL.

In many respects the center of the dry solenoid at 105.5 W is like a boundary-layer version of the solenoid in the control experiment which extends through the depth of the troposphere. In both cases, the up-branch is drifting at the speed of the mean wind (the mean wind is near 0 in the layer below 5 km MSL). It seems that the MCS may in some ways be simply a deepened slope flow solenoid powered by moist rather than dry convection.

Quantitative evidence of the effect of latent heat on mesoscale development is displayed in Figure 7.3, which shows the structural evolution of selected variances over the coarse of the simulation. Compared to the results for the control case, less mesoscale growth is evident. This is most true for the w and θ fields. Some mesoscale growth is evident in the dry case, however, the control has considerably more variance growth in the 250-1000 km wavelength than is attained in a dry simulation. This demonstrates that most of the mesoscale variances of the control arises from the effects of released latent heat energy.

The dry simulation, in some respects, should resemble the mountain boundary layer simulations performed by Banta (1981). In both this case and that of Banta (1981) the effect of latent heat is neglected. These results, however, are not consistent with Banta's findings that the mountain surface convergence line propagated eastward with time. There are several reasons why this simulation should differ. The first is that the "dry" days which Banta studied were characterized by a deep westerly flow extending down to lower elevations not present in this case study day. That, in fact, is why the days were "dry". As a

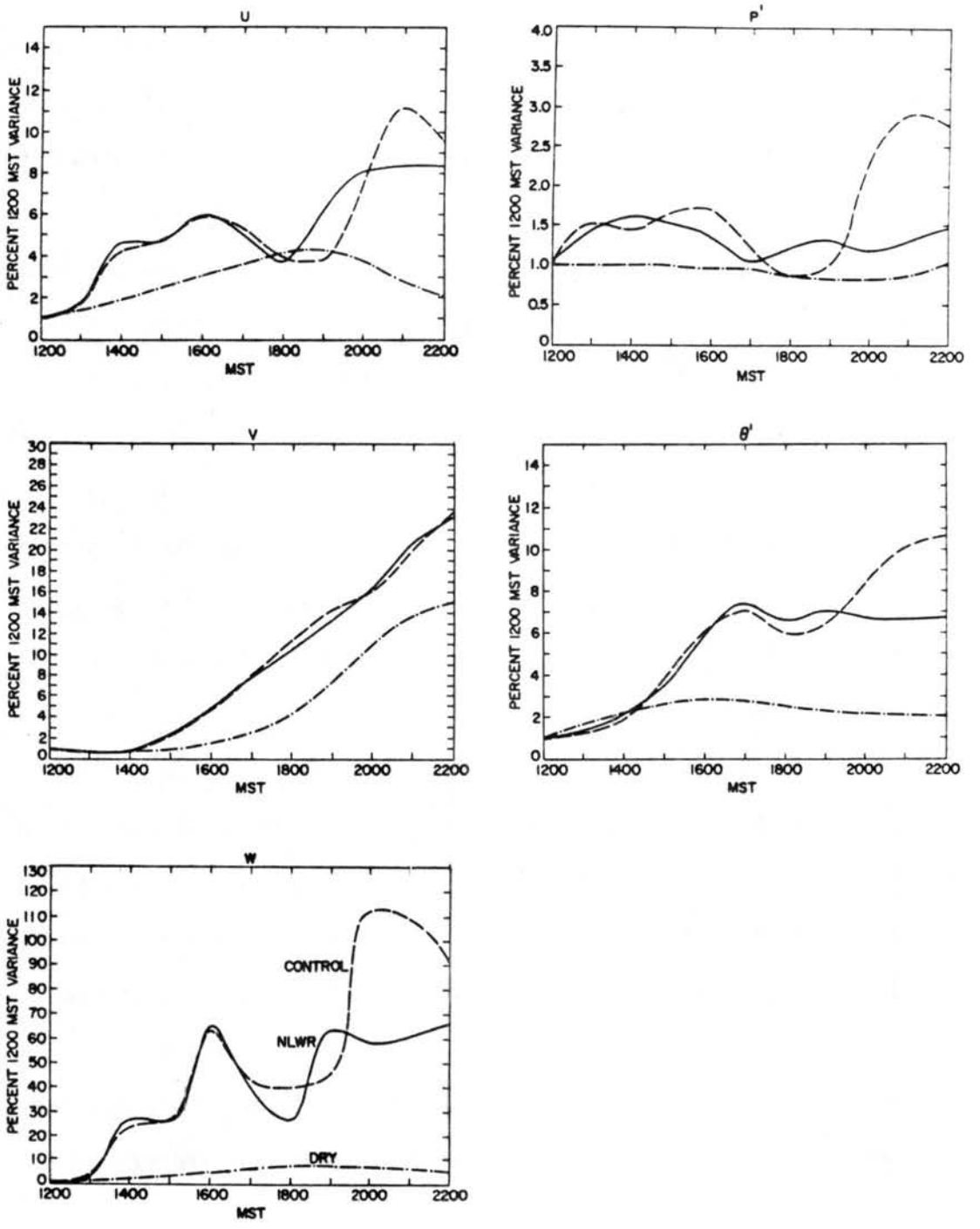

Figure 7.3. Meso-α variance (as in Figure 5.22), except displayed for 3 experiments. Control experiment is dashed line, NLWR is solid line and dry (no latent heat0 is dash-dot line. Vertical axis is 1200 MST meso-α variance (horizontal wave numbers 1-4 and vertical wave numbers 1-2) and horizontal axis is time beginning at 1200 MST and ending at 2200 MST.

result the low level mean flow had a mean westerly component which even this analysis predicts should move.

Second, Banta concentrated on the boundary layer evolution and used much finer horizontal and vertical grid resolution in addition to looking at smaller scale topography. As a result, Banta studied local shallow slope flows which could be within a single vertical grid interval for this case. In fact, the regime Banta was studying would likely exist entirely between the ridge top and the simulated mean convergence at 105.5 W in this case. The so-called valley breeze, or slope circulation on the scale of the entire mountain barrier, was not studied by Banta. The Banta type solenoid may be yet another scale of circulation which occurs early in the morning. It is likely, however, that as a circulation of Banta's type reaches the valley breeze convergence line it will move no further and dissipate with the changing scale of governing dynamics.

7.2 No Precipitation Experiment

Besides the effects of precipitation unloading, this experiment will test the effects of precipitation as a means to permanently incorporate latent heat energy into the system. In this case, which considers only cloud water condensate, the moist adiabatic process is completely reversible. Therefore, much of the heat released will be reabsorbed within sinking motion and mixing downwind of the updraft. This experiment will shed light on the ability of the system to organize with non precipitating convection.

Again, the analysis is begun by examining the fields at 1500 MST, when the control simulation enters stage 3. This experiment looks quite similar overall to the control at this point. There are some important

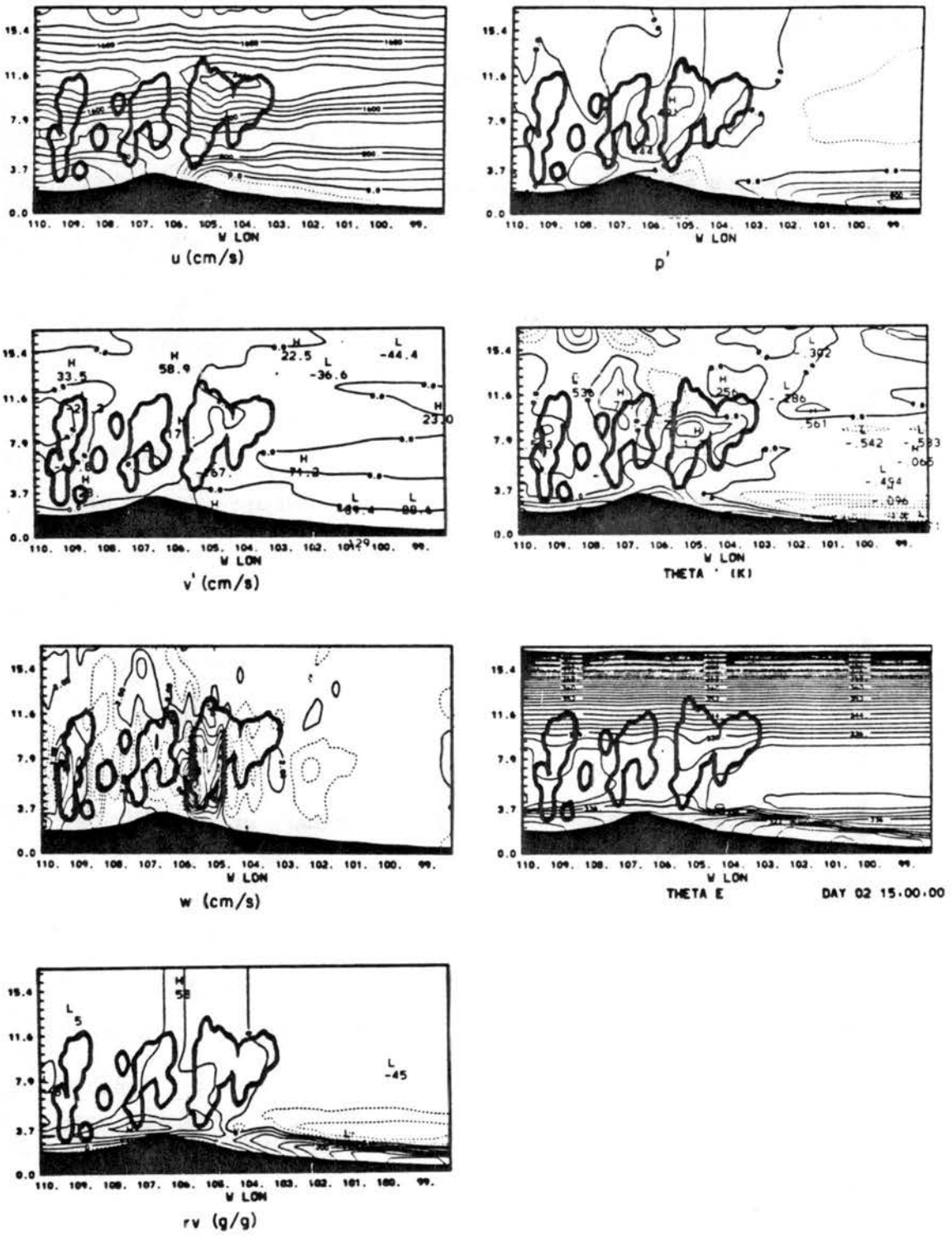

Figure 7.4. Same as Figure 5.1, except for cloud water only case and at 1500 MST.

differences, however. First, the primary updraft appears considerably more concentrated and strong than the control case. At the same time, the eastern rainshaft is much weaker and nearly dissipated. In both cases the surface convergence zone is located near 105.5 W. However the no precipitation experiment seems more well mixed in boundary layer momentum over ridge top leading to a stronger surface convergence. This effect can be attributed to the stronger evaporation of moisture behind the storm which is manifested in the near total evaporation of cloud laterally from the dominant updraft. It seems that the lack of precipitation leads to less resistance from the compensating subsidence and thus allows a greater development of the core updraft, at least initially.

The temperature and pressure response seems to be weaker aloft in the no precipitation case. The surface low seems to be stronger. This is likely due to the fact that the non-precipitating cloud carries almost all of the condensate away from the core and does not allow any precipitation cooling in the region of the primary updraft.

The fields at 1800 MST are displayed in Figure 7.5. At this time the two experiments have diverged considerably. The most important point is that at this time, the no precipitation experiment has failed to move the surface convergence zone at 105.5 W and has thus apparently decoupled from any mesoscale support. In both cases the w field reveals the trapped gravity waves underneath the anvil. The control case, however is rooted into the rich boundary layer air while the no precipitation experiment has become decoupled. This results in the demise of the system core.

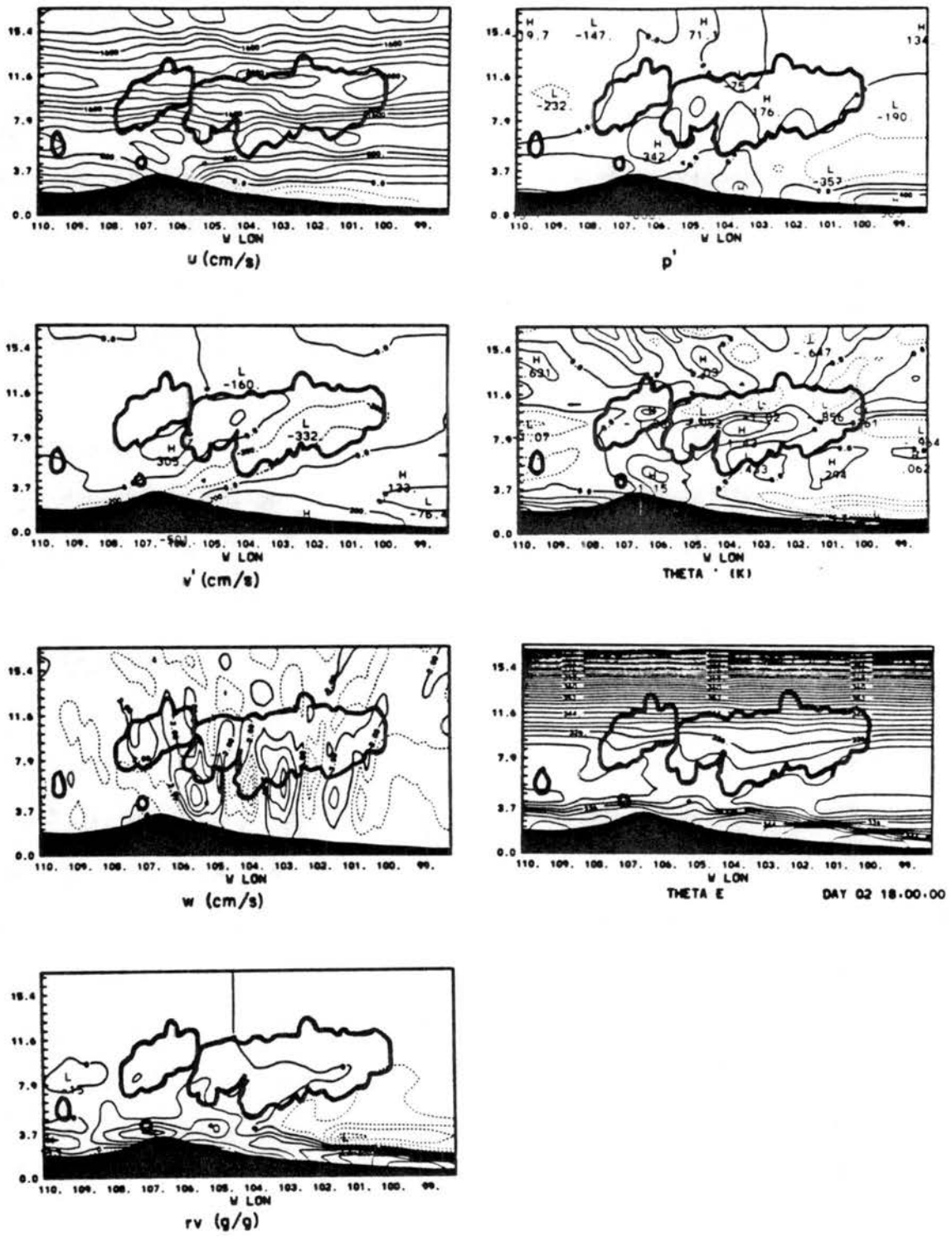

Figure 7.5. Same as Figure 7.4, except 1800 MST.

Reviewing the history of this simulation prior to this time, it can be seen that the decoupling occurred as the system entered the suppression zone between 104 W and 105 W near 1630 MST. Unlike the precipitation (control) case, the suppression decoupled the system core from the boundary layer and it could not regenerate. Recall that, in the control, the intrusion of a precipitation shaft rejuvinated the control simulation as it left the suppression zone. The result of the elimination of precipitation was the residual gravity wave train seen in Figure 7.5 and the loss of the system core.

Because the core no longer dominated, the westward propagating vertical motion regime seemingly restarted convection at 105.5 W by 1900 MST, in the region of the mountain wave favored surface convergence zone. This was the region of the western rainshaft in the control experiment. This time, the surface convergence zone did move with the convection aloft. The situation at 2000 MST is displayed in Figure 7.6. Based on the pressure field, it is not obvious that the surface convergence is at all responding to the convection totally. In fact, it seems that it is at least in some part moving to the region at the base of the steep slope primarily as a result of surface cooling. This is further evidenced in the general weakening of the easterly surface flow to the east. It is likely that cooling will begin sooner in this case than the dry case simply because the surface has been insulated from much of the shortwave for some time because of the upper level cloudiness.

Again at this time, the upper level temperature response and the pressure response at all levels is exceedingly weak in comparison to the control experiment. By 2200 MST, the system core moves eastward,

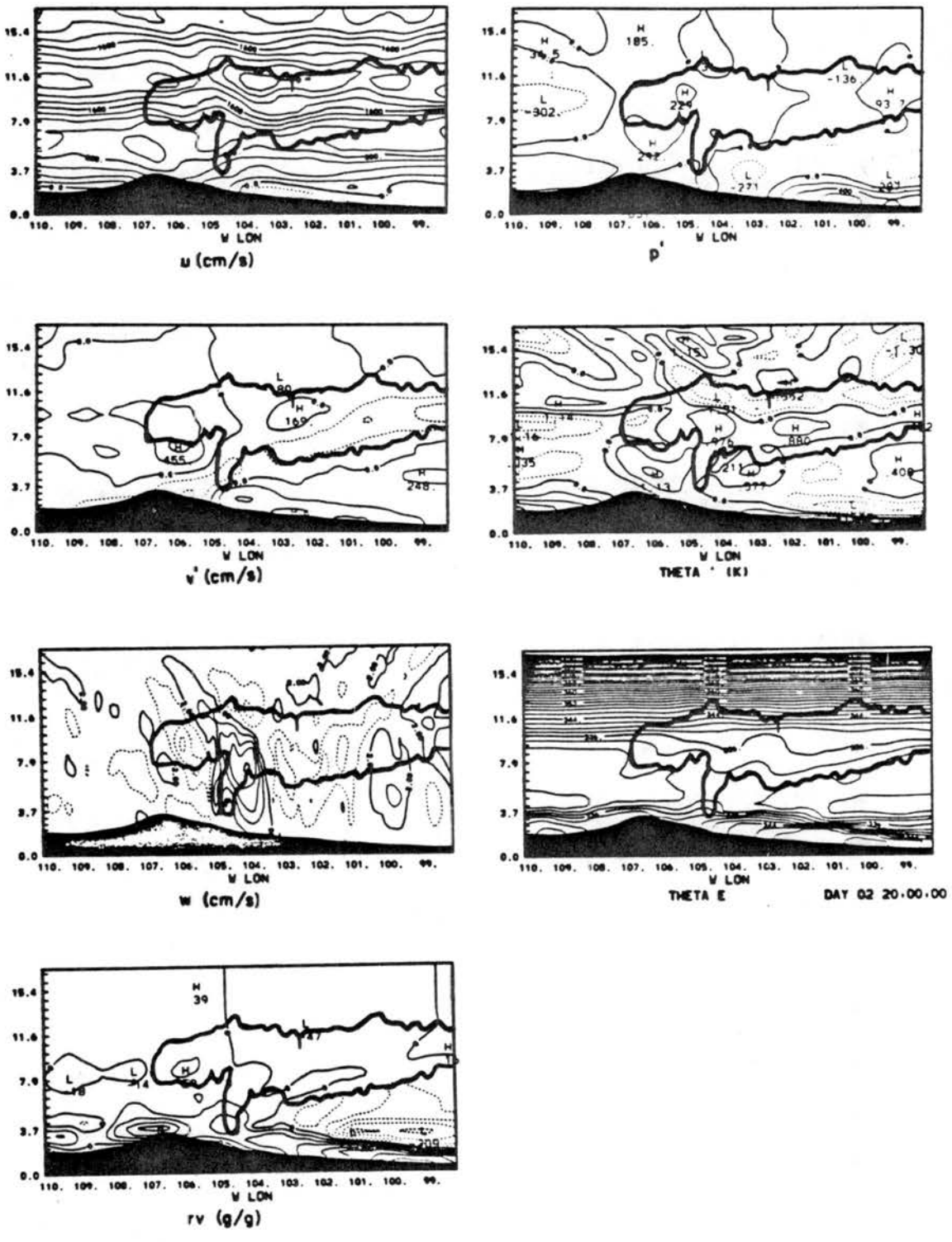

Figure 7.6. Same as Figure 7.4, except 2000 MST.

however the surface convergence zone remains behind. As a result, the system weakens considerably.

It seems that three important effects occurred in the absense of precipitation. First, it seemed that the temperature and pressure response was considerably reduced over the control simulation. This is a predictable effect of having less net latent heat release. Second, the system which tried to form in a similar manner, failed to link up to the surface convergence pattern. In one case, the difference seems to be directly attributable to vertical motion induced in the control experiment by the penetration of a rainshaft into the inversion layer. The third effect is that the convection does not stabilize the boundary layer in the region of the system core. Hence, as the system moves eastward, induced vertical motion to the west initiates competitive convective regimes which lessen the likelihood for a dominant convective core.

Many similarities between the no-precipitation case and the control case were apparent. One similarity is the existence of trapped gravity waves beneath the anvil which acted to rejuvinate the convection to the west. The convective cores, as they existed, moved eastward at the speed of 10-12 m s^{-1} as in the control simulation. However, they could not survive the gravity wave induced fluctuation in mesoscale support.

From these experiments it is concluded that precipitation is important and probably necessary in maintaining time continuity in the meso-β response. The fact that the simulation tended to develop in a similar fashion necessitates the use of the word "probably" because it is not obvious that in a slightly different environment the system might be long lived. It can also be concluded that the precipitation strongly

increases the pressure and temperature response in the system. This, of course, is intuitively obvious.

7.3 The Effect of Cloud Induced Longwave Radiation Heating

This section explores the sensitivity of the MCS growth, propagation and strength to longwave radiation effects induced by the absorption and emmission of condensate. To do so, an experiment was run where the attenuation of longwave radiation by condensate was removed. It was speculated, based on the analysis of radiation produced temperature tendency, that an important effect of radiation is to form an unstable layer near anvil top which acts to trap internal gravity waves emitted by the storm core. In addition, it was deduced that an important effect of the overall cooling produced by longwave divergence at cloud top was to cool the air column ahead of the storm and increase the pressure gradient between the system core and the atmosphere ahead of the storm. These will be effects of particular interest in this section.

The no-longwave radiation experiment (hereafter referred to as the NLWR experiment) was initiated at 1100 MST from the control predicted fields. The two simulations diverged slowly. Since radiation effects build as the cloudiness builds, the greatest differences are expected as the sun sets. Some differences can be already seen at 1600 MST. The NLWR fields are displayed for this time in Figure 7.7. It is first obvious that the anvil or stratoform cloudiness is somewhat deeper in the control case.

An important difference is in the w field aloft of the system core. Even at this early hour, the propagation of the deep internal gravity waves into the lower stratosphere associated with the system core, is

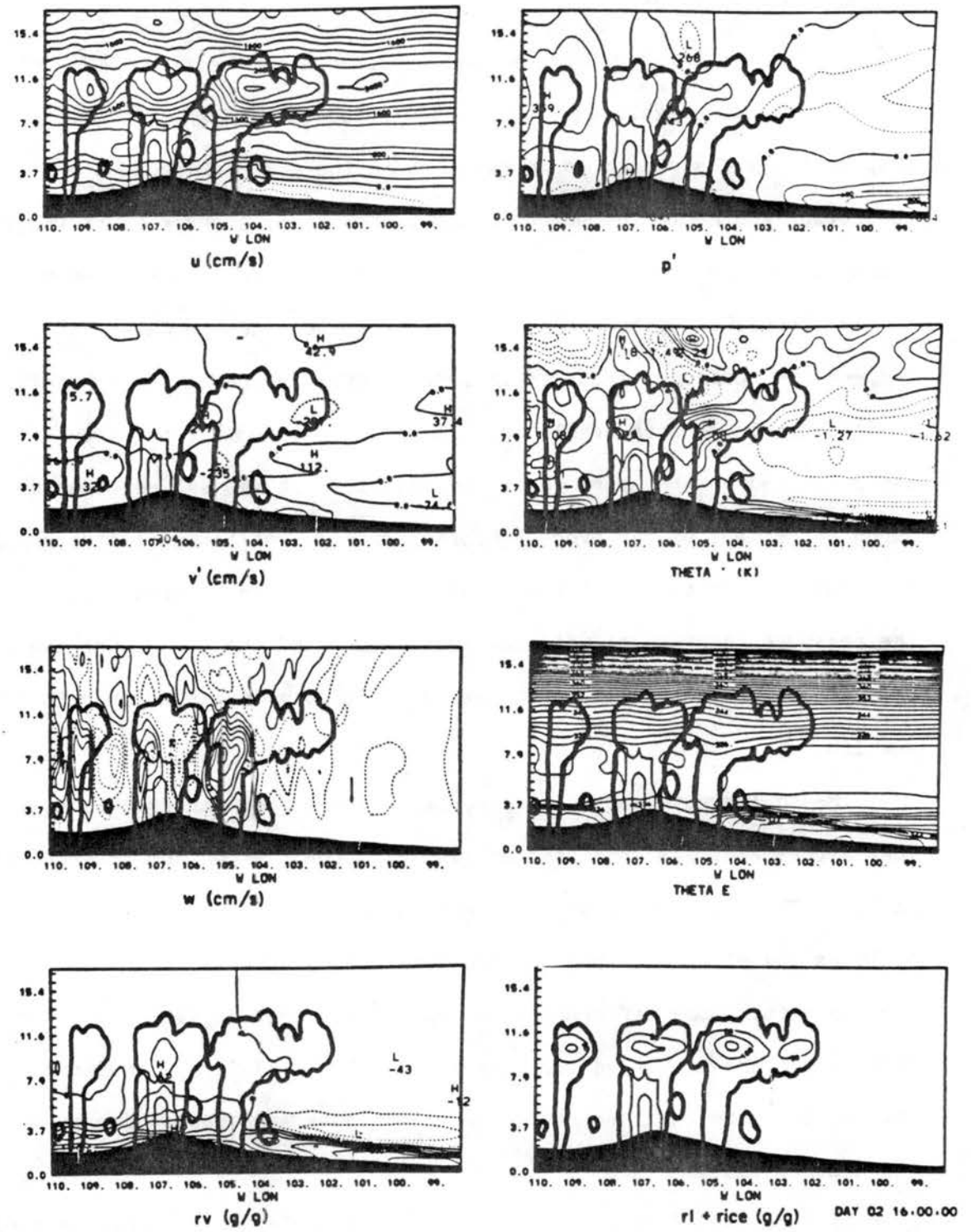

Figure 7.7. Same as Figure 5.1, except for NLWR experiment and at 1600 MST.

somewhat less pronounced in the NLWR case. This is especially true downwind of the system core. It is consistent that the low level wave induced vertical motion forced to the east of the storm core is slightly reduced in amplitude in the NLWR experiment. These features are early signs of the weakened effect of wave trapping by the NLWR case.

Also, at this time, the low pressure ahead of the storm near the surface has been reduced in amplitude and does not even register a center in the NLWR case. At the same time, the pressure amplitude in the lower stratosphere, has increased from a low center of -0.18 mb to one of -0.27. This demonstrates that in the vicinity of the MCS core, pressure affects in the troposphere have weakened while those in the stratosphere have increased. This again suggests the leakage of more energy from the convection region into the stratosphere.

Comparison of perturbation temperature between the two cases again tell a similar story. θ_e temperature perturbations are reduced (from the control case) within the troposphere and increased in the stratosphere.

During the next hour began the critical time of suppression within the control experiment. The 1700 MST time had. perhaps the most feeble meso-β response in the control case. This did not seem to be the case in the NLWR experiment. At this time, unlike the control, mean upward mesoscale vertical motion existed within the system core. Consistent to the control, the laterally propagating internal waves were reduced in magnitude. These results suggest that the hypothesized weaker trapping of gravitv wave energy has worked to the advantage of the system core at this time. In the control case, the westward propagating internal wave helped diminish the flow to the core surface convergence. In the NLWR

case, however, the weakened trapping allowed a greater concentration of upward vertical motion to persist within the system core, preventing the total collapse.

In fact, the time series of peak vertical motion for the NLWR case (Figure 7.8) shows considerably less temporal variability over all. This behavior seems to be directly attributable to the wave trapping affects of the anvil. To some extent these features are exaggerated by the two dimensionality of the problem. In three dimensions both the waves weaken more with distance and the anvil will not be as strong.

It is also evident that the anvil in general has weakened and is beginning to break up to the west of the core in the NLWR case. This may be suggesting that the anvil dynamics are somewhat dependent on the radiation destabilization. This is consistent with the findings of Chen (1986). The dependence may be partially a result of the amplitude of the wave activity which seems to be responsible for much of the anvil level mesoscale vertical motion. There is little evidence of convective scale vertical motion within the anvil, even when the plot resolution is increased.

The NLWR MCS develops generally parallel to the control case. At 2000 MST the system appears as in Figure 7.9. The storm movement has remained similar to that of the control and the surface convergence zone position has not changed dramatically. The meso-β vertical motion response in the system core is considerably reduced and more prominent vertical propagation of laterally emitted internal waves is noted. At this time, there seems to be a greater stratospheric gravity wave response east of the center in the NLWR case than in the control case. The opposite is true within the troposphere. To the west of the system

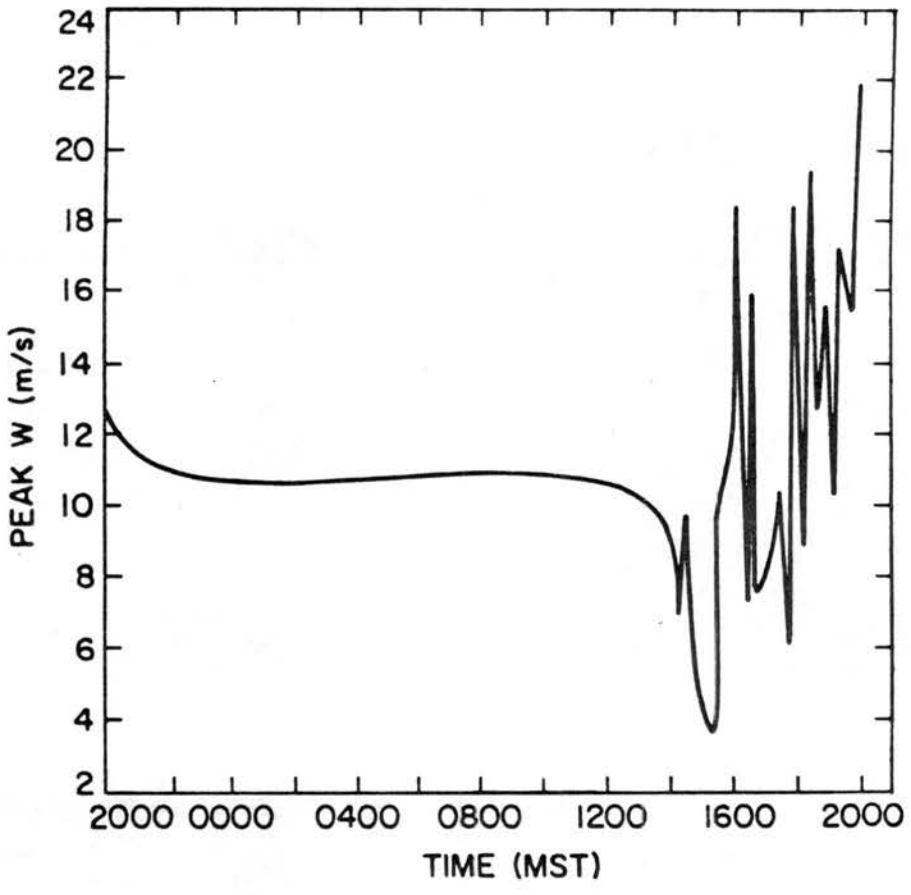

Figure 7.8. Same as Figure 5.12, except for NLWR case.

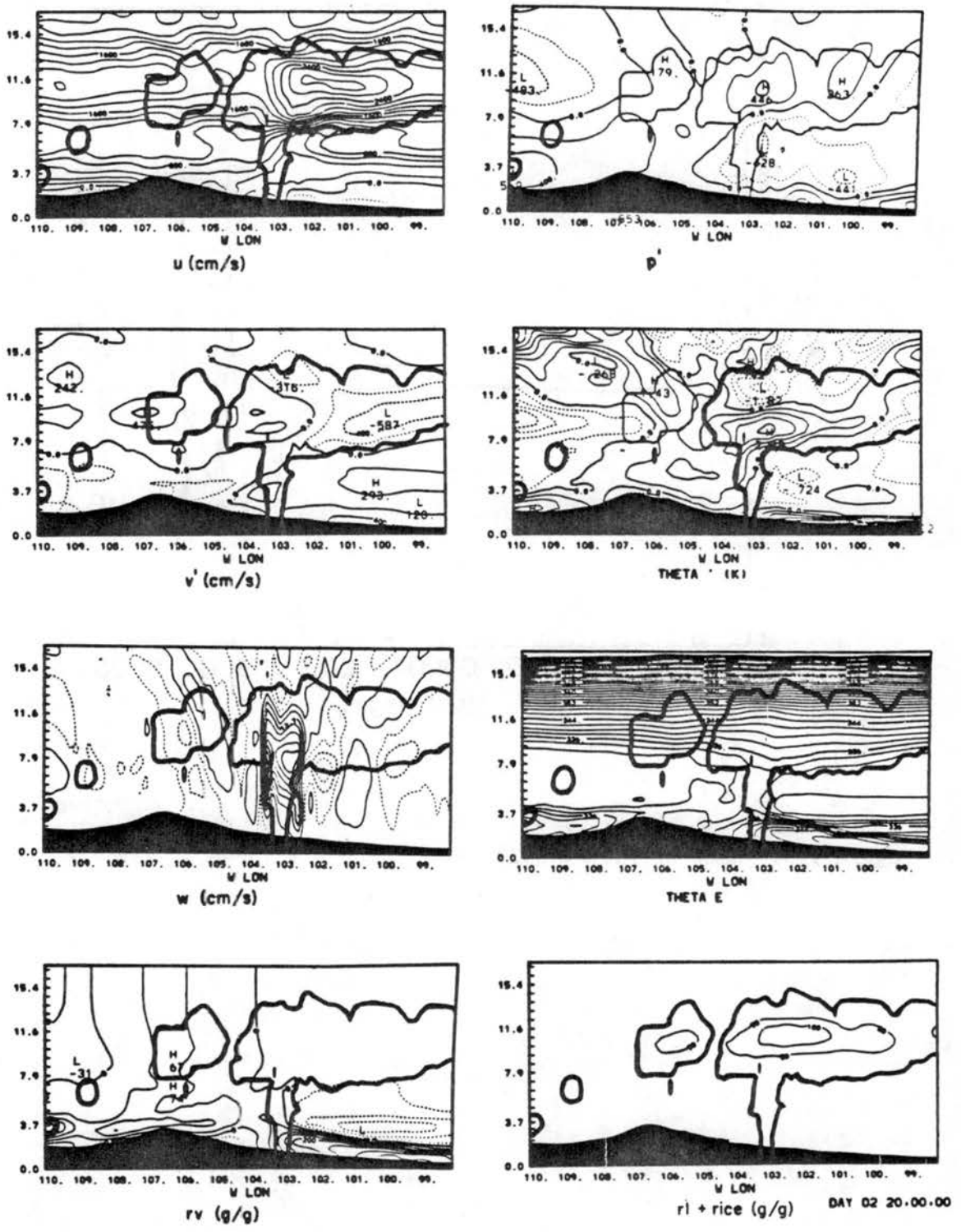

Figure 7.9. Same as Figure 7.7, except at 2000 MST.

core, the vertical motion fields compare more closely, but still display a similar increased vertical wave propagation aloft to the stratosphere.

At this time the pressure low associated with the core of the control case is roughly double in amplitude that of the NLWR case. The temperature response within the system core, however, is only of 20% less amplitude. It is interesting that mid level cooling to the east of the rainshaft is somewhat increased in the NLWR case. This seems to be reducing the magnitude of the low level low.

The western rainshaft has disappeared in the NLWR case and the western anvil is generally weaker overall. This may be attributable to the weakened trapped wave system combined with a more stable anvil. In order to understand the extent to which the wave trapping mechanism has been altered in the NLWR case, the Brunt-Vaisalla frequency field is displayed in Figure 7.10. Comparing with Figure 5.28, it is evident that much of the wave channel definition is lost in the NLWR case. However some weakness in stability still exists. This may be attributable to continued release of latent heat by sublimation as ice crystals continue to grow both as they drive the parcel toward ice saturation and in response to the passing vertical motion fields. The fact that the wave channel has weakened but not dissappeared is consistent with the existence of some apparent trapping especially downwind of the system core.

The w field at 2200 MST is displayed in Figure 7.11 for the NLWR experiment. Note the reduced extent to which downwind trapped wave modes are visible. At this time, there seems to be a greater degree of concentration of vertical motion within a single updraft than with the control case. Since the sun has set, the difference in trapping is

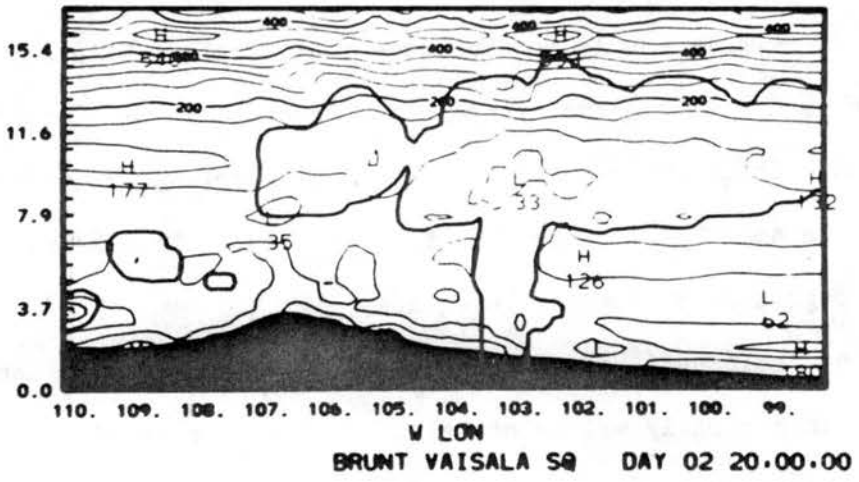

Figure 7.10. Same as Figure 5.28, except for NLWR experiment.

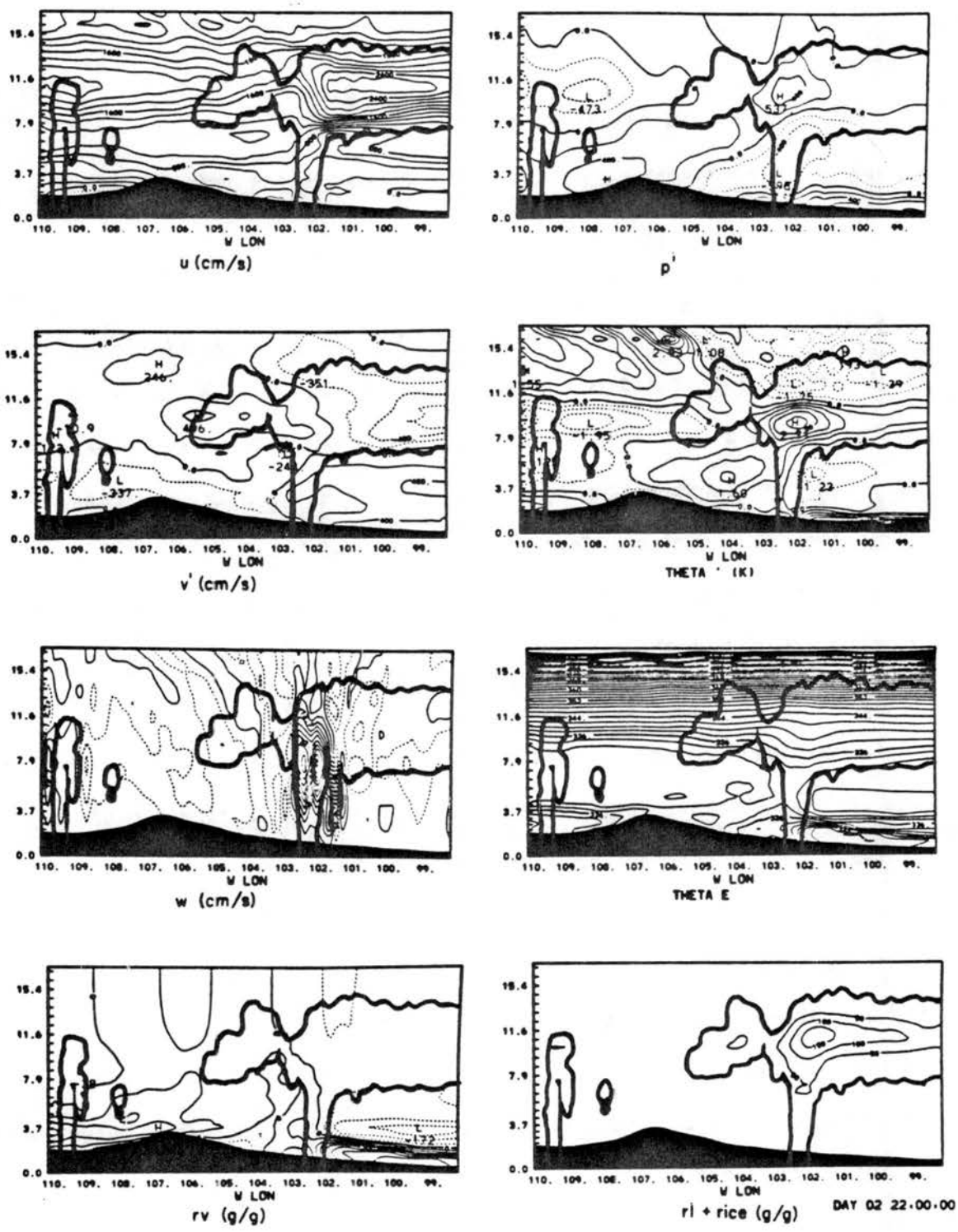

Figure 7.11. Same as Figure 7.7, except at 2200 MST.

likely much more pronounced at this time. It seems that the system core of the control case is clearly inducing vertical motion more strongly at lateral locations away from the system core. Its affect of weakening the core and spreading the vertical motion pattern is clear when compared to a case (such as the NLWR case) with the trapping effect reduced.

It has been observed by Cotton (personal communication), the author and others that a developing nocturnal MCS undergoes a transformation during this time of 1-3 hours after sunset, whereby the core convection weakens and a more general anvil system evolves. These experiments may very well be demonstrating the mechanism. These results indicate a strengthened trapping effect after sunset which acts to retain a greater portion of the released convective energy as trapped internal gravity waves. At the same time, the destabilized anvil is more conducive to unstable convection of its own. The result is that individual packets of vertical motion form throughout the anvil reducing the inflow into the system core and as a result, the strength of the system core. Hence the system expands to the meso-α and becomes a MCC (mesoscale convective complex).

The indirect effect of longwave radiation is apparent in wave space. Figure 7.12 shows the power spectrum for the relevant variables of the NLWR case at 2200. Comparing with the similar spectrum plot in the control case, several points may be made. The increased meso-β wave activity (horizontal wave numbers 5-8 or wavelength 200-125 km) is strongly apparent in the θ' and p' fields. The increased meso-β activity cannot be seen on the w plot because it is dominated strongly

by meso-γ activity. The slight response of the v field in this spectra region indicates these waves have at least some inertial response.

Note that the meso-γ w response is strengthened in the NLWR case. This is because of the strong convective activity which is a result of increased MCS core strength in the NLWR case. It is interesting that the balanced mesoscale response, manifested in the meso-α v response (wave numbers 1-4) is largely unaffected at this time by the radiation scheme. This also seems to be the case with the vapor field which moves only be more persistent, and thus balanced motion fields.

The meso-α variance evolution for the NLWR case is compared to the control and dry case in Figure 7.3. It is clear that the meso-α response of most variables in the control case exceeds that of the NLWR case near 2000 MST when the system was found to be strongest. The gap seems to be closing by 2200 (when the NLWR experiment was terminated), however. The exception is the v component, which is roughly the same as the control throughout the period. It is interesting that the NLWR and control case solution clearly diverge at sunset (1900 MST) for all variables analyzed except v, with the control growing more strongly.

The strong meso-α growth of the control is apparently a transient response, since it is not reflected in the v component. Comparison of meso-α spectral plots at 2200 MST, indicate largest differences are in horizontal wave numbers 2-4 (wavelength 250-500 km). This suggests that the increased meso-α variance is again related to the gravity wave phenomena. Perhaps the energy first builds in the meso-α scale and then moves to the meso-β scale. Comparison of the control spectrum at 2000 MST to that at 2200 MST seems to support that notion. In physical terms, this suggests that a strong meso-α core is broken up into meso-β

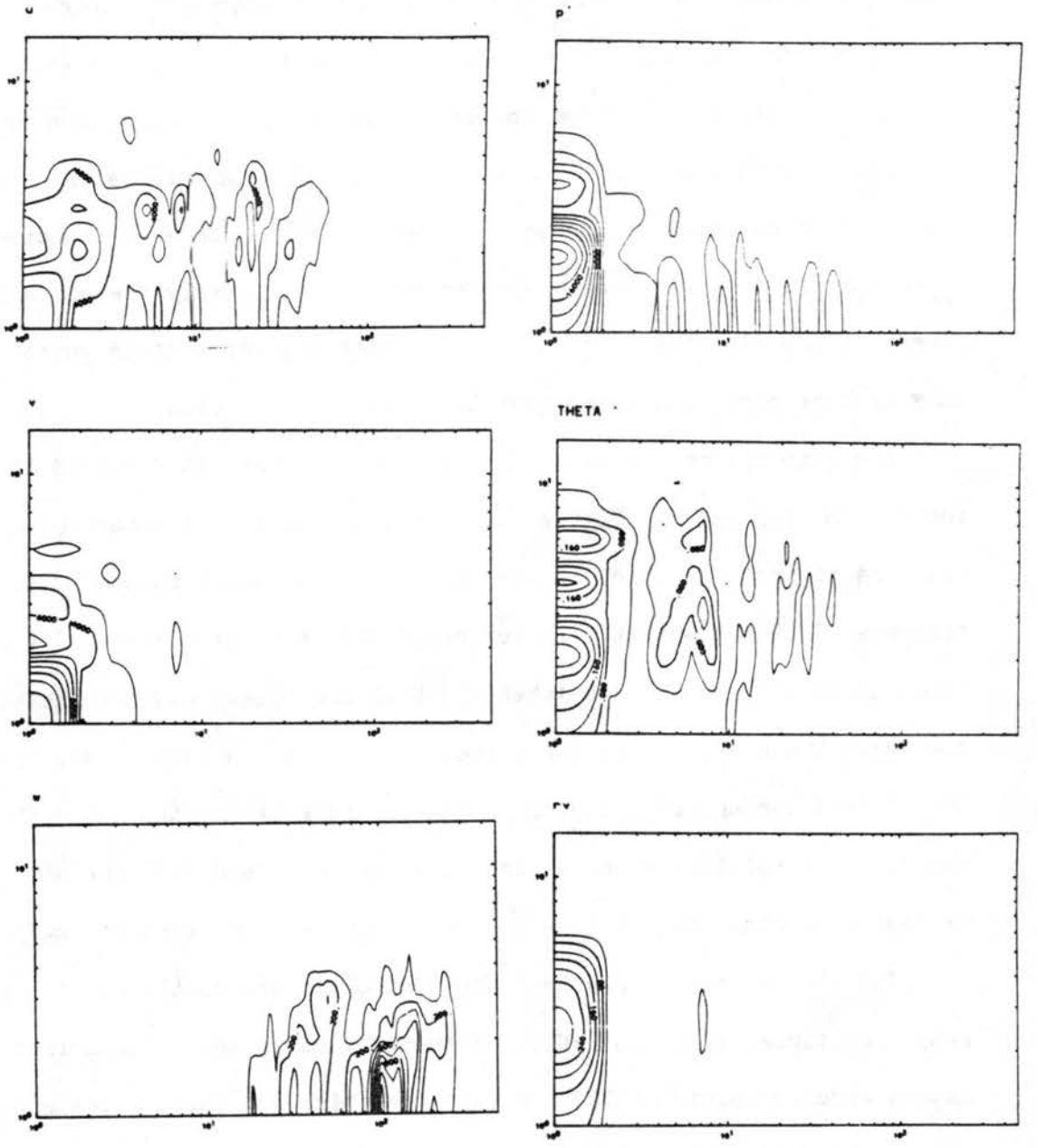

Figure 7.12. Same as Figure 5.20, except for NLWR case at 2200 MST.

circulatory systems by the trapping of gravity waves within and below the anvil. This is thus another way of viewing the transition to "popcorn" convection.

The effect of cloud induced longwave radiation heating on accumulated surface precipitation is displayed in Fig. 5.13. The comparison between the NLWR and control experiment is quite close west of 104° Longitude and prior to the period of suppression in the lee of the foothills. These are the daylight hours when radiation induced cloud-top destabilization is relatively weak.

The rainfall east of 104° Longitude is most affected. The most obvious impact of cloud induced longwave heating (or cooling) is the overall lessening of precipitation. The relative rainfall maxima are also weakened because of the longwave effect. This is consistent with the implications of the NLWR spectra which indicate an overall weakening of convective scale motions by longwave induced heating of mid-levels or the base of the anvil.

It is interesting that the strongest rainfall peak at 103° Longitude, occurring with the strong mesoscale organization of the control at 2000 MST, was much weaker in the NLWR case. This is consistent with earlier arguments suggesting that wave trapping may have led to an increase intensity of the core oscillation following sunset. In fact, points downwind of 103°W (near the region where the system was located as the sunset) indicate a prominent oscillation of precipitation on the length scale of around 75 km in the control which is weaker in the NLWR case. For a system speed of 10 m s^{-1}, this is about a 2 hr period which was shown to be the period of oscillation of the core in the control case. These results again support the hypothesis that cloud

induced longwave heating is augmenting the amplitude of the tropospheric gravity wave response to convection through trapping and that this effect is more noticeable at night.

In summary, the NLWR experiment has succeeded in verifying the hypothesis that the internal waves are trapped primarily by radiative effects. The long wave cooling at cloud top and warming at the anvil base significantly destabilize the upper anvil and increase the stability below slightly. This slows the propagation of the internal waves in the destabilized zone refracting some of their energy back down. It has also shown that the rainshaft to the west of the system core was somewhat dependent on the extent to which these waves are trapped. It showed that as more gravity-wave energy becomes trapped, the system core is weakened and the system dynamics spread laterally. It further demonstrated that the radiation added to the overall strength of the solenoid only slightly and did not affect the propagation at all. The stratospheric response, on the other hand, increased more dramatically as a greater portion of the energy leaked through the anvil in the NLWR case.

7.4 Sensitivity to Gust Front Forcing

It seemed most likely from the analysis of the control experiment that boundary layer precipitation induced cooling was playing a minor role in the system propagation. Because it has been hypothesized that evaporatively-driven density currents are important to the propagation of squall lines (Moncrieff and Miller, 1976), it was desirable to perform a simple test to examine its importance.

A 2 hour period of the control simulation was rerun from the time of 1800 MST until the time of 2000 MST without rain and graupel

evaporation or melting within the boundary layer. The resultant fields at 2000 MST are displayed in Figure 7.13. One apparent difference is that the main updraft core has already begun to split. This happened in the control case as well within 15 minutes after this time so this may be only a minor difference.

Both the low pressure response at low levels and the high pressure response within the anvil in the vicinity of the system core has weakened. In addition, the warm core has weakened in intensity by over 25%. At the same time, the amount of condensate within the anvil has been reduced. These affects may be partly the result of a lowering of vapor content to the west of the system core. This is obviously the result of the lack of precipitation evaporation into the subsiding air. Because the drier air is not cooled by the evaporative and melting effects, it is more readily entrained into the updraft. This has the effect of cooling the updraft, hence the overall intensity is thus reduced.

It is interesting that the surface convergence into the system core is nearly the same or slightly greater than in the control. This indicates that the convergence is not forced by a density current, but is caused by deep atmospheric temperature response associated with internal gravity wave oscillation. Song (1986) found a similiar response of the sea breeze convergence zone to deep convection in the Florida environment.

Despite the slight reduction in intensity, the MCS movement is nearly identical to the control case after two hours without boundary layer cooling. This supports the hypothesis that the density current is not important to the storm propagation. These results further suggest

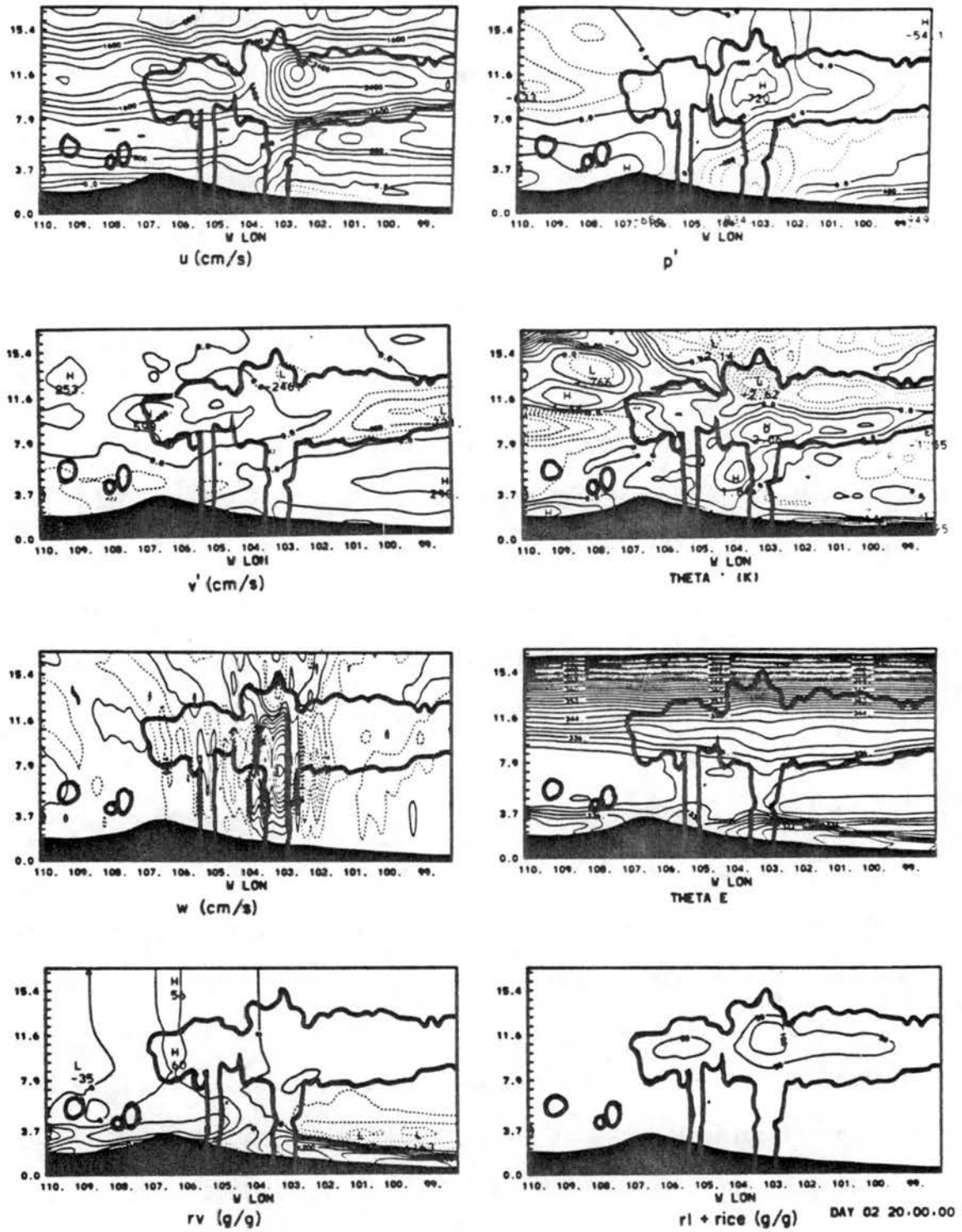

Figure 7.13. Same as Figure 5.1, except for no precipitation cooling case at 2000 MST.

that the rain and graupel precipitation are responsible for much of the moistening behind the MCS. In addition, low level precipitation cooling helps protect the up-branch from the destructive entrainment of drier air from the west and thereby leads to a more intense system.

8. SENSITIVITY TO AMBIENT AIRFLOW

It is beyond the scope and resources of this dissertation to investigate the result of a wide range of possible atmospheric conditions. Instead, the dependence of this particular development scenerio on the local wind will be investigated largely as a sensitivity study. Of particular interest will be the dependence of the storm movement on the mean wind. It was inferred in chapters 5 and 7 that the MCS core movement was dependent on the mean tropospheric wind. Other explanations are possible, given the results of these simulations. For instance, the system may move as a forced or trapped internal gravity wave perhaps trapped by a steering level. It may move with a density current, or it may move as a result of pressure forces at a speed dependent on the Convective Available Potential Energy (CAPE) (see Moncrieff, 1981). In order to narrow the number of possibilities, the experiment will be rerun with a 50% and 100 % reduction of the mean wind. Based on these results, a better understanding of the dependence of the system on ambient wind will be attained.

Besides the MCS movement, the MCS intensity and growth may be dependent on the mean flow. It was shown that the mountain wave induced convergence to the lee of the ridgetop was important to the initial growth of the mesoscale response. In addition, if the storm does move with the mean wind, a slower wind will supply less CAPE and perhaps the MCS will be less intense or develop more slowly as a result.

8.1 The 50% Wind Case

For this case, the entire lifecycle, depicted with streamflow, is given in Figure 8.1. Initial deep convection began approximately 1330 MST, which was nearly 1 hour later than in the control case. Also, only a single deep tower formed instead of two as in the control simulation. The first deep convective tower formed about 30 km east of the ridgetop. This was the mountain wave convergence zone for this reduced wind case. It might be speculated that the reason for only a single tower lies in the fact that the region affected by the augmented west slope moisture advection is considerably closer to the mountain wave convergence zone. It appears to be close enough so that the west slope moisture is explicitly advected into the region of the convergence zone. This then leads to a single convective region instead of two as in the control.

As the initial convection strengthened, the associated rainshaft progressed eastward at approximately the speed of the mean airflow of 5-6 m s^{-1}. The resulting progression of stream flow is depicted for the period from 1400 MST - 2200 MST where the simulation was concluded. During this period, the mid-level rainshaft showed the most consistent movement of 5-6 m s^{-1}. The vertical stream flow, on the other hand, can be seen to fluctuate in peak intensity and move to various positions relative to the rainshaft axis. This behavior is indicative of the influence of propagating internal wave activity.

At 1800 MST, the vertical motion within the updraft core passes through a region of mesoscale subsidence similar to that experienced by the control case. Although nearly 1.5 hours later than the control, the subsidence-induced suppression occurs in the same geographical region around 105° W Longitude. At this time, upward motion has split and

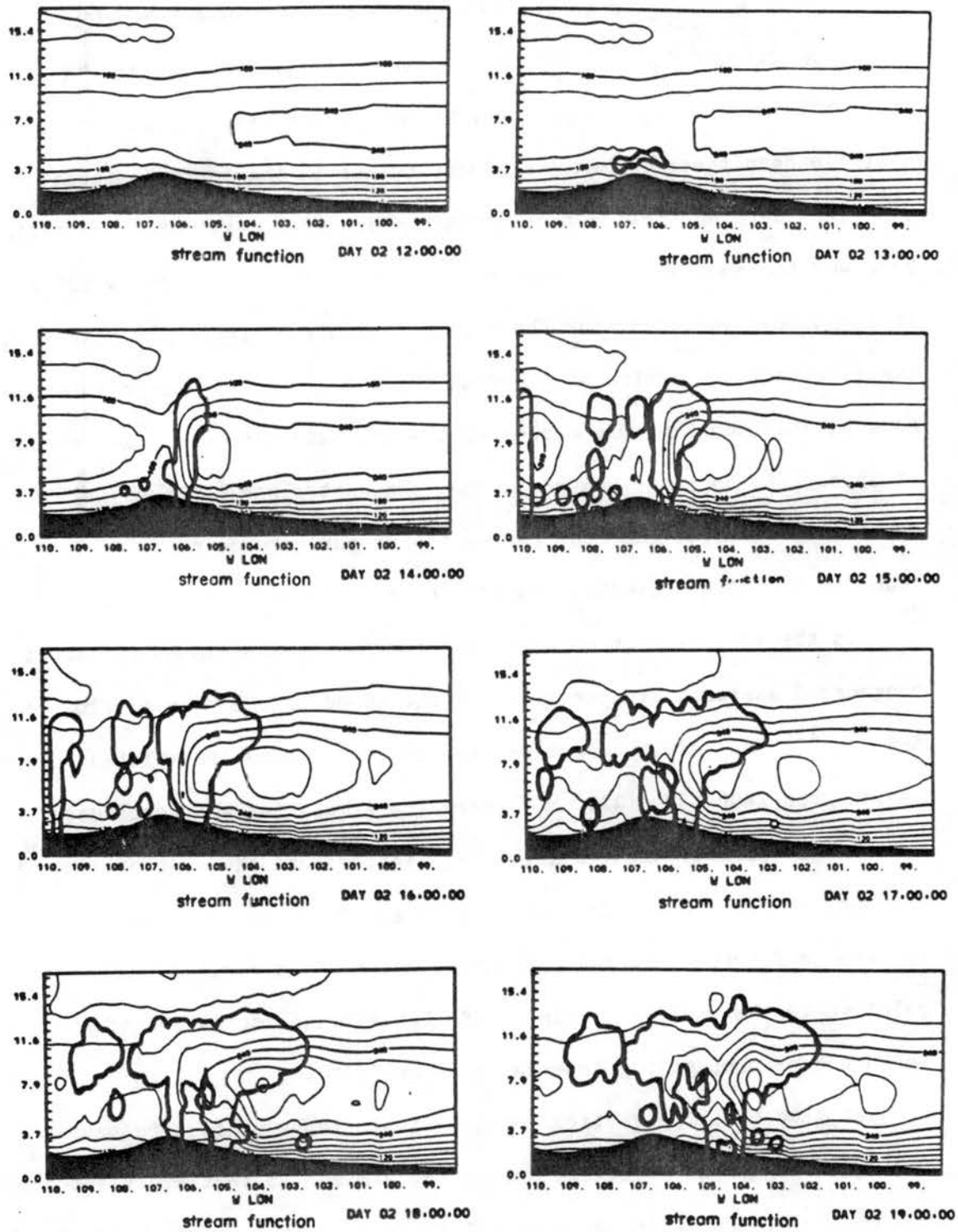

Figure 8.1. Same as Figure 5.17, except for 50% wind case, and storm movement assumed to be 5 m s^{-1}.

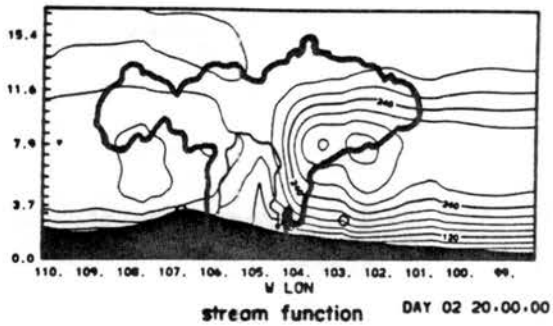

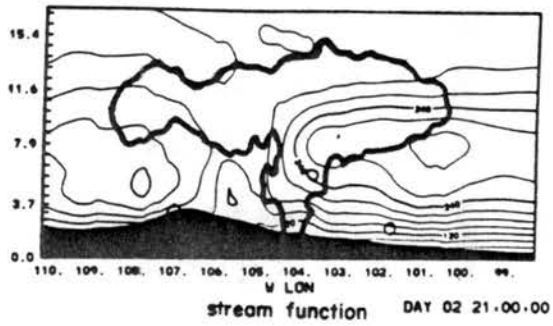

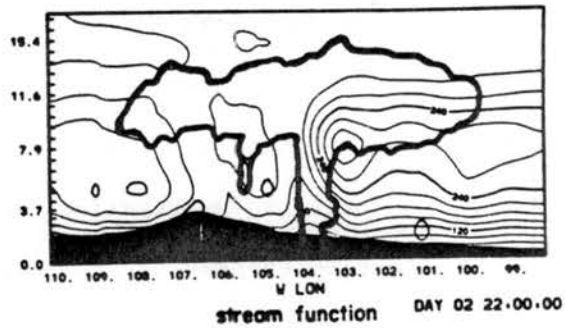

Figure 8.1. Continued.

moved east and west of the core. Convection has been re-initiated near the mountain wave convergence zone in response to the propagating vertical motion field. Some condensate has broken out to the east of the core as well in association with the propagating gravity wave mode. However, the condensate never reaches the level of free convection as the below-inversion-level air is never tapped.

At 1900 MST, the updraft reforms 50 km to the east of the weakened core from vertical motion induced by the sublimation, evporation, and melting of ice condensate precipitated from the anvil. The recovery is reminiscent of that of the control simulation, which also ended with the plunge of a rainshaft into the inversion just east the suppression zone.

By 2000 MST (Figure 8.2), the system strengthens near the region of recovery. It almost appears as if the regenerated updraft stalled and waited for the weakened core zone to catch up. In fact, the primary core overtook the regenerated region and continued at 5-6 m s^{-1} eastward until 2200 MST (Figure 8.3) when the simulation was terminated. This clearly demonstrates that the primary rainshaft best represents the system core because it moved in the most continuous manner. The peak updraft, on the other hand, formed anywhere within 50 km of the core and was far more transient.

The question should be asked: What does the apparent core possess that differentiates it from the reformed rainshaft? Two features seem to be apparent. First, as in the control, the core is always located in the region where the plains inversion is broken and that seems to remain the case even as the regenerated updraft appears to the east. Second, and perhaps dynamically more significant, the core region is lagged by a deep layer of warm air to its west which is the net result of forced

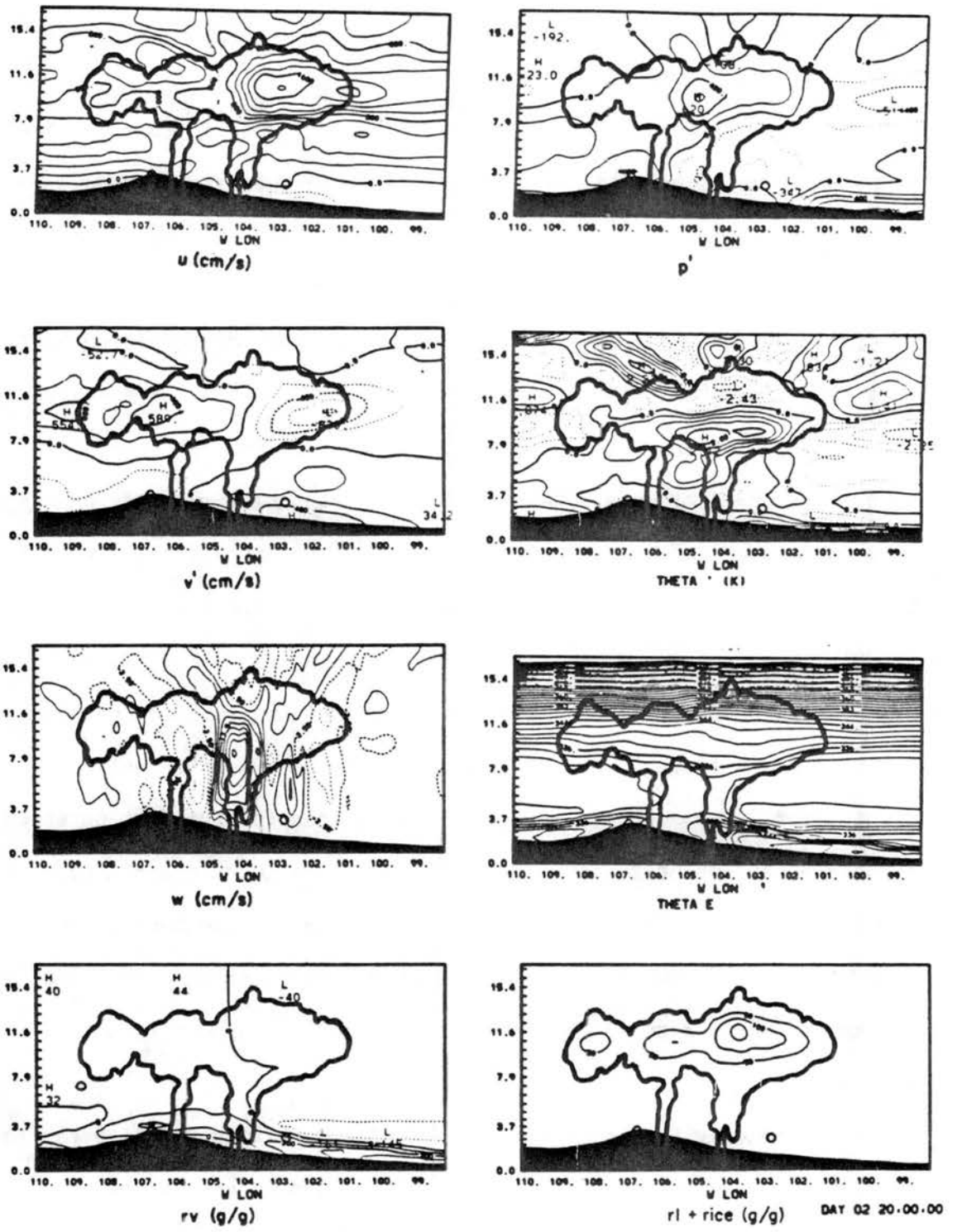

Figure 8.2. Same as Figure 5.1, except for 50% wind case at 2000 MST.

subsidence of the mean flow. This feature is weakened but preserved, even as the core updraft collapses during suppression. Its existence can be seen in Figures 8.2-8.3.

The warm core's persistence could be attributed, in part, to the geostrophic adjustment of the v-component to the warming induced pressure field allowing some of the latent heat to be retained in a balanced state while the great majority is radiated away as gravity waves. This enables a mean low level pressure low to be retained and establishes a dynamically stable persistent system core. The existence of cyclonic flow about the core at low levels and anticyclonic flow about the core aloft was established in the control simulation and is again quite apparent in this 50% wind case. Geostrophic adjustment to a heat source, similar to this, has been studied by Schubert et al. (1980).

The secondary vertical circulations associated with the meso-α scale balanced system then act to support the meso-β transient fluctuation. The support is in the form of mean vertical motion which cancels a portion of the destructive meso-β subsidence associated with the transients. This increases the extent to which the meso-β core can grow before breakdown (by destructive entrainment) occurs. In essence, the meso-β scale response concentrates the meso-α support into the meso-β scale.

The tendency for the transient meso-β circulations to disperse the vertical motion laterally is reduced by the loss of energy upward and the suppression of the plains inversion to the east. The forcing which breaks the inversion is largely derived from the combined effects of mechanical turbulance of convection, boundary layer forcing by density

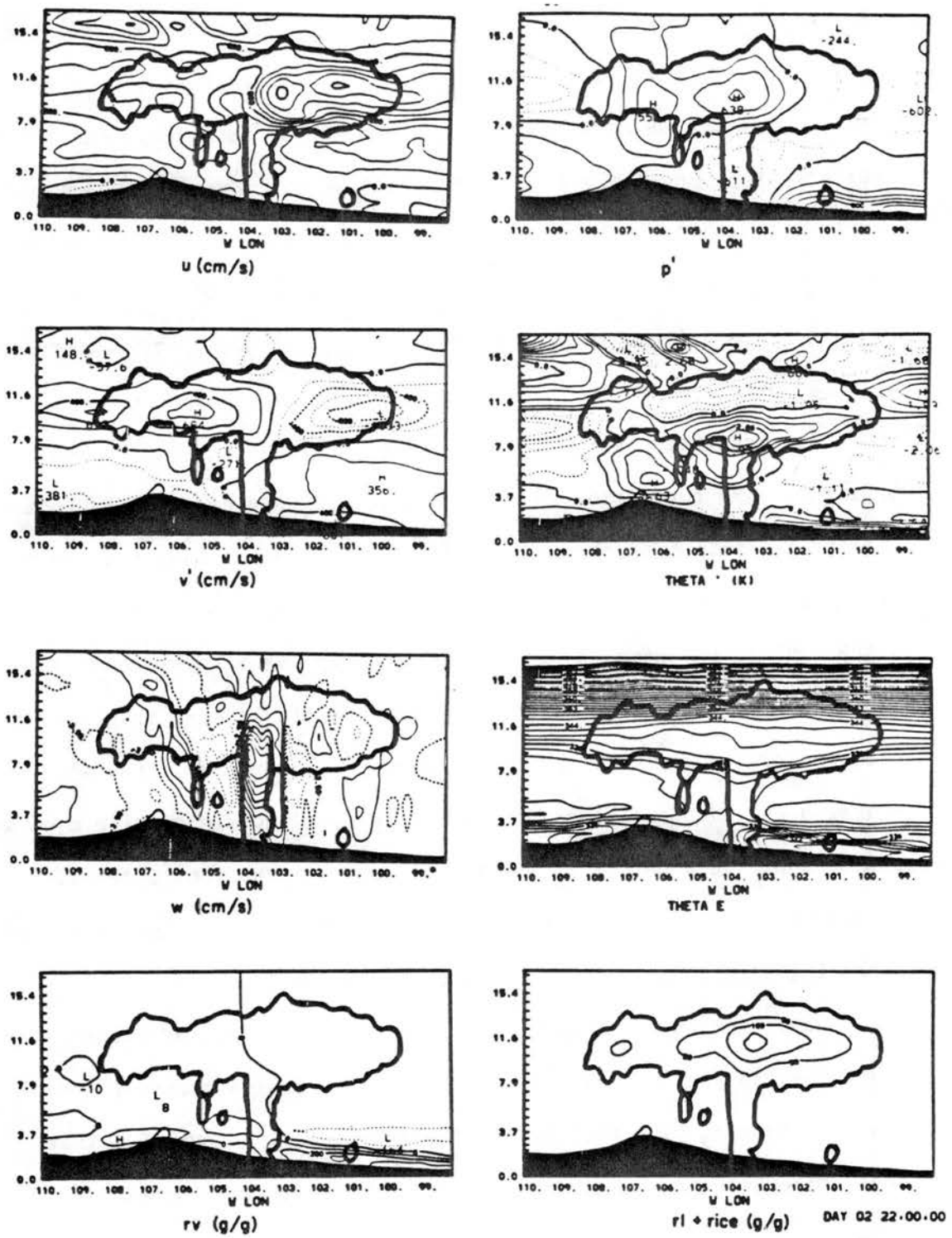

Figure 8.3. Same as Figure 8.2, except for 2200 MST.

current generated by local convection, and weakening of the inversion by virga from above. These features move closely with the mean wind and so the break in the inversion does as well. Therefore, since the meso-β transient propagates faster than those processes, it moves ahead of the inversion break and fails to support convection. However, the same transient leads to a rebound of the meso-β support from the emitting core (which moves also with the mean flow). This is the region where all factors come together for new development and this region moves with the tropospheric mean wind.

An interesting feature of this 50% wind experiment is the enhanced ability of some convection to leap ahead of the system core and form over the inversion. A plausable explanation might be that because the anvil does not extend quite as far ahead of the system, surface warming to the east is enhanced and increased boundary layer development weakens the inversion. Also, the weaker mean wind at mid levels, lessens the advection of the warmed mountain boundary layer air over the plains inversion and mountain-wave induced subsidence, thus leading to a weaker suppression. As a result of an overall weaker inversion, internal gravity wave motion induced by the system core has a greater chance of initiating some convection to the east of the MCS.

Because the anvil is decreased in size as a result of lower winds aloft, the trapping of internal gravity waves remains closer to the core. In concert with this fact, it can be seen in Figure 8.3 that propagating internal gravity wave-induced vertical motion radiates strongly upward east of the anvil edge and does not affect regions as far east of the core as it did in the control simulation. This is

another point of evidence suggesting that the existence of the trapped wave effect is real.

It is perhaps of some significance that the MCS generated within the weaker airflow possessed somewhat less intensity measured by the number of vertical flow streamlines. This would likely be a result of a weaker supply of CAPE caused by a slower movement relative to the surface slope flow. It is significant that the system did not move faster relative to the mean wind. This again suggests that the meso-β response is moving the convection rather than the inverse.

8.2 No Mean Wind Case

The above results are consistent with the theory that the orogenic MCS simply moves by advection of the "warm" system core by tropospheric mean wind. Also, evidence was presented that the strength of the inversion may rely partially on the shear of the flow across the inversion. Its effect is to warm the flow above while cooling it below. Finally, the strength of the system seemed to be dependent on the strength of the flow and in particular the vertical shear. The vertical shear acts to supply a greater relative inflow of CAPE to the core.

The case of no mean wind is interesting because there will be no external advection of the flow. Instead, the role of the internally generated forces dominate. Without this test, these forces may still exist but may be masked by the dynamic effects of the environment.

The experiment was initiated and integrated exactly as the control except that the initial wind was set to zero. Like the other cases, deep convection occurs over the ridge peak initially. However, convection rapidly forms laterally from the ridgetop over the plains at 104^{o} W Limon, Colorado area) and the eastern domain boundary.

Examination of the vapor and the field suggests that the inversion is weakened at these locations relative to the other cases. This is especially true on the western High Plains.

By 1600 MST (see Figure 8.4) the convection is concentrated at ridge top with a minor rainshaft just to the east and a similar region of precipitation to 30 km to the east. Examination of the w field reveals the existence of an extensive train of gravity waves extending laterally east over 350 km and west to the boundary. The waves appear to be generated locally from the initial convection as each possesses oppositely moving upwardly propagating wave fronts aloft. Although the strongest w maximum is associated with the system core, the development of a weaker w maximum is found in association with the laterally displaced minor precipitation shafts.

The pressure field depicts high pressure aloft as with the other cases. Also, as with the control case, there are relatively cold temperatures at cloud top and warm temperatures at the tropopause level and immediately below. Predictably, much of the deep warming upshear of the primary convection is missing in this case as a result of no mean wind. Interestingly, the surface temperature at ridge top has become relatively cool and is characterized by relatively deep high pressure. This is a direct result of the rainshaft falling directly within the system core. The streamflow pattern, given in Figure 8.5, shows that a set of two opposing circulation cells have developed. Hence the lack of mean wind produces a more symmetric circulation about ridge top.

By 1700 MST (not shown) the ridgetop convective core has split. The secondary vertical velocity maxima, situated to the east and west of the primary updraft core, has become dominant, while the central updraft

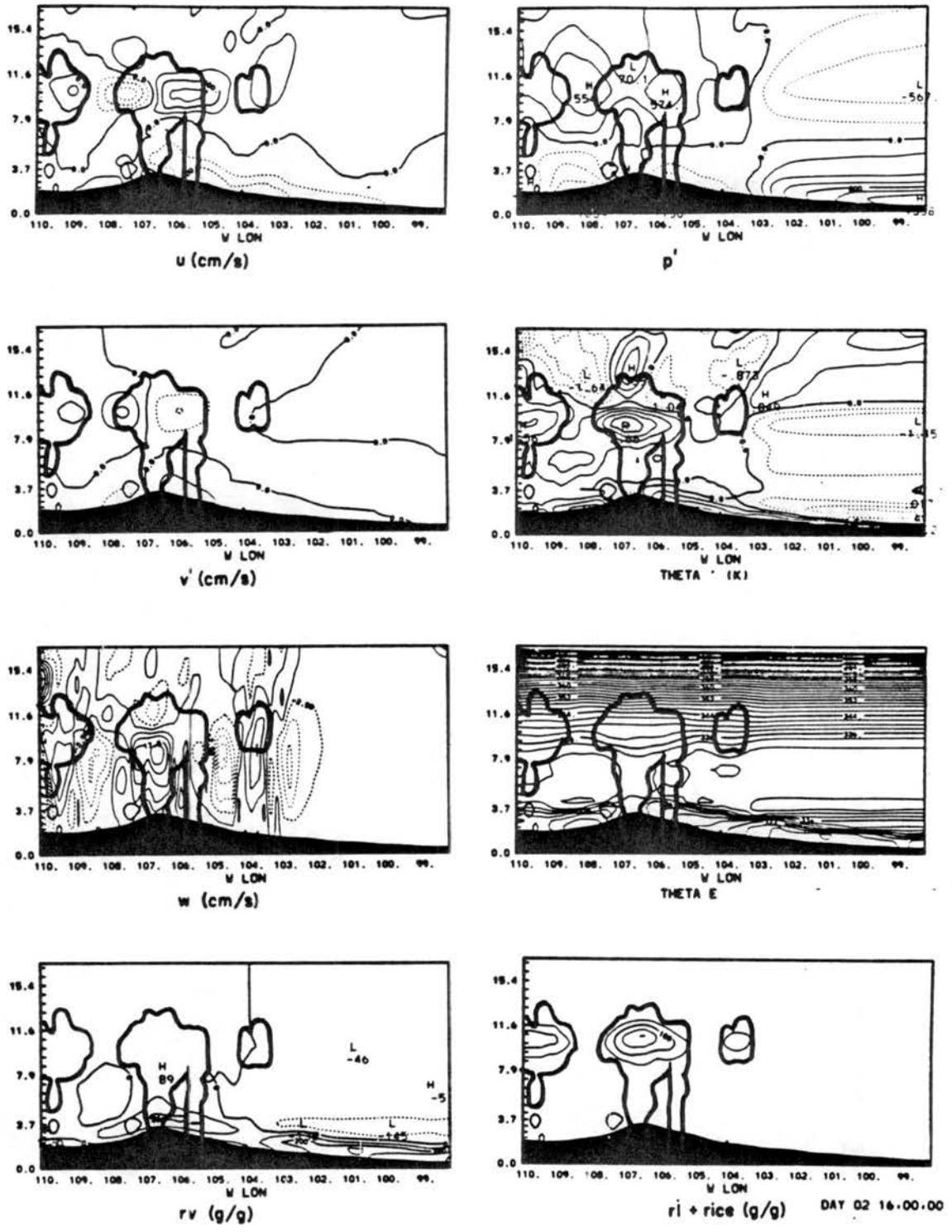

Figure 8.4. Same as Figure 5.1, except for 0% wind case at 1600 MST.

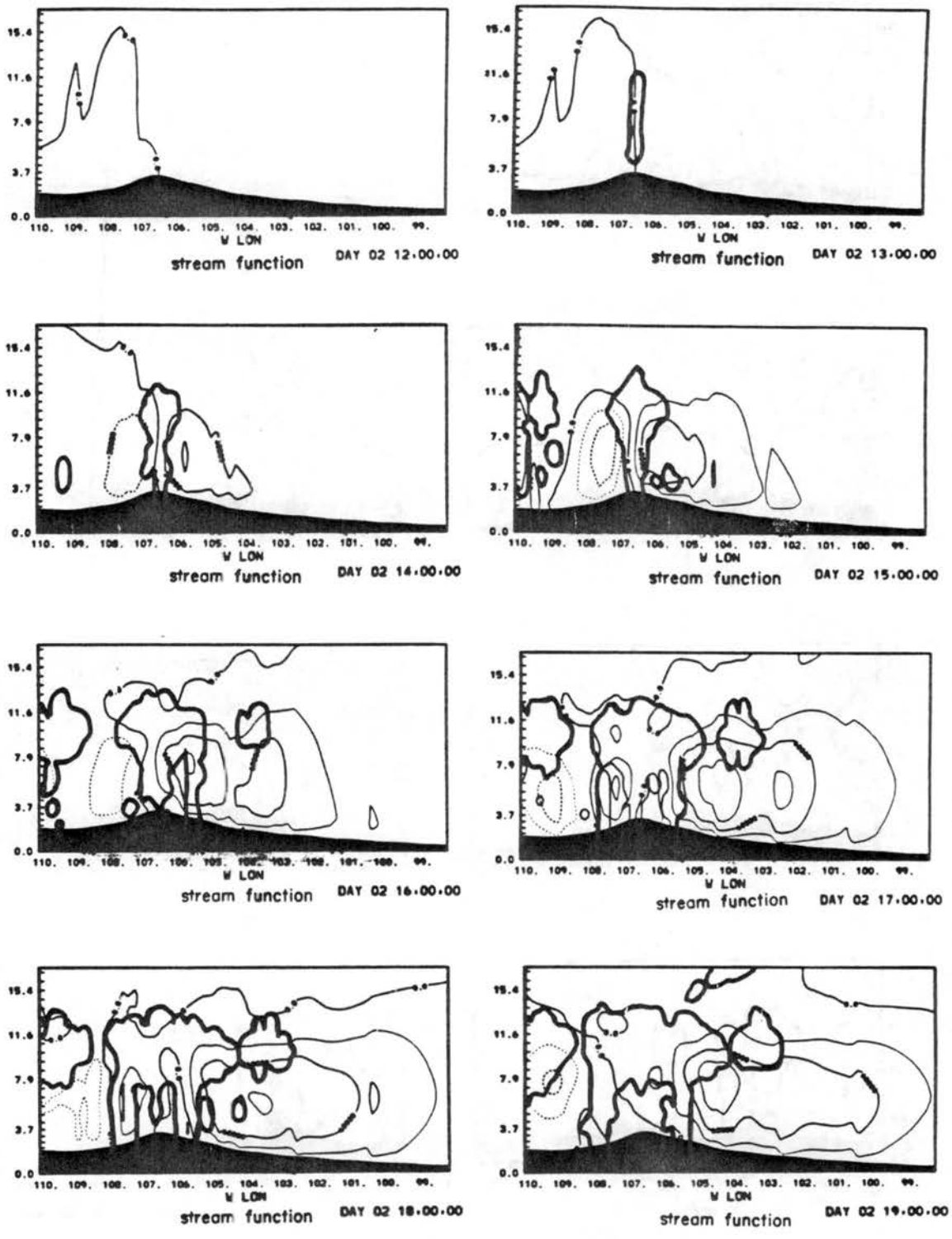

Figure 8.5. Same as Figure 5.17, except for 0% wind case, and storm movement assumed to be 0 m s^{-1}.

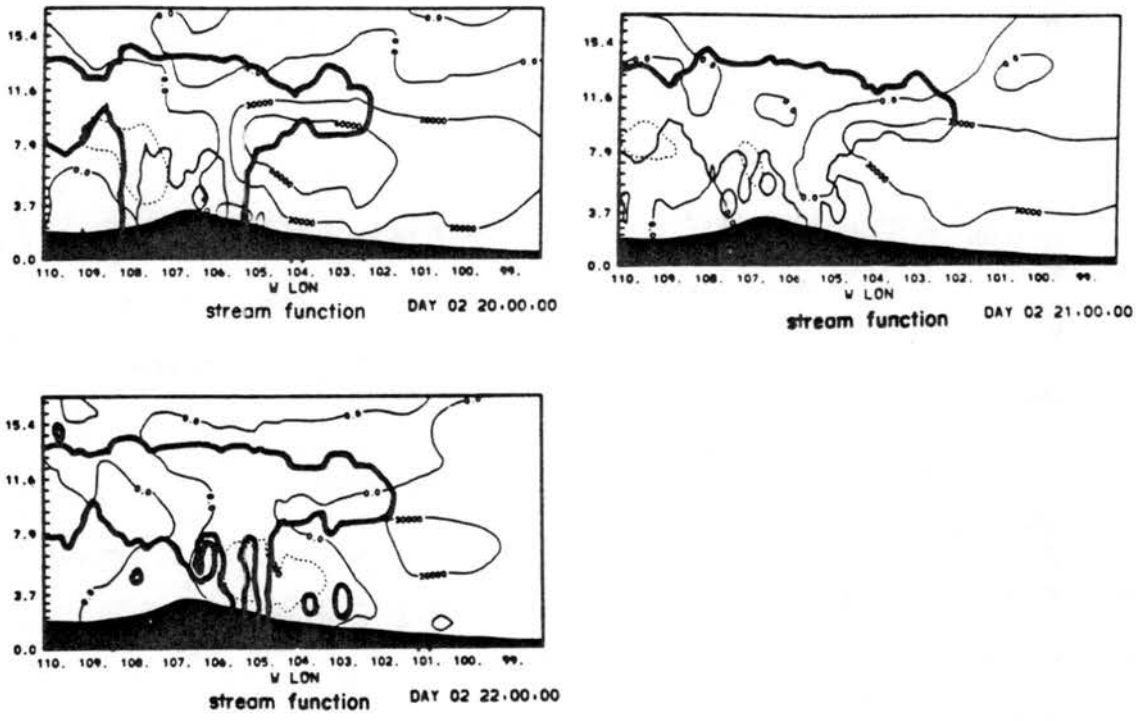

Figure 8.5. Continued.

has now become a downdraft. As a result there are now three precipitation shafts associated with the mountain top regime.

By 1900 MST, the system becomes fully split. Figure 8.6 depicts the convection at 2000 MST. At this time, the sinking motion within the original core has dissipated and some rising motion has returned. There is evidence at this time that the eastern secondary updrafts from the original core has itself split, generating eastward and westward propagating gravity waves.

The gravity waves seem to be of a similar wavelength and intensity to those generated by the convective core in the control case. They appear to be less trapped underneath the anvil, however. Like the control case, vertical motion is again being forced in the original core on the rebound. However, the moisture rich upslope air is diverted to the new convection on the flanks of the original core. The plains inversion does not reach the higher elevations with the intensity it possesses over the plains and so the flanking "daughter" systems were not inhibited by the inversion. The θ_e plot clearly demonstrates the juxtaposition of the plains inversion and the "daughter" circulation cells. Note that the eastward propagating internal gravity wave is not initiating a new convective circulation east of the eastern "daughter" cell. This is attributed to the resistance to convection induced by the plains inversion.

Unlike the control, the meridional wind has formed an anticyclonic circulation jet aloft centered over ridgetop. The diameter is 400 km and peak magnitude is 6 m s^{-1}. A weaker cyclonic flow occurs at the surface with a 4 m s^{-1} intensity.

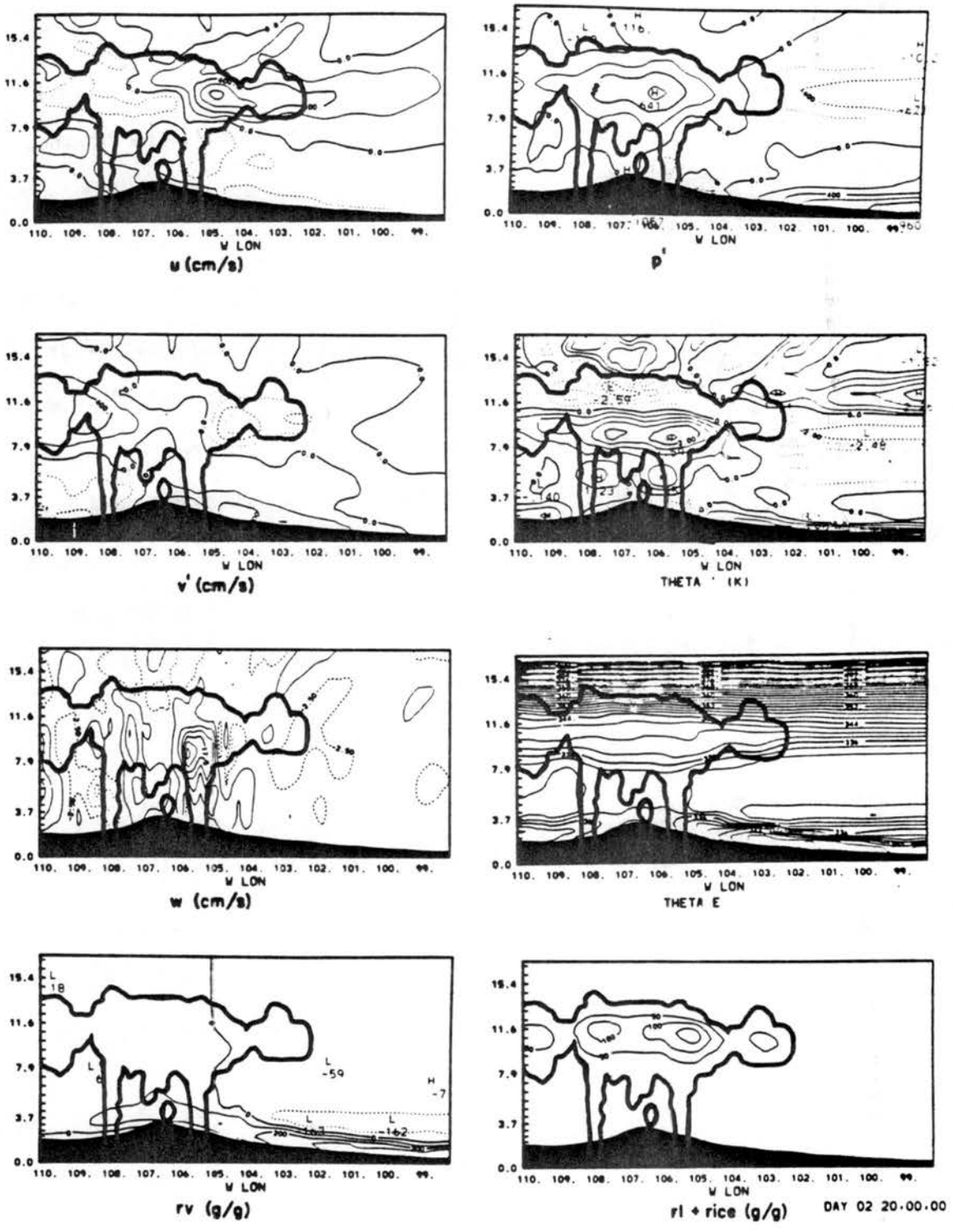

Figure 8.6. Same as Figure 8.4, except at 2000 MST.

The 2000 MST pressure and temperature show a weakly split warm core system centered at ridge top. The peak temperature anomaly of 2.5 C is close to that of the control, despite the lack of mean wind ventilation. This suggests that much of the temperature anomaly aloft is maintained by the balanced system.

The evolution of the circulation up until the time of 2000 MST (Figure 8.5) clearly depicts the formation of the two celled circulation centered at ridgetop. Peak strength of the east slope circulation is attained at 1900 MST and weakening occurs thereafter. The west slope solenoid is weaker, perhaps as a result of the lesser slope.

It is interesting that as darkness falls, after 1900 MST, the thermal downslope circulation begins beneath the mature deep convection solenoid on the east slope. This occurs because the circulation never has moved into the lesser sloped plains, as it had in previous tests by sunset. Even at 2000 MST, the upbranch of the mean east slope circulation has become strongly sloped, and the moisture is reflecting on above ground maxima.

The evolution of the circulation, after 2000 MST (displayed in Figure 8.5), shows a continual deepening and strengthening of the downslope circulation west of 104^{o} W Longitude. As with the control, the depth of the downslope regme is greater than a comparable dry case. It is likely that this is a dynamic response to the weakening convection.

Figure 8.7 shows the variable fields at the time of 2200 MST, when the simulation was terminated. Note that ridgetop sinking motion has deepened to the tropopause and has effectively coupled with the convection at 105^{o} W Longitude as a downbranch to the solenoid. Note

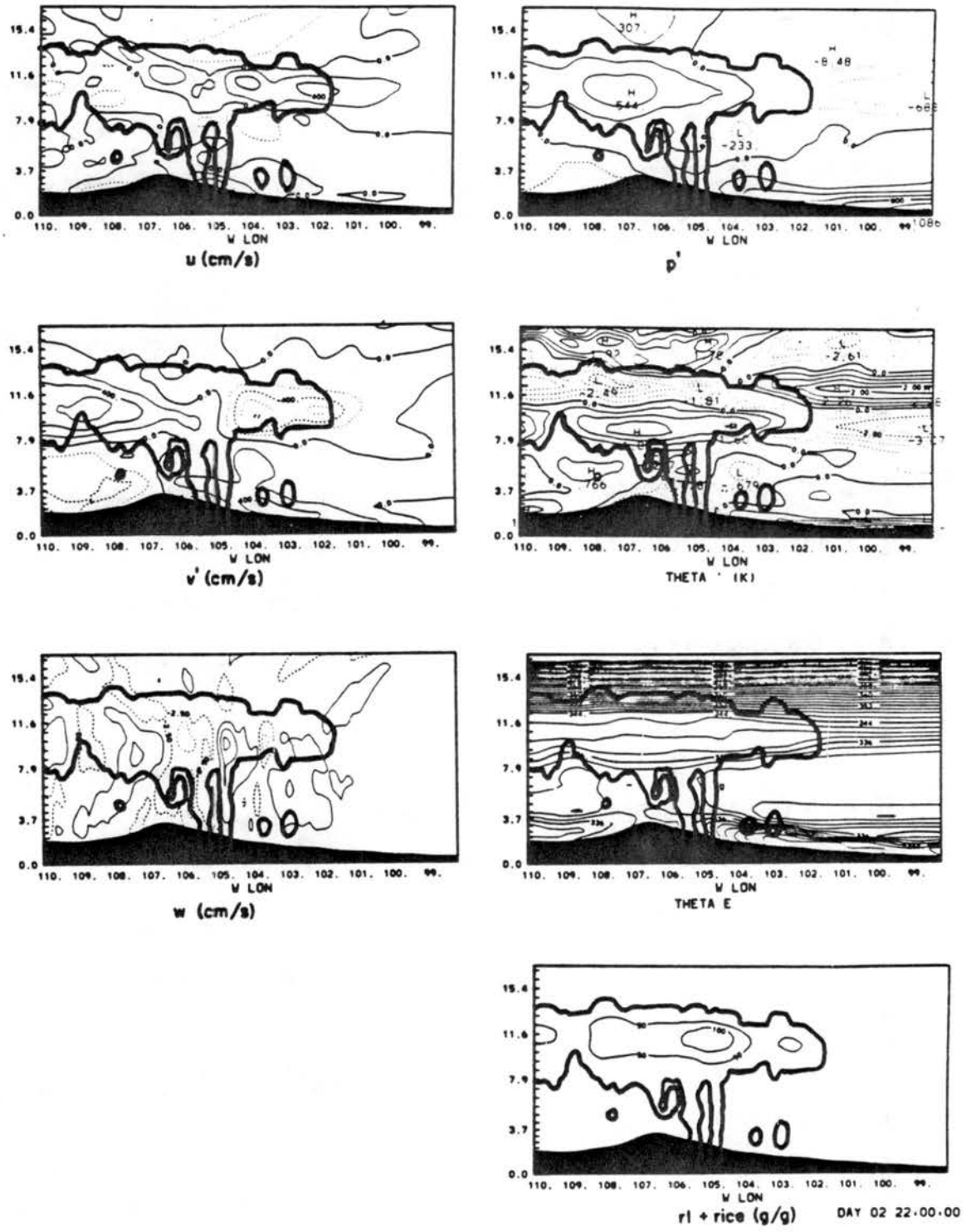

Figure 8.7. Same as Figure 8.4, except at 2200 MST.

also the greater tropospheric trapping of the internal waves beneath the anvil.

The meridional circulation in the upper troposphere remains strong, however the high pressure and warm temperature aloft is weakening in magnitude. It is suggested that the deep downslope is in part fed by convergence aloft. Near the surface it is also modulated by the inertial oscillation of the thermally driven slope flow.

This simulation has again demonstrated the interaction of a general slowly developing cyclonic storm with the action of deep internal gravity waves of wavelength 150-200 km. The result is a persistent pulsating core of convection. The system differs from the control case in that convection intensifies strongly in two daughter circulation cells, while the parent cell retains the combined effect of their heating. The daughter cells persist because they interact directly with the plains and west slope moisture.

This experiment again demonstrates the dominant role played by the inversion in focusing where the dominant convection lies. This inversion is broken in the vicinity of the "daughter" cells independently of the convection, enabling their growth. Propagation into the plains, however, is restricted to regions where the inversion has been destroyed.

It is significant that, in this case, the convection does not move substantially into the inversion. The results again confirm that the movement of the MCS core is governed by the mean wind.

9. CONCEPTUAL MODEL

The numerical simulations of this dissertation have demonstrated that given favorable conditionally unstable conditions, it is possible for a mesoscale local wind system to act to organize deep convection and result in the formation of a long-lived mesoscale convective system. Based on the results of all these experiments, a conceptual model of the organization scenerio can be formed. In this chapter, the results of this dissertation will be summarized by presenting a conceptual model of the Rocky Mountain Convection Cycle (RMCC).

The RMCC, as it took place on 4 August, 1977, can be described in terms of 6 stages of development. The first stage is characterized by the development of the mountain boundary layer and the formation of shallow mountain convection. This stage is best described observationally by Cotton et al. (1983). During this stage, the thermal slope flows occur on a variety of scales. The smaller scale thermally driven circulations develop and dissipate on shorter time scales than the larger ones. During stage 1, the mountain plains circulation is in the process of developing while strong small scale slope flows are already mature. Initial moist convection is formed by these shallow slope flows over especially favorable mountain peaks called "Hot Spots" by Henz (1974).

During stage 1, the mean flow in the lowest 0.5 km MSL on the eastern slope tends to favor a northerly direction relative the ambient flow. This is a residual of the nocturnal downslope regime. As the

nocturnal downslope pressure gradient is replaced by upslope gradient, geostrophic adjustment of the meridional wind hastens the upslope development. In fact, it can be shown that the adjustment of the geostrophic meridional wind can lead to super-geostrophic upslope flow.

Two important convergence zones develop during stage 1. The strongest is located down-wind (east) of the ridgetop about 60 km. It is formed as a result of the interaction of the east slope mountain-plains circulation system with a ambient flow. Stream flows indicate that this region is the point where the mountain lee wave stream flow turns upward from the ground. In fact, because of the strong free air ventilation, the region between the peak and the lee convergence zone experiences a considerably reduced diurnal temperature variation.

During this and subsequent stages, the mountain/east plains circulation system exerts a strong stabilizing influence over the plains. The shallow upslope flow, relatively cools the surface while the downslope flow above the inversion acts to warm the air above the inversion. This creates an inversion which becomes increasingly strong throughout the day. As deep convection forms over the mountains, the strength of the inversion is enhanced to an even greater degree. As a result, convection becomes increasingly localized over the high country during the morning until the convection moves out onto the plains.

Stage 2, shown schematically in Figure 9.1, begins when deep convection starts to form. Cotton et al. (1983) show that the Continental Divide (or ridgetop) is favored over other spots for initial deep convection. Model results indicate this region tends to be favored because deep slope flows develop on the western slopes more rapidly since they are augmented by ambient westerly flow at higher elevations.

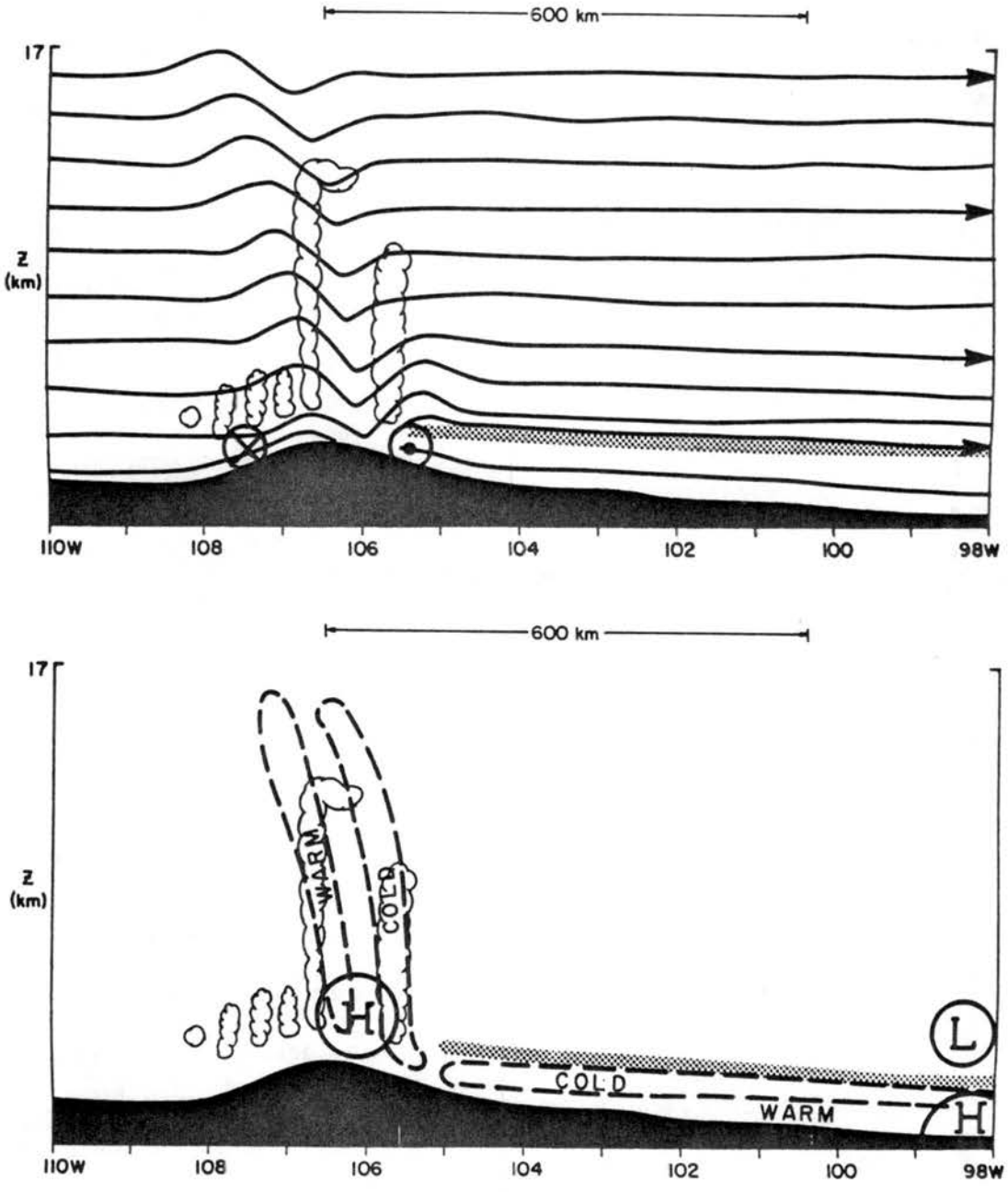

Figure 9.1. Conceptual model showing flow field and position of convective elements at time deep convection forms. Axes and topography are as in Figure 5.1. The stippled line represents the position of the plains inversion. Regions of cloud are indicated. Part a depicts the flow field with ground relative streamlines. Circles depict flow perturbation normal to plane. Part b depicts the pressure and temperature response. Pressure centers are depicted by solid closed contours and temperature by dashed contours. The length scale of 600 km ($2L_R$) is indicated.

This results in the earlier advection of low-level moisture to the ridgetop. These findings are supported by the fact that "episodes" of these orogenic systems seem to be coincident with periods of most monsoonal southwesterly flow into the mountain region. This case study was during such a period.

Deep convection also forms in association with hot spots and the mountainwave convergence zone; however, it tends to be less intense as a result of a reduced moisture supply initially. It takes considerably longer for the east slope upslope to advect moisture to the higher mountains since it is opposed by the mean flow. To some extent this process was probably exaggerated by the model because of the specification of equal moisture with elevation between the west and the east. Observations, however, verify significant moisture supplies into the South Park region from the west (Danielson and Cotton, 1977).

As the deep convective elements form, they drift eastward with the mean tropospheric wind. The deep convection associated with ridgetop moisture possesses greater moisture and is more longlived than those formed further east. As the ridgetop convection moves eastward, western-slope moisture advects with it. As it approaches the mountain wave convergence zone, all elements come together including moisture, strong local surface forcing, and meso-β scale support in response to pressure fields induced by the convection. The mountain wave convergence zone represents the region where mechanically forced, downward advected westerly momentum converges with the diurnal plains valley breeze. In some respects, this is similar to the convergence studied by Banta (1982). The result of interaction with the convergence zone is the explosive development of an ensemble of convection on the

meso-β scale. At the same time, eastern moisture advection is enhanced and greater moisture is brought to the higher elevations. This further acts to intensify the convection into a strong line near the mountain wave convergence zone.

The formation of a mesoscale convective line concludes stage 2 and begins stage 3. The circulation at this time is depicted in Figure 9.2. At this time, the mountain/plains meso-α scale circulation cell deepens from 5 km to a tropopause depth of 12 km MSL. The rapid development of such a circulation is possible through the coupling of upper level westerly flow with low level relatively easterly flow. This is accomplished most efficiently when the system core, defined by the mean position of the up-branch of the cellular circulation, moves with the speed of the mean tropospheric flow, allowing the deepest possible tropospheric circulation. The circulation, on the scale of a single convective cell (see dashed line in Fig. 9.2a) actually crosses the meso-β-scale flow stream lines. The downdraft originates from lower θ_e air to the east of the meso-B-scale core region at mid levels while the updraft originates from the sub-inversion levels. As a result the storm scale flow updraft and downdraft cross in this two dimensional plane view.

In association with the circulation cell is the formation of an outflow level at 10-12 km MSL. Geostrophic adjustment to the persistent cellular circulation forms anticyclonic shear of meridional flow aloft and cyclonic shear at lower levels. If convection is suppressed to the north or south, the outflow and inflow regimes could result in a more curved inflow and outflow pattern. Because of the linear nature of the

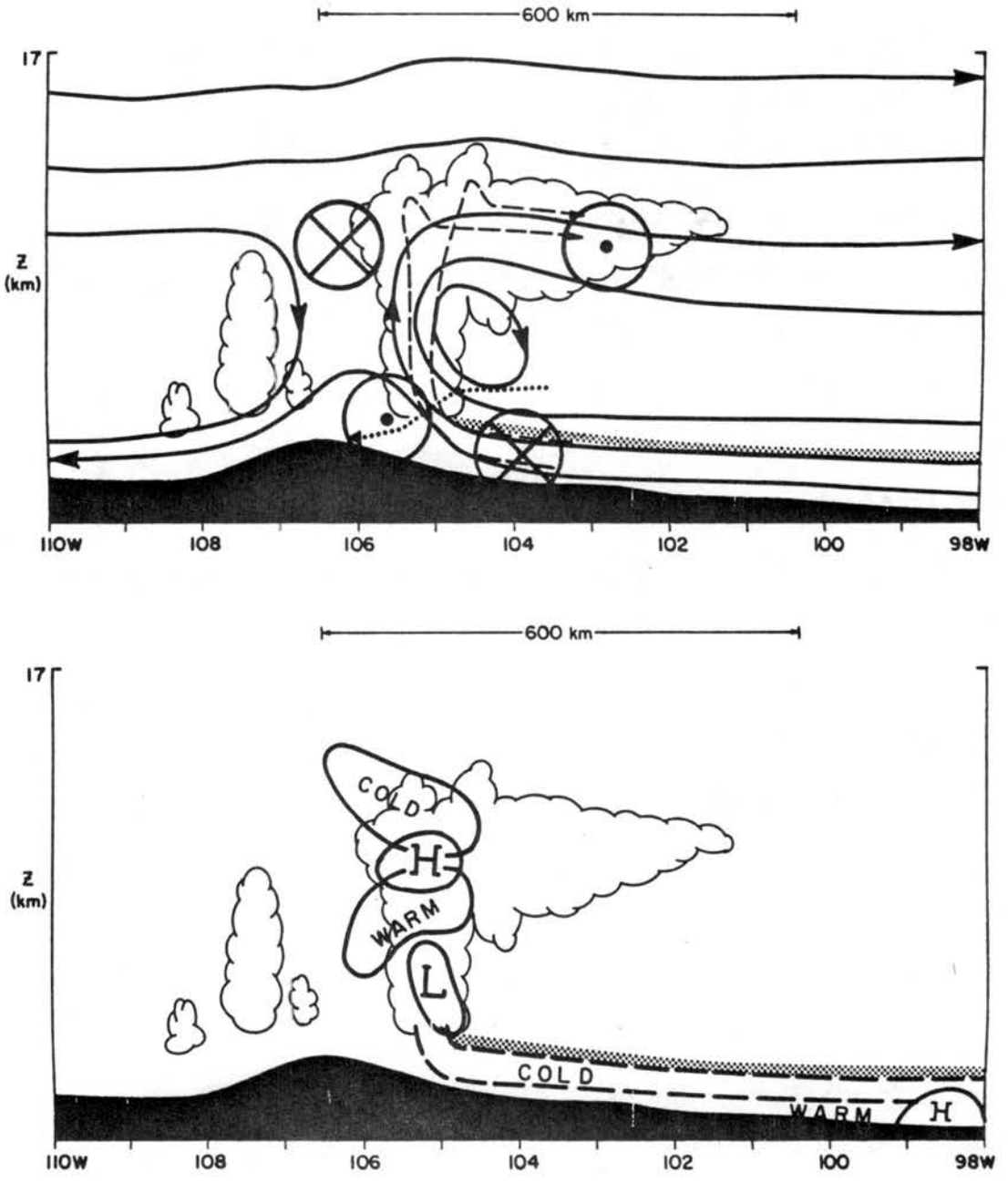

Figure 9.2. Same as Figure 9.1, except for Stage 3. Also flow is storm relative flow. Individual parcel paths are given by dashed (updraft) and dotted (downdraft) lines.

mountain barrier, however, it is likely that the system will remain at least quasi-two-dimensional at this time.

The initial growth rapidly exceeds the available moisture supply from the slope flows. In addition, as the system passes onto the plains, a mesoscale region of subsidence and suppression of convection is encountered. This begins stage 4, given in Figure 9.3, and is characterized by a partial collapse of the newly formed Mesoscale Convective System (MCS). To the west, (Fig. 9.3b) continued heating of the east slope results in an unfavorable low level pressure gradient which forces flow upslope or away from the system core. The tendency is to force deep subsidence within the core. The result of the suppressed convection, combined with the overall response of the developing MCS, is the collapse of upward motion within the system core.

The more persistent low level cyclonic and upper level anticyclonic flow remains, since it adjusts from slow coriolis response which builds up over a period of several hours. This may be termed a "fly-wheel effect" similar to that discussed by Emanuel (1983) in his discussion of the generalized CISK concept. The collapse of the system sends a large 150-200 km horizontal deep internal gravity wave pulse propagating vertically and laterally eastward and westward (not visible in Figure 9.3). The tropospheric energy of these waves weakens considerably within one wavelength horizontal distance from the core as their energy is transmitted upward into the stratosphere. Lifting associated with these waves manages to reinitiate some convection to the west, where some moisture has been resupplied to the mountain wave convergence zone. The convection is relatively weak, however. To the east, the propagating internal wave fails to form convection due to the presence

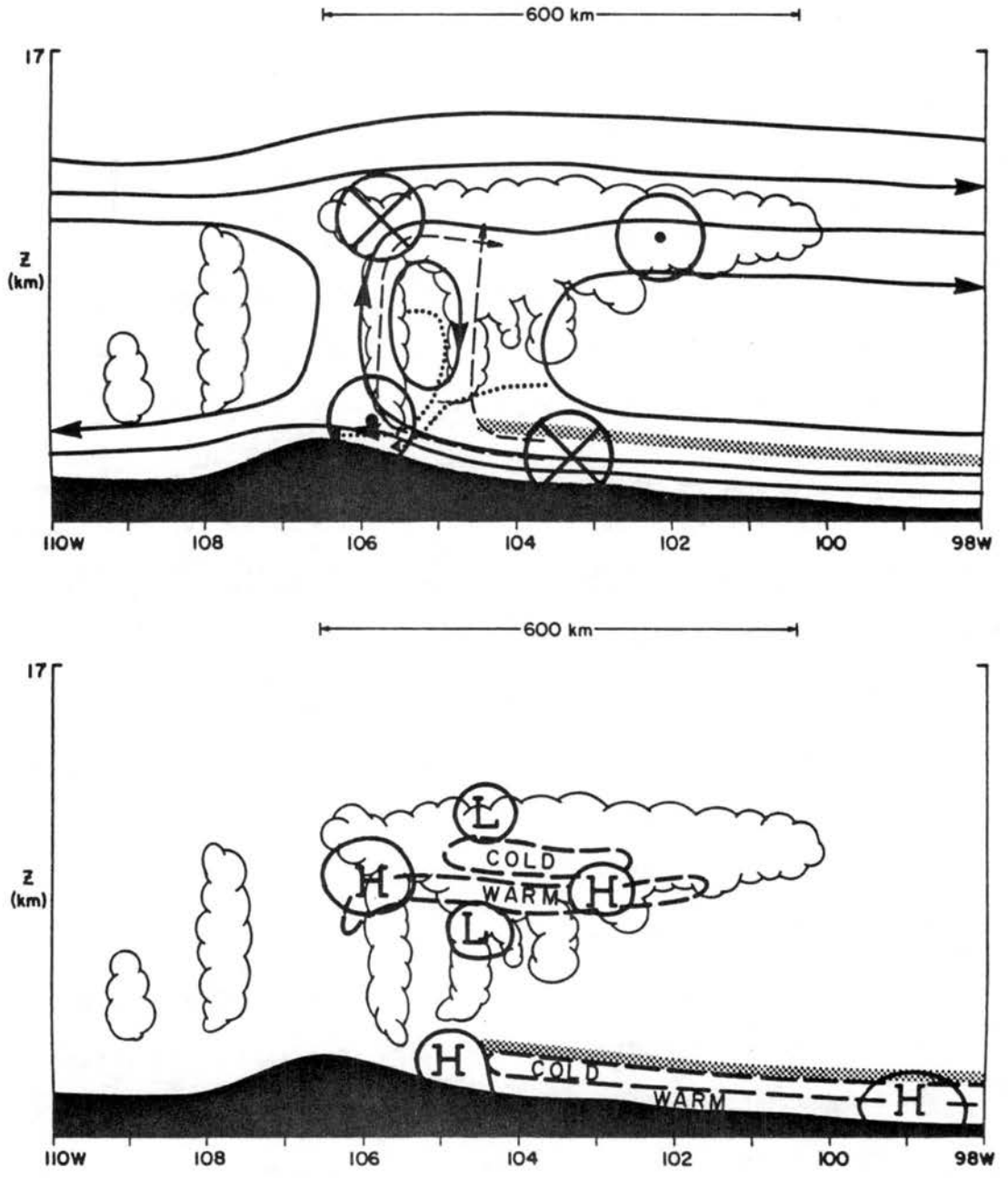

Figure 9.3. Same as Figure 9.2, except for Stage 4.

of the strong, low-level plains inversion, and weakens as much of its energy propagates vertically.

The system collapse, augmented by precipitation and evaporation, overshoots equilibrium and finally as much of the condensate is exhausted, the core becomes overly warm and the mean core vertical motion rebounds upward. At the same time, the core drifts eastward from the suppression zone. With the rebound comes the influx of rich plains moisture from beneath the inversion. The core persistently lies on the western edge of the inversion. This implicates its activity as the primary mechanism for mixing out the plains inversion. It is also responsible for enhancing its strength as a result of the deep solenoid which it forces.

As the meso-β scale core rebounds, individual convective elements are initialized by direct effects of lingering convection or precipitation. Although convection is weakened during suppression, some elements survive long enough to accomplish this purpose. They survive in this unfavorable dynamic environment on the support of moisture supplied from the continuing slope circulation.

Two mechanisms of cell initiation are apparent. First, melting and evaporation of precipitation from previous convection leads to the formation of surface density currents which interact with each other or the local shear to force new meso-γ scale motion. Second, lateral internal gravity wave oscillations produced by the collapse of a local convective element initiate deep meso-γ scale motions forming deep convection. In either case, the initiation is induced by gravity oscillations in conjunction with parent convection. As mentioned in

Chapter 2, this is probably the same as discrete propagation in some cases.

Supporting experiments indicate that the suppression zone over the Platte Valley is considerably stronger than over the Palmer Lake Divide. As a result, the same suppression can completely destroy the meso-β organization over the Platte Valley. This supports Dirks' (1969) conclusion that a zone of suppressed convection exists to the lee of the mountains which we attributed to the climatological minimum of thunderstorm frequency on the western edge of the High Plains.

As the system again strengthens, it again overdevelops and weakens. A total collapse does not re-occur, however. The oscillatory processes of strengthening and weakening continues for the remainder of its lifetime. As it moves eastward, the mean core circulation gradually builds in strength, as the input of latent energy is partially retained by geostrophic adjustment. The production of a gravity oscillation is similar to the development of a tropical depression. It was demonstrated by Schubert et al. (1980) that in the early developing stage, a weak tropical storm circulation retains only a minor fraction of its latent energy as geostrophically adjusted vorticity. Instead, the great majority of the energy is radiated away as internal gravity wave energy. This seems to be the case for MCS growth over the Great Plains as well.

Because the plains inversion localizes persistent convective activity to its western edge, initial growth of the MCS is enhanced. During the initial stages, the weak system tends to take a linear rather than circular form. Individual convective elements are short lived and have complete circulations on the order of 10-20 km. The number of

elements within the 2D cross section varies from 0 to 5 or more. It is possible that a 3D representation of the convection would possess longer lived convective elements as a result of the lessened forced entrainment aloft. The results seem to demonstrate, however, that destructive effects of ambient shear are not responsible for their demise. Instead, they appear to over develop and lose the ability to maintain their circulation with the given mesoscale support.

As with the mesoscale circulation, the collapse of individual convection cells results in the emission of a gravity wave pulses. The development of subsidiary or daughter convective cells occurs only in regions with favorable support. One type of favored region is where upward motion support from two parent cells occurs, i.e., intersecting gravity waves. Another more necessary condition is that of mesoscale support through vertical moisture advection and vertical motion. Attempted initiation over the plains inversion almost always fails as does initiation to the rear of the system core where the air is largely stabilized.

The inversion itself seems to be eroded at its western edge by a number of processes in the system core. First, the persistent vertical motion of the meso-β cellular circulation and the mechanical turbulence generated by the convection itself destroy the western inversion by entraining air mass from the region. Second, and more explicitly seen in the model simulations, precipitation shafts advected downshear of the active convection cool the air above the inversion and destabilize the atmosphere on the westernmost edge of the inversion. There is little evidence that there exists an eastward moving gust front which effectively lifts the sub-inversion layer to free convection. In fact,

experimental evidence indicates that low-level precipitation-evaporation cooling is generally of minor importance to system movement.

Besides the near core advancing precipitation shafts, virga showers are formed at distances in excess of 200 km ahead of the core. These virga showers help intensify the system by cooling the deep column above but not including the inflowing below-inversion air. This causes the surface pressure to increase ahead of the system near the surface and acts to intensify the low-level flow into the core. This is similar to an advective wave-CISK growth mechanism, defined by Raymond (1983), except that precipitation does not reach the ground and stabilize the inflowing airmass.

Peak vertical velocities increase as the system moves eastward into increasingly higher CAPE air. This is due to the combined effect of increased CAPE at lower elevations and increased mesoscale organization. The peak intensity of vertical velocity is reached at 2000 MST. This is the point of combined maximum CAPE and mesoscale forcing and characterized stage 5. The cellular circulation which characterizes this stage is depicted in Figure 9.4. This solenoidal circulation closely resembles the observationally-derived mid-latitude squall line model of Ogura and Liou (1980).

This is the time of strongest meso-β circulation. Circulation on the meso-α scale continues to grow, as long as a geostrophic balance between the forced pressure and wind field are not attained. Since the geostropic adjustment is on the time scale of a half pendulum day (18 hours), the geostrophic circulation's peak intensity lags that of the convection by about 2 hours. The simulated meso-β-scale core weakened after 2000 MST for several reasons including the proximity of the

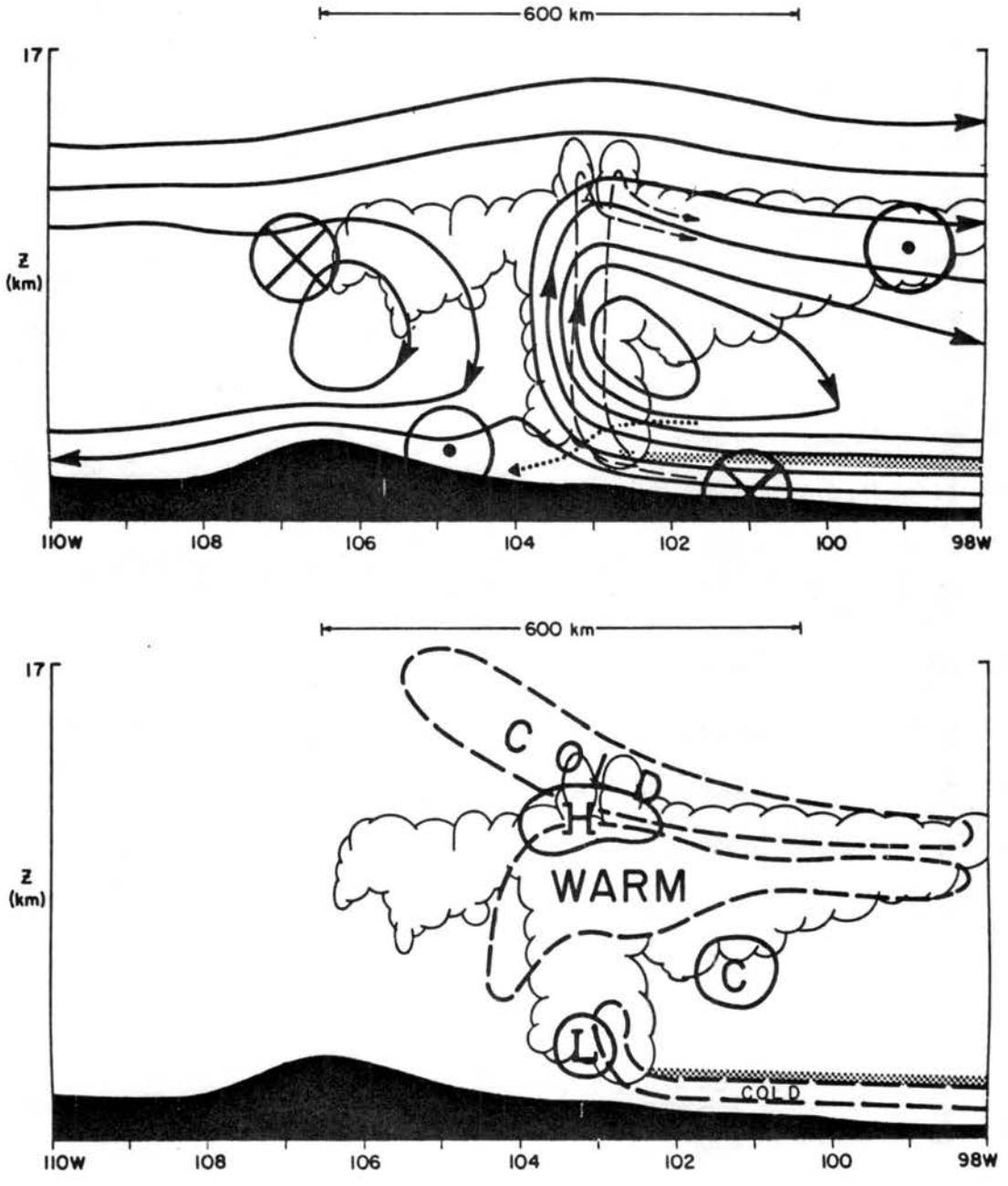

Figure 9.4. Same as Figure 9.3, except for Stage 5.

eastern lateral boundary and, more importantly, the need for a strong moisture supply given in the observations as the result of the southerly low-level jet. The low level jet occurs in a different flow regime, the modeling of which, was beyond the scope of this study. In addition, the simulated location of the system core was lagged 50-100 km to the west of the observed position because of the delay getting started. An earlier start would likely have led to maximum development of greater intensity and to the east of the position depicted in these results.

At the time of peak meso-β circulation, the system core is in a linear north-south orientation. This was observed and forced by the two dimensionality of the simulation. The flow at 350-200 mb (8-12 km) is sheared anticyclonically in the meridional wind, while that at the surface is cyclonic. The system core is typified by a high pressure anomaly of 1-2 mb at the tropopause level while low pressure is found near 3 km AGL of near 1mb anomaly. The vorticity is only partially in balance with the pressure gradient and so the system responds by emitting continued gravity wave oscillations. These are what is referred to as the "transients" in the geostrophic adjustment problem.

The system forms a deep anvil from air exhausted out of the convective cores, which drifts eastward ahead of the system. The radiative effects of the anvil are increasingly important to the system dynamics as darkness approaches. The reason lies in the destabilization of the anvil layer. The divergence of total radiation cools anvil top and warms the anvil base at the rate of 10-20 K day^{-1}. During the night, the cloudtop cooling and thus destabilization is significantly greater. The result is a strong lowering of the Brunt-Vaisalla frequency in the region just below the tropopause. It is conclusively

found that this has a strong effect on trapping of the gravity wave energy emitted by the convective core in the troposphere. It is possible, to some extent, that the gravity wave activity is further enhanced by additional latent heat release from condensation and/or sublimation within the anvil. If so, this would resemble the classical wave-CISK concept but operate in the upper troposphere.

The observations may be suggesting the existence of these meso-β features. As the observed meso-β orogenic complex approached the southerly jet, new meso β convection broke out ahead of the system. Not surprisingly, the meso-β activity was spaced roughly 100-200 km apart. This is close to the simulated wavelength of the trapped gravity wave activity emitted by the orogenic meso-β core. It is hypothesized, that not only was the meso-β system (that was tracked from the Rockies into Kansas) formed by the slope circulation, but so were the meso-β elements ahead of the convective squall (McAnelly and Cotton, 1986).

Some aspects of a nocturnal anvil system were simulated using this numerical model in an independent study of another MCS by Chen (1986). Her study, based on the nocturnal evolution of meso-β MCS fed by the southerly jet, revealed a distinct amplification as a result of longwave radiation heating. This is consistent with the results here which suggest this amplification is, in part, due to wave trapping.

Based on trends established in the model simulation and observational evidence, and some speculation concerning the likely feedback from the southerly jet, stage 6 may then be summarized (hypothetically) as follows (shown in Figure 9.5): after sunset, rapid destabilization of the anvil near 10 km MSL, acts to form an internal gravity wave duct (Lindzen and Tong, 1976) below. Whereas transients

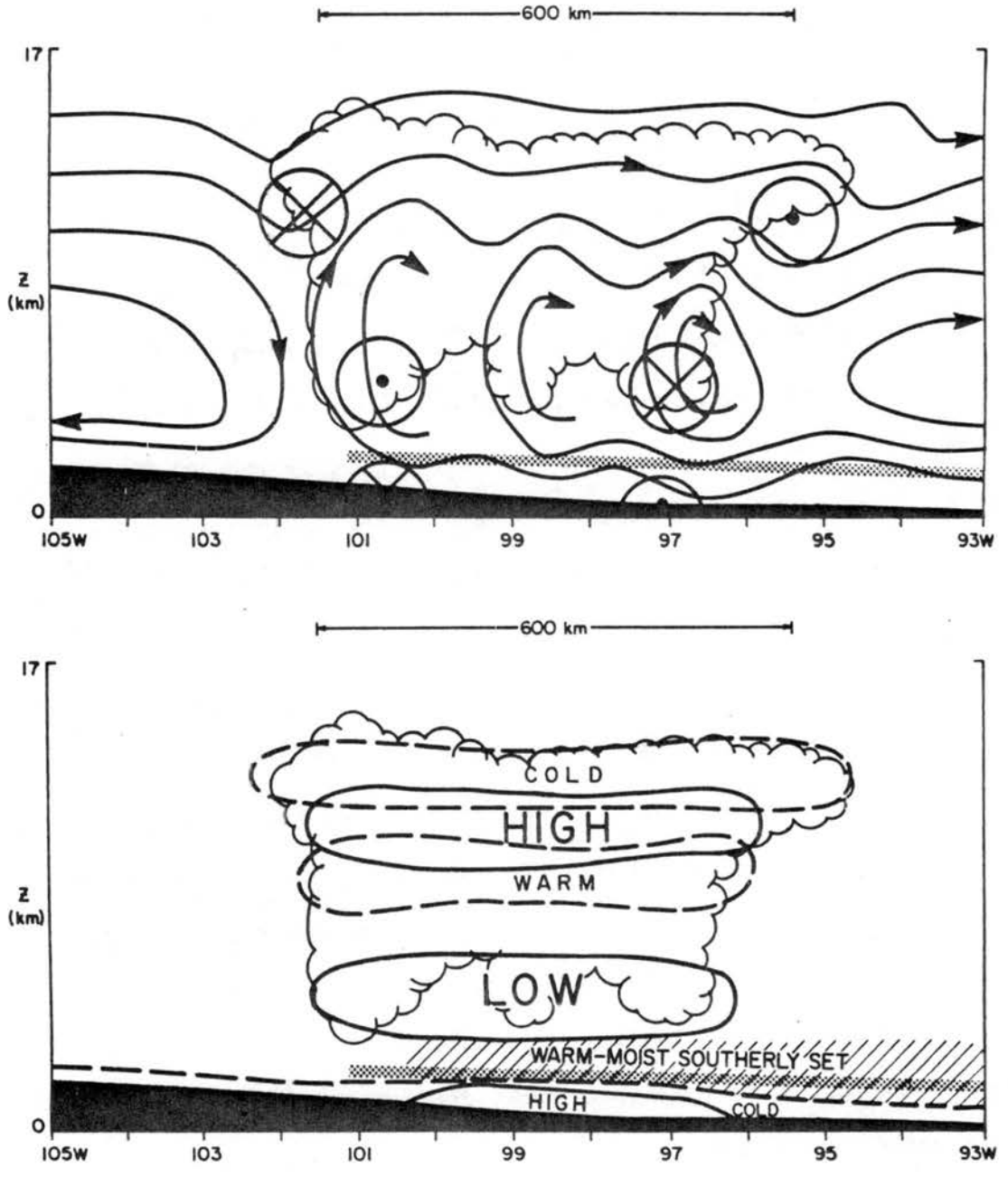

Figure 9.5. Same as Figure 9.3, except for Stage 6. Also, the region of the low level southerly jet is hatched.

(internal gravity waves) generated by cumulus meso-β-scale heating propagated primarily into the stratosphere before sunset, their energy now remains more strongly trapped within the anvil (or stratiform region). This forces associated vertical motion patterns to be maintained with high intensity several hundred kilometers laterally from the central core region.

At the same time, the system moves into the region of the low level southerly jet. This region is typified by substantial convergence of moisture and heat maximizing near the vertical level of the day time arc clouds (Purdom and Marcus, (1982), the meso-β-scale deep trapped inversion. Also, at this time, the surface has begun to cool below the threshold at which vertical meso-α or meso-β scale pressure forces can lift the air into their circulation. As a result these circulations now draw from levels near the level above the day time inversion, which is now the region of the southerly jet. In conjunction with this, the surface low pressure moves upward to mid-levels.

The rapidly horizontally propagating trapped meso-β-scale vertical motion then taps the θ_e rich air of the low level southerly jet. Initiation of convection occurs within the more favorable regions of vertical motion associated with these waves. In a completely synonymous way to the trapped internal waves of intersecting arc clouds (Purdom and Marcus, 1982) the meso-β scale deep internal trapped waves intersect with other such waves (or other boundaries) creating favorable regions for new convection formation on top of the broad southerly jet. Now meso-β convection excites more trapped waves causing the process to spread. Where as arc clouds along surface gust fronts usually move 5-15 ms^{-1}, these deep internal waves can move 20-50 ms^{-1}. The result is the

extremely rapid spread of convection over the surface of the southerly jet and within the stratiform region of trapping. The meso-α vertical motion, concentrated within a single meso-β core during the day, now is divided among many intersection points during the night.

Because the cumulus heating spreads over a diffuse region, its projection onto longer meso-α (Rossby Radius Scale) wavelengths increases. This can be expected to accelerate the growth of the meso-α balanced response. It is possible that as the meso-α horizontal circulation grows, the stratiform region of trapping becomes increasingly well defined, causing the convective heating to be more efficiently projected onto the meso-α scale and so on.

Besides the change in the nature of the distribution of convective heating, it can be expected that other traditionally treated phenomena such as the shrinking Rossby radius and mean mesoscale motions powered by anvil microphysical effects are also important to the growth of the meso-α circulation. For instance, Maddox (1982), Lin (1986) and others recognize an importance of a mid level inflow jet supplying low θ_e air near the melting level. In addition, there are the effects of synoptic scale forcing and baroclinic influences which have not been considered here.

As the meso-β scale core lessens in intensity, the pressure and temperature patterns (Figure 5.5) become more governed by the meso-α to quasi-geostrophic circulation. As a result a stacked system of broad (horizontal scales ~ 500 km) high pressure near the tropopause and low pressure near 700 mb results. Near the surface, precipitation cooled air over a broad region back to the formation of a strong surface meso-high. These features are produced by the numerical simulations of this

thesis, even in the absense of effects of the southerly jet. Lin (1986) and Maddox (1982) observe the broad temperature and pressure pattern in composites of MCC's as well.

A preliminary hypothesis to this dissertation was that the mechanism for eastward convection propagation and growth was a wave-CISK process. The results indicate this is clearly not the case. In fact, a wave CISK type disturbance was generated by using a convective parameterization. The reason for its existence was related to an invalid assumption within the parameterization. That assumption was that the existence of vertical motion at cloud base immediately results in the formation of convective heating. Because of the inversion and the short time scale of gravity wave induced vertical motion, explicit simulation of convection illustrated that the gravity wave induced vertical motion was generally unsuccessful in initiating deep convection during the day. The cases where it was successful were those where other supporting convergence deepened moisture and provided an environment of enhanced instability. This appeared to be particularly true in the radiatively destablized alto-stratus anvil cloud.

10. CONCLUSIONS AND SUGGESTIONS FOR FURTHER RESEARCH

This dissertation involved the use of a complex primitive equation non-hydrostatic model to study the formation of orogenically organized meso-β convection in the Lee of the Rockies. The following conclusions are obtained:

1. Orogenic thermally driven slope flows interact with mechanically driven mountain wave flows to initiate convection on a sustained and organized basis.
2. The orogenically organized convection deepens the normal cellular slope circulation from a depth of 5 km to the tropopause level.
3. For most efficient overturning of air within the cellular circulation, the upbranch of the cell moves with the mean tropospheric flow.
4. The persistent cellular circulation undergoes geostrophic adjustment allowing a long-lived warm convective core to build and more with mean flow! The core is supported by cyclonic sheared flow at low levels and anticyclonically sheared flow aloft. At the same time, the pressure aloft is high and the pressure at low levels is low. A shallow region of high pressure may form directly beneath the core leading to a preferred sloped inflow from the east.
5. The strongest vertical transport of moist static energy is by meso-γ convective motions, although the transport by meso-β motions on the scale of 80 km or more are nearly as great. This indicates a lack of clear separation of scales at which latent heating occurs and

which is normally assumed in a convective parameterization or om wave-CISK models (Raymond, 1983). Similiar scale relationships are found for momentum transport.

6. The unbalanced portion of the cellular circulation is transient in time. As a result, much of the energy released to the system is transported away as internal gravity wave energy. The portion which is retained acts to build a meso-α circulation on the scale of the Rossby Radius of Deformation.

7. The internal gravity wave energy is largely transported into the stratosphere by vertical propagation during the day. At night, however, enhanced destabilization of the anvil by longwave radiation traps a greater portion of the internal gravity wave energy. As a result the concentrated cellular circulation initiates several meso-β scale systems from the action of the emitted trapped internal waves. These then weaken the core and spread the upward motion throughout the meso-α circulation.

8. As the early convection moves eastward onto the plains, it undergoes strong suppression as a result of the slope circulation over varying east-west terrain slope. This suppression can be detrimental over the valleys and completely destroy the system. Since it acts to reform convection in the mountain wave/valley breeze convergence zone, another more successful movement of convection onto the plains may result at a later time.

9. The formation of precipitation was found to be critical to the maintenance of the system. Its importance seemed to be in the ability to form virga and surface precipitation ahead of the core

which acts to break the inversion. The increased net latent heating is likely, but not proven to be, essential.

10. Overall, the two dimensional approach was effective in capturing the essence of the observations. The major shortcoming was the somewhat delayed timing of initial deep convection. This was found to be a result of a lack of 'hot spots' in the initial topography.

11. The three dimensional effects are largely unknown. Some crude 3D coarse simulation results demonstrate such a high degree of unrealism in the convection structure, that they shed little light on the likely nature of the 3D effect. The alternative use of a convective parameterization was found to produce wave-CISK solutions which compare favorably with linear wave-CISK models but show little resemblance to observations (i.e., they travel too fast!). A 3D convective parameterization experiment will likely suffer for an equivalent reason and so was not attempted. It is further concluded that the approach of resolving explicit convection in 2D has revealed mechanisms of convective interaction which would be lost in the parameterization approach. Because the parameterization approach assumes much about the nature of the convection growth and maintenance to begin with, it is less than an effective tool for studying this or any problem hinging on the action of a convection ensemble.

12. It is concluded, based on early failed attempts to model the RMCC during this disseration, that it is of highest importance to model gravity wave propagation accurately. Special attention must be paid to compare the model's solution to known analytic problems as a basis of evaluation. The accurate modeling of gravity waves

requires a grid which radiates its energy laterally through the boundaries and allows them to pass upward without reflection. The accurate modeling of this phenomena then precludes the use of an expanding grid, including a pressure grid, which refracts gravity fluctuations as they move vertically upward.

13. It is important to simulate details of the surface energy budget well or model the diurnal temperature cycle accurately. This includes the emission of water vapor early and the subsequent heating of the soil. The surface moisture supply was essential to the overall maintenance of conditional instability on the plains. Without it, the boundary layer tended to mix erroneously through the plains inversion.

14. There is some evidence that in order to represent some of the important processes reported here, a non-hydrostatic framework is necessary. In particular the forced vertical oscillation of the system core may not be represented well in a hydrostatic framework. In addition the vertically trapped gravity wave activity and resultant convective response may be simulated poorly within a hydrostatic framework as it has features similiar to trapped mountain waves.

Future research on this subject is suggested in the following areas:

1. This study only represents a single case study. Other case study days with and without convection should be studied. The goal should be to gain understanding of the range of atmospheric conditions

conducive to MCS formation. It may very well turn out that several classes of MCS systems can form depending on the conditions.

2. As computers become more sophisticated, less crude 3D experiments should be attempted. The anticipated importance of 3 dimensions to the convective ensemble is only conjecture. It must be addressed if it becomes possible. Some aspects of this problem may be addressed in the more immediate future by use of a two-way nested model approach. Even with such an approach, the simulation of a range of scales represented in this two-dimensional study would be difficult. The ability to capture the important effects of extraneous convection not in the core, would be even more difficult. The nesting approach, however, can give valuable insight into some of the possible three-dimensional effects.
3. Other MCS formation zones should be studied in a similiar manner. Some known formation mechanisms which can be studied, are the dry line formation zone, soil moisture boundaries, sea breeze convergence, stalled frontal zones and others.
4. The growth of a MCS disturbance should be carried out in a more idealized setting in order to gain better insight into the growth process. Such a study should explicitly simulated convective elements in a nonhydrostatic framework if technically feasiable. This suggestion is made because of implied non-hydrostatic gravity oscillations found in this study and because of inherent assumptions within a cumulus parameterization. The goal of such a study should be to explore the relationship of the convection to the growth of a geostrophically balanced disturbance in the mid-latitudes. The pertinant questions are a) Does the secondary circulation of the

balanced meso-α scale disturbance have an important feed-back to the growth of meso-β convection or is it merely an effect? b) How does the meso-α balanced circulation act as a flywheel and lead to a long lasting convective system?...or does it? c) How does meso-β convection grow and spread within the meso-α balanced system? d) What is the affect of the meso-α circulation on trapped internal meso-β scale gravity waves? Is the heating strongly retained within the Rossby Radius by a lateral trapping? e) How does the lateral spread of meso-β convection at night impact the meso-α circulation? f) What is the impact of varying synoptic conditions on the mesoscale growth? In particular, upper and lower level divergence, jet streaks and short waves, frontal zones and the southerly jet should be studied. g) What is the nature of the interaction with the low level jet? Finally, the model developed in the idealized setting should be tested against observations.

5. Ultimately, to properly study MCS growth, vast improvements in cumulus parameterization are necessary. There are some basic problems with the traditional cloud-model parameterizations that may not be solvable for meso-β scale simulations where features on scales less than the Rossby radius of deformation are important. It is critical that the implications of the horizontal scale and vertical structure of specified cumulus heating functions be studied in the context of how these assumptions impact on the geostrophic adjustment process. Since geostrophic adjustment is probably sensitive to the scale of the heating, the scale of the heating should not be arbitrary or tied to the grid scale. To study this problem, simulations of multi-scale interaction (such as this) may

prove valuable. Also, in developing a meso-β scale convective parameritization, serious consideration of a turbulence approach should be made as an alternative to the cloud model approach.

6. Better observations would also be valuable to verify aspects of the model predictions. In particular, the convection leading to MCS growth should be better observed. It is most important to understand the extent to which meso-α or meso-β scale circulations exist prior to the onset of an MCC. This must involve 3D atmospheric observations upstream and prior to the MCC at time intervals of about one hour. Also emphasis should be placed on looking at the true variability of meso-β vertical motion. Care should be taken to resolve frequencies of fluctuation on the order of 1-2 hours with observations. This information is useful in view of the relationship between a coupled balanced regime and a transient regime.

REFERENCES

Bader, D.C. and T.B. McKee, 1983: Dynamical model simulation of the morning boundary layer development in deep mountain valleys. J. Appl. Meteorol., 22, 341-351.

Balachandran, K.N., 1980: Gravity waves from thunderstorms. Mon. Wea. Rev., 108, 804-816.

Banta, Robert Mason, 1982: An Observational and Numerical Study of Mountain Boundary-Layer Flow. Ph.D. Thesis, Colorado State University, Dept. of Atmospheric Science, Fort Collins, CO 80523, 203 pp. (Atmospheric Science Paper No. 350).

Blackadar, A.K, 1957: Boundary layer wind maximum and their significance for the growth of nocturnal inversions. Bull. Am. Meteor. Soc., 38, 283-290.

Bleeker, W., and M.J. Andre, 1951: On the diurnal variation of precipitation, particularly over central U.S.A., and its relation to large-scale orographic circulation systems. Quart. J. Roy. Met. Soc., 77, 260-271.

Bluestein, H.B. and M.H. Jain, 1984: The formation of mesoscale lines of precipitation: Severe squall lines in Oklahoma during the spring. J. Atmos. Sci., 42, 1711-1732.

Bonner, W.D., 1963: Thunderstorms and the low-level jet. Mesometeorology Research Paper No. 22, Univ. of Chicago, 21 pp.

Bonner, W.D. and J. Paegle, 1970: Diurnal variations in boundary layer winds over the south-central United States in summer. Mon. Wea. Rev., 98, 735-744.

Booker, D.P., 1963: Modification of convective storms by lee waves. Meteorological Monographs, 5(27). Severe Local Storms, American Meteorological Society, Boston, 129-140.

Braham, R.R. and M. Draginis, 1960: Roots of orographic cumuli. J. Appl. Meteor., 17, 214-226.

Brown, J.M., 1979: Mesoscale unsaturated downdrafts driven by rainfall evaporation: A numerical study. J. Atmos. Sci., 36, 313-338.

Brunk, I.W., 1949: The pressure pulsatory of 11 April 1944. Journal of Meteorology, 6, 181-187.

Burgess, D.W., and R.P. Davies-Jones, 1979: Unusual tornadic storms in Eastern Oklahoma on 5 December 1975. Mon. Wea. Rev., 107, 451-457.

Byers, H.R. and R.R. Braham, 1949: The Thunderstorm. U.S. Weather Bureau, Washington, D.C., 287 pp.

Caracena, F., R.A. Maddox, L.R. Hoxit and C.F. Chappell, 1978: Mesoanalyses of the Big Thompson Storm. Mon. Wea. Rev., 107, 1-17.

Charba, J., 1974: Application of gravity current model to analysis of squall line gust front. Mon. Wea. Rev., 102, 140-156.

Charney, J.G. and A. Eliassen, 1963: On the trapping of unstable planetary waves in the atmosphere. J. Geophys. Res., 68, 6441-6442.

Chen, C., and W.R. Cotton, 1983a: A one-dimensional simulation of the stratocumulus-capped mixed layer. Boundary-Layer Meteorol., 25, 289-321.

Chen, C., and W.R. Cotton, 1983b: Numerical experiments with a one-dimensional higher order turbulence model: Simulation of the Wangara Day 33 Case. Boundary-Layer Meteorol., 25, 375-404.

Chen, S., 1986: Simulation of the stratiform region of a mesoscale convective system. M.S. Thesis, Department of Atmospheric Science, Colorado State University, Fort Collins, Colorado 80523, 118 pp.

Clark, T.L., 1977: A small-scale dynamic model using a terrain-following coordinate transformation. J. Computational Physics, 24, 186-215.

Clark, T.L., 1981: Cloud modeling in three spatial dimensions. Hailstorms of the High Plains of North America. University of Chicago Press.

Cotton, W.R., R.L. George, and K.R. Knupp, 1982: An intense, quasi-steady thunderstorm over mountanous terrain -- Part I: Evolution of the storm-initiating mesoscale circulation. J. Atmos. Sci., 39, 328-342.

Cotton, W.R., R.L. George, P.J. Wetzel, and R.L. McAnelly, 1983: A long- lived mesoscale convective complex, Part I: The mountain generated component. Mon. Wea. Rev., 111, 1893-1918.

Cotton, W.R., R.A. Pielke, and P.T. Gannon, 1976: Numerical experiments on the influence of the mesoscale circulation on the cumulus scale. J. Atmos. Sci., 33, 2, 252-261.

Cotton, W.R., and G.J. Tripoli, 1978: Cumulus convection in shear flow-- Three dimensional numerical experiments. J. Atmos. Sci., 35, 1503-1521.

Crow, L.W., 1969: Relationships between hail and rain in Kansas, Nebraska and Eastern Colorado. LWC Report No. 76, Final Report, Contract No. NSF C522, National Science Foundation, 18th and G Streets, N.W., Washington, D.C. 20550, 34 pp.

Daly, B.J., and W.E. Pracht, 1968: Numerical study of density current surges. Phys. Fluids, 11, 15-30.

Danielson, K.S. and W.R. Cotton, 1977: SPACE LOG 1977. Dept. of Atmospheric Science, Colorado State University Report, November, 399 pp.

Davies, H.C., 1979: Phase lagged wave CISK. Quart. J. Roy. Met. Soc., 105, 325-353.

Defant, F., 1951: Local winds. Compendium of Meteorology, T.F. Malone, Ed., American Meteorological Society, Boston, pp. 655-672.

Dirks, R., J.D. Mahlman and E.R. Reiter, 1967: Evidence of a mesoscale wave phenomena in the lee of the Rocky Mountains. Atmos. Sci. Paper No. 115, Colorado State University, Dept. of Atmospheric Science, Fort Collins, CO 80523.

Dirks, R., 1969: A climatology of Central Great Plains mesoscale convective systems. Technical Report, Contract E-10-68G, Colorado State Univ., 60 pp.

Droegemeier, K.K., and R.B. Wilhelmson, 1985: Three Dimensional Numerical Modeling of Convection Produced by Interacting Thunderstorm Outflows Part I. Control simulation and low-level moisture variations. J. Atmos. Sci., 42, 2381-2403.

Dutton, J.A. and G.H. Fichtl, 1969: Approximate equations of motion for gases and liquids. J. Atmos. Sci., 26, 241-254.

Ekhart, E., 1940: "Zum Klima der freieu Atmosphare Uber USA." I, II and II. Beitr. Phys. Frei. Atmos., 26, 50-66, 77-106, 210-242.

Emmanuel, K.A., 1982: Inertial instability and mesoscale convective systems. Part II: Symmetric CISK in a baroclinic flow. J. Atmos. Sci., 39, 1080-1097.

Emmanuel, K.A., 1983: "Elementary aspects of the interaction between cumulus convection and the large-scale environment". Mesoscale Meteorology - Theories, Observations, and Models, D.K. Lilly and T. Gal-Chen (eds.), D. Reidel Publishing Co., 551-575.

Eom, J.K., 1975: Analysis of internal gravity wave occurance of 19 April 1970 in the Midwest. Mon. Wea. Rev., 103, 217-226.

Erbes, R.E., 1978: A kinematic description of some Colorado thunderstorms. M.S. Thesis, Department of Atmospheric Science, Colorado State University Fort Collins, Colorado 80523.

Fosberg, M.A., 1967: Numerical analysis of convective motions over a mountain ridge. J. Appl. Met., 6, 889-904.

Frank, W.M., 1983: The cumulus parameterization problem. Mon. Wea. Rev., 111, 1859-1871.

Fritsch, J.M., and C.F. Chappell, 1980: Numerical prediction of convectively driven mesoscale pressure systems. Part I: Convective Parameterization. Part II: Mesoscale model. J. Atmos. Sci., 37, 1722-1762.

Fujita, T.T., 1963: Analytical Mesometeorology: A Review. Meteor. Monogr., 5, 77-125.

Gal-Chen, T., and R.C.J. Somerville, 1975a: On the use of a coordinate transformation for the solution of the Navier-Stokes equations. J. Comp. Physics, 17, 209-228.

Gal-Chen, T., and R.C.J. Somerville, 1975b: Numerical solution of the Navier-Stokes equations with topography. J. Comp. Physics, 17, 276-310.

Gamache, J.F., and R.A. Houze, Jr., 1982: Mesoscale air motions associated with a tropical squall line. Mon. Wea. Rev., 110, 118-135.

Gossard, E., and W. Munk, 1953: On gravity waves in the atmosphere. J. Meterology, 11, 259-269.

Hahn, David C., 1980: Observed characteristics of turbulence in the atmospheric boundary layer over mountainous terrain. Colorado State Univ. Paper No. 332, Colorado State University, Dept. of Atmospheric Science, Fort Collins, CO 80523.

Hane, C.E., 1973: The squall line thunderstorm: Numerical experimentation. J. Atmos. Sci., 30, 1672-1690.

Hann, J. von, 1926: Lehrbuch der Meteorologie, 348-453.

Haurwitz, B., 1947: Internal waves in the atmosphere and convection patterns. Annals of the New York Academy of Science, 48, 727-748.

Hayashi, Y., 1970: A theory of large-scale equatorial waves generated by condensation heat and accelerating the zonal wind. J. Meteor. Soc. of Japan, 48, 140-160.

Henz, J., 1974: Colorado high plains thunderstorm systems - a descriptive radar-synoptic climatology. M.S. thesis, Department of Atmospheric Science, Colorado State University, Fort Collins, Colorado 80523, 82 pp.

Hewson, E.W., 1937: The application of wetbulb potential temperature of air mass analysis. Quart. J. Roy. Meteor. Soc., 63, 323.

Hill, G.E., 1974: Factors controlling the size and spacing of cumulus clouds as revealed by numerical experiments. J. Atmos. Sci., 31, 646-673.

Hodges, H., 1959: Synoptic patterns associated with hail occurrence in Northeastern Colorado. Civil Engineering Report CER59HH29, Colorado State University, Fort Collins, Colorado.

Hosler, C.L., L.G. Davis, and D.R. Booker, 1963: Modification of convective systems by terrain with local relief of several hundred meters. J. Appl. Math and Phys., 14, 410-419.

Hughes, R.L., 1978: A numerical simulation of mesoscale flow over mountainous terrain. M.S. thesis, Department of Atmospheric Science, Colorado State University, Fort Collins, Colorado 80523, 123 pp.

Johnson, R.H., 1982: Vertical motion in near-equatorial winter monsoon convection. J. Meteor. Soc. Japan, 60, 682-690.

Karr, T.W., and R.L. Wooten, 1976: Summer radar echo distribution around Limon, Colorado. Mon. Wea. Rev., 104, 728-734.

Kincer, J.B., 1916: Daytime and nighttime precipitation and their economic significance. Mon. Wea. Rev., 44, 628-633.

Klemp, J.B. and D.R. Durran, 1983: An upper boundary condition permitting internal gravity wave radiation in numerical mesoscale models. Mon. Wea. Rev., 111, 430-444.

Klemp, J.B., and D.K., Lilly, 1978: Numerical simulation of hydrostatic mountain waves. J. Atmos. Sci., 35, 78-107.

Klemp, J.B., and D.K. Lilly, 1980: Mountain waves and momentum flux. Chap. 4, GARP Publ. Ser., No. 23, Orographic Effects in Planetary Flows, ICSU/WMO, 116-141. [World Meteorological Organization, Case postale No. 5, CH-1211 Geneva 20, Switzerland.]

Klemp, J.B. and R. Rotunno, 1983: A study of the tornadic region within a supercell thunderstorm. J. Atmos. Sci., 40, 359-377.

Klemp, J.B. and R.B. Wilhelmson, 1978a: The simulation of three-dimensional convective storm dynamics. J. Atmos. Sci., 35, 1070-1096.

Klemp, J.B. and R.B. Wilhelmson, 1978b: Simulations of right- and left-moving storms produced through storm splitting. J. Atmos. Sci., 35, 1097-1110.

Klitch, M.A., J.F. Weaver, F.P. Kelly, and T.H. VonderHaar, 1985: Convective cloud climatologies constructed from satellite imagery. Submitted to Mon. Wea. Rev.

Knupp, Kevin Robert, 1985: Precipitation convective downdraft structure: A synthesis of observations and modeling. Ph.D. dissertation, Colorado State University, Dept. of Atmospheric Science, Fort Collins, CO 80523.

Kreitzberg, C.W. and D.J. Perkey, 1977: Release of potential instability: Part II. The mechanism of convective/mesoscale interaction. J. Atmos. Sci., 34, 1569-1595.

Lilly, D.K., 1962: On the numerical simulation of buoyant convection. Tellus, XIV, 2, 148.

Lilly, D.K., 1983: Dynamics of rotating thunderstorms. Mesoscale Meteorology - Theories, Observations and Models. D.K. Lilly and T. Gal-Chen, Eds., D. Reidel Publishing Co., Dordrecht, 531-543.

Lin, Ming-sen, 1986: The evolution and structure of a composite meso-α-scale convective complexes. Ph.D. Dissertation, Colorado State University, Dept. of Atmospheric Science, Fort Collins, CO 80523.

Lin, Y.L., and R.B. Smith, 1986: Transient dynamics of airflow near a local heat source. J. Atmos. Sci., 43, 40-49.

Lindzen, R.S., 1974: Wave-CISK in the tropics. J. Atmos. Sci., 31, 156-179.

Lindzen, R.S., and K.K. Tung, 1976: Banded convective activity and gravity waves. Mon. Wea. Rev., 104, 1602-1617.

Louis, J.F., 1979: A parametric model of vertical eddy fluxes in the atmosphere. Boundary-Layer Meteorol., 17, 187-202.

Maddox, R.A., 1981: The structure and life-cycle of midlatitude mesoscale convective complexes. Atmospheric Science Paper No. 336, Dept. of Atmospheric Science, Colorado State University, Fort Collins, Colorado, 80523, 311 pp.

Mahrer, Y., and R. Pielke, 1977: A numerical study of airflow over irregular terrain. Beitrage zur Physik der Atmosphare, 50, 98-113.

Marwitz, J.D., T.J. Henderson, and R.A. Schleusener, 1965: Radar climatology of hail storms in and near Northeastern Colorado 15 May - 31 July 1964. Civil Engineering Report CER65JDM19, Colorado State University, Fort Collins, Colorado. 15 pp.

McAnelly, R.L., and W.R. Cotton, 1986: Meso-β-scale characteristics of an episode of meso-α-scale convective complexes. Mon. Wea. Rev., To be published.

McCarthy, J., and S.E. Koch, 1982: The evolution of an Oklahoma dryline. Part I. A meso- and synoptic-scale analysis. J. Atmos. Sci., 39, 225-236.

McCumber, M.C., and R.A. Pielke, 1981: Simulation of the effects of surface fluxes of heat and moisture in a mesoscale numerical model. 1. Soil Layer. J. Geophys. Res., 86, 9929-9938.

McNider, T. and R.A. Pielke, 1981: Diurnal boundary layer development over sloping terrain. J. Atmos. Sci., 38, 2198-2212.

Means, L.L., 1944: The nocturnal maximum occurrance of thunderstorms in the midwestern states. Univ. of Chicago Press, Misc. Rpt. #16.

Means, L.L., 1952: On thunderstorm forecasting in the central United States. Mon. Wea. Rev., 80, 165-189.

Miller, D.A., and F. Sanders, 1980: Mesoscale conditions for the severe convection of 3 April 1974 in the East-Central United States. J. Atmos. Sci., 37, 1041-1055.

Molinari, J. and M. Dudek, 1985: Meso-α numerical experiments on rainfall prediction in a mesoscale convective complex. Seventh Conference on Numerical Weather Prediction, June 17-20, 1985, Preprint volume.

Moncrieff, M.W., 1978: The dynamical structure of two-dimensional steady convection in constant vertical shear. Quart. J. Roy. Meteor. Soc., 104, 543-567.

Moncrieff, M.W., 1981: A theory of organized steady convection and its transport properties. Quart. J. Roy. Met. Soc., 107, 29-50.

Moncrieff, M.W. and J.S.A. Green, 1972: The propagation and transfer properties of steady convective overturning in shear. Quart. J. Roy. Met. Soc., 98, 336-352.

Moncrieff, M.W., and M.J. Miller, 1976: The dynamics and simulation of tropical cumulonimbus and squall lines. Quart J. Roy. Met. Soc., 102, 373-394.

Motallebi, Nehzat, 1982: Doppler Radar Observation of the Evolution of Downdrafts in Convective Clouds. M.S. Thesis, Dept. of Atmospheric Science, Colorado State University, Fort Collins, CO 80523. (Atmospheric Science Paper No. 355).

Nehrkorn, Thomas, 1985: Wave-CISK in a baroclinic basic state. Ph.D. dissertation, Massachusetts Institute of Technology, Cambridge, Massachusetts, 171 pp.

Ogura, Y., and M.-T. Liou, 1980: The structure of a midlatitude squall line: A case study. J. Atmos. Sci., 37, 553-567.

Ooyama, K.V., 1982: Conceptual evolution of the theory and modeling of the tropical cyclone. J. Meteor. Soc. Japan, 60, 369-379.

Orlanski, I., 1975: A rational subdivision of scales for atmospheric processes. Bull. Amer. Meteor. Soc., 56, 527-530.

Orlanski, I., 1976: A simple boundary condition for unbounded hyperbolic flows. J. Comput. Phys., 21, 251-269.

Orlanski, I., and B.B. Ross, 1984: The evolution of an observed cold front. Part II. Mesoscale dynamics. J. Atmos. Sci., 41, 1669-1703.

Orville, H.D., 1964: On mountain upslope winds. J. Atmos. Sci., 21, 622-633.

Orville, H.D., 1965: A numerical study of the initiation of cumulus clouds over mountainous terrain. J. Atmos. Sci., 22, 684-699.

Orville, H.D., 1968: Ambient wind effects on the initiation of development of cumulus clouds over mountains. J. Atmos. Sci., 25, 385-403.

Paegle, J., W.G. Zdunkowski, and R.M. Welch, 1976: Implicit differencing of predictive equations of the planetary boundary layer. Mon. Wea. Rev., 104, 1321-1324.

Philipp, C.B., 1979: Observation of progressive convective interactions from the Rocky Mountain Slopes to the plains. Atmospheric Science Paper No. 316, Colorado State University, Dept. of Atmos. Sci., Fort Collins, CO, 100 pp.

Pielke, R.A., 1974: A three dimensional model of the sea breezes over South Florida. Mon. Wea. Rev., 102, 115-139.

Pielke, R.A., and Y. Mahrer, 1975: Representation of the heated planetary boundary layer in mesoscale models with coarse resolution. J. Atmos. Sci., 32, 2288-2308.

Purdom, J.F.W., and K. Marcus, 1982: Thunderstorm trigger mechanisms over the southeastern United States. 12th Conf. on Severe Local Storms, Jan. 11-15, 1982, San Antonio, Texas, 487-488.

Raymond, D.J., 1975: A model for predicting the movement of continuously propagating convective storms. J. Atmos. Sci., 32, 1308-1317.

Raymond, D.J., 1976: Wave-CISK and convective mesosystems. J. Atmos. Sci., 33, 2392-2398.

Raymond, D.J., 1983: Wave-CISK mass flux form. J. Atmos. Sci., 40, 2561-2572.

Rosenthal, S.L., 1979: The sensitivity of simulated hurricane development to cumulus parameterization details. Mon. Wea. Rev., 107, 193-197.

Ross, B.B., and I. Orlanski, 1982: The evolution of an observed cold front. Part I. Numerical simulation. J. Atmos. Sci., 39, 296-327.

Ryan, R.F., G.J. Tripoli and William R. Cotton, 1986: Virga: A trigger for the development of convective squalls. Manuscript in preparation.

Schleusener, R.A., and A.H. Auer, Jr., 1964: Hailstorms in the High Plains. Civil Engineering Report CER64RAS36, Colorado State University, Fort Collins, Colorado, 100 pp.

Schleusener, R.A., T.J. Henderson, and H. Hodges, 1963: Radar climatology of hail storms in and near Northeastern Colorado 15 May - 31 July 1963 with comments on the relation of radar climatology to selected synoptic parameters. Civil Engineering Report CER63RAS69, Colorado State University, Fort Collins, Colorado, 19 pp.

Schubert, W.H., J.J. Hack, P.L. Silva Dias, and S.R. Fulton, 1980: Geostrophic adjustment in an axisymmetric vortex. J. Atmos. Sci., 37, 1464-1484.

Scorer, R.S., 1949: Theory of airflow over mountains. Quart. J. Roy. Meteor. Soc., 75, 41-56.

Smith, R.B., 1979: The influence of the mountains on the atmosphere. Advances in Geophysics, 11, 87-230.

Stephens, G.L., 1978a: Radiation profiles in extended water clouds. Webster Theory. J. Atmos. Sci., 35, 2111-2122.

Stephens, G.L., 1978b: Radiation profiles in extended water clouds. II: Parameterization schemes. J. Atmos. Sci., 35, 2123-2132.

Sun, Wi-Yo and Y. Ogura, 1979: Boundary layer forcing as a possible trigger to a squall line formation. J. Atmos. Sci., 36, 235-254.

Tepper, M., 1950: A proposed mechanism of squall lines: The pressure jumpline. J. Meteorology, 8, 24-29.

Tepper, M., 1952: The application of the hydraulic analogy to certain atmospheric flow problems. Res. Paper No. 35, Washington, D.C., U.S. Weather Bureau, 50 pp.

Tepper, M., 1955: On the generation of pressre jumplines by the impulsive addition of momentum to simple current systems. J. Meteor., 12, 287-297.

Thorpe, A.J., M.J. Miller, and M.W. Moncrieff, 1982: Two-dimensional convection in non-constant shear: a model of mid-latitude squall lines. Quart. J. R. Meteor. Soc., 108, 739-762.

Thyer, H.H., 1966: A theoretical explanation and mountain and valley winds by a numerical method. Arch. Meteor. Geophys. Bioklim., 15(A), 318-348.

Thyer, H.H., and K.J.K. Buettner, 1962: Part A: On valley and mountain winds III; Part B: Valley wind theory. Final report, Unversity of Washington, Air Force Contract 19(604)7201.

Toth, J.J., and R.H. Johnson, 1985: Summer surface flow characteristics over Northeast Colorado. Mon. Wea. Rev., 113, 1458-1469.

Tremback, C.J., 1986: A numerical study of the synoptic-mesoscale interactions of mesoscale convective systems. Ph.D. Dissertation (in preparation), Department of Atmospheric Science, Colorado State University, Fort Collins, Colorado.

Tremback, C.J., G.J. Tripoli, and W.R. Cotton, 1984: A comparison of the performance of a hydrostatic and time-split compressible numerical model in several mesoscale applications. Presented at the International Conference on Mesoscale Meteorology , 6-10 February 1984, Melbourne, Australia.

Tremback, C.J. and R. Kessler, 1985: A surface temperature and moisture parameterization for use in mesoscale numerical models. Preprints, 7th Conference on Numerical Weather Prediction, 17-20 June 1985, Montreal, Canada, AMS.

Tripoli, G.J. and W.R. Cotton, 1980: A numerical investigation of several factors contributing to the observed variable intensity of deep convection over South Florida. J. Appl. Meteor., 19, 1037-1063.

Tripoli, G.J. and W.R. Cotton, 1981: The use of ice-liquid water potential temperature as a thermodynamic variable in deep atmospheric models. Mon. Wea. Rev., 109, 1094-1102.

Tripoli, G.J., and W.R. Cotton, 1982: The Colorado State University three-dimensional cloud/mesoscale model - 1982. Part I: General theoretical framework and sensitivity experiments. J. de Rech. Atmos., 16, 185-220.

Tripoli, G.J., and W.R. Cotton, 1986. An intense quasi-steady thunderstorm over mountainous terrain. Part IV: Three-dimensional numerical simulation. J. Atmos. Sci., 43, 896-914.

Uccellini, L.W., 1975: A case study of apparent gravity wave initiation of severe convective storms. Mon. Wea. Rev., 103, 497-513.

Uccellini, L.W., and D.R. Johnson, 1979: The coupling of upper and lower tropospheric jet streaks and implications for the development of severe convective storms. Mon. Wea. Rev., 107, 682-703.

Wagner, A., 1931: Klimatologie der freren atmosphare. Handbuch der Klimatologie. W. Koppen and R. Geiger, Hsgbr. Bd. I, Teil F.

Wagner, A., 1939: Uber die Tageswinde in der freien Atmosphare. Beitrage zur Physik der freien Atmosphare, 25, 145-170.

Wallace, J.M., 1975: Diurnal variations in precipitation and thunderstorm frequency over the conterminous United States. Mon. Wea. Rev., 103, 406-419.

Weisman, M.L., R. Rotunno and J.B. Klemp, 1985: The structure and evolution of numerically simulated squall lines. Second Conference on Mesoscale Processes, June 3-7, 1985, University Park, PA.

Weisman, M., and J. Klemp, 1982: The dependence of numerically simulated convective storms on vertical wind shear and buoyancy. Mon. Wea. Rev., 110, 504-520.

Weisman, M., and J. Klemp, 1984: The structure and classification of numerically simulated convective storms in directionally varying wind hsears. Mon. Wea. Rev., 112, 2479-2498.

Wetzel, P.J, 1973: Moisture sources and flow patterns during the Northeast colorado hail season. M.S. Thesis, Dept. of Atmospheric Science, Colorado State University, Fort Collins, CO.

Wetzel, P.J., W.R. Cotton and R.L. McAnelly, 1983: A long-lived mesoscale convective complex. Part II: Evolution and structure of the mature complex. Mon. Wea. Rev., 111, 1919-1937.

Wexler, H., 1961: A boundary layer interpolation of the low level jet. Tellus, 13, 368-378.

Williams, D.T., 1953: Pressure wave observations in the central midwest, 1952. Mon. Wea. Rev., 81, 289-295.

Xu, Q., and J.H.E. Clark , 1984: Wave-CISK and mesoscale convective systems. J. Atmos. Sci., 41 , 2089-2107.

Yamada, T., 1983: Simulations of nocturnal drainage flows by a $q^2 l$ turbulence closure model. J. Atmos. Sci., 40, 91-106.

APPENDIX A

The Numerical Model

The model used for this study is a modified form of the CSU cloud/mesoscale model described by Tripoli and Cotton (1982) and Cotton et al. (1983) which is now part of the CSU Regional Atmospheric Modeling System (RAMS). The cloud/mesoscale model is non-hydrostatic, fully elastic, employing the quasi-Boussinesq approximation described by Dutton and Fichtl (1967), for deep convection and is integrated using the "time-split" numerical technique. A "sigma-z" type terrain following coordinate system is employed. The nine predictive variables include the three cartesian velocity components (u,v, and w), exner function (, ice-liquid water potential temperature (θ_{il}), total water mixing ratio (r_T), rain water mixing ratio (r_r), ice crystal mixing ratio (r_i) and graupel mixing ratio (r_g). The following is a detailed description of the model.

A.1 The Quasi-Boussinesq System

In order to separate the high-frequency variable of density from the navier-stokes predictive equations, the quasi-Boussinesq approximation (Dutton and Fichtl, 1967) is employed. Unlike the fully Boussinesq approximation, elasticity is permitted and the base state varies with height. As a result, this system is valid for deep convection and over extensive horizontal areas as long as the departure from the base state is small.

Following Dutton and Fichtl (1969), Cotton and Tripoli (1978) and Tripoli and Cotton (1980), any variable may be decomposed as

$$A(x,y,z,t) = \bar{A}(x,y,z,t) + A''(x,y,z,t) =$$
$$A_o(z) + \overline{A'}(x,y,z,t) + A''(x,y,z,t), \qquad (A.1)$$

where the overbar represents an average over a time and space scale resolvable by the numerical model, and the double primes represent the deviations from that average. The subscript "0" refers to an arbitrary horizontally homogenous reference state, from which the resolvable deviations (detonated by a prime and referred to as perturbation quantities) should be small. The double prime represents subgrid scale fluctuations from the resolvable scale fluctuations.

The application of eq. A.1 to the Navier stokes equations lead to the existence of ratios of perturbation quantities to their base state. The quasi-Boussinesq approximation is to consistently neglect such ratios except for the case where the ratio is multiplied by gravity. Its use will be apparent throughout the following development. Since the total form of the variable in eq. A.1 is never used in the finite difference model, the overbars will be dropped from here on for convenience.

A.2 Coordinate System

The coordinate system used is identical to that reported earlier by Tripoli and Cotton (1982), but will be described again here for completeness. In order to facilitate simulations over varying topography, the terrain following coordinate system developed by Gal-Chen and Somerville (1975a,b) is employed. The cartesian coordinates x, y and z (x and y are horizontal directions, usually applied to zonal and

meridional directions respectively) are related to the transformed coordinates x^*, y^* and z^* by:

$$x^* = x \ ,$$

$$y^* = y \ , \tag{A.2}$$

$$z^* = H \ (z - z_s)/(H - z_s) \ ,$$

where H is the height of the domain and z_s is the height of the topography. Following Clark (1977), these coordinate definitions lead to the transformations of derivatives for some variable A:

$$\partial A/\partial x_i = (1/a) \ [\partial a b^{ij} A/\partial x_j^*] \ , \tag{A.3}$$

where a is given by

$$a(x^*,y^*) = 1 - z_s(x^*,y^*)/H = \partial z/\partial z^* \tag{A.4}$$

and the tensor b^{ij} is defined

$$b^{ij} = \begin{bmatrix} 1 & 0 & \frac{1}{a}\frac{\partial z_s}{\partial x}\left[\frac{z^*}{H} - 1\right] \\ 0 & 1 & \frac{1}{a}\frac{\partial z_s}{\partial y}\left[\frac{z^*}{H} - 1\right] \\ 0 & 0 & \frac{1}{a} \end{bmatrix} \ . \tag{A.5}$$

These transformations then lead to the following relationship between the cartesian velocity components (u,v,w) and their transformed counterparts:

$$u^* = u$$

$$v^* = v \tag{A.6}$$

$$w^* = (uab^{13} + vab^{23} + w) / a$$

A.3 Thermodynamics

The thermodynamics employed remain essentially the same as those reported by Tripoli and Cotton (1982), except that the roles of perturbation density as a predictive quantity and perturbation pressure as a diagnostic quantity have been reversed. For convenience, pressure is predicted in the form of exner function (π). These changes were necessitated because of shortcomings found when comparing results of the density based formulation to linear theory.

The thermodynamic system is composed of the predictive variables θ_{il}, r_T, r_r, r_i, and r_g. The exner function is defined:

$$= C_p(P/P_{oo})^{R/C_p} . \tag{A.7}$$

where C_p is the specific heat capacity for dry air at constant pressure, P is the total ambient air pressure, P_{oo} is 100 kPa, and R is the gas constant for dry air. From Tripoli and Cotton (1981), the empirical relationship for θ_{il} is given by:

$$\theta = \theta_{il}\left[1+\frac{L_{vl}r_l + L_{iv}r_{ice}}{C_p MAX(T,253)}\right] \tag{A.8}$$

where the potential temperature θ and the temperature (T) are related to each other by Poisson's equation, given by:

$$T = \theta \frac{\pi}{C_p} . \tag{A.9}$$

The liquid water (r_l) and ice water (r_{ice}) mixing ratios are defined by:

$$r_l = r_c + r_r \tag{A.10}$$

and

$$r_{ice} = r_i + r_g . \tag{A.11}$$

The latent heats of condensation and sublimation are L_{vl} and L_{iv}, respectively.

Cloud water (r_c) and vapor (r_v) are diagnosed from r_T, r_r, and r_{ice} assuming zero supersaturation. If $r_{vs}(T,P)$ is the saturation mixing ratio of liquid over vapor, the relations for cloud water and vapor are:

$$r_c = \text{Max}(r_T - r_{vs} - r_r - r_{ice}, 0 .) \tag{A.12}$$

and

$$r_v = r_T - r_l - r_{ice} \tag{A.13}$$

Equations A.8-A.13 can be solved iteratively (see Tripoli and Cotton, 1982) to produce a diagnosis of T, θ, r_{vs}, r_v, and r_c from predictions of θ_{il}, , r_T, r_i, r_g, and r_r.

In order to force complete freezing at a specified homogenous nucleation temperature (T_H), the above set of equations is changed as follows, when $T < T_H$:

$$r_c = 0$$

$$r_r^* = 0 \qquad \text{(A.14)}$$

$$r_i^* = r_i + r_r + \text{MAX}(r_T - r_{vs} - r_{ice}, 0.)$$

where the asterisk means temporary values during iteration. After iteration the permanent values of r_r and r_i are altered to the temporary values.

Instead of diagnosing perturbation density for the vertical equation of motion, it is convenient to write perturbation density (ρ') as a function of predictive quantities. As with Tripoli and Cotton (1982), the quasi Boussinesq approximation is applied to the equation of state to produce the relationship:

$$\rho'/\rho_o = (1/\gamma)P'/P_o - \theta'/\theta_o + 1.61r_v \ , \qquad \text{(A.15)}$$

where γ is;

$$\gamma = \frac{c_p}{c_v} \qquad \text{(A.16)}$$

and where c_v is the specific gas constant for dry air at constant volume. The base state is taken to be dry, and in hydrostatic balance, and satisfies the ideal gas law.

A.4 Time Dependent Equations

The quasi-Boussinesq equations of motion in tensor form are:

$$\frac{\partial}{\partial t}\rho_o u_i + \frac{\rho_o \theta_o}{a}\frac{\partial ab^{ij}}{\partial x_i^*}\pi' = \text{ADV}(\rho_o u_i) + \rho_o \text{TURB}(u_i)$$

$$+ g(\theta'/\theta_o + 1.61r_v - r_T)\delta_{i3} + \varepsilon_{ijk} f_3 (\bar{u}_{ik} - u_{ok}) \qquad (A.17)$$

where the advective operator (ADV) and turbulence operator (TURB) are defined later, g is the acceleration of earth's gravity, SM is a numerical smoother, f is vertical component of coriolis vorticity, and δ_{i3} is the Kronecker delta function. The coriolis acceleration term is affected only by perturbation velocity which is nearly equivalent to assuming the basic state is in geostrophic balance, except that the reference state is assumed horizontally homogenous. If applied to systems of light winds and limited domain sizes the error involved with this approximation is small. For this study a domain of one thousand kilometers in the x direction and up to 200 km in the y direction will be used. Because the base state meridional winds are light and the domain is either two dimensional in the x direction or relatively small in the y direction, the neglect of implied horizontal variations of the reference state should be unimportant.

The exner function tendency, defined in the same way as Klemp and Wilhelmson (1978), is given by:

$$\frac{\partial \pi'}{\partial t} + \frac{1}{a} \frac{R}{c_v} \frac{\pi_o}{\rho_o \theta_o} \frac{\partial}{\partial x_j^*} (ab^{ij} \rho_o \theta_o u_j) = 0 \qquad (A.18)$$

where several terms have been neglected. As demonstrated by Klemp and Wilhelmson (1978), Durran (1981) and tests by Chen (personal communication) with this model, the assumption is of negligible consequence and strongly increases the efficiency of the code.
The thermodynamic energy equation is given by:

$$\frac{\partial \rho_o \theta_{il}}{\partial t} = ADV(\rho_o \theta_{il}) + \rho_o TURB(\theta_{il}) + \rho_o S(\theta_{il}) \tag{A.19}$$

where S is an operator representing a source or sink to θ_{il}. Since θ_{il} is conserved over all water phase changes, S is due only to the effects of precipitation movement relative to the parcel (see Tripoli and Cotton, 1982) and radiational diabatic heating. Equations (A.17-A.19) represent a complete system of equations for a dry system. When moisture is present, the mass continuity equations for water substance are:

$$\frac{d\rho_o r_k}{dt} = ADV(\rho_o r_k) + \rho_o TURB(r_k) + PR(\rho_o r_k) + \rho_o S(r_k) \tag{A.20}$$

where k represents any of the water mixing ratio categories (T, r, i, g), S is the source or sink of r_k, and PR is the precipitation advection tendency given by:

$$PR(r_k) = \begin{cases} -1/(a\rho_o)\ \partial(\rho_o V_k r_k)/\partial x_3^* & k \neq T \\ \sum_{k \neq T} PR(r_k) & k = T \end{cases} \tag{A.21}$$

where V_k is the mean terminal velocity for the mixing ratio category k and ρ_o is reference state air density.

Equations (A.17-A.20) are a complete set of time dependent equations for a moist system. All 'acoustic terms', or those containing sound waves are given by the terms on the left hand side of equations (A.17-18) as deciphered by Klemp and Wilhelmson (1978) and used by others. This separation is made so the system can be integrated using the 'time Split' numerical technique, to be described later. Next a

brief description of the advective operator, turbulence operator, and source/sink operators will be given.

A.5 Advective Operator

For any dependent variable A, the advective operator is given by:

$$ADV(\rho_o A) = -(1/a)[\partial/\partial x_k^*(ab^{jk}\rho_o u_j A) - A\ \partial/\partial x_k^*(ab^{jk}\rho_o u_j)] \qquad (A.22)$$

where j,k range from 1 to 3. The advective operator is purposely written as the difference between a mass flux divergence term and a momentum divergence term to increase numerical conservation. The flux divergence term may be finite differenced to conserve mass exactly, leaving the momentum divergence term as a possible net source or sink to A, when integrated over the entire domain. Since A is a specific quantity, i.e. 'amount per mass of dry air', local tendencies in A must account for both the change in mass weighted A and the mass of air. For an anelastic model, the local tendency of air density simply disappears. Because these elastic fluctuations have high frequencies, their treatment as a low frequency term may lead to numerical difficulties. However, to the extent that the system tends toward anelasticity, the numerical impact of this elastic effect should be small.

A.6 Turbulence Parameterization and Numerical Smoothing

The turbulence parameterization has undergone some important redesign since its former description by Tripoli and Cotton (1982) and hence will be formulated here in some detail. While remaining basically a down gradient mixing process, the buoyancy enhancement process has been improved. The basic form of the operator remains the same as:

$$TURB(A) = -(1/a)\ \partial/\partial x_k^*[ab^{jk}\overline{(A'' u_j'')}] \qquad (A.23)$$

where the turbulent flux term is parameterized as:

$$\overline{-u_i'' u_j''} = (K_{m_j}/a)[\partial/\partial x_l^*(ab^{jl}\bar{u}_i) + \frac{\partial}{\partial x_l^*}(ab^{il}u_j)] \tag{A.24}$$

for velocity variables and

$$-A''u_j'' = (K_{H_j}/a)[\partial/\partial x_l^*(ab^{il}A)] \tag{A.25}$$

for scalar variables. The eddy exchange coefficients for momentum and heat (and all non-velocity quantities) are given by K_{m_j} and K_{H_j} and are related to each other by:

$$K_{H_j} = 3K_{m_j} \quad . \tag{A.26}$$

The turbulent fluxes at the surface are specified via a surface layer parameterization described below.

The form of the eddy exchange coefficient has changed somewhat from Tripoli and Cotton (1982), and is currently written:

$$K_{m_j} = [(0.25)\ \sqrt{2}](l_j^2\ [D + \{MAX\ (-N^2,\ 0)\}^{1/2}] \tag{A.27}$$

where l_j is the scale length used for application to the j direction, D is the deformation defined as:

$$D^2 = \left[\sum_j \sum_k (\partial u_j/\partial x_k + \partial u_k/\partial x_j)^2\right]^{1/2} \tag{A.28}$$

and N is the Brunt-Vaisalla frequency defined as:

$$N^2 = g/\theta \ (\partial \theta/\partial z) \quad . \tag{A.29}$$

The additional use of N with D was suggested by Hill (1975). Tests of its use within this parameterization demonstrated superior representation of boundary layer development. As with Tripoli and Cotton (1982), a different scale length is applied to the vertical than is applied to the horizontal to represent preferred vertical buoyant mixing in situations where higher vertical than horizontal resolution is used. Also a slight change in the philosophy of the buoyancy enhancement has been made, whereas the buoyancy enhancement is to the vertical scale length only, rather than the whole eddy viscosity. The new mixing length definition is:

$$l_1 = l_2 = (\Delta x^2 + \Delta y^2)^{1/2}$$

$$l_1^2 = \text{MIN}\{L_1^2 \text{Min}[(1-K_H/K_m Ri)^{1/2}, 1], \Delta x\} \tag{A.30}$$

and where L_1 is defined as:

$$L_1^2 = L_1^2 = \begin{cases} 0 & Ri > 0.25 \\ (\Delta z)^2 & 0.25 \leq Ri \geq 0 \\ -(z-z_1)^2 & Ri < 0 \end{cases} \tag{A.31}$$

and where z_1 is the nearest grid level below the current level having a potential temperature less than the current grid level, or the surface.

The Richardson number is given by:

$$Ri = N^2/D^2 \quad . \tag{A.32}$$

Using this diagnostic turbulence, considerable success has been obtained in simulating daily boundary layer development. In fact, comparisons of this parameterization to the Yamada (1983) 2.5 level closure scheme, which is also a functioning option in the RAMS framework, shows no appreciable difference when applied to the simulation of the daytime boundary layer. Its application to cumulonimbus simulations has shown it to perform sufficiently, although some there are some limitations. In particular, as resolutions become coarse, subgrid scale microphysical processes are not represented, nor is the important process of cloud top entrainment well represented. The economy and simplicity of this scheme, however, make it ideal for a study of this type.

Because the turbulence parameterization is only activated in regions where deformation or thermal instability is present, mixing may be almost entirely shut down over much of the domain. Also, poor numerical resolution can lead to undesirable numerical 'noise', in the form of short wave length fluctuations which cannot be handled accurately by the 2nd and 4th order differencing schemes. In order to control the development of these features, a short wavelength 4th order filter is optionally added to the equations.

The form of this filter is taken from Klemp and Wilhelmson (1978), and is given by:

$$SM(A) = K_s\left[(\partial/\partial x)^4 + (\partial/\partial y)^4\right] A \qquad (A.33)$$

where the smoothing coefficient (K_s) is defaulted to 0.0025. The use of this filter by Durran (1981) was somewhat different to the above form. In his application, only the perturbations from the base state were smoothed. This filter is used rather than a background K_m, as Tripoli

and Cotton (1982), because it is highly selective on removing only short wavelengths. For instance, if the diffusion coefficients for a second order and fourth order scheme are chosen so smoothing is equal at he $2\Delta x$ wavelength, then the fourth order smoother will smooth only .25 as much over a single iteration as the 2nd order at $6\Delta x$. When applied over many timesteps, the difference will be substantially greater.

A.7 Surface Layer Parameterization

The surface layer parameterization of vertical heat, vapor and momentum fluxes is based on the Louis (1979) scheme. The scheme provides fluxes as a function of vertical gradients of θ, r_v, u and v between the top of the surface layer at height z and the surface. For the application to RAMS, the height of the surface layer is taken as the height of the first integrated theta point above the surface. For the simulations in this study, this was 250m.

While u and v are assumed to vanish at the surface, values of θ and r_v are predicted from the upper level of a multilevel prognostic soil model developed by McCumber and Pielke (1981) and modified for RAMS by Tremback and Kessler (1985). At the upper soil level, a surface energy balance is formed among the predicted terms of longwave radiation loss of heat to the atmosphere, longwave gain from atmospheric emission, shortwave radiation gain from direct and scattered solar radiation, downward diffusion of heat into the soil, loss to eddy transfer of sensible heat upward, loss due to vertical eddy transport of latent heat, and loss due to sensible and latent cooling by precipitation. All of the above terms except the surface longwave emission and downward diffusion of heat are calculated independently from the soil model. Likewise, for moisture, a surface balance is formed among terms for

upward diffusion from the deep soil, loss upward by vertical eddy transport, and gain by moistening effects of predicted precipitation.

Because the scheme is applied prognostically, rather than diagnostically as with McCumber and Pielke (1981), the above terms do not form an exact balance at any given time. Instead, they tend toward a balance over a period of several timesteps. The result is that the degree of balance is slightly timestep dependent, but is very efficient.

A.8 Radiation

The longwave and shortwave radiation parameterization developed by Chen and Cotton (1983) is employed. The longwave scheme takes into account of both the effects of clear air and cloudy air absorption. Within clear air, the effects of both water vapor and carbon dioxide absorption are predicted. The parameterization of cloud effects is based on an empirically derived scheme proposed by Stephens (1978).

The shortwave parameterization considers effects of absorption, reflection and scattering in both clear and cloudy conditions. Absorption by both water vapor and ozone are considered. Within a cloudy atmosphere, short wave absorption is based on Stephens (1978a,b).

The parameterization of both long wave and shortwave absorption by clouds assumes a cloud droplet form and does not recognize variations in droplet size distribution nor the existence of ice. Stephens (personal communication) feels this is only a minor shortcoming, however.

A.9 Microphysics

The microphysics parameterization is essentially identical to that reported by Cotton et al. (1983). In this scheme, the precipitation categories of rain droplet mixing ratio, pristine ice crystal mixing ratio, and graupel mixing ratio are predicted. Although a more complex

version of the ice parameterization ia available to RAMS (see Cotton et al., 1986), the additional computer resources necessary to implement it for this study led to the decision to use the less complex version reported earlier.

This decision was made for two main reasons. First, this was to be primarily a dynamic study of a wave phenomena rather than a detailed microphysical study. It was therefore decided that it would be more appropriate to devote the limited resources to increases in grid resolution, rather than more complex microphysics. Secondly, this author's recent participation in the International Cloud Modeling Workshop held in Aspen, Colorado in 1983 and Irsee, FGR in 1985 led to the observation that the inclusion of complex microphysics within cloud models in large part fails to verify with cloud physics observations. Therefore, given the strong need for the computer resources by the dynamics prediction, it was felt that it would be wasteful to use it to predict extra precipitation categories for which the level of skill is highly questionable.

A.10 Finite Differencing

All finite differencing is carried out on the staggered grid described by Tripoli and Cotton (1982). Briefly, the simulation domain is divided into a series of rectangular volumes (or rectangles for 2D) where non velocity time dependent variables are defined at the box center and are thought to represent their average over the volume. Velocity components are defined on the face of the box in the direction of the component, and are taken to represent the average flow between boxes. The lowest box rests on the ground and hence the mean flow through the bottom is zero.

The above set of time dependent and associated diagnostic equations are a complete set of complex partial differential equations that have a unique solution given initial conditions and spatial boundary conditions. The basic numerical approach is to integrate the acoustically active terms, described above, with a small timestep while the remaining slow frequency terms are integrated on a small time step. The very slow response radiation tendency is integrated on a very long time step.

The space and time differencing schemes used have changed somewhat from the earlier report by Tripoli and Cotton (1982). In order to obtain efficiency with accuracy several differencing schemes are employed. The basic time march remains in the form of a Leap-Frog scheme, operating on the advective terms, the precipitation terms, the buoyancy term (3rd term on the RHS of eq. A.18), and the coriolis acceleration terms. The advective terms employ fourth order differencing in the horizontal and second order in the vertical. This was done because higher order vertical differencing was found to lead to increased 'ringing' associated with sharp cutoffs in precipitation variables. The ringing leads to numerical adjustments for negative mixing ratios which then produce an undesirable temperature response. There is currently an effort to find a more accurate scheme, perhaps one which is positive definite, which will prevent these problems.

The horizontal turbulence terms (TURB) are integrated in a forward sense along the two time-step leap of the leapfrog advection term. The vertical part of the turbulence operator is integrated using the Crank-Nicholson scheme suggested by Paegle et al. (1976). Using this approach, the prior need to truncate high mixing coefficients is

unnecessary. The numerical smoothing operator, SM, is also differenced with a forward scheme.

The acoustic frequency tendencies of pressure gradient and heat divergence (within the pressure equation) are calculated using a second order forward/backward operator for the horizontal terms. As with Klemp and Wilhelmson (1978), terms containing vertical gradients are integrated using Crank-Nicholson implicit scheme. This prevents relatively high vertical resolutions from influencing the small timestep, significantly increasing the economy of the scheme when the ratio of vertical to horizontal grid spacing falls below 0.5. When the vertical and horizontal resolutions are comparable, the fully explicit forward backward scheme is optional.

Tendencies calculated from physical parameterizations, such as the microphysics or surface layer parameterization, are calculated in a forward sense. This is done in order to inhibit leapfrog solution "splitting". It was found that leap frog integration of these terms leads to splitting because forcing in one solution produces a reaction in the other. Then, the other solution's reaction to the forcing promotes a response within the forcing solution. The result is that the solutions increasingly diverge from each other.

The forward integrations of the radiation and convective parameterization tendencies are performed on a long time step of several leap frog steps in length. They are computed from the past time level and so as the ratio of their time step to the $2\Delta t$ leap frog step approaches 1, they become pure forward schemes.

A.11 Spatial Boundary Conditions

The lower boundary condition of the atmosphere is specified from the surface layer parameterization which provides turbulent fluxes of heat, vapor and momentum. For mean resolvable fluctuations, the boundary is assumed to be free slip, and the vertical profile of perturbation pressure is linear. Also, mean vertical motion normal to the lower surface is assumed to vanish, removing any need to specify most variables at the surface.

The top boundary condition used for this study is the Klemp and Durran (1983) normal mode gravity wave radiation condition which is applied to the pressure. This boundary condition is derived to allow the free upward propagation of gravity waves through the model top for linear hydrostatic steady state waves. Klemp and Durran (1983) have also shown reasonably good results for nonlinear non-hydrostatic waves as well. Tests of this condition for the application to this study also indicate exceptionally good results. The normal mode condition on pressure is applied implicitly during the evaluation of the Crank-Nicholson small timestep. The Crank-Nicholson scheme involves the formation of a tri-diagonal matrix system in the vertical which is evaluated using an "up-down" solver. The normal mode condition is applied after the "up" pass as a boundary condition for the "down" pass. For all other quantities, forward upstream differencing is used on outflow and the base state vertical gradient on inflow.

For lateral boundary conditions, a gravity wave radiation scheme is used in conjunction with a mesoscale compensation region (MCR) as described by Tripoli and Cotton (1982). The radiation condition used is the modified Klemp and Lilly (1978) scheme described by Durran (1981).

This boundary condition has the advantage that the predicted vertical profile of momentum at the boundary is a linear combination of the previous flow at the boundary and the flow at the vertical grid column adjacent to the boundary. Unlike a pure Orlanski (1976) or Klemp and Wilhelmson (1977) radiation condition, large imbalances of horizontal momentum flux integrated in the vertical do not occur which lead to domain scale pressure trends. This seems to be especially valuable in simulations of flow over topography where a mountain barrier tends to rearrange the vertical profile of horizontal momentum severely. The lateral boundary conditions for turbulent fluxes assume free slip.